

REPORT DOCUMENTATION PAGE				Form Approved OMB No. 0704-0188	
Public reporting burden for this collection of information is estimated to average 1 hour per response, including the time for reviewing instructions, searching existing data sources, gathering and maintaining the data needed, and completing and reviewing the collection of information. Send comments regarding this burden estimate or any other aspect of this collection of information, including suggestions for reducing the burden, to Department of Defense, Washington Headquarters Services, Directorate for Information Operations and Reports (0704-0188), 1215 Jefferson Davis Highway, Suite 1204, Arlington, VA 22202-4302. Respondents should be aware that notwithstanding any other provision of law, no person shall be subject to any penalty for failing to comply with a collection of information if it does not display a currently valid OMB control number. PLEASE DO NOT RETURN YOUR FORM TO THE ABOVE ADDRESS.					
1. REPORT DATE (DD-MM-YYYY) 30-10-2006		2. REPORT TYPE Conference Proceedings		3. DATES COVERED (From – To) 12 September 2005 - 16 September 2005	
4. TITLE AND SUBTITLE MICROMECHANICS AND MICROSTRUCTURE EVOLUTION: Modeling, Simulation and Experiments				5a. CONTRACT NUMBER FA8655-05-1-5027	
				5b. GRANT NUMBER	
				5c. PROGRAM ELEMENT NUMBER	
				5d. PROJECT NUMBER	
6. AUTHOR(S) Conference Committee				5d. TASK NUMBER	
				5e. WORK UNIT NUMBER	
7. PERFORMING ORGANIZATION NAME(S) AND ADDRESS(ES) Polytechnic University of Madrid E. T. S. de Ingenieros de Caminos Madrid 28040 Spain				8. PERFORMING ORGANIZATION REPORT NUMBER N/A	
9. SPONSORING/MONITORING AGENCY NAME(S) AND ADDRESS(ES) EOARD PSC 821 BOX 14 FPO AE 09421-0014				10. SPONSOR/MONITOR'S ACRONYM(S)	
				11. SPONSOR/MONITOR'S REPORT NUMBER(S) CSP 05-5027	
12. DISTRIBUTION/AVAILABILITY STATEMENT Approved for public release; distribution is unlimited. (approval given by local Public Affairs Office)					
13. SUPPLEMENTARY NOTES					
14. ABSTRACT The aim of this conference is to bring together scientists who are working on the modeling and simulation of the deformation behavior of materials, and on material microstructural evolution. The focus will be on the interplay between behaviors at different length scales, in particular the atomistic, nano/mesoscales, and continuum aspects necessary to describe the processes that lead to changes in microstructure. Of particular interest are investigations that discuss the bridging of length scales, and the prediction of material properties from theory and computation. Experimental validation of the approaches is also important to differentiate between competing theories. Novel experimental techniques, to guide or verify the modeling and simulation efforts, also pertain to the theme of the conference. The session topics are: Atomistic, Dislocation Dynamics, Microstructure Evolution, Continuum, and Experimental.					
15. SUBJECT TERMS EOARD, Modeling & Simulation, Structural Materials, Micromechanics, Nanotechnology					
16. SECURITY CLASSIFICATION OF:			17. LIMITATION OF ABSTRACT UL	18. NUMBER OF PAGES 95	19a. NAME OF RESPONSIBLE PERSON KEVIN J LAROCHELLE, Maj, USAF
a. REPORT UNCLAS	b. ABSTRACT UNCLAS	c. THIS PAGE UNCLAS			19b. TELEPHONE NUMBER (Include area code) +44 (0)20 7514 3154

Micromechanics and Microstructure Evolution: Modeling Simulation and Experiments



**September 12-16, 2005
Madrid, Spain**



SCOPE OF THE CONFERENCE AND MAJOR THEMES

This conference will bring together scientists who are working on the modeling and simulation of the deformation behavior of materials, and material microstructural evolution.

The focus will be on the interplay between behaviors at different length scales, in particular the atomistic, nano/mesoscales, and continuum aspects necessary to describe the processes that lead to changes in microstructure. Of particular interest are investigations that discuss the bridging of length scales, the prediction of material properties from theory and computation, and the experimental validation of such approaches.

Experimental validation is also important to differentiate between competing theories. Novel experimental techniques, to guide or verify the modeling and simulation efforts also pertain to the theme of the conference.

This conference will provide a forum for exchange of ideas, collaborations and future directions by scheduled roundtable discussion sessions, besides regular presentations.

Main Topics:

1. Single and multi-phase behavior of metals and alloys, crystalline and amorphous systems (defects, defects dynamics and grain boundary controlled mechanisms and reinforcements).
2. Microstructural evolution (Recrystallization, nucleation, grain growth, precipitation kinetics).
3. Novel experimental techniques on deformation and microstructural evolution.
4. Simulation techniques (atomistic, discrete dislocation, phase field, Monte Carlo, level set and numerical techniques, for constitutive models and homogenization theories in continuum mechanics, FEM, BEM).
5. Quasicontinuum, multiscale and parallel computational approaches.

Preface

This issue of Acta Materialia comprises a set of select contributions from the meeting “Micromechanics and Microstructure Evolution: Modeling, Simulation and Experiments”, held in Madrid, Spain, September 11–16, 2005. The aim of this conference was to bring together scientists who are working on the modeling and simulation of deformation behavior and microstructural evolution in materials. The focus was on the interplay between behaviors at different length scales, in particular the atomistic, nano-scale, and continuum descriptions of processes that lead to changes in microstructure. Of particular interest were investigations that discussed the bridging of length scales, and the prediction of material properties from theory and computation. Papers dealing with the experimental validation of the approaches were also important to differentiate between competing theories, including novel experimental techniques, to guide or verify the modeling and simulation efforts.

The meeting brought in over 150 researchers from industry and academia from 27 countries. A total of 15 plenary lectures, 25 invited lectures, 60 oral communications and over 30 posters were presented during the five days of the conference. We, the organizers, were honored by the great response and by the quality of the presentations, which exceeded our expectations. The papers in this issue are representative of the depth and high quality of the work presented at the meeting. The conference was followed by a Satellite Workshop on “Ductile Fracture and Damage”, organized by Professors D. Wilkinson and D. Embury (McMaster University) and

Professors C. González and J. Segurado (Polytechnic University of Madrid) on September 16th–17th.

Most of all, we would like to thank the participants for making the meeting a success. We would like to thank Günter Gottstein for his assistance in editing and publishing these articles. The meeting would also not have been possible without our sponsors, including the Acta Materialia board, the Spanish Ministry of Science and Education, the Polytechnic University of Madrid, the Office of Naval Research Global (ONRG) and the European Office of Aerospace Research and Development (EOARD). Organizational support was provided by Engineering Conferences International.

S.B. Biner

Ames Laboratory/Iowa State University, USA

J. LLorca

Polytechnic University of Madrid, Spain

J.R. Morris

*Oak Ridge National Laboratory/University of Tennessee,
USA*

L. Kubin

LEM CNRS-ONERA, France

Y. Shibutani

Osaka University, Japan

Available online 12 May 2006

The glide of screw dislocations in bcc Fe: Atomistic static and dynamic simulations [☆]

Julien Chaussidon, Marc Fivel, David Rodney ^{*}

Génie Physique et Mécanique des Matériaux (UMR CNRS 5010), Institut National Polytechnique de Grenoble, 101 rue de la Physique, 38402 Saint Martin d'Hères, France

Received 12 October 2005; received in revised form 24 February 2006; accepted 23 March 2006
Available online 19 June 2006

Abstract

We present atomic-scale simulations of screw dislocation glide in bcc iron. Using two interatomic potentials that, respectively, predict degenerate and non-degenerate core structures, we compute the static 0 K dependence of the screw dislocation Peierls stress on crystal orientation and show strong boundary condition effects related to the generation of non-glide stress components. At finite temperatures we show that, with a non-degenerate core, glide by nucleation/propagation of kink-pairs in a {110} glide plane is obtained at low temperatures. A transition in the twinning region, towards an average {112} glide plane, with the formation of debris loops is observed at higher temperatures.

© 2006 Acta Materialia Inc. Published by Elsevier Ltd. All rights reserved.

Keywords: Molecular dynamics; Dislocation mobility; Iron

1. Introduction

The origin for the specific plastic behavior of bcc metals at low temperatures can be traced down to the non-planar extended core configuration of the screw dislocations in these materials [1]. The latter configuration implies a large value for the lattice-friction Peierls stress, overcome by the gliding screw dislocations with the help of thermal activation. In the present paper, bcc α -Fe is of specific interest.

At the macroscopic scale, plastic properties of bcc metals have been extensively studied, mostly by means of uniaxial tension/compression tests (for a review, see Ref. [2]; for α -Fe, see Refs. [3–5]). A key observation is that, at low temperature, bcc metals do not follow the Schmid law, which states that glide on a given slip system starts

when the Resolved Shear Stress (RSS) on that system reaches a critical value. There are two types of deviations [6]: first, the critical RSS depends on the sign of the applied stress (which is a consequence of the twinning/antitwining asymmetry of the bcc lattice), and second, the critical RSS is influenced by non-glide components of the applied stress tensor. The latter are of two types [7]: shear stresses in the Burgers vector direction acting on planes other than the glide plane, and shear stresses perpendicular to the Burgers vector.

At the atomic scale, the study of bcc screw dislocations was one of the first applications of atomistic simulations to plasticity (see [8]; for a recent review, see [9]). However, one has to be cautious about the results of these simulations for several reasons. First, different interatomic potentials may predict different core structures, even for the same material [6,10,11]. In the case of α -Fe, earlier simulations using pair potentials [8] and later calculations with many-body embedded atom method (EAM) potentials [12,13] predicted a *degenerate* core, spread asymmetrically on the three {110} planes of the [111] zone, yielding two distinct

[☆] This manuscript was presented at the “Micromechanics and Microstructure Evolution: Modeling, Simulation and Experiments” held in Madrid/Spain, September 11–16, 2005.

^{*} Corresponding author. Tel.: +33 4 76 82 63 37; fax: +33 4 76 82 63 82.
E-mail address: david.rodney@inpg.fr (D. Rodney).

and equivalent configurations related by a diadic symmetry around a $\langle 110 \rangle$ axis normal to the dislocation line. However, more recent and accurate structure calculations based on the density functional theory (DFT) yielded a *non-degenerate* core [14], spread symmetrically into the three $\{110\}$ planes. This structure is now predicted by the latest EAM potentials [15].

Second, most atomic-scale simulations in α -Fe [12,13] cannot be reconciled with experiments because they predict average $\{112\}$ glide planes, while experimentally at low temperature, glide is observed on $\{110\}$ planes (except when the Maximum Resolved Shear Stress Plane (MRSSP) is close to $\{112\}$) [3]. In particular with degenerate cores, even if in most simulations the MRSSP is a $\{110\}$ plane, the screw dislocations glide on an average $\{112\}$ plane by elementary steps on two $\{110\}$ planes.

Finally, dynamic simulations at finite temperature are computationally expensive because accurate results require large 3D simulation cells, with long dislocation segments in order to capture double-kink nucleation/propagation events, which are the finite temperature glide mechanism. Most simulations are therefore static and quasi-2D. Only recently [13] were large 3D simulations performed, with a potential yielding a degenerate core. This study confirmed the double-kink mechanism with an average $\{112\}$ twinning glide plane.

In the present article, we employ two EAM potentials [15,16] that predict the two types of dislocation cores, and characterize both the static and dynamic properties of the screw dislocations modeled by these potentials. In the static case (Section 3), we compute the Peierls stress as a function of crystal orientation and show strong boundary condition effects. In the dynamical case (Section 4), we perform a series of large 3D MD simulations for a range of temperatures and applied stresses and show in particular that, with a non-degenerate core, the glide plane is the $\{110\}$ MRSSP at low temperatures, with a transition towards the $\{112\}$ twinning plane at higher temperatures and stresses. The relevance of the present simulations to experimental data and previous works published in the literature is finally discussed (Section 5).

2. Computational model

2.1. Crystallography

The simulation cell used here is schematically shown in Fig. 1(a). Its orientation around the $Y=[111]$ axis which is the close-packed Burgers vector direction, is defined by the angle χ between the horizontal MRSSP of the cell and the $(\bar{1}01)$ plane, used as a reference (as will be detailed below, the boundary conditions produce a σ_{YZ} shear stress with horizontal MRSSP). The MD simulations were performed in a cell with $\chi=0$, i.e. horizontal $(\bar{1}01)$ planes. In the static simulations, we computed the dependence of the Peierls stress on the crystal orientation by rotating the cell around the Y -axis. Fig. 1(b) presents the plane

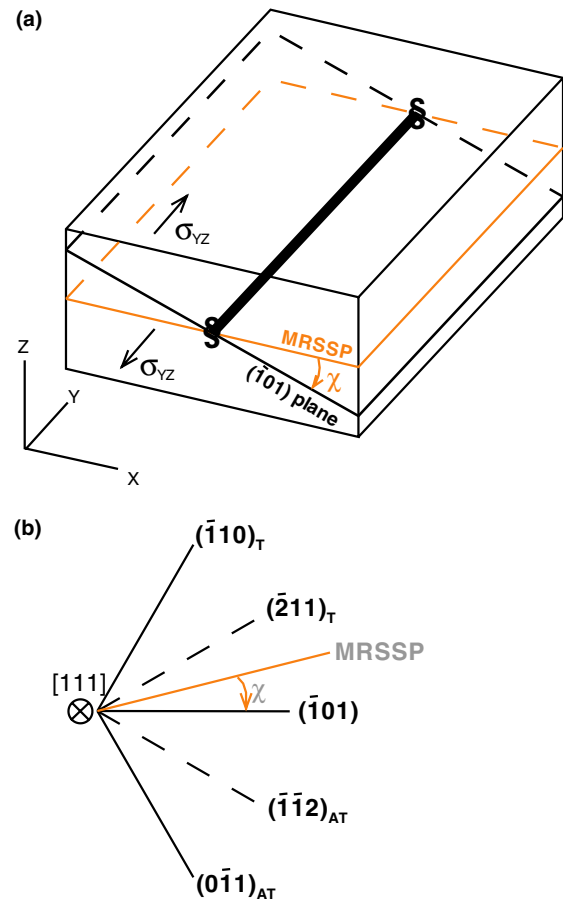


Fig. 1. Definition of the angle χ (a) in the simulation cell and (b) with respect to the $\{110\}$ and $\{112\}$ planes of the $[111]$ zone.

indexes of the $[111]$ zone and recalls that three $\{110\}$ and three $\{112\}$ planes intersect along the $[111]$ direction and that each $\{110\}$ plane is bordered by two $\{112\}$ planes and vice versa. Because of the symmetries of the bcc lattice, all orientations are considered if χ is varied between $\pm 30^\circ$, but because of the asymmetry of shear parallel to $\{112\}$ planes, positive and negative χ angles are not equivalent. In the simulations, only positive σ_{YZ} shear stresses are applied, such that the $(\bar{2}11)$ planes are sheared in the twinning sense, while the $(\bar{1}12)$ planes in the antitwining sense (see Ref. [10] for more details). We will refer to the region $\chi < 0$ (resp. $\chi > 0$) as the twinning (resp. antitwining) region and will use subscripts T and AT to recall to which region the planes belong. Each $\{110\}$ plane is thus bordered by two $\{112\}$ planes, one sheared in the twinning sense, the other, in the antitwining sense.

2.2. Boundary conditions

The cell dimensions used here are $L_X = 25.2$ nm, $L_Z = 13.1$ nm in the X and Z directions, respectively. Along the dislocation line, the static simulations were quasi-2D with $L_Y = 2.5$ nm while for the dynamic simulations, in order to capture the double-kink mechanism, we

needed long dislocation segments and employed $L_Y = 64.2$ nm.

We tested different types of boundary conditions. In all cases, periodic boundary conditions were applied in the Y -direction along the dislocation line and free boundary conditions in the X -direction. In the Z -direction, we applied either full or modified free boundary conditions. In the latter case, referred to as *2D-dynamics*, atoms lying in slabs of width equal to the potential cut-off distance from the upper and lower Z surfaces are fixed in the Z -direction and free to move in the X and Y directions. This type of boundary conditions has been used in fcc metals (see Ref. [17,18] and references therein). It can be viewed as *Rigid* in the Z -direction but allows to apply stress-controlled boundary conditions. An $a/2[111]$ screw dislocation is introduced in the center of the cell, along the Y -direction, by means of its elastic displacement field.

In order to force the screw dislocation to glide, we apply stress-controlled boundary conditions by superimposing to the atoms in the upper and lower slabs (as defined above) constant and opposite forces in the Y -direction, in order to produce a σ_{YZ} external shear stress. As said in previous section, only positive shear stresses were applied.

Atomic configurations are visualized either by differential displacement maps [8] where first-neighbor $[111]$ atomic columns are linked by arrows of length proportional to their relative displacement in the Burgers vector direction, or by a first-neighbor analysis [18] where are shown only those atoms which do not have 8 first neighbors close to perfect bcc positions. The latter atoms are called *core atoms* in the following.

2.3. Interatomic potentials

We employ two iron interatomic EAM potentials. One potential was developed by Simonelli et al. [16] in order to describe α -Fe crystals and has been used for example to study twin nucleation at crack tips [19]. The other more recent potential was developed by Mendelev et al. [15] (Potential 2 in the reference) in order to describe crystalline as well as liquid iron by including in the fitting procedure first-principle forces obtained on a model liquid configuration. In the following, the potential developed by Simonelli et al. (resp. Mendelev et al.) will be noted *potential S* (resp. *M*).

We computed the kink-pair formation energy predicted by both potentials and found very contrasted results. Potential *M* predicts high values of 0.67 eV for the vacancy-type kink and 1.02 eV for the interstitial-type kink, while potential *S* predicts a low and identical value for both kinks, equal to 0.2 eV. The value extrapolated from experimental data is 0.8 eV for the kink pair [12], i.e. about twice that of potential *S* and half that of potential *M*.

Fig. 2 presents the differential displacement maps of the screw dislocation cores obtained with both potentials. As can be seen, potential *S* predicts a degenerate core, asym-

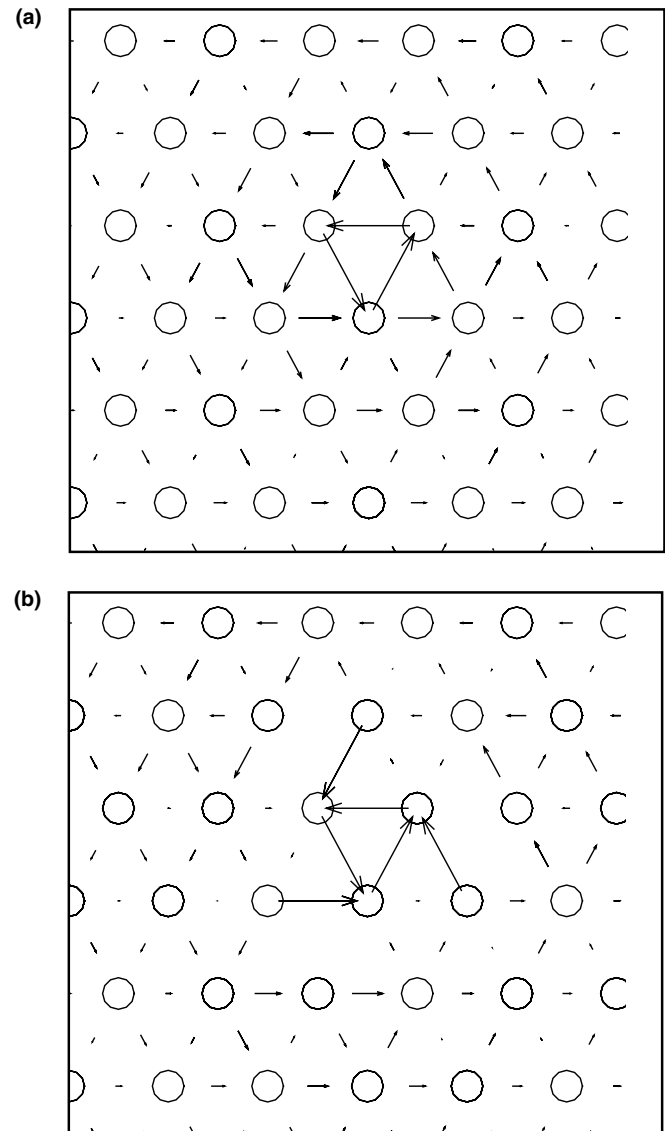


Fig. 2. Differential displacement maps of screw dislocation cores showing (a) the non-degenerate structure of Mendelev et al. potential [15] and (b) the degenerate structure of Simonelli et al. potential [16].

metrically spread in the three $\{110\}$ of the $[111]$ zone. Potential *M* predicts a non-degenerate symmetric core (close to the elastic solution) in close agreement with recent DFT calculations [14]. We will use this fundamental difference to study the influence of the core structure both on the static and dynamic properties of a screw dislocation. Note also for later use that the stable configuration (called *soft*) of the dislocation cores shown here is centered on a triangle pointing downward in this $[111]$ projection. There exists also an unstable configuration (called *hard*) where the core is centered on an upward triangle (see Ref. [8] for details).

3. Static properties and boundary effects

We consider here the dependence of the Peierls stress of the $a/2[111]$ screw dislocation on crystal orientation. We performed static simulations by increasing the applied

stress incrementally and relaxing the configuration between each increment. The energy-minimization algorithm used here is based on zeroing atomic velocities whenever their dot product with the atomic force is negative.

With potential M , the Peierls stress is well defined since, when the applied stress is increased, there is a critical stress below which the dislocation is stable, and above which dislocation motion is unbounded. By way of contrast, there are two critical stresses with potential S : when the applied stress reaches a lower critical stress, the dislocation advances by one atomic distance, adopts a metastable configuration and remains fixed until a second upper critical stress is reached, above which the motion becomes unbounded. Double critical stresses were found with other potentials (see, for example, Ref. [20]). Whenever Peierls stresses are shown with potential S , both critical stresses are shown.

Fig. 3(a) shows the evolution of the Peierls stress as a function of the crystal orientation χ obtained with potential M employing either free boundary conditions or 2D dynamics in the Z -direction. The plane on which the dislocation glided is noted in the figure.

We see a strong influence of the boundary conditions both on the numerical values of the Peierls stress and on the glide plane selection. For $\chi < 0$ with 2D dynamics, the dislocation glides on a $(\bar{2}11)_T$ plane (empty symbols in Fig. 3(a)), while with free boundary conditions, the dislocation glides on a $(\bar{1}01)$ plane for all orientations plain symbols in Fig. 3(a) except when χ is close to -30° , i.e. when the MRSSP is close to $(\bar{2}11)_T$. Numerically, in the region $\chi > 0$ where in both cases the dislocation glides on $(\bar{1}01)$, the Peierls stress with 2D dynamics is about 300 MPa lower than that obtained with free boundary conditions. Note also that the Peierls stress is discontinuous when the glide plane changes from $(\bar{1}01)$ to $(\bar{2}11)_T$. The Peierls stress for $\chi = +30^\circ$, i.e. when the MRSSP is $(\bar{1}\bar{1}2)_{AT}$, is not reported on the figure because it is unrealistically high (about 5.4 GPa) and in that case, the plastic deformation is not due to a dislocation but rather to a plate of intense shear.

This strong influence of the boundary conditions is due to a shear/tension coupling associated to the twinning/antitwinning asymmetry of shear on $\{112\}$ planes. Indeed, the bcc lattice is not symmetrical with respect to $\{112\}$ planes: the $[111]$ atomic columns are shifted by $b/3$ with respect to each other, with reference positions $-b/3, 0, b/3, \dots$. When the lattice is sheared parallel to a $\{112\}$ plane, the reference positions of the columns become $-b/3 - e, 0, b/3 + e$, with $e > 0$ (resp. $e < 0$) when the crystal is sheared in the twinning (resp. antitwinning) sense and thus, the distance between atoms in the neighboring $[111]$ columns increases (resp. decreases). Correspondingly, in the twinning case, the lattice tends to compress perpendicularly to the $\{112\}$ plane, while in the antitwinning case, it expands. The 2D dynamical boundary conditions forbid these expansion and contraction because they are rigid in the Z -direction and no out-of-plane motion is allowed in the

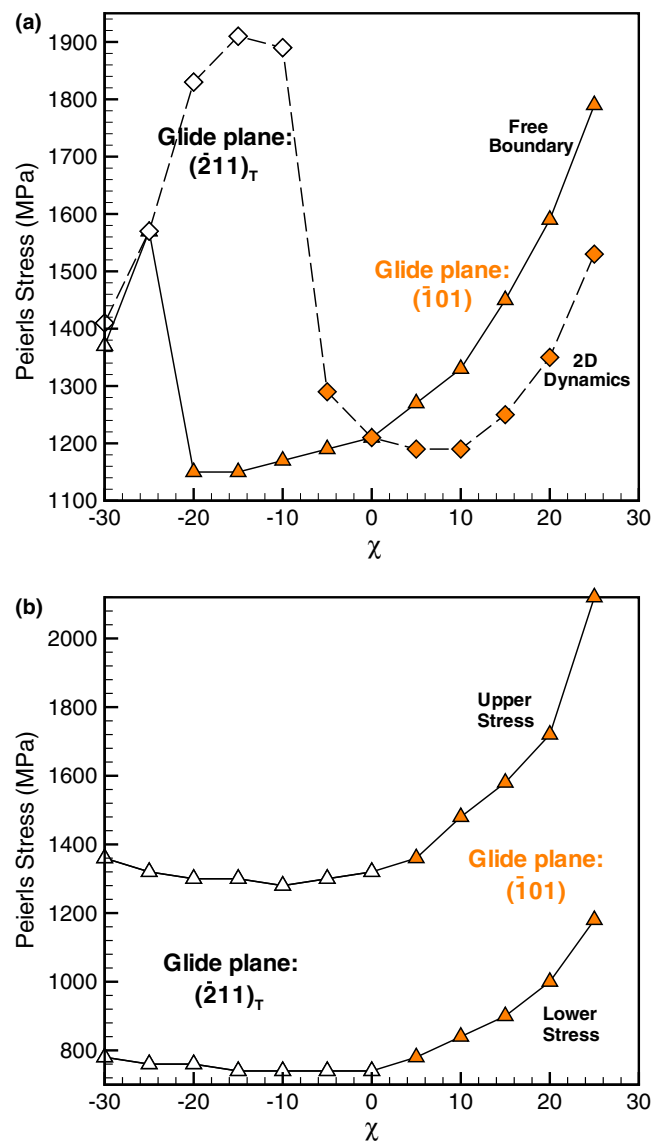


Fig. 3. Variation of Peierls stress with crystal orientation for 2 EAM potentials: (a) potential M where two boundary conditions are compared (free boundary or 2D-dynamics), and (b) potential S where the upper and lower critical stresses are shown.

upper and lower crystal surfaces. Tensile stresses in the Z -direction are thus generated which in turn produce shear components perpendicular to the Burgers vector of the screw dislocation. As said in Section 1, these non-glide components are known to affect the Peierls stress [7] and are at the origin of the differences observed between the two boundary conditions. In Fig. 3(a), the 2 curves cross at $\chi = 0$, i.e. when the MRSSP is $(\bar{1}01)$ because it is the only orientation for which shear is symmetrical and no stress is generated in the Z -direction with 2D dynamics. Note also that the shear/tension coupling is volumic and its effect is therefore independent of the size of the simulation cell. In fact, this coupling is found in any crystal with cubic symmetries: a shear deformation ϵ_{YZ} with $Y = [111]$ and $Z = [\bar{1}\bar{1}2]$ applied to a crystal with cubic symmetries (and elastic constants c_{11}, c_{12}, c_{44}) produces a stress tensor

with a component $\sigma_{ZZ} = \sqrt{2}/3(-c_{11} + c_{12} + 2c_{44})\epsilon_{YZ}$, thus showing the coupling between the shear ϵ_{YZ} and the tension σ_{ZZ} in the direction perpendicular to the plane of application of the shear.

Fig. 3(b) shows the evolution of the Peierls stress obtained with potential S and free boundary conditions. Both the lower and upper Peierls stresses are noted on the figure, the lower stress being about 600 MPa below the upper one. The latter is close to the Peierls stress obtained with potential M . The glide plane is $(\bar{1}01)$ in the antitwinning region and $(\bar{2}11)_T$ in the twinning region. Note that with the present potential, the Peierls stress is continuous at the transition between glide planes. Also, the Peierls stress is almost constant in the twinning region.

Fig. 4 illustrates the well-known fact that the Peierls stress in bcc crystals does not obey the χ -dependence of Schmid law. Fig. 4 reproduces the data obtained with potential M in the region where the dislocation glides on $(\bar{1}01)$. First, the twinning/antitwinning asymmetry is clearly visible when comparing the regions $\chi > 0$ and $\chi < 0$. Second, the dashed curve is Schmid law ($\sigma_P^0/\cos(\chi)$) fitted on the Peierls stress at $\chi = 0$. We see in particular that the Peierls stress in the region $\chi > 0$ decreases much faster than Schmid law and does not increase for $\chi < 0$. The solid curve is the fit obtained using the effective yield stress criterion proposed by Vitek et al. [21], who suggested that the effect of non-glide resolved shear stresses on planes other than the glide plane should be accounted for in the form of a linear combination. Based on their simulations, they found that the important shear stress is that acting on $(\bar{1}10)_T$. With our notations, the Peierls stress is then expressed as:

$$\sigma_P = \frac{\sigma_P^0}{\cos(\chi) + a \cdot \cos(60 + \chi)} \quad (1)$$

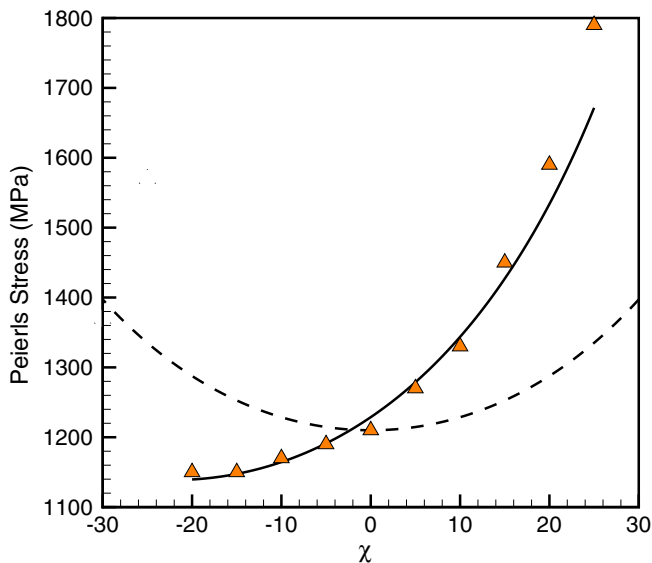


Fig. 4. Comparison between Schmid law (dashed curve) and an effective Peierls stress relation (solid curve) [21].

Fig. 4 shows that this fit with $\sigma_P^0 = 1604$ MPa and $a = 0.61$ improves greatly the prediction of the Peierls stress, except in the region close to 30° , which could be due to the unrealistic Peierls stress for $\chi = 30^\circ$.

4. Dynamic properties

We performed a series of large 3D MD simulations with a 64 nm-long screw dislocation in a cell with $(\bar{1}01)$ MRSSP. In this section, we will focus mainly on simulations performed with potential M . The duration of the simulations was set to 100 ps. The temperature was varied in the range 50–150 K, i.e. within the experimental range where plasticity is dominated by the thermally activated motion of screw dislocations. No temperature control was used, because the dislocation glides over limited distances and the temperature raises by less than 2 K. The applied stress was varied in the range 200–700 MPa, i.e. well below the Peierls stress, which is 1210 MPa for this $\chi = 0$ orientation (see Fig. 3(a)). Free boundary conditions are applied in X and Z directions (see Fig. 1(a)). From the energy of the dislocation as a function of its position in the cell, we found that the image stress on the dislocation produced by the free surfaces is below 50 MPa for glide distances below 25 Peierls valleys. The results presented hereafter are thus computed within this range. The dislocation is first relaxed at 0 K under the desired stress before the target temperature is set and the MD simulation started.

Fig. 5 is a map of the dislocation average velocity and average glide-plane angle ψ with respect to the horizontal $(\bar{1}01)$ MRSSP. A similar velocity map was obtained by

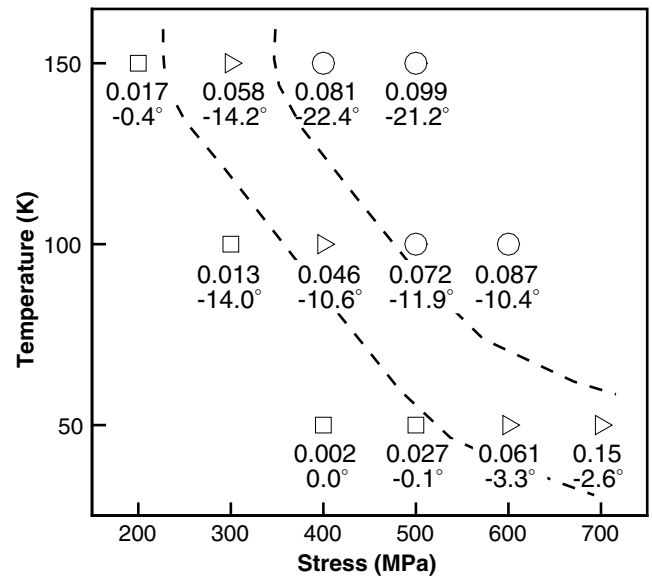


Fig. 5. Map of the dislocation average velocity and glide-plane angle ψ with respect to the horizontal $(\bar{1}01)$ MRSSP. For each temperature and applied stress condition, the velocity is given in nm ps^{-1} and the corresponding angle in degrees. Squares, right-triangles and circles refer to glide regimes: single kink pair, multiple kink pair with avalanches and rough multiple kink pair, respectively (see the text for details).

Marian et al. [13] with an EAM potential that predicts a degenerate core structure.

The glide mechanism is the nucleation and propagation of kink pairs in $\{110\}$ planes, as illustrated in Fig. 6 which displays dislocation core positions at different times for different stress and temperature conditions. The core was determined by taking the center of gravity of the core atoms (as defined by the first-neighbor analysis presented in Section 2) in slices of width $2b$ along the dislocation line.

At low temperatures and stresses, there is a *Single Kink-Pair (SKP) regime* where glide is intermittent with waiting times separated by the nucleation of kink pairs that appear one-by-one and annihilate with themselves through the periodic boundary conditions along the dislocation line. The process, illustrated in Fig. 6(a), occurs by the successive nucleation and propagation of two kink pairs of height

$0.5d$, where $d = 2\sqrt{2}b/3$ is the distance between Peierls valleys. The first kink pair brings the dislocation from a stable *soft* position to an unstable *hard* position, while the second kink pair brings the dislocation back into a stable *soft* position, in the next Peierls valley. The *hard* dislocation segment is metastable presumably because of the line tension effect of the edge kinks. The kinks expand with high saturated velocities, of the order of 4.5 nm ps^{-1} , mostly independent of the temperature and stress in the range considered here. Also, vacancy-type and interstitial kinks have similar velocities although their formation energies are very contrasted with potential M . In the map of Fig. 5, the points corresponding to this SKP regime are noted as squares. This figure shows that the glide plane angle ψ is 0° at 50 K and reaches -14° at 100 K. The reason is the activation of cross-slip with temperature

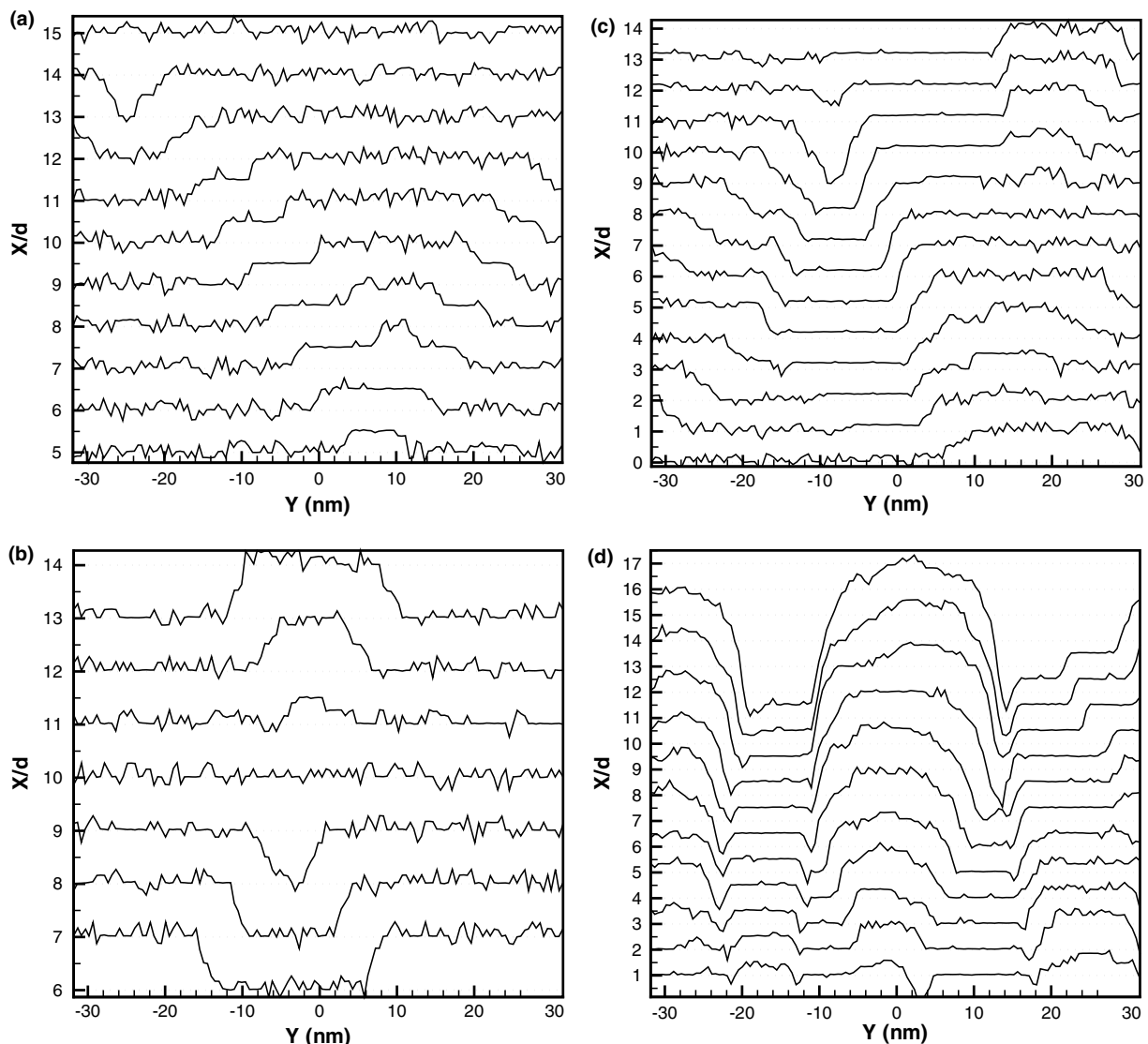


Fig. 6. Dislocation core motion in (a) the single-kink pair regime (300 MPa, 100 K), (b) the single-kink pair regime (500 MPa, 50 K) where a nucleation following an annihilation is shown, (c) the multiple-kink pair regime with avalanches (400 MPa, 100 K) and (d) the rough multiple-kink pair regime (600 MPa, 100 K). The lines connect the centers of gravity of the core atoms along the dislocation line in a $\bar{1}01$ projection. They are shown every 0.8 ps and, for the sake of clarity, the curves are shifted by d with respect to each other, where d is the width of the Peierls valley.

(see Section 5) that leads to an increasing proportion of double kinks nucleated in inclined $(\bar{1}10)_T$ planes at $\chi = -60^\circ$ in the twinning region (see Fig. 1(b)). The glide plane is therefore the $(\bar{1}01)$ MRSSP only at low temperatures and rotates towards the twinning region at higher temperatures. In the simulations, as illustrated in Fig. 6(b), we often observe that a new kink pair nucleates within less than a ps at the position where two kinks annihilated, which is due to the energy locally released by the annihilation.

If temperature and/or stress are increased, the kink-pair nucleation rate increases and we observe a transition to a *multiple kink-pair (MKP) regime* where several kink-pairs coexist on the dislocation line. First, there is an *intermediate regime* where dislocation motion is characterized by waiting times separated by avalanches, i.e. rapid successions of kink-pairs, mostly in horizontal $(\bar{1}01)$ planes. An example of such an avalanche is shown in Fig. 6(c). A kink pair first nucleates and, while it expands along the dislocation line, several other kink pairs appear on this initial kink-pair and also propagate along the dislocation line. Usually, the avalanches comprise 2–3 kink pairs. In this intermediate regime, noted as right triangles in Fig. 5, the glide angle is again mostly a function of the temperature and does not exceed -15° .

At even higher temperatures and/or stresses, the kink-pair nucleation rate as well as the number of kink pairs in inclined $(\bar{1}10)_T$ planes increase. At 150 K, the latter becomes almost equal to the number of kink pairs in horizontal $(\bar{1}01)$ planes and consequently, the angle ψ approaches -30° (see Fig. 5) and the average glide plane rotates to $(\bar{2}11)_T$. Fig. 6(d) shows the almost simultaneous nucleation of two kink pairs in different $\{110\}$ planes, leading to a self-pinning of the dislocation by a mechanism that was described in details by Marian et al. [13]: when kink pairs on different $\{110\}$ planes intersect, they lock each other and become pinning points for the dislocation, called *cross-kinks* [22]. The dislocation may then unlock by two mechanisms. One was reported by Marian et al. [13] and involves a combination of kink pairs in both $\{110\}$ planes which allows the dislocation to reconnect in a single $\{110\}$ plane. This mechanism results in the formation of two closed loops, one of vacancy-type, the other interstitial. In the present simulations, we observed another mechanism: when the dislocation velocity is slow enough, we see that the cross-kinks are mobile, glide along the dislocation line and annihilate with one another. No debris loops are formed in this case. The driving force of the motion of the cross-kinks can have two origins: (1) the difference in RSS between the kinks in the inclined and the horizontal $\{110\}$ planes and (2) a possible difference in the length of the two kinks [22]. No waiting times are observed in this regime, that was called *rough* by Marian et al. [13] and, as illustrated in Fig. 7(b), a large density of debris loops is left in the wake of the dislocation. As shown in Fig. 6(d), atomic-scale kinks are no more visible, but are more

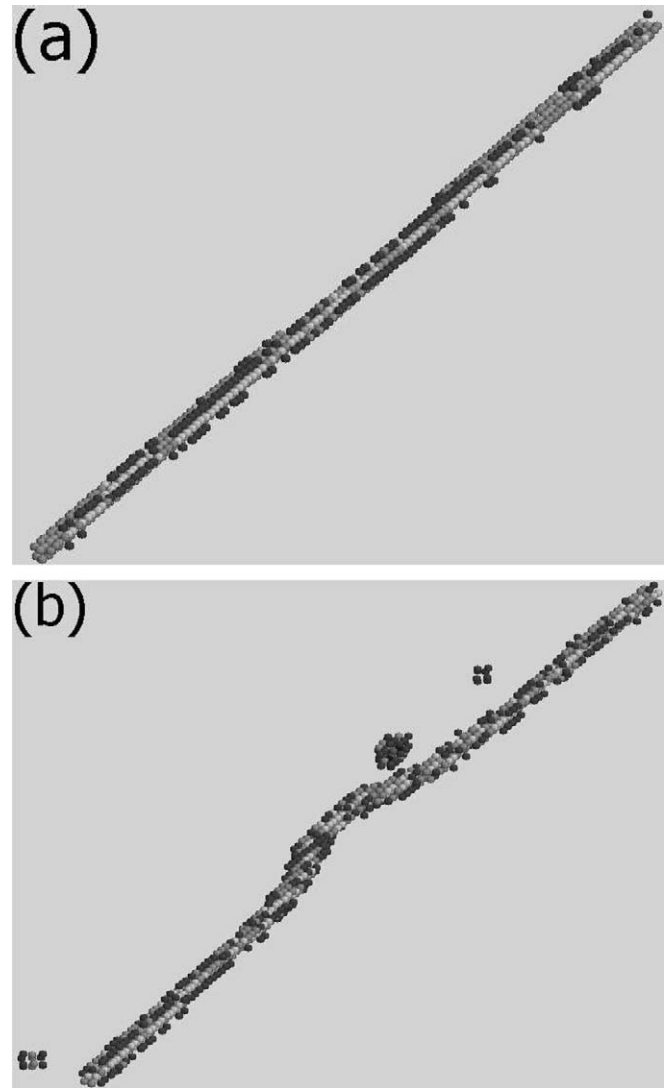


Fig. 7. Core structures obtained with a first-neighbor analysis in (a) the single-kink pair regime (400 MPa, 50 K), (b) the rough multiple-kink pair regime (500 MPa, 150 K).

rounded with heights equal to several interatomic distances.

5. Discussion

We identified three regimes: single kink-pair (SKP) regime, multiple kink-pair (MKP) regime with avalanches, and rough multiple kink pair regime, in a window of temperatures and stresses primarily determined by the duration of the simulations: the simulations can be carried out only with temperatures and stresses for which the dislocation advances by several Peierls valleys within 100 ps, which limits us to stress levels higher than in traction/compression tests on single crystals, leading to relatively high dislocation velocities. Such stresses can however easily be reached near heterogeneities, such as cracks, and in small-scale microstructures. Also, note that since the MKP regimes require several kink-pairs along

the dislocation, the stress to enter these regimes will decrease if a longer dislocation line length is used. Finally, the observations made here remain mostly qualitative since we could not perform the number of runs required for accurate statistics due to the computational load of the simulations.

5.1. Glide plane predictions for potentials *M* and *S*

It is known experimentally that in α -Fe single crystals, slip takes place on $(\bar{1}01)$ planes over the whole temperature range when these planes are MRSSP [3]. Such slip plane is possible if kink-pairs are systematically nucleated in this plane, or if they nucleate in all three $\{110\}$ planes of the $[111]$ zone such that, on average, the dislocation glides on $(\bar{1}01)$. At the atomic scale, the first case is compatible only with a non-degenerate core that retains the same configuration after each atomic move and can systematically emit kink pairs in a $(\bar{1}01)$ plane. The present simulations show that indeed, with potential *M* which predicts a non-degenerate core, glide on $(\bar{1}01)$ is possible.

The second option, pencil glide on an average $(\bar{1}01)$ plane, is impossible at least with potential *M*, because we never observed any kink pair nucleating in a $(0\bar{1}1)_{AT}$ plane in the antitwinning region. The glide plane can deviate only towards the twinning region, with no possibility for the dislocation to glide back towards the central $(\bar{1}01)$ plane. To our knowledge, kink pairs on $(0\bar{1}1)_{AT}$ planes have never been observed in atomic-scale simulations.

With a degenerate core such as that predicted by potential *S*, the asymmetry of the two core variants implies that for a given sign of the applied stress and a $(\bar{1}01)$ MRSSP, one variant will emit kink pairs only in a $(\bar{1}01)$ plane (case of the variant shown in Fig. 2(a) if the stress drives the dislocation to the right) while the other variant will emit kink pairs in a $(\bar{1}10)_T$ plane. With degenerate cores, no $(0\bar{1}1)_{AT}$ -kink pair have either ever been observed in atomic-scale simulations. The flip from one variant to the other each time the dislocation moves by one Peierls valley implies the nucleation of kink pairs alternatively on $(\bar{1}01)$ and $(\bar{1}10)_T$, resulting on an average $(\bar{2}11)_T$ -glide plane, as described in earlier publications [12,13].

5.2. Rotation of the glide plane

The map of Fig. 5 shows that the glide plane angle ψ is mostly a function of the temperature and results from the activation with temperature of kink pairs in $(\bar{1}10)_T$ planes. This effect can be understood as least qualitatively from a simple cross-slip model [25] where one assumes that kink pairs nucleate in $(\bar{1}01)$ and $(\bar{1}10)_T$ planes with thermally activated probabilities that depend on the RSS in these planes: $E_0 - V \cdot \sigma$ and $E_0 - V \cdot \sigma/2$, respectively (we thus neglect all non-glide effects). The glide plane angle then follows the relation:

$$\tan(-\psi) = \frac{\sqrt{3}}{1 + 2 \exp(V \cdot \sigma / 2k_{BT})} \quad (2)$$

With an activation volume $V = 0.45b^3$, we obtain a variation of ψ with temperature of the same order, though less rapid, than observed in the simulations. The cross-slip events may be helped by a change of dislocation core structure. Fig. 8(a) shows the differential displacement map obtained at 500 MPa and 150 K, using atomic positions averaged over 10 ps. We can see in this figure a dissymmetry between the two arrows just above the core triangle, corresponding to an extension of the dislocation core in the inclined $(\bar{1}10)_T$, which favors the nucleation of kink pairs in this plane. The effect is favored by higher stresses since as seen in Fig. 8(b), at 200 MPa and 150 K, the core dissymmetry is much less pronounced.

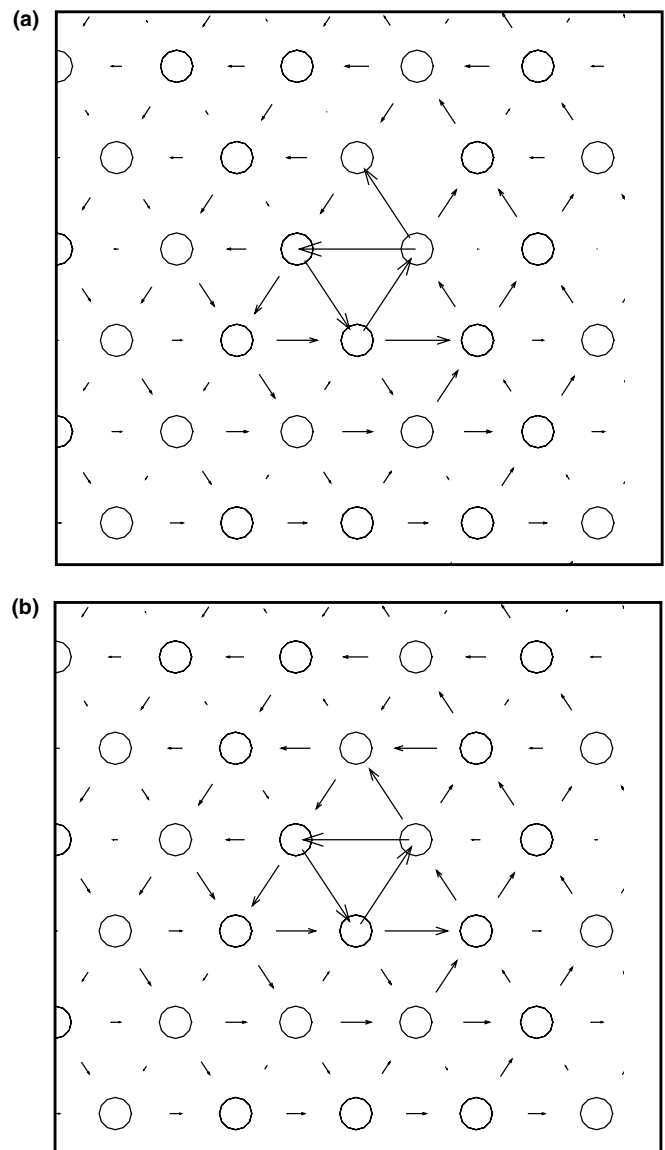


Fig. 8. Average differential displacements of screw dislocation cores at 150 K and (a) 500 MPa, (b) 200 MPa.

The activation with temperature of kink pairs in $(\bar{1}10)_T$ planes is in agreement with the experimental observation that in α -Fe, slip takes place on $\{110\}$ at low temperatures (77 K) over the whole orientation range but at higher temperatures, only if the crystal is stressed in the antitwinning region; if the stress is in the twinning region, slip becomes non-crystallographic with an average glide plane parallel to the MRSSP [2,10]. Indeed, combinations of $(\bar{1}01)$ - and $(\bar{1}10)_T$ -kink pairs can yield any average glide plane in the twinning region, while, in the absence of $(0\bar{1}1)_{AT}$ -kink pairs, slip in the antitwinning region can only take place in $(\bar{1}01)$ planes. Similarly, at low temperatures, in absence of $(\bar{1}10)_T$ -kink pairs, slip can also take place only in $(\bar{1}01)$ planes. This point should be verified by 3D MD simulations at different temperatures with different crystal orientations.

The present simulations also predict that the slip plane in a crystal oriented with $(\bar{1}01)$ MRSSP should rotate from $(\bar{1}01)$ towards $(\bar{2}11)_T$ when the temperature is increased, which has not been observed experimentally to our knowledge. However, the experimental determination of slip planes [3] was performed on single crystals with low yield stresses below 300 MPa where the evolution of the core structure is not pronounced. An analysis of slip traces in high stress environments, as obtained in small-scale microstructures (for example bainitic steels [24]) would be very informative.

5.3. Rough MKP regime

The rough MKP regime requires two conditions: several kinks have to expand simultaneously and in different $\{110\}$ planes. The first condition is controlled by the nucleation probability, while the second depends on the core structure.

In the case of a degenerate core, the fact that the variants emit kink pairs in distinct planes makes the coexistence of such kinks difficult and restricts the rough MKP regime (if any) to very high temperatures and stresses. Indeed, using potential S , we observed no rough regime over the entire stress and temperature ranges considered here. With this potential, at high stresses, the dislocation core is nearly planar, extended in a $(\bar{2}11)_T$ plane, and the motion appears continuous, with no visible atomic-scale kinks. Marian et al. [13] observed a rough regime with a degenerate core, that can have two reasons: either a change in dislocation core allowing the simultaneous formation of kinks in two $\{110\}$ planes or the activation of flips between core variants along the dislocation, as considered by Duesberry [23]. Interestingly, the applied stress for the transition to the rough regime obtained by these authors at low temperature (50 K) is the same as in the present simulations. But, in their case, this transition stress is mostly independent of the temperature while in our case, it is strongly dependent. Also, in agreement with the observations of Marian et al., the interstitial

debris loops tend to have large sizes while the vacancies are released one-by-one or in small clusters. Such debris loops were observed in TEM in high yield stress bainitic steels [24], where the RSS is about 450 MPa at 77 K, indicating that in these alloys, the deformation may be in the rough MKP regime, as opposed to single crystals where the applied stress is lower and the deformation is in the SKP regime.

5.4. Influence of the boundary conditions

Boundary conditions have a strong influence on the Peierls stress at 0 K as shown in Section 3, when the crystal is sheared in an orientation different from $\chi = 0$, because of the shear–tension coupling associated with the twinning/antitwinning asymmetry. This effect is due to the rigid boundary conditions imposed in the Z -direction when 2D dynamics are used. The boundary conditions also affect the selection of the glide plane at finite temperatures. We used 2D-dynamics in the Z -direction in MD simulations and found $(\bar{2}11)_T$ glide planes over most of the temperature and stress ranges. In addition, we tested periodic boundary conditions in the X -direction and found that these boundary conditions also favor slip in $(\bar{2}11)_T$ planes. Great care must therefore be taken in the choice of the boundary conditions and, from the present simulations, free boundary conditions in both X and Z directions seem to be the most adapted and rigid boundary conditions should not be used outside the orientation $\chi = 0$.

6. Conclusion

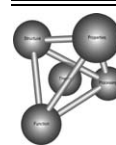
The present simulations show that if a potential predicting a non-degenerate core is used, glide at finite temperature on a $\{110\}$ plane can be stabilized, in agreement with experimental data and in contrast with MD simulations performed with degenerate cores that predict $\{112\}_T$ average glide planes. For this reason, we believe that, although neither potential M nor S are physically based models for bcc iron because they do not account for magnetism, potential M is more realistic because it stabilizes $\{110\}$ glide planes. Also, a transition to a rough regime is obtained with a stronger temperature dependence than with degenerate cores. Finally, the simulation results appear to be very dependent on the boundary conditions, mainly because the latter may produce non-glide stress components that affect dislocation glide.

Acknowledgments

The authors thank Pr. François Louchet and Dr. Christian Robertson for fruitful discussions, as well as Thomas Nogaret who greatly participated in the development of the parallel MD code used here.

References

- [1] Hirsch P. Proceedings of the fifth international conference on crystallography. Cambridge: Cambridge University Press; 1960. p. 139.
- [2] Christian J. Metall Trans A 1983;14:1237.
- [3] Spitzig WA, Keh AS. Acta Metall 1970;18:611.
- [4] Spitzig WA, Keh AS. Acta Metall 1970;18:1021.
- [5] Kuramoto E, Aono Y, Kitajima K, Maeda K, Takeuchi S. Philos Mag A 1979;39:717.
- [6] Duesberry M, Vitek V. Acta Mater 1998;46:1481.
- [7] Ito K, Vitek V. Philos Mag A 2001;81:1387.
- [8] Vitek V. Cryst Latt Def 1974;5:1.
- [9] Cai W, Bulatov VV, Chang J, Li J, Yip S. In: Nabarro F, Hirth JP, editors. Dislocations in solids, vol. 12. Amsterdam: Elsevier; 2004. p. 1.
- [10] Duesberry M. In: Nabarro F, editor. Dislocations in solids, vol. 8. Amsterdam: North-Holland; 1989. p. 67.
- [11] Vitek V. Philos Mag 2004;84:415.
- [12] Wen M, Ngan A. Acta Mater 2000;48:4255.
- [13] Marian J, Cai W, Bulatov VV. Nat Mater 2004;3:158.
- [14] Frederiksen SL, Jacobsen KW. Philos Mag 2003;83:365.
- [15] Mendelev MI, Han S, Srolovitz DJ, Ackland GJ, Sun DY, Asta M. Philos Mag 2003;83:3977.
- [16] Simonelli G, Pasianot R, Savino E. Mater Res Soc Symp Proc 1993;291:567.
- [17] Rodary E, Rodney D, Provaille L, Bréchet Y, Martin G. Phys Rev B 2004;70:054111.
- [18] Rodney D. Acta Mater 2004;52:607.
- [19] Farkas D. Philos Mag 2005;85:387.
- [20] Duesberry MS, Vitek V, Bowen DK. Proc R Soc A 1973;332:85.
- [21] Vitek V, Mrovec M, Bassani JL. Mat Sci Eng A 2004;365:31.
- [22] Louchet F, Viguier B. Philos Mag A 2000;80:765.
- [23] Duesberry M. Acta Mater 1984;31:1759.
- [24] Obrtlík K, Robertson CF, Marini B. J Nucl Mat 2005;342:35.
- [25] The authors thank V.V. Bulatov for this suggestion.



Dual role of deformation-induced geometrically necessary dislocations with respect to lattice plane misorientations and/or long-range internal stresses [☆]

H. Mughrabi ^{*}

Institute für Werkstoffwissenschaften, Universität Erlangen-Nürnberg, Martensstr. 5, 91058 Erlangen, Germany

Received 21 October 2005; received in revised form 13 January 2006; accepted 23 March 2006

Available online 15 June 2006

Abstract

This work is part of a continuing effort to develop a unified picture of the role of geometrically necessary dislocations (GNDs) in the evolution of the dislocation distribution of unidirectionally and cyclically deformed crystals. In particular, the dual role of the GNDs in the development of long-range internal stresses and lattice plane misorientations which arise because of the heterogeneity of the dislocation substructure is explored. Available experimental data of cyclically and tensile-deformed copper single crystals were evaluated as quantitatively as possible in the framework of the composite model. Valuable complementary information to TEM was obtained from well-designed X-ray diffraction experiments (line broadening, broadening of rocking curves, Berg–Barrett X-ray topography). The evolution of the long-range internal stresses and of the density of the GNDs with increasing deformation could be determined quantitatively as a function of deformation for cases of both single and multiple slip. In all cases studied, the GND density was found to be small and amounted only to some per cent of the total dislocation density. From the rate of evolution of the misorientations of different types of dislocation boundaries, the latter could be classified either as so-called geometrically necessary boundaries or incidental dislocation boundaries. A number of semi-empirical relationships between the microstructural parameters on a mesoscale and the parameters of deformation that were derived in this study can provide valuable guidance in future modelling.

© 2006 Acta Materialia Inc. Published by Elsevier Ltd. All rights reserved.

Keywords: Dislocation distribution; Deformed crystals; Geometrically necessary dislocations; Long-range internal stresses; Lattice plane misorientations

1. Introduction

1.1. Motivation, general remarks on geometrically necessary dislocations in deformed crystals

The characteristic features of the dislocation microstructures in unidirectionally plastically deformed face-centred cubic (fcc) crystals have been studied extensively in the past, as reviewed in Refs. [1–5]. In many of these studies,

transmission electron microscopy (TEM) was the most frequently employed observational technique. In most cases, quantitative analysis concentrated on features such as the dislocation density and the spacings between the dislocation cell walls. For a more complete quantitative characterization of the dislocation patterns, it is important to consider that, even in macroscopically homogeneous deformation, e.g. in a simple tensile test, deformation is microscopically non-homogeneous as a consequence of the heterogeneity of the deformation-induced dislocation microstructure (e.g. a cell structure). Hence, those prominent microstructural features which arise on a larger scale as a consequence of the microstructural heterogeneity of the dislocation pattern such as long-range internal stresses and lattice plane misorientations should also be assessed as

[☆] This manuscript was presented at the Engineering Foundation Conference “Micromechanics and Microstructure Evolution: Modeling, Simulation and Experiments” held in Madrid/Spain, September 11–16, 2005.

^{*} Tel.: +49 91 385275 01; fax: +49 91 385275 04.

E-mail address: mughrabi@ww.uni-erlangen.de.

quantitatively as possible. The evolution of these two important features is intimately related to the formation of specific arrays of geometrically necessary dislocations (GNDs); compare Ref. [6].¹ Hence, the study of internal stresses and misorientations is in fact considered as the key to understand better the important role played by the GNDs in the evolution of the dislocation microstructure, irrespective of the fact that the GND density represents only a few per cent of the total dislocation density; compare Refs. [7–9]. Ideally, all microstructural features named above should of course be integral parts of work-hardening theories.

These questions are addressed in this study, which is complementary to a parallel paper [6] as part of an attempt to develop a unified picture of the special role played by GNDs in the plastic deformation of crystals. For this purpose, some earlier experimental studies of plastic deformation in which relevant information on long-range internal stresses and/or lattice plane misorientations had been obtained are reconsidered. Emphasis is laid on the dual role of GNDs as sources of both internal stresses and misorientations, as exemplified in terms of simple models. In the present context, the particularly promising experimental approach of X-ray diffraction techniques as complementary tools to TEM is recalled briefly (Section 1.2). Available data are analysed as quantitatively as possible in terms of microstructurally based models with the goal of extracting semi-empirical relationships between the microstructural parameters and the parameters of deformation.

1.2. X-ray diffraction: a complementary tool to TEM

While TEM does reveal lattice plane misorientations giving rise to changes in the background intensity, this information remains qualitative and is hampered by the fact that partial relaxation of lattice plane bending and twisting cannot be avoided in thin TEM foils. Long-range internal stresses are not directly measurable by TEM except through the tedious evaluation of radii of curvature of dislocations which must, however, have been pinned before by some means in order to prevent dislocation rearrangement; compare Refs. [5,10]. Moreover, the small field of view of TEM does not allow easy access to microstructural variations over larger distances of some 10 μm , which are known to exist and which have been evidenced by other techniques such as, in particular, surface observations [11] or X-ray topography [12–14]. For these reasons, it is important to recall the usefulness of a combination of X-ray diffraction techniques that allows one to obtain a more global and a more quantitative picture of the deformation-induced dislocation substructure.

In order to investigate those microstructural features that are considered in the present study, the following three X-ray diffraction techniques, used in combination with TEM, are considered particularly suitable:

- (1) X-ray line broadening.
- (2) Broadening of X-ray rocking curve.
- (3) Berg–Barrett X-ray topography.

The first two diffraction techniques are based on the broadening of the X-ray diffraction peaks of plastically deformed crystals. In the picture of the Ewald sphere in reciprocal space (compare Refs. [9,15]) the diffraction spots are broadened in all three dimensions. The broadening of the X-ray linewidth originates from the elastic distortions due to the strain fields of the dislocations which cause a spread of lattice parameters. Hence, the Bragg equation is fulfilled over an accordingly broadened range of glancing (Bragg) angles $\theta \pm \Delta\theta$ or, equivalently, lattice plane spacings $d \pm \Delta d$. Typically, the halfwidths $\Delta\theta_{1/2}$ of broadened intensity line profiles, measured on the scale of the glancing angle, is of the order of minutes, corresponding to rather small lattice parameter variations $\Delta d/d$ of the order of some 10^{-4} . For our purpose, Wilkens' theory of X-ray line broadening [15,16] is considered most suitable, since it considers explicitly characteristic properties of real dislocation patterns in the form of so-called restrictedly random dislocation distributions. The analysis yields the total dislocation density and a so-called arrangement factor which allows one to distinguish between dislocation distributions of high and low internal stresses. In deformed crystals with high internal stresses, asymmetric X-ray line broadening is sometimes observed [17–21] and can be analysed to yield the *local* dislocation densities and the internal back (forward) stresses in the cell interior (cell wall) regions.

The broadening of the so-called rocking curve is caused by the deformation-induced lattice plane misorientations (mean angle of misorientation β) which can be characterized by tilt and/or twist axes. In order to bring mutually misorientated areas into Bragg reflection, the specimen must be rotated appropriately through the so-called rocking angle; compare Refs. [9,22,23]. The rocking curve is obtained as a plot of the diffracted intensity versus the rocking angle. Maximum broadening occurs when the axis of misorientation lies perpendicular to the plane of incidence [13,14,23]. Typically, the halfwidths of broadened rocking curves, $\Delta\beta_{1/2}$, are of the order of a degree and thus exceed the halfwidths of line profiles by one to two orders of magnitude. By rotating the specimen in steps through the so-called azimuthal angle φ around the normal to the reflecting lattice plane and recording a series of rocking curves for different azimuthal angles φ , the axes of misorientation can be determined, and a rather complete characterization of the misorientations can be achieved [13,14,23].

Berg–Barrett X-ray topography is performed by recording a diffraction spot on a film (or with a position-sensitive detector) and blowing up the “image” by a factor of ~ 50 ;

¹ In the present work, the term GNDs refers to local arrays of excess dislocations of one sign, irrespective of whether they are geometrically necessary or not, as elaborated elsewhere [6].

compare Refs. [12–14,23]. The image of the blown-up diffraction spot contains a fine structure which can be interpreted in terms of extinction contrast from regions of high local dislocation density and/or orientation contrast from misorientated regions fulfilling the Bragg condition for the given glancing angle. The axes of misorientation can be obtained in a similar way as in the case of rocking-curve broadening by probing in a series of topographs the dependence of the contrast observed on the azimuthal angle. While the resolution of the technique is much lower ($\sim 5 \mu\text{m}$) than in TEM, it is particularly suited to detect long-range microstructural features with a periodicity of, typically, some tens of micrometres, which are not easily accessible by TEM.

With today's possibilities of high-energy high-intensity synchrotron radiation [24–26], all the X-ray diffraction techniques described above can be applied with better resolution and higher degree of accuracy than in the classic experiments that have been performed with standard laboratory equipment hitherto. In addition, as shown by Borbély recently, the electron backscattering diffraction (EBSD) technique available today in scanning electron microscopes can be used elegantly to measure the broadening of rocking curves in dependence on the azimuthal angle [27].

2. Dislocation pile-ups and kink walls: exemplifications of the dual role of GNDs

Although it is now clear that dislocation pile-ups in the classic sense [28] are only observed occasionally in deformed metals [1–5], a discussion of dislocation pile-ups is suitable to illustrate the dual role that GNDs can play as sources of both long-range internal stresses and lattice plane misorientations. Dislocation pile-ups are associated with local deformation gradients and represent a

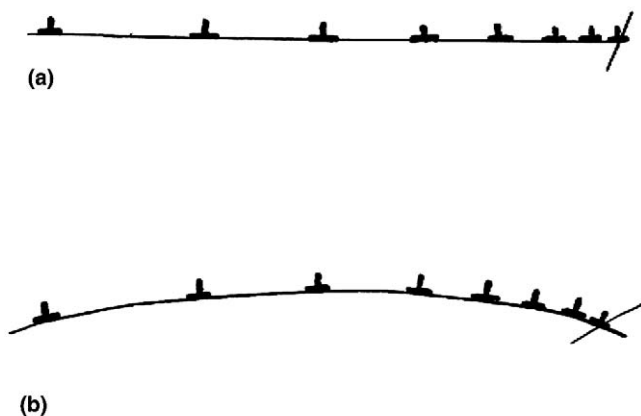


Fig. 1. Schematic of edge dislocations piling up against an obstacle. (a) Fully constrained, internal stresses unrelaxed, with no misorientations. (b) Constraints and internal stresses (partially) relaxed, with tilt bending.

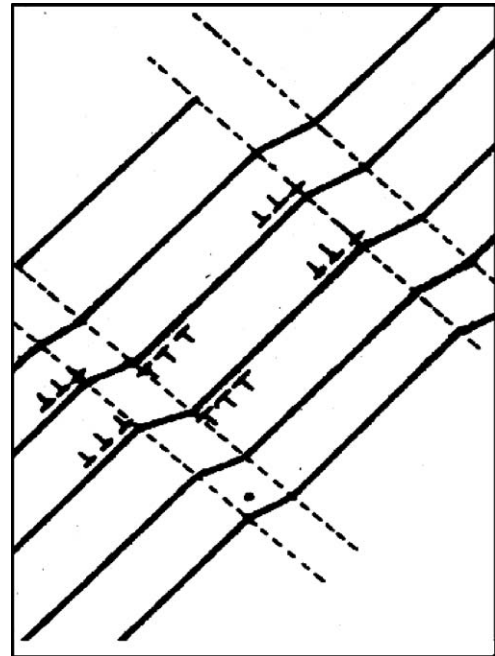


Fig. 2. Schematic of the formation of "nucleus" of kink bands. (After Ref. [11], courtesy of the authors.)

characteristic GND array. A group of edge dislocations of one sign piling up against an obstacle, as shown schematically in Fig. 1(a), would give rise to long-range internal stresses; compare, for example, Ref. [29]. When the pile-up is heavily constrained by the neighbouring material, bending will be negligible. In contrast, once the constraints are relaxed (partially), e.g. in a thin foil or near a free surface, then the glide plane will be expected to assume a curvature, as shown in Fig. 1(b), and at the same time the internal stresses would relax to some extent. Hence, the example shown in Fig. 1(b) shows that one and the same GNDs can in general give rise to both long-range internal stresses and lattice plane misorientations.

More generally, groups of dislocations, piling up against obstacles on both sides of the dislocation sources, would have to be considered, e.g. in the form of the array shown schematically in Fig. 2, as proposed by Mader and Seeger [11] long ago to illustrate the formation of the nucleus of so-called kink bands in work-hardened fcc crystals. Here, again, one and the same GND arrays act simultaneously as sources of long-range internal stresses and misorientations. In Section 4.2, a recently proposed simple microstructural model which relates the density of GNDs to the misorientations in kink bands [9] is discussed.

3. Long-range internal stresses and geometrically necessary dislocations in the composite model of crystal plasticity

In order to take into account the heterogeneity of the deformation-induced dislocation pattern, the author has developed the so-called composite model [8,18,30] which

has been thoroughly reviewed recently [31]. Hence, only those features will be summarized briefly that are essential for the present work. In the composite model, the deformation of a crystal containing, for example, a dislocation wall or cell structure, is controlled by the local flow stresses of the hard dislocation-rich cell walls and the softer dislocation-poor cell interiors. An important ingredient of the model is the natural building up of deformation-induced long-range internal forward stresses in the hard phase and back stresses in the soft phase. These internal stresses can be determined either by the analysis of asymmetrically broadened X-ray diffraction line profiles [8,17–21,31] or by measuring the local variations of dislocation curvatures in TEM micrographs [5,8,10,31,32]. In the present context, it is important that these internal stresses arise as a consequence of the formation of GNDs at the interfaces between the hard dislocation walls and the softer regions between the walls.

3.1. Composite model of single slip deformation

The composite model for single slip was proposed to describe the plastic deformation of the dipolar dislocation wall structure in persistent slip bands (PSBs) in cyclically deformed fcc crystals; compare Fig. 3(a). GND arrays of one sign at the interfaces between the walls and the channels between the walls, as illustrated in Fig. 3(b), give rise to long-range internal stresses that superimpose on the applied stress. The local shear flow stresses τ_w and τ_c in the dislocation walls and cell interiors are then given by

$$\tau_w = \tau + \Delta\tau_w \quad (1)$$

and

$$\tau_c = \tau + \Delta\tau_c \quad (2)$$

where $\Delta\tau_w$ (>0) and $\Delta\tau_c$ (<0) are the deformation-induced long-range internal forward and back stresses. The macroscopic shear flow stress τ then follows by a rule of mixtures:

$$\tau = f_c \tau_c + f_w \tau_w \quad (3)$$

where f_c and f_w are the volume fractions occupied by the channels and the walls, respectively.

The mean density ρ_{GND} of the GNDs, averaged over the wall spacing d , is easily derived [6,8,18,31] and can be expressed as

$$\rho_{\text{GND}} = \frac{2n}{d} = \frac{2(\tau_w - \tau_c)}{bdG} \quad (4)$$

where n is the line density of the GNDs, measured perpendicular to the glide plane, d is the wall spacing, b is the modulus of the Burgers vector and G is the shear modulus. Alternatively, ρ_{GND} can also be written in terms of the long-range internal forward and back stresses [6]:

$$\rho_{\text{GND}} = \frac{2(\Delta\tau_w - \Delta\tau_c)}{bdG} \quad (5)$$

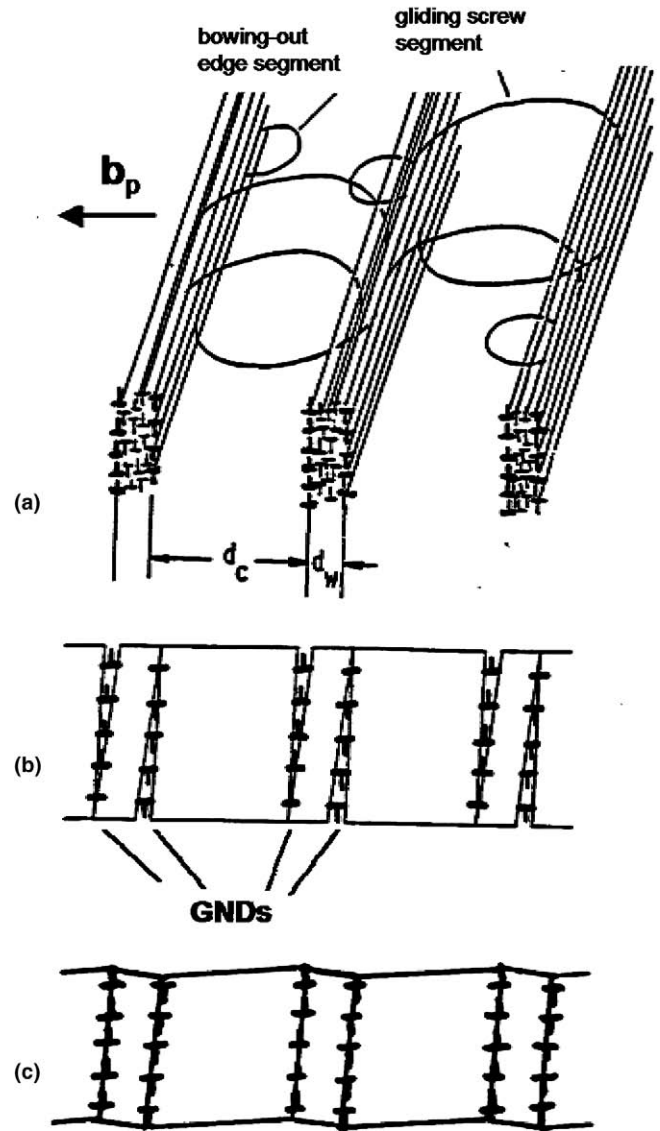


Fig. 3. Composite model for single slip deformation in PSB wall structure of cyclically deformed fcc single crystals. (a) Dislocation glide mechanisms in channels and interfacial GNDs (bold). (After Refs. [8,30].) (b) GNDs compensating unequal plastic shear deformations in PSB walls and channels. Fully constrained configuration. (After Ref. [8].) (c) Same as (b), but now with constraints and internal stresses (partially) relaxed by bending.

The quantity $(\Delta\tau_w - \Delta\tau_c)$ or, equivalently, the term $(\tau_w - \tau_c)$, compare Eqs. (4) and (5), represent the sum of the long-range internal forward and back stresses and are therefore suitable measures of the magnitude of the internal stresses.

In spite of their low density, the GNDs give rise to appreciable internal stresses. They would not, however, lead to the development of misorientations, unless the constraints of the PSB slab were allowed to relax. In the latter case, the lattice planes would be expected to undergo some to-and-fro bending, as indicated schematically in Fig. 3(c), which would, at the same time, lead to a partial relaxation of the internal stresses, as discussed in Section 4.1.

3.2. Composite model of symmetrical multiple slip

The composite model for multiple slip [8,18,30,31] describes the symmetrical operation of intersecting glide systems; compare Fig. 4(a). Pairs of dislocations of Burgers vectors \mathbf{b}_1 and \mathbf{b}_2 are held up at the interfaces between the cell walls and the cell interiors. These pairs of interface dislocations are equivalent to resultant interfacial dislocations with Burgers vectors $\pm\mathbf{b}_{\text{res}}$ lying parallel to the stress axis. They take the role of GNDs and give rise to axial long-range internal forward and back stresses $\Delta\sigma_w$ and $\Delta\sigma_c$, respectively; compare Fig. 4(b). Similar to the case of single slip, the mean density ρ_{GND} of the GNDs can be formulated as [6,8,18,31]

$$\rho_{\text{GND}} = \frac{2n}{d} = \frac{2(\sigma_w - \sigma_c)}{b_{\text{res}}Ed} \quad (6)$$

or as

$$\rho_{\text{GND}} = \frac{2(\Delta\sigma_w - \Delta\sigma_c)}{b_{\text{res}}Ed} \quad (7)$$

where σ_w and σ_c are the local axial flow stresses of the cell walls and cell interiors, respectively, d is the transverse dislocation cell diameter and E is Young's modulus. With an appropriate Schmid orientation factor ϕ , the model can be formulated equally well in terms of resolved shear stresses τ_w and τ_c . The macroscopic flow stress is again given by a rule of mixtures.

4. Assessment of long-range internal stresses, lattice plane misorientations and GNDs

4.1. Cyclically deformed fcc specimens

In the case of PSBs in cyclically deformed copper crystals of single slip orientation (primary slip system $[\bar{1}01](111)$), all quantities that relate to the internal stresses and the local shear flow stresses (Eqs. (3)–(5)) have been determined experimentally [8,30–32]. Regarding the internal stresses and the local flow stresses and their relation to the shear flow stress τ_{PSB} of the PSBs, it has recently been shown that these quantities are related by the following approximate linear relations [6]:

$$\tau_c \approx 0.63\tau_{\text{PSB}}, \quad \Delta\tau_c \approx -0.37\tau_{\text{PSB}} \quad (8)$$

and

$$\tau_w \approx 2.3\tau_{\text{PSB}}, \quad \Delta\tau_w \approx +1.3\tau_{\text{PSB}} \quad (9)$$

Typical values of the density ρ_{GND} of those GNDs responsible for the long-range internal stresses were obtained according to Eqs. (6) or (7) [6,8,9,18,31] and were found to be small ($\approx 7 \times 10^{12} \text{ m}^{-2}$), i.e. just a few per cent of the total dislocation density of $\sim 10^{15} \text{ m}^{-2}$.

TEM observations and Berg–Barrett X-ray topography have indicated that, on the average, the misorientations occurring on the scale of the PSB wall spacings are very small [33]. However, the surprising observation has been made by both techniques that appreciable misorientations exist with a long-range wavelength extending over some

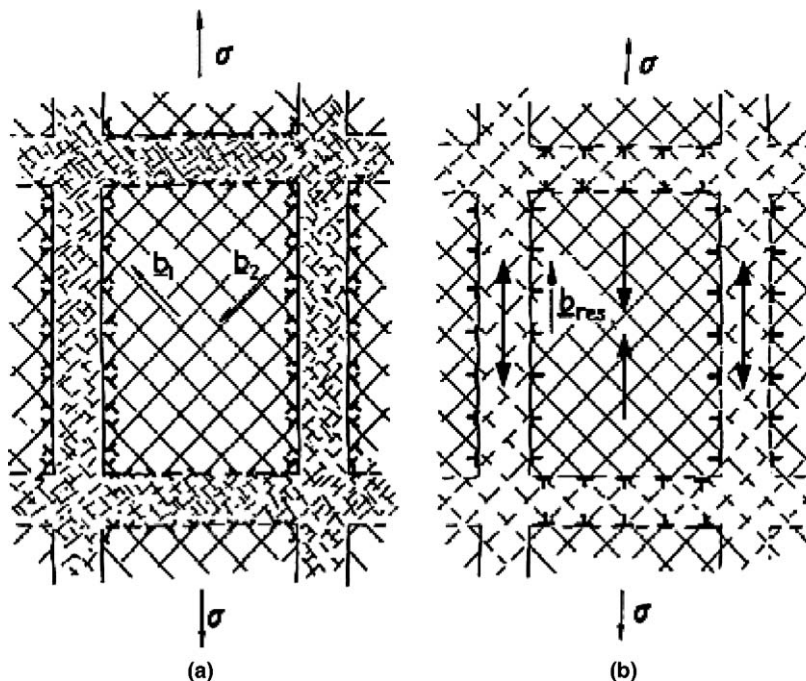


Fig. 4. Composite model for symmetrical multiple slip in a dislocation cell structure. (a) Symmetric intersecting glide systems; glide dislocations held up at dislocation cell walls. (b) Representation of held-up dislocations by "resultant" interfacial GNDs, illustrating the generation of internal stresses. (After Ref. [8].)

10 walls [6], reminiscent of the kink-band-like features observed on the surface pattern of cyclically deformed copper single crystals [34]. Similar long-range misorientations are also apparent in the (low-magnification) scanning electron microscopy (SEM)/electron channelling contrast (ECC) work of Hecker et al. [35] on cyclically deformed nickel single crystals, of Li et al. [36] on cyclically deformed copper single crystals and of Buque et al. [37] in individual grains of cyclically deformed nickel polycrystals. In copper single crystals, deformed cyclically in the so-called plateau regime of PSB formation, a kink-band-like to-and-fro tilt (misorientation angle $\beta \approx 20'$) around the line direction $[1\bar{2}1]$ of the primary edge dislocations [6,33] with a wavelength extending over some 10 wall spacings was observed. Examples of similar observations made after cyclic deformation at a higher plastic shear strain amplitude at which increasing secondary slip superimposes [33] are shown in Figs. 5 and 6. Fig. 5 shows a low-magnification TEM micrograph of a foil cut parallel to the $(1\bar{2}1)$ plane, showing a rather strong orientation contrast with a wavelength of some $10\ \mu\text{m}$. The Berg–Barrett X-ray topographs shown in Fig. 6(a) and (b) provide complementary information. Altogether, it can be concluded from contrast experiments that, at the higher plastic strain amplitude, these misorientations with rather long wavelengths have major twist and tilt components around axes roughly parallel to the normal $[111]$ to the glide plane and the line direction of the edge dislocations $[1\bar{2}1]$, respectively. The twist component is reminiscent of the twist misorientations around the normal $[111]$ to the primary glide plane which are observed in the layer-like so-called sheets/grids which develop in tensile stage II work hardening (for more details, see Section 4.2). A characteristic feature of the dislocation patterns in both cases is the increasing interaction of secondary slip

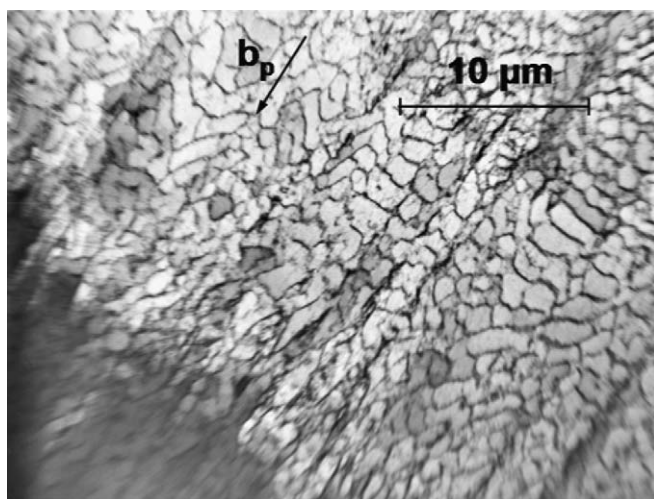


Fig. 5. Low-magnification TEM micrograph of $(1\bar{2}1)$ foil from copper single crystal deformed cyclically at a shear strain amplitude of $\gamma_{\text{pl}} = 1.45 \times 10^{-2}$, showing strong orientation contrast with long-range periodicity. (After Ref. [33].)

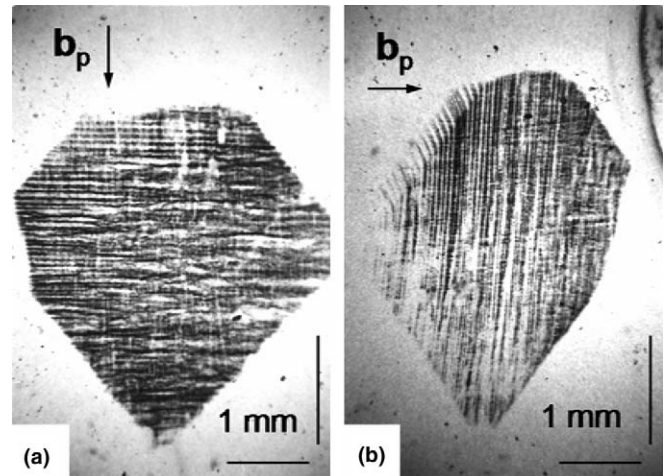


Fig. 6. Berg–Barrett X-ray topographs of $(1\bar{2}1)$ section of copper single crystal deformed cyclically at a shear strain amplitude of $\gamma_{\text{pl}} = 1.45 \times 10^{-2}$ for two azimuthal positions. (a) Primary Burgers vector perpendicular to plane of incidence, strong contrast from horizontal “kink bands”, weak contrast from vertical dislocation layers corresponding to PSB-like layer structures parallel to primary glide planes with superimposed secondary slip. (b) Same as (a), but with primary Burgers vector lying in the plane of incidence; strong contrast from kink bands (vertical), weak contrast from PSB-like layer structures. (After Ref. [33].)

systems with the primary slip system. However, the origin of the rather long wavelengths of these misorientations in cyclic deformation is still unclear, since it is generally believed that, in contrast to tensile deformation, the to-and-fro dislocation glide paths are rather short and do not extend over many wall spacings [6]. The local plastic strain amplitude in the (PSB) wall structure is much larger than the imposed plastic strain amplitude which could mean that the dislocation glide events do extend over correspondingly larger distances.

Under the (unrealistic) assumption that the PSB wall structure is completely unconstrained and would be able to relax in such a way that all GNDs contribute exclusively to the tilt misorientation as in Fig. 3(c), one obtains a value for the tilt angle $\beta \approx 9'$, based on the GND line density n (estimated as $n \approx 10^7\ \text{m}^{-1}$ via Eq. (4), from the value $\rho_{\text{GND}} \approx 7 \times 10^{12}\ \text{m}^{-2}$ stated above, using $d \approx 1.4\ \mu\text{m}$ [8,31]). The value $\beta \approx 9'$ is at least a factor of two smaller than the measured misorientations [38]. Hence, it is considered much more probable that the measured misorientations are largely due to the long-range “kink-band-like” walls. This would imply that the local GND densities at the “kink walls” is about a factor of two to three larger than the value estimated on the basis of the internal stresses according to Eqs. (4) and (5).

4.2. Copper single crystals deformed in tension in single slip

It appears that so far the only systematic quantitative studies of lattice plane misorientations in deformed single

crystals are those that were made mainly on copper single crystals by X-ray diffraction by the former research group of the late Manfred Wilkens [6,9,13–15,38–40]. In the following, some of these rather old data will be reassessed in the light of further recent developments of the composite model with respect to the role of the GNDs [6].

The dislocation microstructures in fcc single crystals deformed in single slip into work-hardening stage II exhibit two dominant features extending over larger distances, namely kink walls/bands, as mentioned previously in Section 3, and the so-called sheets/grids [1–5,31] in the form of layer-like networks which are composed of primary and secondary dislocations and their reaction products and which lie roughly parallel to the primary glide plane (111). Fig. 7(a) shows an example of a TEM micrograph of the sheets/grids in a deformed copper crystal from the work of Essmann [41], viewed in a section perpendicular to the primary glide plane. Fig. 7(b) illustrates schematically how the network is built up of primary and secondary (conjugate) dislocations and their reaction products (Lomer–Cottrell dislocations). The main misorientation introduced by these planar networks consists of to-and-fro twist misorientations around the normal $[1\bar{1}1]$ to the primary glide plane (and a to-and-fro tilt misorientation around the axis $[1\bar{2}1]$; compare Refs. [14,41]. The twist misorientation is recognized best in Berg–Barrett X-ray topographs. The example shown in Fig. 8 refers to a copper single crystal that had been deformed into the stage I/stage II transition at which secondary glide is just beginning to operate. To-and-fro displacements of the Cu $K\alpha_1$ line show clearly the twist misorientations around the axis $[111]$, caused by the formation of the sheets/grids with spacings of the order of 100 μm .

In a recently proposed model, the misorientations originating from both kink bands and sheets/grids in stage II work hardening were related to characteristic microstructural parameters, parameters of deformation and the density of the GNDs [9]. The following relationships were obtained for the maximum halfwidths of the rocking curves

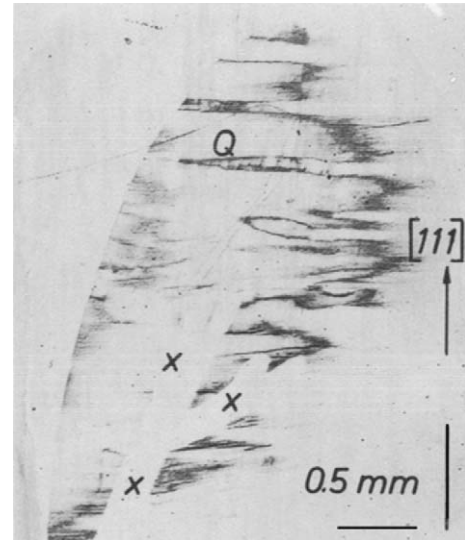


Fig. 8. Berg–Barrett X-ray topograph of $(\bar{1}01)$ section of copper single crystal deformed into stage II at 4.2 K. Note to-and-fro twist orientation contrast between neighbouring layers lying horizontally parallel to the trace of the primary glide plane (111). (After Refs. [13,14], courtesy of the authors.)

Kink walls, tilt axis $[1\bar{2}1]$:

$$\Delta\beta_{1/2} \approx 0.0169 \frac{\rho_{\text{GND}}}{\rho} \cdot \tau \quad \text{with } \tau \text{ in MPa} \quad (10)$$

Sheets/grids, twist axis $[111]$:

$$\Delta\beta_{1/2} \approx 0.00189 \frac{\rho_{\text{GND}}}{\rho} \cdot \tau \quad \text{with } \tau \text{ in MPa} \quad (11)$$

In both cases, the numerical constants contain only fairly well-known quantities. The analysis of available experimental data on the relation between $\Delta\beta_{1/2}$ and the flow stress τ obtained for copper single crystals deformed into stage IIa allows the following conclusions.

Kink walls. In this case (compare Refs. [6,9]), a linear increase of $\Delta\beta_{1/2}$ with increasing flow stress τ is found, in accord with Eq. (10), implying that the ratio ρ_{GND}/ρ remains constant in stage II work hardening and in fact assumes a value $\rho_{\text{GND}}/\rho \approx 0.045$. Thus, the density of GNDs is found to be quite small, although the GNDs play

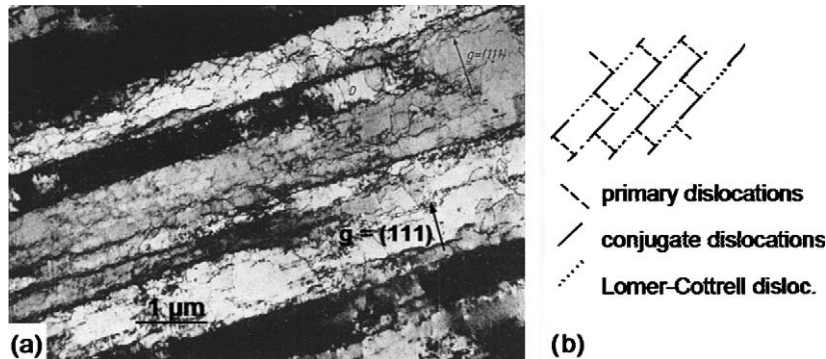


Fig. 7. Sheet/grid microstructure of copper single crystal deformed into stage II at 4.2 K. (a) TEM micrograph of $(\bar{1}01)$ section perpendicular to primary Burgers vector, showing layer-like sheet/grid structure with alternating contrast between neighbouring regions. (From Ref. [40], courtesy of the author.) (b) Schematic view of dislocation reactions in sheet/grid network. View on primary glide plane (111) (After Ref. [5]).

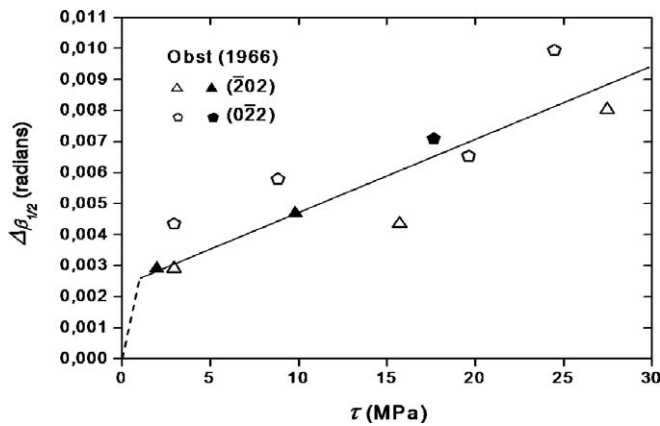


Fig. 9. Halfwidths $\Delta\beta_{1/2}$ of X-ray rocking curves measured on $(\bar{1}01)$ and (022) sections of copper single crystals deformed into stage II at 293 K (filled symbols) and 78 K (open symbols). (From Ref. [9].)

a very important role in the evolution of important features of the dislocation distribution.

Sheets/grids. Fig. 9 shows that the rocking-curve halfwidths $\Delta\beta_{1/2}$ of copper single crystals which had been deformed into stages I and II, first increase steeply as a function of the flow stress τ . Subsequently, $\Delta\beta_{1/2}$ increases more or less linearly with τ (and hence also with the resolved shear strain γ). It follows that, whereas the kink walls start to develop almost from the start of deformation, the sheets/grids begin to evolve only after secondary slip has been initiated. A more detailed analysis with some additional considerations [9] shows that, once the deformation enters into the stage I/stage II transition range, the density of GNDs “jumps” rapidly to an “early” value of $\rho_{\text{GND}} \approx 6.4 \times 10^{10} \text{ m}^{-2}$, whereupon the ratio ρ_{GND}/ρ approaches a constant value of only a few percent in the range in which $\Delta\beta_{1/2}$ increases linearly. Thus, it is found again that the density ρ_{GND} of the GNDs is relatively low.

The finding that, in both cases discussed, the magnitude of the misorientations increases linearly as a function of the resolved shear strain γ has important consequences. Statistical considerations by Pantleon [42,43] have shown that a linear relationship between the misorientations and the shear strain γ implies that the dislocation structures responsible for the misorientations are so-called geometrically necessary boundaries (GNBs) in the terminology of Kuhlmann-Wilsdorf and Hansen [44]. These latter authors distinguish between GNBs and incidental dislocation boundaries (IDBs). In the case of IDBs, as shown by Pantleon and previously, in less detail, by others [45,46], the misorientations are expected to increase with $\sqrt{\gamma}$ and not linearly with γ . An example for this behaviour is presented in the following section.

4.3. $[001]$ -Orientated copper single crystals deformed in multiple slip

In the following, the case of deformed $[001]$ -orientated copper single crystals [17,18] that develop a typical disloca-

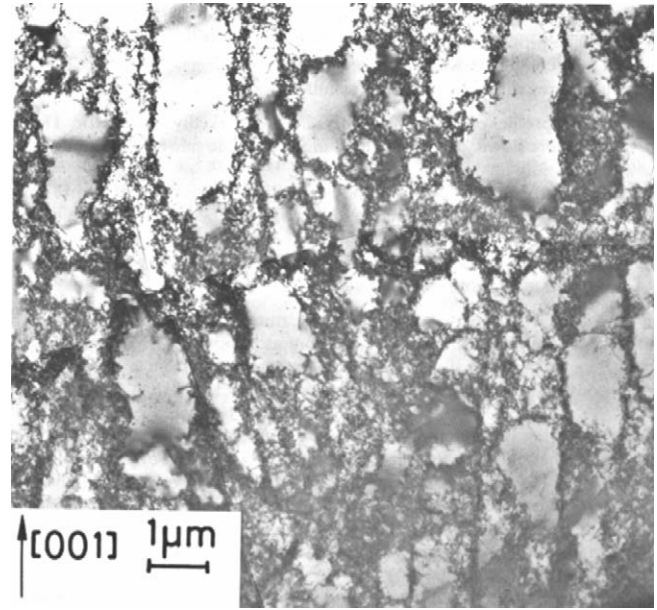


Fig. 10. Composite TEM micrograph of dislocation cell structure in (010) section of $[001]$ -orientated copper single crystal deformed to a resolved shear flow stress of $\tau = 75.6 \text{ MPa}$. (From Refs. [17,18].)

tion cell structure during deformation, as shown in the example of Fig. 10, is discussed. For this purpose, use is made of the relevant values of the macroscopic axial flow stresses σ , the internal stresses $\Delta\sigma_w$ and $\Delta\sigma_c$ and, correspondingly, the local axial flow stresses σ_w and σ_c (equivalent to the sums of σ and the internal stresses $\Delta\sigma_w$ and $\Delta\sigma_c$, respectively) that had been obtained by the evaluation of asymmetrically broadened intensity line profiles [18], taking into account the corrections stated in an erratum [47]. With the value of Young's modulus in the $[001]$ direction, $E_{[001]} = 67,000 \text{ MPa}$, and with the values d from the detailed TEM studies of Göttler [48], the values ρ_{GND} (of those GNDs responsible for the internal stresses) were then evaluated according to Eqs. (6) or (7). It should be noted that these values refer to “resultant” GNDs whose Burgers vector \mathbf{b}_{res} is larger by a factor of about 1.5 than the usual Burgers vector. The GND values obtained are only quantitatively correct within a factor of ~ 2 , because the simple dislocation glide geometry assumed in the composite model of multiple slip (Fig. 4) does not correspond in detail to the crystallography of multiple slip in $[001]$ -orientated fcc crystals.

All the data are presented in Table 1, together with the values ρ of the total dislocation densities obtained by X-ray diffraction [17,18]. The ratios ρ_{GND}/ρ are also included in Table 1. It should be noted that the GND density ρ_{GND} is found to be relatively small and increases with increasing deformation at such a rate that the ratio ρ_{GND}/ρ remains approximately constant at a value of only about 1–1.5%.

Next, the evolution of the local flow stresses τ_w and τ_c and the internal stresses $\Delta\tau_w$ and $\Delta\tau_c$ as a function of deformation are considered. For this purpose all axial stresses were converted into resolved shear stresses (using the

Table 1

Parameters of deformation (axial stresses σ , resolved shear strains γ were calculated from the axial strains ε , using the Schmid factor $\phi = 0.408$), local flow stresses σ_c and σ_w , determined from asymmetric X-ray line broadening [17,18,47], cell wall spacings d (interpolated values from the TEM work of Götter [48]), GND densities ρ_{GND} , calculated according to Eqs. (6) or (7) and the ratio ρ_{GND}/ρ

σ (MPa)	$\gamma = \varepsilon/\phi$	σ_c (MPa)	σ_w (MPa)	d (μm)	ρ (10^{14} m^{-2})	ρ_{GND} (10^{12} m^{-2})	ρ_{GND}/ρ
64.2	0.068	57.11	94.12	2.3	0.68	1.36	0.02
91.42	0.11	83.58	125.0	1.85	1.1	1.89	0.017
147.3	0.24	130.15	204.9	1.015	2.48	6.21	0.025
185.3	0.52	164.2	248.3	0.807	3.46	8.79	0.025

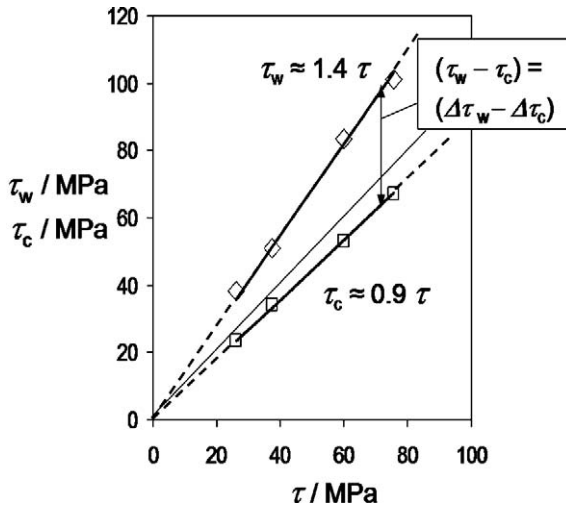


Fig. 11. Plot of local shear flow stresses τ_w and τ_c of tensile-deformed [001]-orientated copper single crystals against the macroscopic resolved shear flow stress τ . The faint line under 45° would correspond to the equality of local stresses and applied stresses. Note linear relationships and linear increase of $(\tau_w - \tau_c) = (\Delta\tau_w - \Delta\tau_c)$.

Schmid factor $\phi = 0.408$ for glide on eight equivalent octahedral slip systems in fcc [001]-orientated single crystals) in order to obtain the local shear flow stresses τ_w and τ_c (and the internal stresses $\Delta\tau_w$ and $\Delta\tau_c$) as a function of the macroscopic shear flow stress τ , as shown in Fig. 11. The most important result is that the local shear flow stresses (and hence also the internal stresses) increase linearly with increasing macroscopic shear flow stress. As indicated in the diagram, the differences $(\tau_w - \tau_c)$ and $(\Delta\tau_w - \Delta\tau_c)$ are identical and reflect simply the relationships $\tau_w = \tau + \Delta\tau_w$ and $\tau_c = \tau + \Delta\tau_c$. The results can be expressed to a good approximation as

$$\tau_c \approx 0.9\tau, \quad \Delta\tau_c \approx -0.1\tau \quad (12)$$

and

$$\tau_w \approx 1.4\tau, \quad \Delta\tau_w \approx +0.4\tau \quad (13)$$

We note that these linear relationships are qualitatively similar to the results obtained for PSBs (Eqs. (8) and (9)) and that Hieckmann has obtained similar relationships also for both cyclically and tensile-deformed nickel single crystals [49]. As discussed elsewhere [50], the above linear relationships have the interesting implication in the framework of the composite model that the ratio of the local

dislocation densities in the dislocation cell interiors and cell walls must remain constant.

The density ρ_{GND} of those GNDs that are responsible for the internal stresses (seventh column of Table 1) follows with little scatter a linear relationship with the square of the macroscopic flow stress (expressed as τ^2 or σ^2) as follows:

$$\rho_{\text{GND}} \approx 2.62 \times 10^8 \sigma^2 \text{ m}^{-2} \quad \text{with } \sigma \text{ in MPa} \quad (14a)$$

or

$$\rho_{\text{GND}} \approx 15.74 \times 10^8 \tau^2 \text{ m}^{-2} \quad \text{with } \tau \text{ in MPa} \quad (14b)$$

Since the cell wall spacing d can be assumed to vary inversely with the stress, this result is in accord with Eqs. (4) and (5), supplemented by Eqs. (12) and (13). Moreover, assuming that σ^2 and τ^2 are proportional to the total dislocation density ρ (Taylor flow-stress law), this result is also consistent with the earlier finding that $\rho_{\text{GND}}/\rho \approx \text{constant}$ (Table 1, seventh column).

Fortunately, X-ray rocking curve data also exist for the same [001]-orientated copper single crystals discussed above. The relation between the rocking curve halfwidths $\Delta\beta_{1/2}$, reported earlier by Wilkens et al. [40], and the resolved shear strain γ (see Table 1) is plotted in Fig. 12. in the form $\Delta\beta_{1/2}$ versus $\sqrt{\gamma}$. The figure refers to the maximum and minimum halfwidths that were observed for the two azimuthal angles $\varphi = 0^\circ$ and $\varphi = 90^\circ$, respectively.

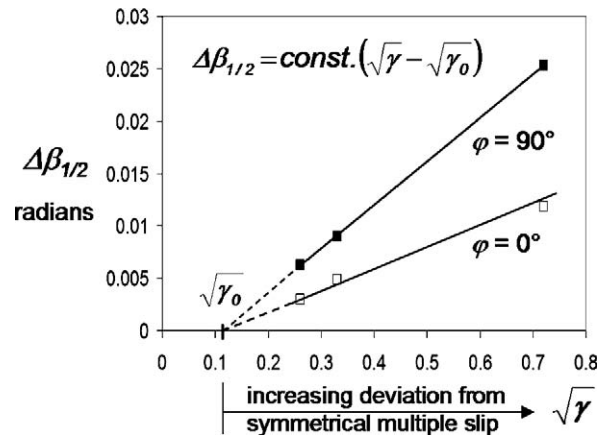


Fig. 12. Plot of halfwidths $\Delta\beta_{1/2}$ of X-ray rocking curves, measured on tensile-deformed [001]-orientated copper single crystals with (002) or (020) reflections for two different azimuthal positions as a function of $\sqrt{\gamma}$. Note linear relationships and intercepts with abscissa at $\sqrt{\gamma} \approx 0.12$. See text for further details.

These two azimuthal angles correspond to the [001] direction lying either perpendicular to or in the plane of incidence, respectively. A remarkably good linear relationship with $\sqrt{\gamma}$ is found in both cases. It is interesting that, for both azimuthal positions, the data points fall precisely on straight lines that do not go through the origin but intersect the abscissa at the same value of $\sqrt{\gamma_0} \approx 0.12$, corresponding to a resolved shear strain $\gamma_0 \approx 0.014$. Hence, both straight lines can be defined by relations of the form

$$\Delta\beta_{1/2} \approx \text{constant} \times (\sqrt{\gamma} - \sqrt{\gamma_0}) \quad (15)$$

This result is interesting, since misorientations would not be expected to develop in ideally symmetric multiple slip. Hence, the misorientations observed must have resulted from deviations from symmetric multiple slip. More specifically, it is proposed that the value $\gamma_0 \approx 0.014$ is that shear strain up to which multiple slip is symmetric and beyond which increasing deviations occur. Another important conclusion follows from the linear increase of $\Delta\beta_{1/2}$ with $\sqrt{\gamma}$. According to Pantleon [42,43], Argon and Haasen [45] and Nabarro [46], this evolution law is characteristic of a pure stochastic process of dislocation accumulation in IDBs. Presently, no microstructural model of the evolution of the misorientations and of the responsible GNDs in deformed [001]-orientated single crystals exists. The model proposed by Wilkens et al. [40] to explain the observed rather unexpected azimuthal dependence of the broadening of the rocking curves is quite intricate. Hence, it will probably not be as easy to derive a model for multiple slip (with deviations from symmetry) as it was in the case of the kink walls and sheets/grids observed in single slip.

5. Concluding remarks

The novel aspects of this study can be summarized as follows:

- The evolution of internal stresses and lattice plane misorientations in deformed crystals has been analysed for the first time in a unified approach which relates in simple semi-quantitative models these long-range features of the dislocation pattern to the arrangement and density of geometrically necessary dislocation (GNDs).
- Important new insights could be gained from a systematic analysis of available experimental TEM data and, in particular, X-ray data of internal stresses and misorientations in unidirectionally and cyclically deformed copper crystals.
- Rather simple relationships were found to exist between the macroscopic flow stress and the long-range internal stresses, the local flow stresses in hard and soft regions, the lattice plane misorientations and the related densities of GNDs.

- In spite of the fact that the density of the GNDs is usually only a few per cent of the total dislocation density, they play an important dual role in giving rise to the deformation-induced long-range internal stresses and/or the lattice plane misorientations.

It has so far not been possible to incorporate the long-range features of the deformation-induced dislocation distribution studied in the present work in current theories of plastic deformation and work hardening. On the other hand, some aspects discussed here such as the development of internal stresses have also been revealed qualitatively in discrete dislocation dynamics (DDD) studies of plastic deformation [51]. Current DDD work is limited in the size of the volumes studied and confined to rather small deformations, whereas the long-range features of the dislocation distribution which are of interest here evolve mainly at larger strains. Nonetheless, it is hoped that the current work will stimulate more systematic DDD studies of the long-range correlations of the dislocation pattern, as greater computing power becomes available and as the DDD techniques are developed further. At the same time, comprehensive analytical modelling of the evolution of internal stresses and misorientations is desirable. The results obtained in this study can provide valuable guidelines in both kinds of future work.

Acknowledgements

The author is indebted to the reviewer for drawing attention to a serious error in the numerical evaluation. The foundation of this work goes back to studies performed 20–40 years ago by the author and others at the Max-Planck-Institut für Metallforschung in Stuttgart. These studies were strongly inspired by the late Dr. Manfred Wilkens to whom this article is dedicated and by the head of the institute, Professor Alfred Seeger. Their contributions are deeply appreciated.

References

- [1] Nabarro FRN, Basinski ZS, Holt DL. *Adv Phys* 1964;13:193.
- [2] Seeger A. In: Hirth JP, Weertman J, editors. *Work hardening*. New York (NY): Gordon and Breach; 1968. p. 27.
- [3] Hirsch PB. In: Hirsch PB, editor. *The physics of metals: 2. Defects*. Cambridge: Cambridge University Press; 1975. p. 189.
- [4] Basinski SJ, Basinski ZS. In: Nabarro FRN, editor. *Dislocations in solids*, vol. 4. Amsterdam: North-Holland; 1979. p. 261.
- [5] Mughrabi H. In: Argon AS, editor. *Constitutive equations in plasticity*. Boston (MA) and London: MIT Press; 1975. p. 199.
- [6] Mughrabi H. *Philos Mag* [in press].
- [7] Ashby MF. *Philos Mag* 1970;21:399.
- [8] Mughrabi H. *Acta Metall* 1983;31:1367.
- [9] Mughrabi H, Obst B. *Z Metallkd* 2005;96:686.
- [10] Mughrabi H. *J Microsc Spectrosc Electron* 1976;1:571.
- [11] Mader S, Seeger A. *Acta Metall* 1960;8:513.
- [12] Honeycombe RWK. *J Inst Metals* 1951–1952;80:49.
- [13] Wilkens M. *Can Phys* 1967;45:567.
- [14] Obst B, Auer H, Wilkens M. *Mater Sci Eng* 1968/1969;3:41.

- [15] Wilkens M. In: Hessel Anderson N et al., editors. Microstructural characterization of materials by non-microscopical techniques. Proceedings of the 5th Risoe international symposium on metallurgy and materials science. Roskilde: Risoe National Laboratory; 1984. p. 153.
- [16] Wilkens M. *Phys Stat Sol (A)* 1970;2:359.
- [17] Ungár T, Mughrabi H, Rönnpágel D, Wilkens M. *Acta Metall* 1984;32:333.
- [18] Mughrabi H, Ungár T, Kienle W, Wilkens M. *Philos Mag* 1986;53:793.
- [19] Ungár T. *Mater Sci Forum* 1994;166–169:23.
- [20] Hecker M, Thiele E, Holste C. *Z Metallkd* 1998;89:203.
- [21] Hecker M, Thiele E, Holste C. *Acta Mater* 2002;50:2357.
- [22] Hirsch PB. *Prog Metal Phys* 1956;6:283.
- [23] Wilkens M, Eckert K. *Z Naturforsch* 1964;19a:459.
- [24] Pantleon W, Poulsen HF, Almer J, Lienert U. *Mater Sci Eng A* 2004;387:339.
- [25] Nielsen SF, Lauridsen EM, Juul-Jensen D. *Mater Sci Eng A* 2001;319–321:179.
- [26] Barabash RI, Ice GE, Larson BC, Yang W. Fundamental research series, from proteins to semiconductors: beyond the average structure. Kluwer Academic/Plenum; 2002. p. 49.
- [27] Borbély A. Private communication; 2005.
- [28] Eshelby JD, Frank FC, Nabarro FRN. *Philos Mag* 1951;42:351.
- [29] Cottrell AH. Dislocations and plastic flow in metals. London: Oxford University Press; 1953. p. 104.
- [30] Mughrabi H. *Revue Phys Appl* 1988;23:367.
- [31] Mughrabi H, Ungár T. In: Nabarro FRN, Duesberry MS, editors. Dislocations in solids, vol. 11. Amsterdam: Elsevier Science; 2002. p. 343.
- [32] Mughrabi H. *Phys Stat Sol (A)* 1987;104:107.
- [33] Ackermann F, Mughrabi H. Unpublished work; 1976.
- [34] Mughrabi H. *Mater Sci Eng* 1978;33:207.
- [35] Hecker M, Thiele E, Holste C. *Z Metallkd* 1997;88:321.
- [36] Li Y, Li SX, Li GY. *Mater Sci Eng A* 2004;372:75.
- [37] Buque C, Bretschneider J, Schwab A, Holste C. *Mater Sci Eng A* 2001;300:254.
- [38] Wilkens M, Herz K, Mughrabi H. *Z Metallkd* 1980;71:376.
- [39] Obst B. Diplomarbeit, Technische Hochschule Stuttgart; 1966.
- [40] Wilkens M, Ungár T, Mughrabi H. *Phys Stat Sol (A)* 1987;104:157.
- [41] Essmann U. *Phys Stat Sol* 1965;12:723.
- [42] Pantleon W, Hansen N. *Mater Sci Eng A* 2001;309–310:246.
- [43] Pantleon W. *Solid State Phenom* 2002;87:73.
- [44] Kuhlmann-Wilsdorf D, Hansen N. *Scripta Metall Mater* 1991;25:1557.
- [45] Argon AS, Haasen P. *Acta Metall Mater* 1993;41:3289.
- [46] Nabarro FRN. *Scripta Metall Mater* 1994;30:1085.
- [47] Ungár T, Mughrabi H, Wilkens M, Hilscher A. *Philos Mag A* 1991;64:495.
- [48] Göttler E. *Philos Mag* 1973;28:1057. Doctoral thesis, Technische Universität Braunschweig; 1973.
- [49] Hieckmann E. Personal communication; 2004/2005.
- [50] Mughrabi H. *Int J Mat Res (formerly Z Metallkd)* 2006;97:594.
- [51] Devincre B, Kubin LP. *Mater Sci Eng A* 1997;234–236:8.

Dislocation structures in cyclically strained X10CrAl24 ferritic steel [☆]

M. Petrenec ^{*}, J. Polák, K. Obrtlík, J. Man

Institute of Physics of Materials, Academy of Sciences of the Czech Republic, Group of Low Cycle Fatigue, Žitkova 22, 616 62 Brno, Czech Republic

Received 14 October 2005; received in revised form 14 February 2006; accepted 23 March 2006

Available online 13 June 2006

Abstract

Dislocation structures in polycrystalline X10CrAl24 ferritic stainless steel cyclically strained with constant plastic strain amplitude to failure at room temperature were studied using transmission electron microscopy. The spatial arrangement of dislocations in the individual grains was determined using the oriented foil technique. The characteristic types of dislocation structures for plastic strain amplitudes from 10^{-5} to 10^{-2} were determined. The typical dislocation structures consisted of a random arrangement of mostly screw dislocations for the lowest plastic strain amplitudes ($\epsilon_{ap} < 5 \times 10^{-5}$), veins and walls intersected by ladder-like structure for medium plastic strain amplitudes ($5 \times 10^{-5} < \epsilon_{ap} < 2 \times 10^{-3}$) and predominantly wall, labyrinth and cellular structures for the highest plastic strain amplitudes ($\epsilon_{ap} > 2 \times 10^{-3}$). Their relative fractions dependent on the applied plastic strain amplitude were quantitatively evaluated. Special attention was paid to cyclic softening which is discussed in terms of specific properties of dislocations in a body-centered cubic structure and the localization of cyclic plastic strain to persistent slip bands.

© 2006 Acta Materialia Inc. Published by Elsevier Ltd. All rights reserved.

Keywords: Transmission electron microscopy; Ferritic steel; Fatigue; Dislocation structures; Persistent slip band

1. Introduction

The fatigue damage of material produced by cyclic loading is closely related to the internal dislocation structure. The initial stages of the fatigue of numerous structural materials are characterized by the evolution of a heterogeneous dislocation configuration which becomes unstable during cycling. Localized bands with a specific substructure called persistent slip bands (PSBs) are formed. Due to the localized deformation, a characteristic surface relief (persistent slip markings, PSMs) develops and subsequently fatigue cracks are initiated within them [1,2]. Thus, in order to understand the cyclic stress–strain response as well as fatigue crack initiation and its modeling, it is essential to know the dislocation structure, especially the structure of localized bands.

Body-centered cubic (bcc) metals represent a very important group of materials widely used in engineering practice. Their cyclic plastic behavior is strongly dependent on temperature, strain rate and amount of interstitial or substitutional atoms [1,3–6]. This is caused by specific properties of screw dislocations in the bcc lattice, which possess a threefold symmetry and a high Peierls stress. Due to these properties, the long-range motion of screw dislocations is thermally assisted via the formation of kink pairs which help to transfer the dislocation from one Peierls valley into the next one [7]. Owing to the strong temperature dependence of screw dislocation mobility, a “low-temperature regime” and a “high-temperature regime” can be found in bcc metals. The transition or knee temperature T_k depends on the strain rate and for iron-based alloys and usual strain rates it is close to or slightly above room temperature. Therefore, room temperature cyclic straining corresponds to the intermediate or low-temperature regime [1]. The high-temperature regime is characterized by small effective stress (a thermally activated component) and the dislocation arrangement is similar to

[☆] This manuscript was presented at the “Micromechanics and Microstructure Evolution: Modeling, Simulation and Experiments” held in Madrid/Spain, September 11–16, 2005.

^{*} Corresponding author. Tel.: +420 532290338; fax: +420 541218657.

E-mail address: petrenec@ipm.cz (M. Petrenec).

that of face-centered cubic (fcc) metals. The main characteristic of the low-temperature regime is large effective stress, large stress asymmetry and easy activation of secondary slip systems. With increasing temperature the thermal activation increases the mobility of screw dislocations and at the transition temperature T_k it approximately reaches the mobility of edge dislocations. Thus, above T_k there is a similar situation as in fcc metals, while below T_k the plastic deformation is controlled by the mobility of screw dislocations [4,7].

Studies of the dislocation structures of cyclically strained bcc materials are limited. α -iron or low-carbon steel single crystals have been studied by Mughrabi et al. [4,5]. Ferritic stainless steel single crystals with 13 wt.% Cr have been studied by Šesták et al. [7], those with 26 wt.% Cr by Magnin et al. [8,9], those with 30 wt.% Cr by Kaneko et al. [10] and those with 35 wt.% Cr containing fine precipitates by Li and Umakoshi [11]. Ferritic Fe–Si single crystals with 0.5–3 wt.% Si by Šesták et al. [12] and those with 3 wt.% Si by Mori et al. [13].

The effect of the temperature and the carbon content on the fatigue behavior of polycrystalline α -Fe has been studied by Sommer et al. [6]. The dislocation arrangement in carbon steels has been studied by Pohl et al. [14,15] and by Lloyd et al. [16], and in low-alloy polycrystalline ferritic steel by Roven and Nes [17], Petersmeier et al. [18] and Pohl et al. [19]. The only studies of the dislocation arrangement in ferritic polycrystalline stainless steels have been reported by Fielding and Stobbs [20] and Magnin et al. [21]. Fielding and Stobbs analyzed the dislocation arrangements produced in 25% Cr stainless steel cyclically strained with a plastic strain amplitude of 3.5×10^{-3} . Magnin et al. showed an example of channel and wall structures produced with a plastic strain amplitude of 2×10^{-3} at the early stage of cyclic straining.

Specific dislocation structures that could be responsible for cyclic strain localization have thoroughly been studied in fcc single and polycrystals [1–3,22–25] in which the PSBs typically have a ladder structure. This ladder-like structure of PSBs in bcc metals has been observed only in polycrystalline low-carbon steel [14,15], polycrystalline Fe–25% Cr [20] and Fe–30% Cr alloy single crystals [26]. Most structures ascribed to PSBs were the walls [12,17,27,28], cells [7,12] or dislocation-poor channels [4–6,15,29]. There have been no systematic studies of the internal dislocation structure and its relation to the cyclic stress–strain response over a wide interval of constant plastic strain amplitude loading in polycrystalline stainless ferritic steel.

The aim of the study reported in the present paper was to investigate the internal dislocation structures in polycrystalline X10CrAl24 ferritic stainless steel cyclically strained up to fracture with plastic strain amplitudes in a wide interval. Our attention is focused on the documentation of a three-dimensional picture of the dislocation arrangement by means of the technique of oriented foils and on the quantitative evaluation of the different types of dislocation structures present in the specimens that were

cycled with different amplitudes. The fatigue softening observed is discussed in relation to the production of low-energy dislocation configurations.

2. Experimental

Ferritic X10CrAl24 stainless steel in the form of a bar of 30 mm in diameter was supplied by Thyssen (Germany). Its chemical composition is shown in Table 1. The material was hot rolled in the temperature interval from 1100 to 800 °C and annealed at 800 °C. The average grain size was 38 μm (found using the linear intercept method); strings of carbides (M_{23}C_6) lying parallel to the longitudinal direction and aluminum nitride inclusions were detected in metallographic sections. The texture analysis was performed using a Philips XL30 scanning electron microscope equipped with an electron backscatter diffraction (EBSD) facility. From the pole figures (Fig. 1) the concentration of (001) planes in three perpendicular directions (RD, parallel to the bar axis; TD, transverse; and ND, normal) is apparent. These results clearly indicate rolling texture in which the cross-section of the specimen is nearly parallel with {001} planes. The concentrations of the {001} pole planes have statistical significance which is nine times as high as the significance corresponding to random distribution (the upper limit of the last category in Fig. 1). The orientation of the major fraction of grains is towards a multiple slip. The monotonic tensile properties of X10CrAl24 ferritic steel are characterized as follows: $\sigma_{0.2} = 488 \text{ MPa}$, $\sigma_{\text{UTS}} = 588 \text{ MPa}$, $A_5 = 28.2\%$ and the reduction of the area 65.6%.

Cylindrical specimens of 8 mm in diameter and 12 mm in gauge length were produced with the axis parallel to the axis of the bar by machining and final grinding. They were cycled in a computer-controlled MTS 880 electrohydraulic machine. A symmetrical strain cycle with a strain rate of $\dot{\epsilon} = 2.5 \times 10^{-3} \text{ s}^{-1}$ was applied at room temperature. The plastic strain amplitude equal to the half-width of the hysteresis loop was kept constant by using the computer “outer loop”. Using this control several initial cycles were necessary to achieve the desired plastic strain amplitude (3–100 cycles). More details concerning the testing procedure are given elsewhere [27,28].

The fatigued specimens were sectioned in the gauge area either parallel to or at an angle of 45° to the specimen axis using a spark-cutting machine. Slices with a thickness of 0.8 mm were ground mechanically to a thickness of about 80 μm . Discs with a diameter of 3 mm were cut from the slices (marking the direction of the specimen axis) and then thinned using the double-jet technique until a perforation appeared. An electrolyte consisting of 90% acetic acid

Table 1
The chemical composition (wt.%) of the X10CrAl24 ferritic stainless steel

C	Si	Mn	P	S	Cr	Ni	Mo	Al	Fe
0.077	1.0	0.56	0.02	0.002	24.4	0.26	0.11	1.4	Balance

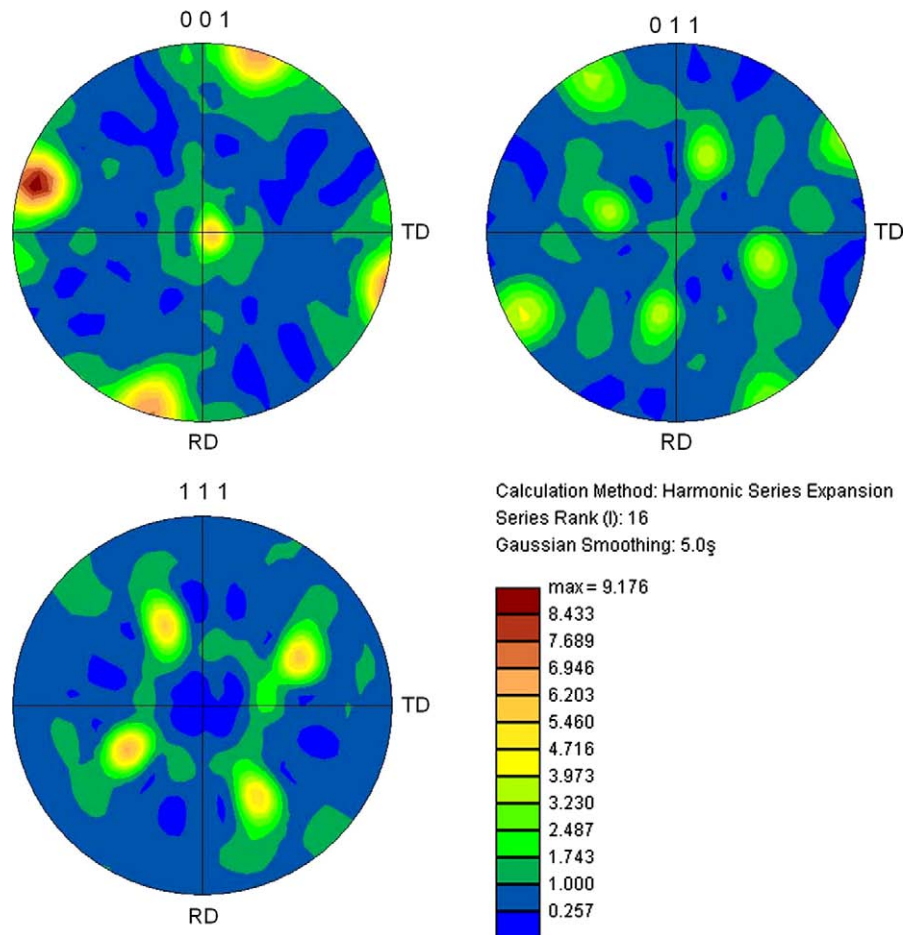


Fig. 1. Pole figures of a texture analysis for ferritic X10CrAl24 steel as obtained using EBSD.

and 10% perchloric acid was used for electrolytic thinning at 90–110 V at a temperature of 12–14 °C.

The internal dislocation structures were observed using a Philips CM-12 scanning transmission electron microscope operating at 120 kV using a double tilt holder and a MegaView II digital camera. Special care was taken to preserve the direction of the specimen axis so that the orientation of each grain relative to the loading axis could be determined [30]. Mostly bright-field imaging conditions were adopted and the diffraction patterns and Kikuchi lines were used to determine the grain orientation (stress axis, SA, and foil plane, FP).

The dislocation structures were examined in the specimens cyclically strained with plastic strain amplitudes of 10^{-5} , 5×10^{-5} , 10^{-4} , 2×10^{-3} and 10^{-2} up to the end of the specimen life. Another specimen was subjected to a constant stress amplitude of 360 MPa (saturation plastic strain amplitude of 5×10^{-5}) up to fracture [27,28].

3. Results

3.1. Cyclic stress–strain response

A thorough study of the stress–strain relation under constant plastic strain amplitude loading was reported ear-

lier [27,28,31]. In order to be able to compare the dislocation structures with the cyclic stress–strain response, two characteristic results are presented here. Fig. 2 shows the cyclic hardening–softening curves corresponding to the specimens from which thin foils for a dislocation structure study were prepared. Initial cyclic hardening for the medium and high plastic strain amplitudes is followed by cyclic softening for all amplitudes. The cyclic stress–strain curve in Fig. 3 was plotted using the stress amplitudes at half-life

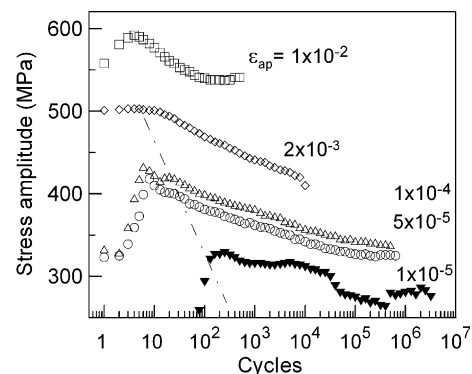


Fig. 2. Cyclic hardening–softening curves for ferritic X10CrAl24 steel in constant plastic strain amplitude cycling (the dotted curve separates the initial region before the desired strain amplitude was reached).

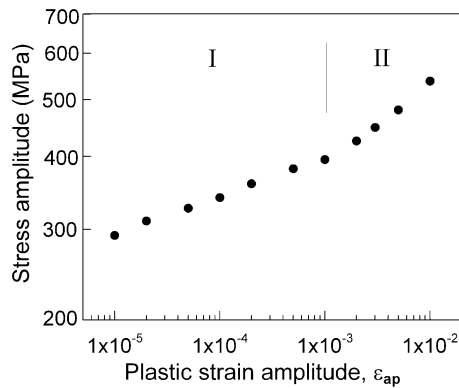


Fig. 3. Cyclic stress–strain curve for ferritic X10CrAl24 steel.

of all specimens. Two different regimes denoted as I and II are seen for this curve. In regime I the slope of the curve is lower than that in regime II.

3.2. Dislocation structures

In order to obtain information on the typical dislocation arrangement in three dimensions, the foil plane was oriented in relation to the externally applied stress and in relation to the characteristic crystallographic planes of the grain. We have adopted the usual notation, in which the stress axis is located within the basic stereographic triangle $[001]$, $[\bar{1}11]$, $[011]$. The analysis of the dislocation arrangement in materials with a bcc structure is complicated by the fact that dislocations can glide not only on $\{110\}$ planes, but also on $\{211\}$ and $\{123\}$ planes. The orientation of the grain with respect to the stress axis does not unequivocally determine which slip system is the primary one. The analysis of the possible slip systems considering all three types of slip planes and the simplified nomenclature is shown in Table 2 and Fig. 4. Fig. 4 shows a map of the Schmid factor in the basic stereographic triangle for the slip on $\{110\}$ planes, on $\{110\}$ and $\{211\}$ and on all three $\{110\}$, $\{211\}$ and $\{123\}$ planes. The Schmid factors of the primary slip systems are shown. The black lines in Figs. 4(b) and (c) denote the lines where the Schmid factors of both competing slip planes are equal. The white lines show the

boundaries of the areas where the Schmid factors of the primary and secondary systems differ by less than 5%. This delimits the orientation of the grains where a secondary slip is probable. If $\{110\}$ planes were active, there is only one primary slip system $(\bar{1}01)$ $[111]$ (denoted as **ap**) with the maximum of the Schmid factor $\mu = 0.5$ for the orientation of the stress axis $[\bar{1}49]$ (see Fig. 4(a)). If the stress axis is close to the sides of the triangle, the respective secondary systems (denoted as **as**) could be active (see Fig. 4). In the vertexes of the stereographic triangle further slip systems could be activated.

If the dislocations glide on $\{110\}$ and $\{211\}$ slip planes, three domains are identified in the basic triangle (Fig. 4(b)). The middle domain corresponds to the **ap** system and the two new domains to **bp1** and **bp2** systems. Possible additional secondary systems are **bs1**, **bs2** and **bs3**. Additional secondary systems could be activated in the vertexes of the triangle. If the dislocations glide on all three systems of slip planes $\{110\}$, $\{211\}$ and $\{123\}$, five domains could be identified in the basic triangle (Fig. 4(c)). In comparison with Fig. 4(b) two more domains appear. They correspond to the slip systems **cp1** and **cp2**. In the domain of **cp1** the secondary systems **cs1** and **cs2** could be active. On the boundary of the domain **cp2** the secondary slip systems **cs3**, **cs4** and **cs5** could be active.

A further analysis is based on the assumption that the slip is predominantly on the $\{110\}$ planes. In order to obtain the information on the dislocation arrangement in three dimensions, only the sections that were close to the three mutually perpendicular crystallographic planes within a grain were chosen from numerous foils and individual grains in these foils, as shown schematically in Fig. 5: section A, the foil plane was close to the primary slip plane $(\bar{1}01)$; section B, the foil plane was close to the plane perpendicular to the primary Burgers vector; section C, the foil plane was close to the plane perpendicular to the primary slip plane and parallel to the primary Burgers vector. Using these three sections a true picture of the individual dislocation structures and their proportions found at different plastic strain amplitudes could be obtained.

3.3. Regime I

The material in an as-supplied state contained low, but detectable density of dislocations belonging to various slip systems. Most of them were screw in character and formed subgrain boundaries [28]. Cycling at the lowest level ($\varepsilon_{ap} = 10^{-5}$) did not change the initial dislocation arrangement substantially and no specific spatial dislocation arrangement was formed. The dislocation density was rather high and the arrangement was qualitatively similar to that in the virgin material. An example of subgrains, which are disoriented $\pm 1^\circ$ in a specimen cycled with $\varepsilon_{ap} = 10^{-5}$, is shown in Fig. 6(a). The dislocation density is highly inhomogeneous. Fig. 6(b) shows another grain with high dislocation density. Straight primary screw dislocations in the primary slip plane $(\bar{1}01)$ could be identified.

Table 2
The description of the symbols used in Fig. 4

Slip planes	Primary slip systems		Secondary slip systems				
a.. $\{110\}$	ap		as1	as2	as3		
	$(\bar{1}01)$		(101)	$(1\bar{1}0)$	(011)		
	$[111]$		$[\bar{1}11]$	$[111]$	$[\bar{1}\bar{1}1]$		
b.. $\{211\}$	bp1	bp2	bs1	bs2	bs3		
	$(1\bar{1}2)$	(211)	$(\bar{1}\bar{1}2)$	(211)	$(\bar{1}21)$		
	$[\bar{1}11]$	$[111]$	$[111]$	$[\bar{1}11]$	$[\bar{1}\bar{1}1]$		
c.. $\{123\}$	cp1	cp2	cs1	cs2	cs3	cs4	cs5
	$(2\bar{1}3)$	(312)	$(2\bar{1}3)$	$(1\bar{2}3)$	(312)	(321)	$(\bar{1}32)$
	$[\bar{1}11]$	$[111]$	$[111]$	$[\bar{1}11]$	$[\bar{1}11]$	$[111]$	$[\bar{1}\bar{1}1]$

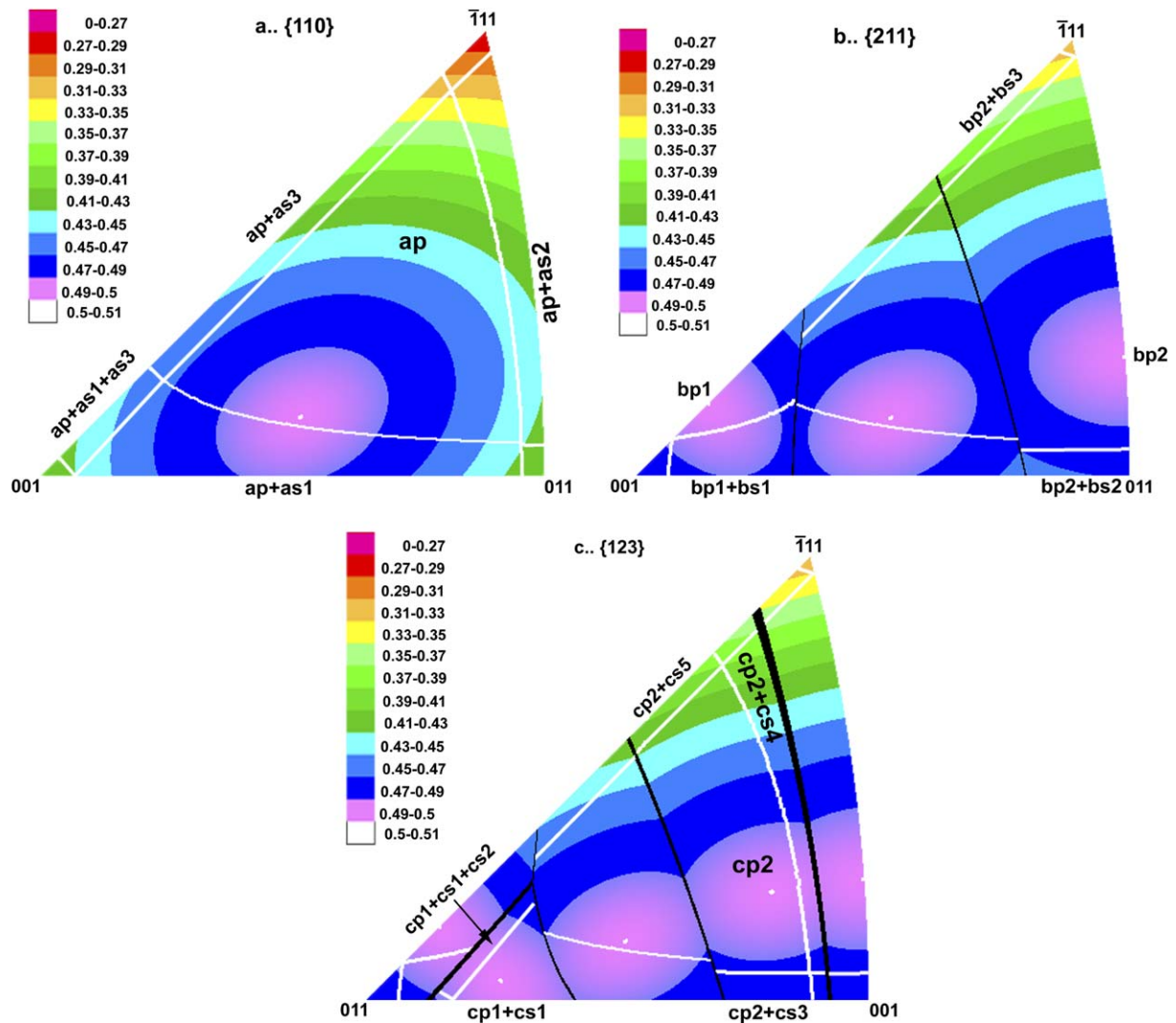


Fig. 4. Basic stereographic triangles showing the values of the Schmid factors of the primary slip systems for slip planes: (a) $\{110\}$, (b) $\{211\}$ and (c) $\{123\}$. The white lines demarcate the regions where the Schmid factor of the secondary slip system differs by less than 5%. (The symbol description is given in Table 2.)

In the specimens cycled with a higher plastic strain amplitude ($\varepsilon_{ap} = 5 \times 10^{-5}$) the dislocation arrangement in most grains was similar to that at the lowest amplitude, but in a small fraction of grains a distinctive spatial arrangement was formed. Fig. 7(a) shows such an arrangement in the grain oriented mainly towards a single slip. In the section close to $(1\bar{2}1)$ plane, long straight screw dislocation segments running in the $[111]$ direction together with edge dislocations lying in the primary $(\bar{1}01)$ planes can be distinguished. The detail in Fig. 7(a) shows the secondary slip of screw dislocations with Burgers vector $a/2[\bar{1}11]$. This arrangement resembles the planar structure in fatigued fcc austenitic steel since dislocations are arranged in thin sheets separated by dislocation-free layers. In the primary slip plane this arrangement corresponds to irregular bundles or bands formed by the dislocation dipoles and loops elongated in $[1\bar{2}1]$ direction. The second type of dislocation arrangement, though less frequent, is

the vein structure. This is shown in Fig. 7(b) in a grain oriented mainly to a single slip. The foil plane was again close to the $(1\bar{2}1)$ plane. The detailed micrograph in Fig. 7(b) shows that veins are formed predominantly by the edge dislocation dipoles. In the primary slip plane the dislocation network might condense into clusters and dislocation-free channels are formed.

In the specimens fatigued with constant stress amplitude of $\sigma_a = 360$ MPa up to fracture (saturated plastic strain amplitude was $\varepsilon_{ap} = 5 \times 10^{-5}$) most grains have the arrangement that corresponds to the saturated plastic strain amplitude (Fig. 7). However, some grains with a dislocation arrangement resembling the ladder structure were also found. In the overview low-magnification image in Fig. 8 one can see four ladders in the grain oriented for a single slip in the section close to the $(1\bar{2}1)$ plane and corresponding to the slip plane $(\bar{2}11)$. Fig. 8(b) shows the end of a larger grain (see Fig. 8(a)) with the detailed image of the ladder

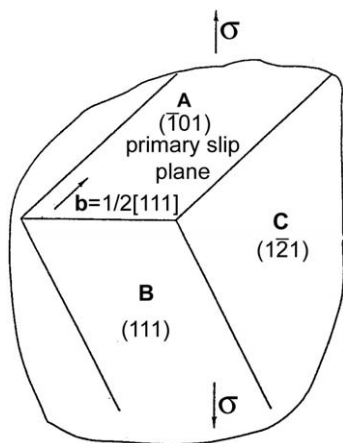


Fig. 5. Schematic showing the approximate orientation of the foil planes in sections A, B and C of an arbitrary grain.

structure and part of the neighboring grains. The walls consist of edge dipoles and between the neighboring walls parallel screw dislocation segments extend in the $[111]$ direction. The matrix is formed by high dislocation density.

In the specimen cycled with plastic strain amplitude of 10^{-4} , besides the structures mentioned above, a characteristic wall structure was observed in about 50% of the grains. Most of these grains had higher density of screw dislocations in the form of a network and dislocation walls in the middle of the grains or directly at the grain boundaries. An example of a grain with high dislocation density surrounded by walls is shown in Fig. 9(a). In Fig. 9(b) there are well-developed dislocation walls separated by channels of low dislocation density. The separation distance is about $0.8 \mu\text{m}$. The detail of the walls in areas with high screw dislocation density is shown in Fig. 9(c).

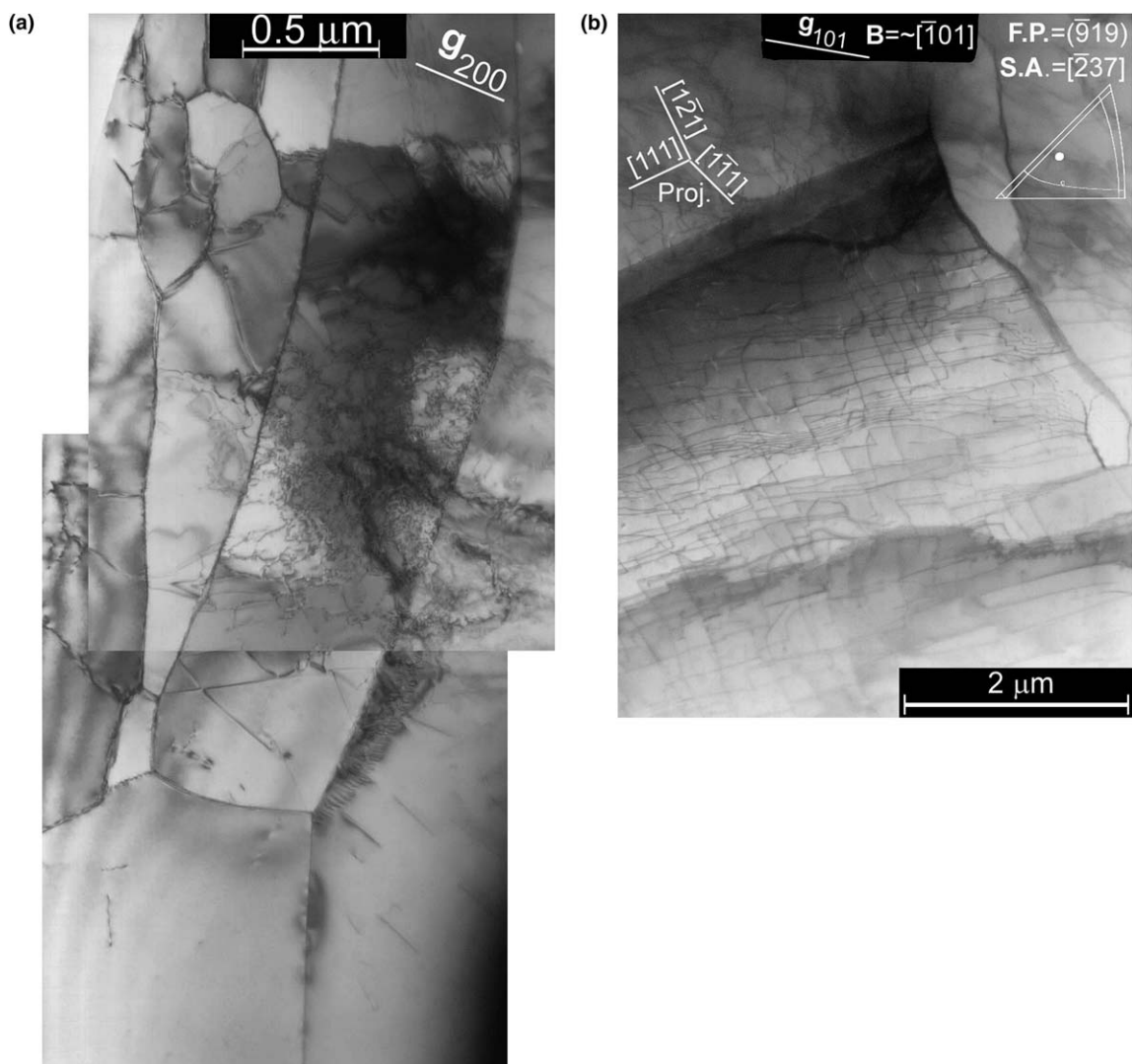


Fig. 6. Dislocation structure in a specimen cycled with $\varepsilon_{\text{ap}} = 10^{-5}$: (a) subgrains with varying dislocation density; (b) screw dislocations on the primary slip plane (section A).

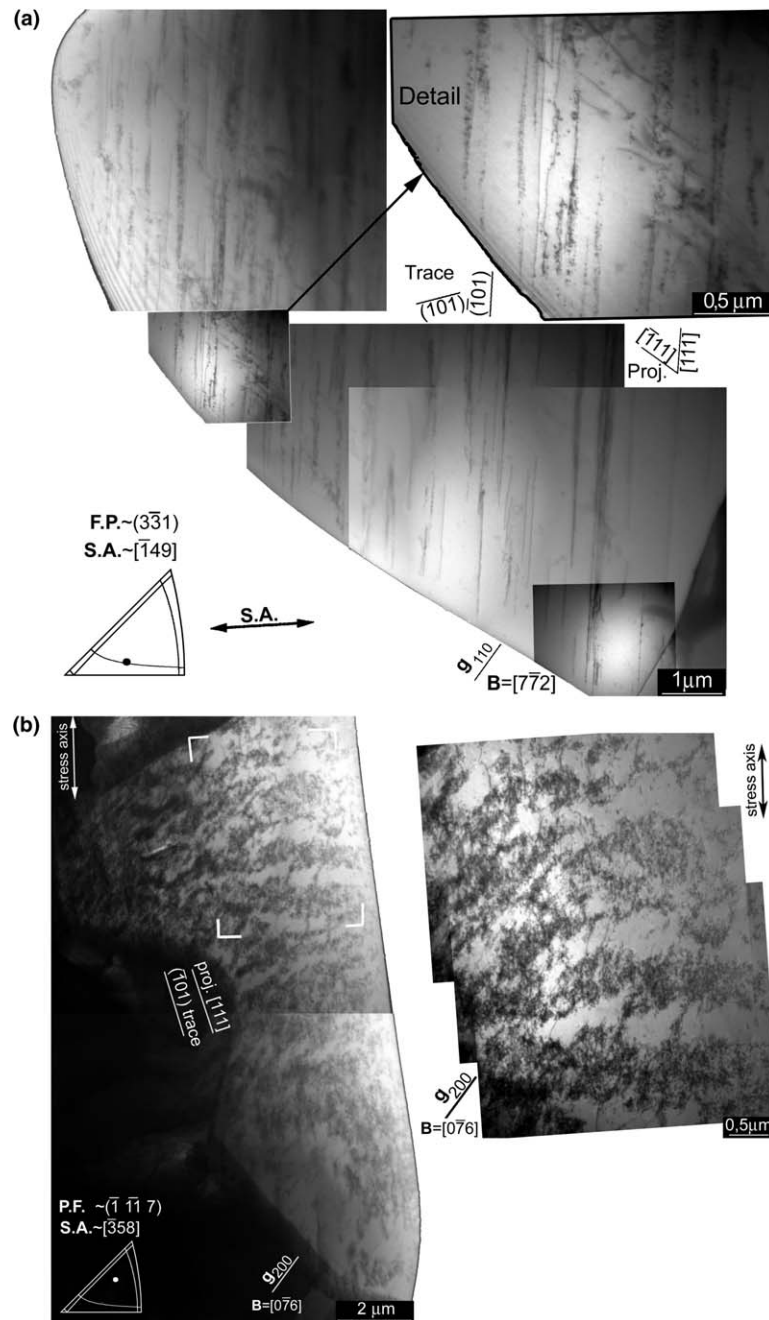


Fig. 7. Dislocation structure (section C) in a specimen cycled with $\epsilon_{ap} = 5 \times 10^{-5}$: (a) planar and (b) vein arrangements.

The dislocation structure in Fig. 10 corresponds to a grain oriented for the double slip. The ladder-like structure of a PSB is formed in the area with high screw dislocation density having the directions of the primary $[111]$ and secondary $[\bar{1}\bar{1}1]$ Burgers vectors. Most of the developed PSB running across the whole grain caused displacement of the neighboring grain boundaries corresponding to an extrusion. The specific contrast producing a sharp tip image in one system of dislocations arises in locations where the dislocations of the first slip system are traversed by dislocations of the second slip system. The screw dislocations of the primary system with Burgers vector $a/2[111]$ are invis-

ible in Fig. 10(a) under the diffraction conditions used. Fig. 10(b) shows detail of PSBs under a different diffraction condition in which screw dislocations of the primary system with Burgers vector $a/2[111]$ are visible.

3.4. Regime II

Cycling with high plastic strain amplitudes results in the formation of structures different from those formed at low plastic strain amplitudes. In the specimens cycled with $\epsilon_{ap} = 2 \times 10^{-3}$ the dominant types of structure were wall structures (ladders, unidirectional walls and labyrinths).

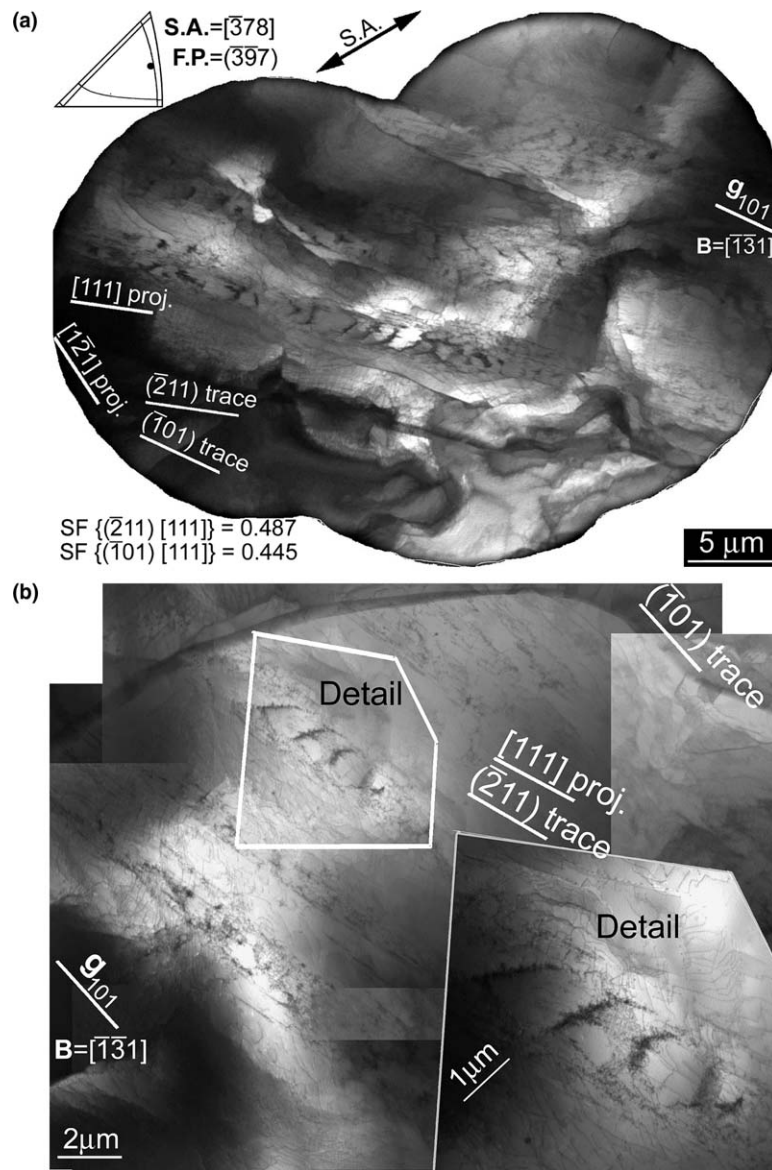


Fig. 8. Ladder-like structures of PSBs and the matrix in section C in a specimen cycled with $\sigma_a = 460$ MPa (saturation plastic strain amplitude $\varepsilon_{ap} = 5 \times 10^{-5}$): (a) an overall view; (b) a detail of the band.

Vein structure similar to that shown in Fig. 7(b) can occasionally be found only in the matrix. The type of the structure is often dependent on the proximity to the grain boundary. Close to the grain boundary more complicated formations were found, while in the center of grains simple walls were present.

Three ladder-like bands (PSB structures) passing through the center of the grain surrounded by labyrinth structure in the center and cell structure close to the boundary are shown in Fig. 11(a). A detail of the ladder structure is shown in Fig. 11(b). The thin foil producing images in Fig. 11 was cut parallel to the specimen axis only 300 μm under the surface. The grain is oriented for a single slip with the tendency of a double slip and the foil plane is nearly parallel to the $(1\bar{2}1)$ plane. The ladders in Fig. 11(b) are parallel to the primary slip plane $(\bar{1}01)$

and consist of alternating thin dislocation walls separated by thick channels of low dislocation density. The primary screw dislocations with Burgers vector $a/2$ $[111]$ extend in the channels between neighbors. Dislocation walls forming the rungs of the ladders consist of high density of edge dipoles with an identical Burgers vector. The typical separation of the rungs was 0.8–1.1 μm and the width of the lamellas was 0.6–1.1 μm . The Burgers vector analysis of the dislocations running between or within the rungs of the three ladders is shown in Figs. 11(c)–(e). Fig. 11(c) shows the detail of the center of the three ladders under a diffraction condition $\mathbf{g} = \bar{1}01$. The screw dislocations parallel to the $[111]$ direction are invisible while the edge dislocations display a residual contrast. The neighboring matrix consists of the remnants of the vein structure formed by the primary edge dipoles of the same type as

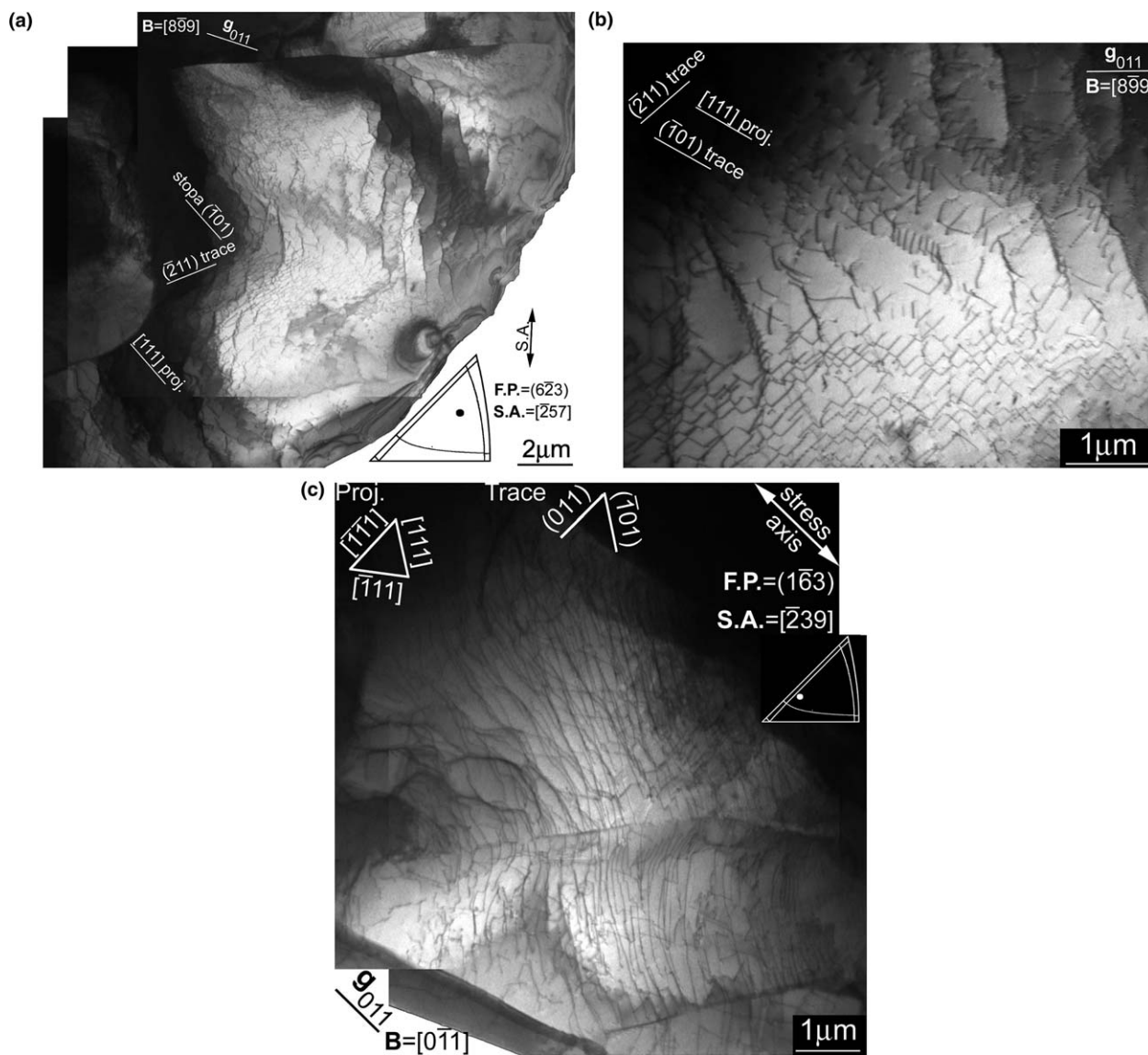


Fig. 9. Dislocation structure (section C) of grains oriented for a single slip in a specimen cycled with $\epsilon_{ap} = 10^{-4}$: (a) an overall picture of the first grain; (b) detail of the center part of the micrograph (a); (c) start of the wall formation in the second grain.

in the rungs of the ladders. This is apparent in the dark-field image (Fig. 11(e)) where the edge segments in the rungs as well as in the veins are bright.

Fig. 12(a) provides a view of the section close to C plane of another grain oriented for a single slip. The dislocation arrangement of five ladders in Fig. 12(b) has a similar structure to the case shown in Fig. 11(b), but the ladders are not straight and the neighboring matrix is formed by a random arrangement with higher dislocation density. The formation of dislocation walls is often affected by the dislocation arrangement in the neighboring subgrain.

Fig. 13 shows the labyrinth structure in a section parallel to (121) plane of the grain oriented for the double slip. An overall view in Fig. 13(a) shows the labyrinth structure in the center of the grain, the unidirectional walls at the bottom of the image and the cells at the top of the image close

to the grain boundary. Figs. 13(b) and (c) show, under two diffraction conditions, the central part of the labyrinth structure consisting of two systems of perpendicular walls separated by the channels in which screw dislocations of both slip systems are present. The walls lie in the directions that bisect the angles between the screw dislocations of both active slip systems with the highest Schmid factors ($(\bar{1}01)[111]$ and $(101)[\bar{1}11]$). The screw dislocations parallel to the $[\bar{1}11]$ direction are invisible under the diffraction condition with $\mathbf{g} = 110$ (see Fig. 13(c)).

The dislocation arrangement in the specimen cycled with the highest plastic strain amplitude ($\epsilon_{ap} = 10^{-2}$) consists of a mixture of wall and cell structures. At least two slip systems are active in all the grains. Therefore, in one grain two to three types of dislocation arrangements may be found (see Fig. 14). Fig. 14(a) shows a mixture of wall and

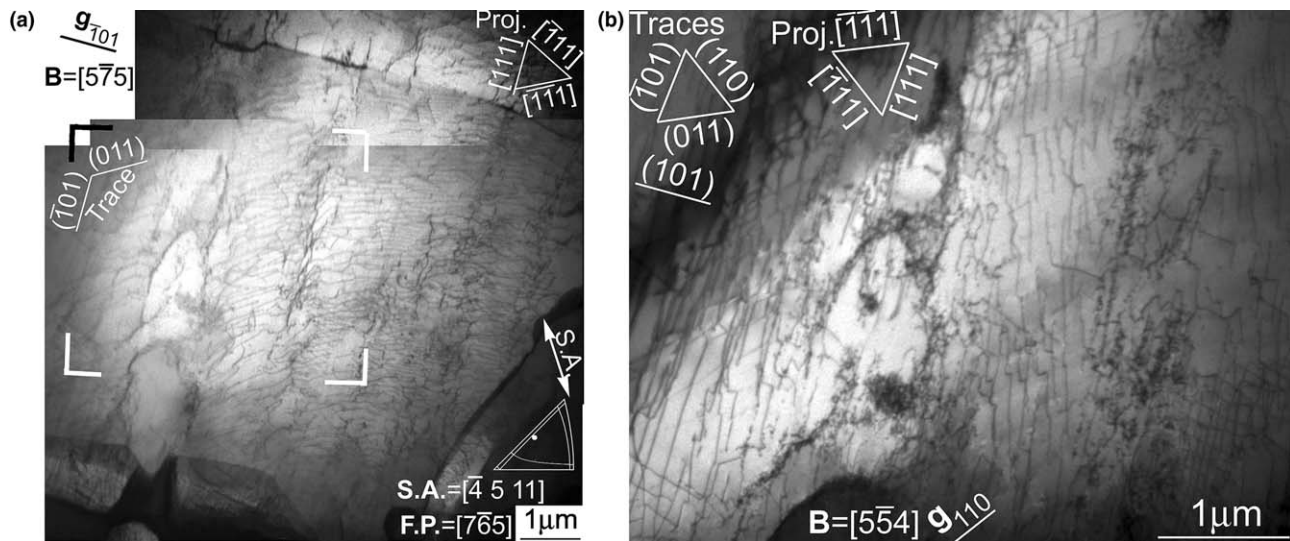


Fig. 10. Dislocation structure showing the early stages of PSB formation (section C) of a grain oriented for a double slip in a specimen cycled with $\varepsilon_{ap} = 10^{-4}$: (a) screw dislocations of the secondary slip system (011) $[111]$ are visible; (b) screw dislocations of the primary slip system $(101) [111]$ are visible.

labyrinth structures with an average wall distance of $0.52 \mu\text{m}$ and cells with an average diameter of $0.47 \mu\text{m}$ with a different contrast showing the cell disorientation. The grain oriented for a multiple slip contains labyrinth and cell structures (Fig. 14(a)) and the grain oriented for a single slip consists only of cell structure (Fig. 14(b)). The diameter of the cells varies from 0.32 to $0.85 \mu\text{m}$ and the cell disorientation is up to $\pm 2^\circ$.

3.5. Fractions of individual dislocation structures

A number of thin foils were examined to obtain the statistics of the types of dislocation structures present in ferritic stainless steel cycled with different plastic strain amplitudes to the end of the fatigue life. Five basic types of dislocation structures were identified: a random arrangement of mostly screw dislocations (low dislocation density) present at low ε_{ap} , vein structures, unidirectional walls and ladder-like structure (PSBs) for a medium ε_{ap} and labyrinth and cell structures for the highest ε_{ap} . Table 3 shows the average percentage of the dislocation structures evaluated for different applied plastic strain amplitudes ε_{ap} . For the smallest ε_{ap} the original dislocation distribution is slightly modified with cyclic loading and partially transforms to the vein and wall structures. For the medium ε_{ap} the fraction of the random arrangement decreases. Both wall and vein structures intersected by ladder-like structures can be found. For the highest ε_{ap} the labyrinth and predominantly cell structures are formed.

4. Discussion

Our observations of the fatigue dislocation structures in ferritic stainless steel can be compared with the previous results obtained for Fe–Cr single crystals [7–9,11,26] and

with the results for similar polycrystalline material [4,14,17,20,21]. Observations of a dislocation arrangement in single crystals were made for medium plastic strain amplitudes for specific crystal orientations and for a low number of cycles. All studies were carried out on single crystals for a single slip on the $\{110\}$ plane; only Magnin et al. [9] and Yamasaki et al. [26] studied single crystals oriented for double and single slip on one or two $\{112\}$ planes. The results for single crystals show that depending on the crystal orientation the slip can be active either on $\{110\}$ or $\{112\}$ planes. Several dislocation configurations were recorded, namely loop patches and dislocation bundles, wall structures and cell structures. Yamasaki et al. [26] report wide ladders (alternating thin walls and thick channels) parallel to the $\{112\}$ plane.

Dislocation structures in polycrystalline 25% Cr steel cycled with one plastic strain amplitude of 3.5×10^{-3} [21] were described with reference to the Schmid factors of the active slip systems of individual grains. Mostly labyrinth structures, condensed walls and cells were observed and some areas of the labyrinth structure were interpreted as ladder structures. No individual ladder-like structure was reported. Magnin et al. [21] report regular wall and channel structures in a large area of a single grain cycled with a plastic strain amplitude of 2×10^{-3} .

Our observations report structures in specimens cycled to fracture (except the specimen cycled with $\varepsilon_{ap} = 10^{-5}$) and comprise a wide interval of plastic strain amplitudes. The specific observations of single crystals are in reasonable agreement with our results, except that no wide ladder-like structures were observed. The width of the ladder was always around $1 \mu\text{m}$. The specific results of Fielding and Stobbs [20] and of Magnin et al. [21] are in good agreement with our results corresponding to medium plastic strain amplitudes.

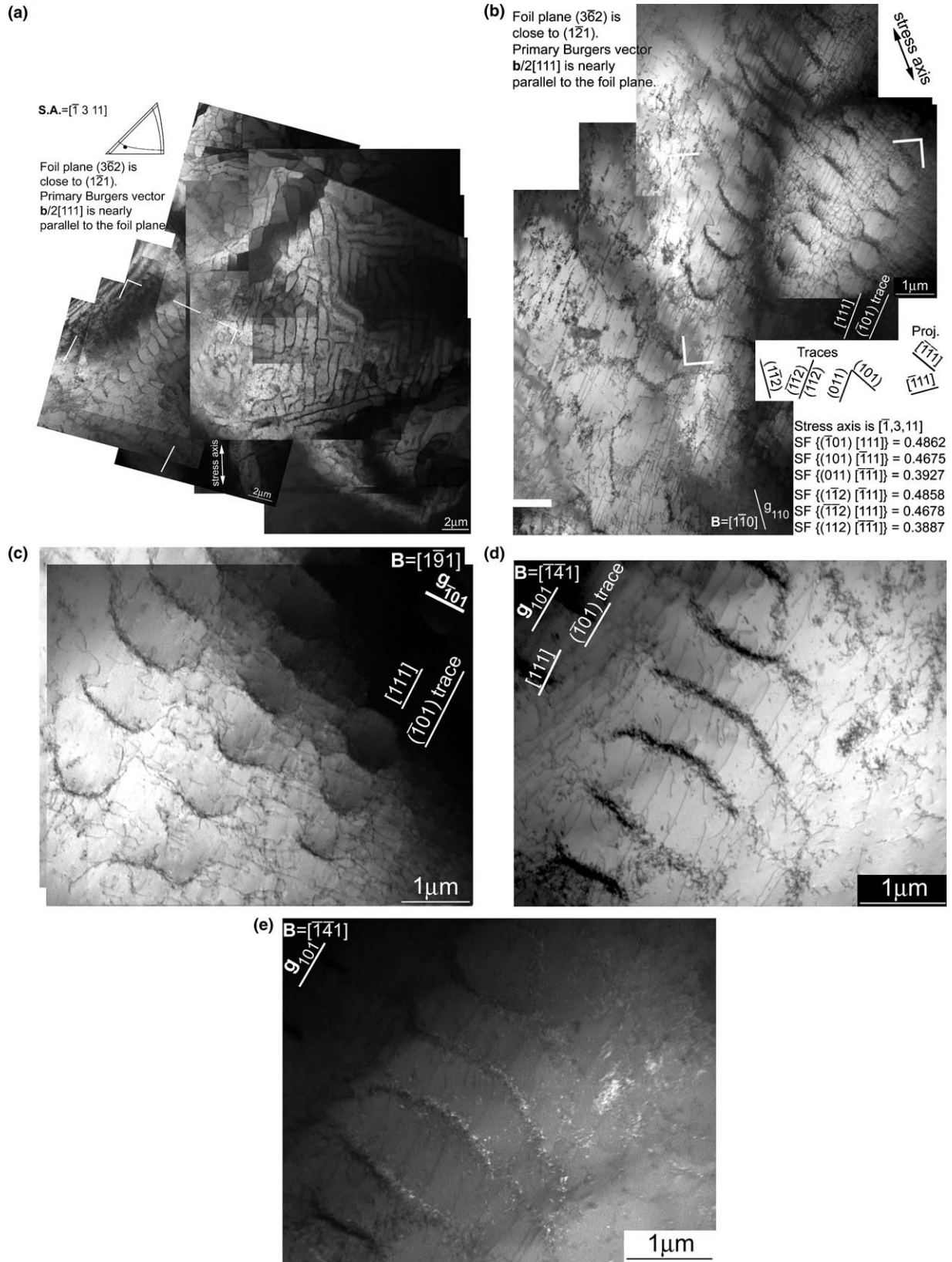


Fig. 11. Dislocation structure (section C) of a grain oriented to the boundary between the single and double slip in a specimen cycled with $\varepsilon_{ap} = 2 \times 10^{-3}$: (a) coexistence of ladder, labyrinth and cell structures; (b) a detail of ladder structure of PSBs; (c) a detail of the same area as in (b), but in a different diffraction condition ($g = \bar{1}01$) the screw $[111]$ dislocations are invisible; (d) a detail of the same area as in (b) in a bright field; (e) the same area, but in a dark field ($g = 101$).

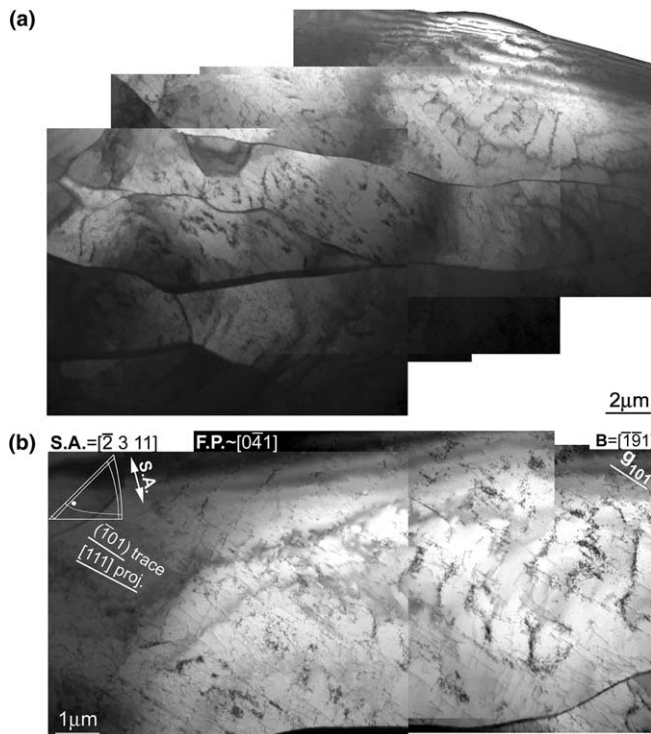


Fig. 12. Dislocation structure (section C) of a grain oriented for a single slip in a specimen cycled with $\epsilon_{ap} = 2 \times 10^{-3}$: (a) ladder structures in subgrains; (b) a detail of ladder structure.

In the present work the most important results refer to specific dislocation configurations which are responsible for cyclic strain localization. No such structures were observed at the lowest plastic strain amplitude ($\epsilon_{ap} = 10^{-5}$) and this specimen did not fracture after 3×10^6 cycles. In the low-amplitude domain ($\epsilon_{ap} = 5 \times 10^{-5}$) PSBs with the ladder-like structure were observed. Ladders represent lamellae in which thin dislocation-rich walls alternate with thick channels containing primary screw dislocations that are hanging between neighboring walls. The walls in the PSB lamella correspond to the primary walls formed by the edge dislocation dipoles and multipole resulting from the interaction of dislocations of the primary slip system. They are embedded in the matrix which, contrary to fcc metals [1–3,22–25], does not consist of vein structures, but typically of a network with high density of screw dislocations. For medium strain amplitude the neighboring matrix contains dislocation bundles.

At medium and high strain amplitudes the individual ladders are not able to accommodate the applied plastic strain and the larger part of this strain is carried by wall and labyrinth structures and finally also by cell structures. All these structures, which are formed after long-term cycling, are characterized by alternating volumes of high and low dislocation density and represent low-energy dislocation configurations. At medium and high plastic strain amplitudes the walls are secondary walls, which are formed by simultaneous actions of two slip systems acting

in one slip plane as described by Turenne et al. [32] and bisect the angle between the two systems of screw dislocation extending between the walls in the channels. The walls can develop in two perpendicular directions which results in the formation of labyrinth structures. Therefore, the degree of strain localization in wall and labyrinth structures is expected to be lower than that in PSB lamellae.

The existence of the structures capable of carrying high cyclic plastic strain contributes to the explanation of the fatigue softening observed. However, more factors should be considered. In low-amplitude regime I the effective stress component represents an important fraction of the total stress amplitude. The saturated effective stress in this stainless steel was evaluated to 89 MPa [33]. In the specimens cycled with $\epsilon_{ap} = 10^{-5}$ the character of the dislocation arrangement does not differ qualitatively from that of non-deformed material, only the dislocation density in some grains is increased. An important fraction of the applied plastic strain amplitude is due to extra magnetoelastic strain produced in ferromagnetic materials in cyclic loading. The extra magnetoelastic strain is due to the reverse magnetoelastic effect (Villari effect) often referred to as the ΔE effect (“elastic modulus defect” in ferromagnetic materials). The applied axial loading causes magnetic anisotropy in the specimen and the magnetic domains align parallel or perpendicular to the stress axis depending on the sign of the applied stress and the type of the material. The magnetic domain alignment results in magnetic induction and, due to magnetostriction, an extra strain is produced in the direction of the acting stress. This was evaluated to be about 10^{-5} [34], which is of the same order of magnitude as the applied plastic strain amplitude. The irreversible plastic strain amplitude carried by mobile dislocations is only some fraction of the applied plastic strain amplitude and the dislocation rearrangement will thus be very slow. No low-energy dislocation configurations and very moderate fatigue softening for the lowest plastic strain amplitude result.

Fatigue softening is more important for medium plastic strain amplitudes. It is connected with the evolution and modification of the dislocation structure. The presence of the texture in an as-supplied state results in a multiple slip in most grains. During cyclic straining the number of active slip systems in the individual grains is reduced until one or two systems carry the major part of the plastic strain. The production and annihilation of dislocations accompanied by point defect production and migration leads to the formation of low-energy dislocation configurations. The dislocation configurations were established depending on the applied plastic strain amplitude and the relative fractions are shown in Table 3. The amount of the strain carried by individual structures is difficult to determine since it depends on the critical yield stress and only relative contributions of various structures can be estimated from simultaneous structural and surface observations.

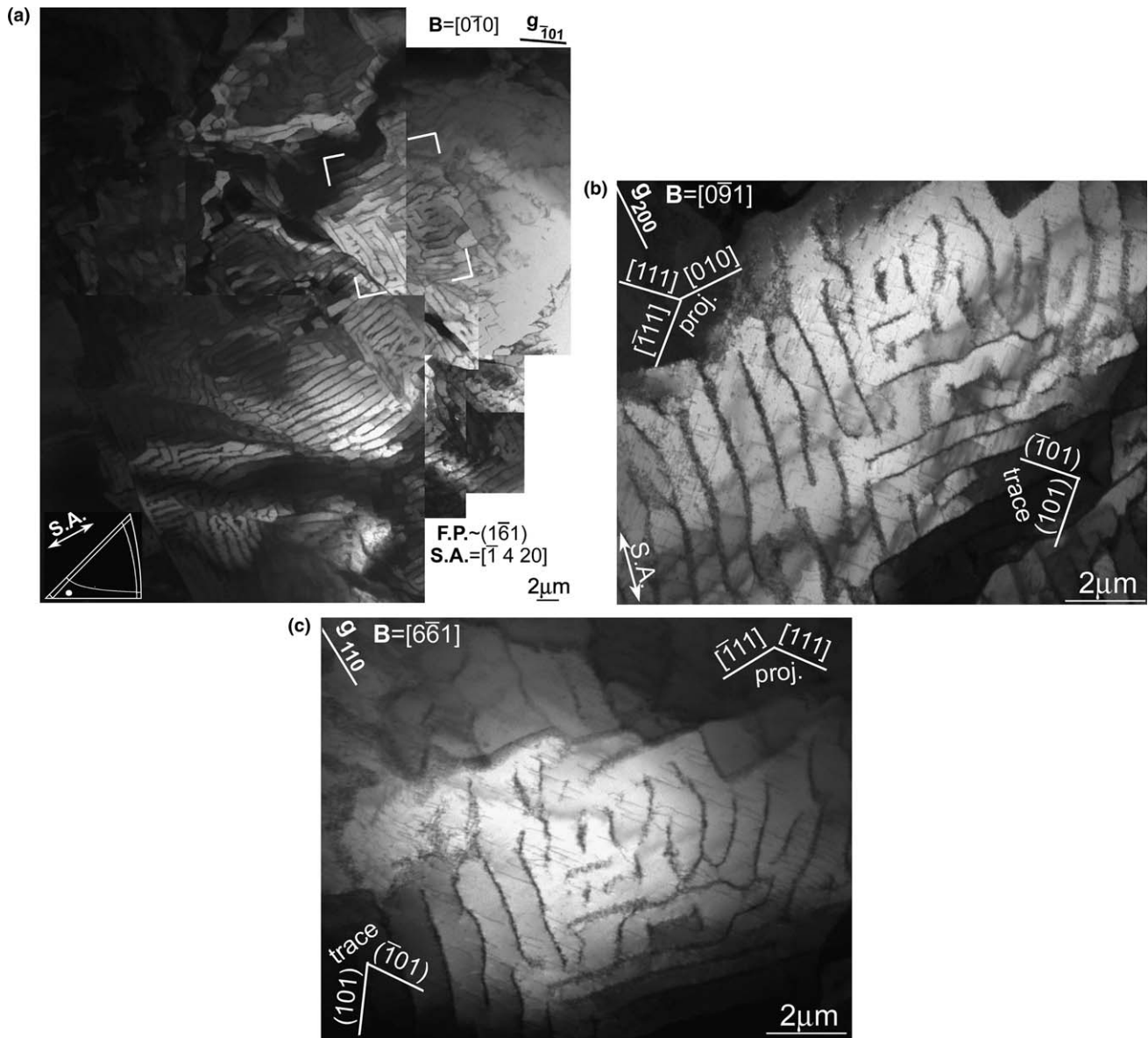


Fig. 13. Labyrinth dislocation structure (section C) of a grain oriented for a double slip in a specimen cycled with $\varepsilon_{ap} = 2 \times 10^{-3}$: (a) coexistence of unidirectional walls, labyrinth and cells structures in one grain; (b) a detail of the middle area – the labyrinth structure; (c) a detail of the middle area under a different diffraction condition (the $[111]$ screw dislocations are invisible).

The transformation of the original dislocation structure to low-energy configurations is thus the main reason for the observed fatigue softening. Some of these low-energy dislocation arrangements are important for the evolution of the fatigue damage. In particular, the ladder-like structures can carry appreciable plastic strain in the neighboring elastic matrix which leads to surface relief formation and crack initiation [31]. The slope of the cyclic stress–strain curve is low in regime I and starts to increase if the single slip of most of the grains cannot accommodate the applied plastic strain. The double slip results in the formation of secondary walls, labyrinths and cells and a higher slope of the cyclic stress–strain curve in regime II.

Thorough mapping of the dislocation structures in cyclic straining is important for the formation of models of cyclic plastic straining [1,3] and for checking the results of computer simulations of the dislocation motion in cyclic loading [35]. Until now only the early stages of cyclic straining could be modeled, but the inhomogeneous distribution of dislocations with low-energy dislocation configurations were found in agreement with experimental observations. Cyclic plastic strain starts to concentrate in the localized bands leading to the formation of a surface relief. A comparison of the dislocation structures produced by computer simulations with the three-dimensional configurations determined experimentally contributes to the improvement of the models.

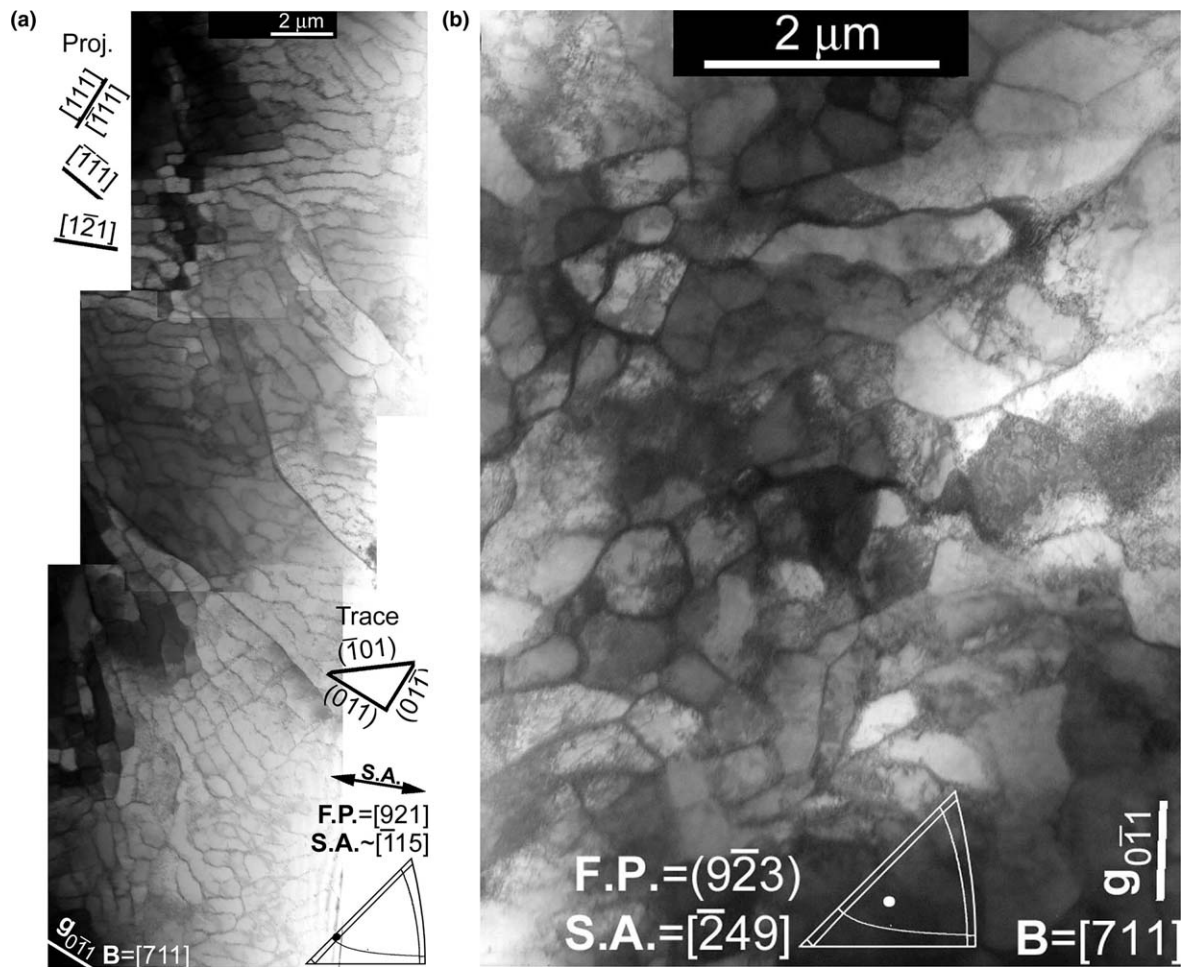


Fig. 14. Dislocation structure (section C) in two grains in a specimen cycled with $\epsilon_{ap} = 10^{-2}$: (a) coexistence of walls, labyrinth and cells structures in grain oriented for a double slip; (b) cell structure in a grain oriented for a single slip.

Table 3
The percentage and the number of the grains containing the characteristic types of dislocation structures in ferritic steel at the end of fatigue life

ϵ_{ap}	5×10^{-5}		10^{-4}		2×10^{-3}		10^{-2}	
	%	Number of grains	%	Number of grains	%	Number of grains	%	Number of grains
Random arrangement of mostly screw dislocations	96	94	56	28	4	3		
Vein structure	2	2	4	2	18	12		
Wall structures, i.e., ladders and unidirectional walls	2	2	40	20	60	41	30	25
Wall structures and labyrinths					8	5	10	8
Cell structures					10	7	60	50
Sum	100	98	100	50	100	68	100	83

5. Conclusions

The detailed study of the dislocation arrangement developed under constant plastic strain amplitude cycling and constant stress amplitude cycling up to fracture of ferritic stainless steel leads to the following conclusions:

(i) In order to obtain true information about the types of the individual dislocation structures and their proportions as a function of the plastic strain

amplitude, the spatial distribution of the dislocations in individual grains of the material has to be determined. This can be achieved using the technique of oriented foils.

(ii) During repeated application of medium plastic strain amplitudes the random arrangement of mostly screw dislocations transforms into vein and wall structures intersected by ladder-like structures. In high-amplitude cyclic loading wall, labyrinth and cell structures are produced.

- (iii) The proportions of the individual dislocation structures were obtained as a function of the plastic strain amplitude. The increase in the volume fraction occupied by wall structures (including PSBs) is responsible for cyclic softening.
- (iv) Two domains of the cyclic stress–strain curve correspond to different types and proportions of dislocation structures. A higher slope in regime II is linked to the action of double slip.

Acknowledgments

The authors acknowledge the help of J. Tobiáš with the digital processing of transmission electron micrographs and the mathematical processing of stereographic triangles. The work was carried out within the research projects AV0Z 204 10507 of the Academy of Sciences of the Czech Republic and was also supported by Grant No. 106/05/P521 of the Grant Agency of the Czech Republic.

References

- [1] Polák J. Cyclic plasticity and low cycle fatigue life of metals. Prague/Amsterdam: Academia/Elsevier; 1991.
- [2] Polák J. In: Milne I, Ritchie RO, Karihaloo B, editors. Comprehensive structural integrity. Cyclic loading and fatigue, vol. 4. Amsterdam: Elsevier; 2003. p. 1.
- [3] Mughrabi H. Dislocations and properties of real materials, book no. 323. London: Institute of Metals; 1985. p. 244.
- [4] Mughrabi H, Ackermann F, Hertz K. In: Fong JT, editor. Fatigue mechanisms, ASTM STP 675. Philadelphia (PA): ASTM; 1979. p. 69.
- [5] Mughrabi H, Herz K, Stark X. *Int J Fract* 1981;17:193.
- [6] Sommer C, Mughrabi H, Lochner D. *Acta Mater* 1998;46:1527.
- [7] Šesták B, Vicherková Z, Novák V, Libovický S, Brádler J. *Phys Stat Sol (a)* 1987;104:79.
- [8] Magnin T, Driver JH. *Mater Sci Eng* 1979;39:175.
- [9] Magnin T, Fourdex A, Driver JH. *Phys Stat Sol (a)* 1981;65:301.
- [10] Kaneko Y, Mimaki T, Hashimoto S. *Acta Mater* 1999;47:165.
- [11] Li XW, Umakoshi Y. *Scr Mater* 2003;48:545.
- [12] Šesták B, Novák V, Libovický S. *Philos Mag A* 1988;57:353.
- [13] Mori H, Tokuwame M, Miyazaki T. *Philos Mag A* 1979;40:409.
- [14] Pohl K, Mayr P, Macherauch E. *Scr Metall* 1980;14:1167.
- [15] Pohl K, Mayr P, Macherauch E. In: Sih GC, Provan JW, editors. Defects, fracture and fatigue. The Hague: Martinus Nijhoff; 1983. p. 147.
- [16] Lloyd JRT, Caceres P, Ralph B. *Scr Metall* 1985;19:1475.
- [17] Roven HJ, Nes E. *Acta Metall Mater* 1991;39:1719.
- [18] Petersmeier T, Martin U, Eifler D, Oettel H. *Int J Fatigue* 1998;20:251.
- [19] Pohl K, Mayr P, Macherauch E. *Int J Fract* 1981;17:221.
- [20] Fielding SE, Stobbs WM. *J Microsc* 1983;130:279.
- [21] Magnin T, Ramade C, Lepinoux J, Kubin LP. *Mater Sci Eng A* 1989;118:41.
- [22] Klesnil M, Lukáš P. Fatigue of metallic materials. 2nd ed. Prague/Amsterdam: Academia/Elsevier; 1992.
- [23] Basinski ZS, Basinski SJ. *Prog Mater Sci* 1992;36:89.
- [24] Laird C. In: Cahn RW, Haasen P, editors. Physical metallurgy. Amsterdam: Elsevier Science; 1996. p. 2293.
- [25] Suresh S. Fatigue of materials. 2nd ed. Cambridge: Cambridge University Press; 1998.
- [26] Yamasaki T, Kaneko Y, Miyamoto H, Hashimoto S, Mimaki T. *Mater Sci Eng A* 2001;319–321:569.
- [27] Polák J, Kruml T. *Metall Mater* 2000;38:239.
- [28] Kruml T, Polák J. *Mater Sci Eng A* 2001;319–321:564.
- [29] Wilson DV, Tromans JK. *Acta Metall* 1970;18:1197.
- [30] Obřtlík K, Kruml T, Polák J. *Mater Sci Eng A* 1994;187:1.
- [31] Man J, Petrenec M, Obřtlík K, Polák J. *Acta Mater* 2004;52:5551.
- [32] Turenne S, L'Espérance G, Dickson JI. *Acta Metall* 1988;36:459.
- [33] Petrenec M. Cyclic plasticity of stainless steels – effective and internal stresses and dislocation arrangement. Ph.D. Thesis, Brno University of Technology; 2004.
- [34] Polák J, Petrenec M, Degallaix S. *Scr Metall* 2002;47:731.
- [35] Déprés C, Robertson CF, Fivel MC. *Philos Mag* 2004;84:2257.

Detailed assessment of indentation size-effect in recrystallized and highly deformed niobium [☆]

J. Alkorta ^{*}, J.M. Martínez-Esnaola, J. Gil Sevillano

Department of Materials, CEIT and TECNUN (University of Navarra), Paseo de Manuel Lardizabal 15, 20018 San Sebastián, Spain

Received 14 October 2005; received in revised form 20 December 2005; accepted 23 March 2006

Available online 8 June 2006

Abstract

The nanoindentation hardness H of polycrystalline niobium in the recrystallized condition and after up to eight room temperature 90° equal-channel angular pressing passes (equivalent deformation ~ 9) has been studied in detail. An important indentation size effect (ISE) that progressively disappears as the indentation depth h decreases has been observed at all pre-deformation levels. Qu et al. [J Mater Res 2004;19:3423] have explained such behaviour as a deviation from the ISE expected for conical or pyramidal indenters (a $H^2 - 1/h$ proportionality) because of the rounded shape of real tips. The Nix and Gao ISE model [J Mech Phys Solids 1998;46:411], further refined by taking into account the tip roundness and other unnoticed contributions to ISE, has been compared with the niobium results. Quantitative agreement between observed and predicted ISE requires the true dislocation pattern under the indentation being much denser than the very idealized geometrically necessary dislocations pattern assumed in the Nix and Gao model.

© 2006 Acta Materialia Inc. Published by Elsevier Ltd. All rights reserved.

Keywords: Equal-channel angular pressing; Nanoindentation; Strain gradient plasticity; Dislocations

1. Introduction

Indentation hardness experiments of crystalline materials have repeatedly displayed a strong size effect [1–5]. Based on the classic dislocation strengthening relationship and a kinematically admissible model of geometrically necessary dislocations (GNDs) underneath a perfectly sharp conical indenter, Nix and Gao [2] concluded that the relation between microindentation hardness, H , and indentation depth, h , should be

$$\left(\frac{H}{H_0}\right)^2 = 1 + \frac{h^*}{h} \quad (1)$$

where h^* is a characteristic parameter (with length dimensions) which depends on both the properties of the material

and the indenter shape. H_0 is the extrapolated hardness for very large indentation depths, for which the contribution of the GNDs is negligible. This relation holds up to the sub-micrometre level but, recently, several nanoindentation experiments [6–9] have shown a consistent deviation of hardness from the expected Nix and Gao (NG) relationship at very small depths ($<0.2 \mu\text{m}$). Elmustafa and Stone [9], for instance, showed that in aluminium and alpha brass the nanoindentation data show an abrupt deviation from the slope of the NG relation (H^2 vs. $1/h$) for depths below 200 nm. Different explanations have been given to this deviation: Swadener et al. [6], for example, suggested that the repulsive forces between dislocations would cause an increase of the volume in which GNDs are confined leading to a lower GND density as indentation size decreases. Recently, Qu, Nix and other authors, based on the conventional theory of mechanism-based strain gradient plasticity [10], have linked this deviation to the tip radius present in real micro- and nanoindenters [11,12]. The tip radius causes a transition from a typical behaviour of a sharp indenter in which the average plastic strain underneath the

[☆] This manuscript was presented at the “Micromechanics and Microstructure Evolution: Modeling, Simulation and Experiments” held in Madrid/Spain, September 11–16, 2005.

^{*} Corresponding author.

E-mail address: jalkorta@ceit.es (J. Alkorta).

indenter is constant and the strain gradient is proportional to $1/h$ to a rounded tip behaviour (spherical indenter) in which the average plastic strain is proportional to the contact radius ($\sim 0.2a/R$, where a is the contact radius and R is the tip radius [13,14]). The strain gradient becomes independent of the indentation size in the latter case [6]. This transition could even lead to an inverse indentation size effect (ISE) for strain hardening materials. Moreover, even in the absence of strain hardening, a decrease in contact hardness with depth is expected due to the transition from an elastic–plastic to a purely elastic contact in spherical indentation [14].

Lim and Chaudhri [7], in contrast, proposed a qualitative model (ignoring the contribution of the GNDs) which consists of three different indentation stages, each of them characterized by a particular deformation mechanism. However, the contribution of GNDs is still the most widely accepted explanation for the ISE. In this context, and even if the tip radius effect could partially explain the anomalous behaviour of hardness, we want to point out that there is another possible contribution to the ISE deviation from the Nix model that has up to now been overlooked.

The NG relation is based on the assumption that the dislocation strengthening obeys the classic relationship

$$\tau = \alpha \cdot \mu b \sqrt{\rho_T} \quad (2)$$

where μ is the shear modulus (44.3 GPa for Nb [15]), b the Burgers vector (0.286 nm for Nb [15]), ρ_T the total dislocation density and α a proportionality constant ($\alpha \sim 0.36$). However, it is well known that Eq. (2) is only an approximation that should be corrected for large departures from a reference density (see Gil Sevillano [16] for a review). Since the NG relation predicts a decrease of GND density of some orders of magnitude with indentation depth, this correction should be included in the model.

In this paper, starting from the original NG model, a novel expression which takes into account both the rounded tip and the modified dislocation strengthening relationship is derived. The results obtained with this expression are then compared with experimental nanoindentation results for a commercially pure Nb subjected to different levels of deformation imparted by equal-channel angular pressing (ECAP), i.e., on a material with a wide range of initial dislocation densities.

2. Theory

Our analytical derivation starts from basically the same arguments given by Nix and Gao [2] for a conical indenter. The NG model assumes that a conical indentation generates a set of GND concentric prismatic loops under the indenter, as shown schematically in Fig. 1.

We will consider a rounded-tip conical indenter for which the relation between the indentation depth and contact area can be expressed as follows:

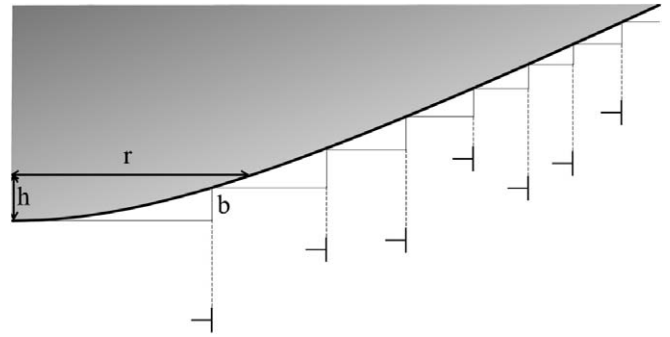


Fig. 1. Generation of GNDs due to a rounded tip conical indentation according to the NG kinematically admissible model based on a pattern of concentric prismatic dislocation loops.

$$S = \pi a^2 = \pi (\tan \phi)^2 \cdot h_f^2 + 2\pi R \cdot h_f = \pi (\tan \phi)^2 (h_f^2 + \delta h_f) \quad (3)$$

with

$$\delta = \frac{2R}{(\tan \phi)^2} \quad (4)$$

where ϕ is the semi-angle of the conical indenter (note that this angle and that used by Nix and Gao are complementary), R is the tip radius, h_f is the depth, S is the area and a is the contact radius. Following the NG model, Swadener et al. [6] found that for an indenter with a smooth axisymmetric profile (as is our case) the total length of the GND loops is

$$\lambda = \int_0^{h_f} \frac{2\pi}{b} \cdot r(h) dh = \frac{2\pi \tan \phi}{b} \int_0^{h_f} \sqrt{h^2 + \delta h} dh \quad (5)$$

If we define χ as:

$$\chi = \frac{\delta}{2h_f} = \frac{R}{h_f (\tan \phi)^2} \quad (6)$$

then finally we get

$$\lambda = \frac{\pi \tan \phi}{b} \cdot h_f^2 \cdot \left[(1 + \chi) \cdot \sqrt{1 + 2\chi} + \chi^2 \ln \left(\frac{\chi}{1 + \chi + \sqrt{1 + 2\chi}} \right) \right] \quad (7)$$

Note that at very large depths the expression within the brackets is very close to 1 and we recover the expression obtained by Nix and Gao [2]. Assuming, as in the NG model, that the GNDs are confined within a volume $V = 2\pi a^3/3 = (2\pi/3)(h_f \tan \phi)^3(1 + 2\chi)^{3/2}$, the average GND density is

$$\begin{aligned} \rho_G &= \frac{\lambda}{V} \\ &= \frac{3}{2b(\tan \phi)^2} \cdot \frac{1}{h_f} \cdot \left[\frac{1 + \chi}{1 + 2\chi} + \frac{\chi^2}{\sqrt{(1 + 2\chi)^3}} \ln \left(\frac{\chi}{1 + \chi + \sqrt{1 + 2\chi}} \right) \right] \quad (8) \end{aligned}$$

Note, again, that at very large indentation depths we recover the expression obtained by Nix and Gao [2]. In contrast, at very low indentation depths ρ_G reaches a stationary state independent of the indentation depth, as previously shown by Swadener et al. [6]:

$$\rho_G \rightarrow \frac{1}{bR} \quad (9)$$

Assuming the classic dislocation strengthening relationship (Eq. (2)), we get

$$\tau_c = \alpha\mu b\sqrt{\rho_T} = \alpha\mu b\sqrt{\rho_s + \rho_G} \quad (10)$$

where ρ_s is any statistically stored dislocation (SSD) density present in the plastic zone developed by the indentation and τ_c is the average critical resolved shear flow stress for crystallographic slip. The tensile flow stress is related to the shear flow stress through the Schmid factor $M \sim 3$ and hardness is related to the tensile flow hardness through a constant ($H \sim 3\sigma$). Therefore,

$$H \approx 9\alpha\mu b\sqrt{\rho_s + \rho_G} \quad (11)$$

Fig. 2 shows the NG relation for differently rounded conical indenters with $\alpha = 0.36$, $\mu = 42$ GPa, $b = 0.255$ nm (adequate for copper) and $\rho_s = 10^{14} \text{ m}^{-2}$.

Xue et al. [12] carried out elastic–plastic numerical simulations using a mechanism-based strain gradient (MSG) plasticity theory in order to observe the influence of the tip radius on the ISE and compared hardness evolution with depth for both MSG plasticity and classic plasticity. If we use the results obtained by Xue et al. for copper [12] we will be able to check the validity of Eq. (8). From the evolution of hardness with depth using size-independent classic plasticity the average SSD density can be obtained as follows:

$$\rho_s \approx \left(\frac{H_{\text{class}}}{9\alpha\mu b} \right)^2 \quad (12)$$

If we define β as a correction factor which relates the GND density obtained from Eq. (8) to that simulated numerically by Xue et al. [12], then

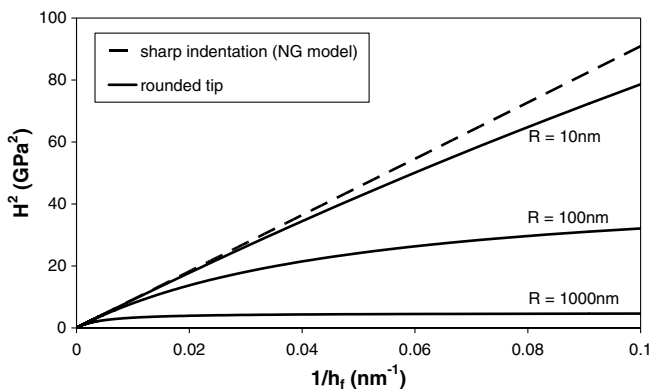


Fig. 2. Square of hardness vs. the inverse of indentation depth (H^2 vs. $1/h$) according to Eq. (11), with $\alpha = 0.36$, $\mu = 42$ GPa, $b = 0.255$ nm (copper) and $\rho_s = 10^{14} \text{ m}^{-2}$. The dotted line corresponds to a perfect conical indenter (NG model); the continuous lines correspond to rounded conical tips with different spherical tip radius.

$$H \approx 9\alpha\mu b\sqrt{\left(\frac{H_{\text{class}}}{9\alpha\mu b}\right)^2 + \beta\rho_G} \quad (13)$$

Fig. 3 shows that the results obtained by Xue et al. [12] confirm the validity of Eq. (8) with a correction factor that lies between 0.8 and 1. The divergence at very small indentation depths is due to the fact that the proportionality between hardness and tensile flow stress falls well below 3 ($H < 3\sigma$) due to the elastic contribution to the penetration depth for very shallow spherical contacts (see Tabor [13] or Johnson [14]).

Elastic contributions have to be taken into account when considering contact hardness since it is upper-bounded by purely elastic indentation. For a perfectly sharp conical indenter, elastic apparent contact hardness (load divided by contact area) is independent of depth. For a spherical indenter, in contrast, it drops linearly to zero with depth [17,18]. This implies that, from the point of view of the contact hardness, the NG model must unavoidably fail at very low indentation depths, even if the indenter is purely sharp, since it is upper-bounded by the elastic contact limit. Thus, an explanation of the divergence between the experimental observations at very small depths and the results of the NG model is, therefore, the rounded end of the indenter. However, this is not the only explanation.

As mentioned above, the average GND density may span several orders of magnitude with increasing depth. An important departure from the proportionality between the critical resolved shear stress and the square root of the dislocation density is then to be expected [19], the linear approximation being only a consequence of the assumption of a fixed dislocation line tension [20]. For large departures from a reference density, the critical resolved shear stress should be corrected as follows:

$$\tau_c = -\alpha' \ln(b\sqrt{\rho_T}) \cdot \mu b\sqrt{\rho_T} \quad (14)$$

and, therefore

$$H \approx -9\mu\alpha' \ln(b\sqrt{\rho_T}) \cdot b\sqrt{\rho_T} \quad (15)$$

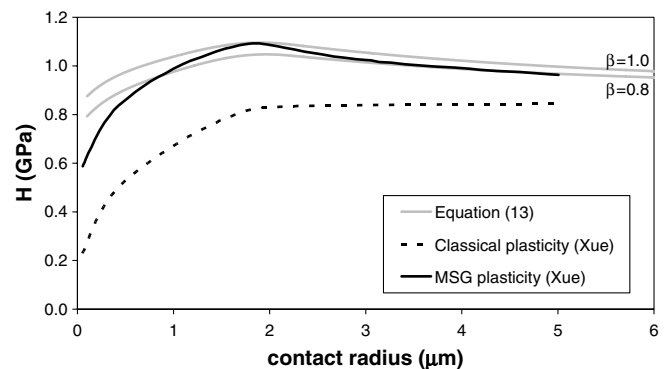


Fig. 3. Evolution of hardness with contact radius as calculated numerically for copper by Xue et al. [12] for classic plasticity and MSG plasticity assuming a tip radius $R = 5 \mu\text{m}$. Comparison with present analytical calculations (Eq. (13)) assuming $H \sim 3\sigma \sim 9\tau_c$.

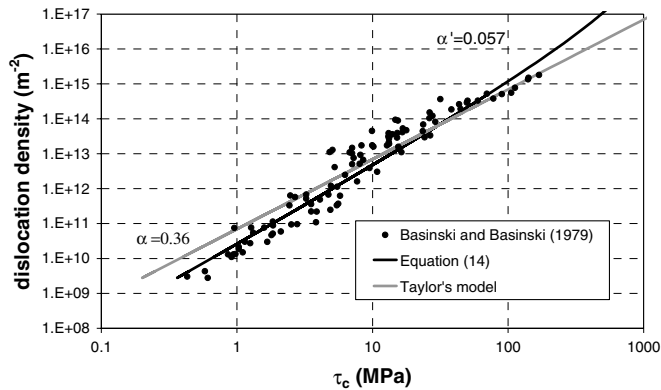


Fig. 4. Compilation of measures of dislocation densities vs. shear flow stress of Cu and Ag normalized for Nb. The black line corresponds to the least-squares fitting line to Eq. (14) and the dark grey line corresponds to the classic dislocation strengthening model (Eq. (2)) with $\alpha = 0.36$.

where α' is a dimensionless constant. Fig. 4 shows the compilation of measures of ρ vs. τ_c for Cu and Ag carried out by Basinski and Basinski [21], normalized for Nb; the black curve corresponds to a fitting with Eq. (14), the dark grey one to the classic dislocation strengthening relationship (Eq. (2)) with constant $\alpha = 0.36$. Very recent numerical results of the strengthening by a random dislocation density using discrete dislocation dynamics [22] confirm the validity of Eq. (14) for face-centred cubic metals with a constant α' very close to the empirical one of Fig. 4. The same behaviour is expected for Nb at room temperature (or for other body-centred cubic (bcc) metals at high enough temperature or dislocation density) when the Peierls stress makes a small contribution to the critical resolved shear stress [16].

This correction has important implications since the NG relationship (H^2 vs. $1/h_f$), for ideally sharp indenters, is no longer valid for shallow indentations as shown in Fig. 5. Note also that Fig. 5 should show a saturation of hardness at very low indentation depths due to the fact that Eq. (14)

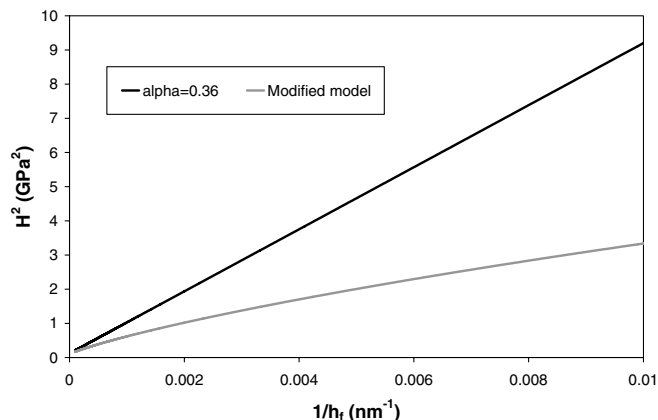


Fig. 5. Square of hardness vs. the inverse of penetration depth (H^2 vs. $1/h_f$) for sharp conical indenters according to the original NG model (Eq. (11)) with $\alpha = 0.36$ (black curve) and according to Eq. (14) with $\alpha' = 0.057$ (dark grey curve), for $\mu = 42$ GPa, $b = 0.255$ nm and $\rho_s = 10^{14}$ m $^{-2}$.

has a maximum at $\rho_T \sim 0.135/b^2$, although such dislocation density is physically non-realistic.

Therefore, even for perfectly sharp indenters an important deviation from the simplified NG relationship is predicted.

Finally, the attainment of a physical saturation of the total dislocation density for very small indentation sizes should not be discarded. A saturation of the tensile strength at about 1400 MPa has been observed in heavily axisymmetrically room temperature cold-drawn Nb [23], in which a strong work-hardening rate due to the additional contribution of GNDs to dislocation storage occurs up to very large strains ($\varepsilon > 10$) because of the internal curling of the elongating grain structure [24]. Such tensile strength would represent a GND dislocation density upper bound of about 6×10^{16} m $^{-2}$ for Nb at room temperature according to Eq. (14) and $\sigma \sim 3\tau_c$.

3. Experimental

In this study, five rods (10 mm diameter and 60 mm long) of a commercially pure Nb (99.9%, supplied by Goodfellow Cambridge Ltd.) with initial grain size of about 20 μ m were subjected to ECAP (route B_C) up to different numbers of passes: up to 0, 1, 2, 4 and 8 passes (B0, B1, B2, B4 and B8, respectively). The fundamentals of ECAP and the description of the routes can be found elsewhere [25,26]. The angle between channels is 90°, so that the induced equivalent plastic strain per pass is about 1.15.

Samples were cut, ground and mechanically polished including a final polishing with colloidal silica. Samples were then subjected to nanoindentation using a Nanoindenter® II at constant effective strain rate, i.e., at constant $\dot{P}/P = 2 \times 10^{-2}$ s $^{-1}$ (where \dot{P} is the loading rate and P is the load) which corresponds to an effective strain rate of about 10^{-3} s $^{-1}$ [27,28] up to a penetration depth of 1700 nm. The standard tip shape calibration method was used (Nanoindenter II operating instructions v. 2.2. (1996), Nano Instruments Inc., Oak Ridge, TN) which led to the following expression:

$$S \cong 24.5 \cdot h^2 + 748.49 \cdot h \quad (\text{with } h \text{ in nm}) \quad (16)$$

where S is the indentation area and h is the indentation depth measured by the instrument. According to Eq. (3), this corresponds to $\phi \sim 70.3^\circ$ and $R \sim 120$ nm. Topographic measurements carried out using atomic force microscopy (AFM) confirm these results.

The method of Oliver and Pharr (OP) [29] for extracting the real contact area from nanoindentation load–displacement data has been the most common method until now for measuring the hardness or the elastic modulus from nanoindentation experiments. However, this method has been proved to be inaccurate for work-hardened materials since it does not include pile-up effects. Recently, Alkorta et al. [30] have found that the mechanical properties (including hardness and the real contact area) cannot be

uniquely extracted from nanoindentation load–displacement data unless further data from the test are known. For example, if Young's modulus were known then the area of contact could be extracted from the following expression [17,29]:

$$S = \frac{dP}{dh} \Big|_{h_{\max}} = \frac{2\gamma \cdot E_r}{\sqrt{\pi}} \sqrt{A_c}; \quad \frac{1}{E_r} = \frac{1 - \nu^2}{E} + \frac{1 - \nu_i^2}{E_i} \quad (17)$$

where E , ν and E_i , ν_i are, respectively, Young's modulus and Poisson's ratio of the sample and the indenter and γ is a correction factor introduced by Hay et al. [31] (~ 1.05 for conical indenters; ~ 1.11 for Berkovich indenters [32]).

The contact areas obtained from nanoindentation data (assuming that $E = 104.9$ GPa and $\nu = 0.39$ [33] for Nb) were compared with direct AFM measurements for different indentation depths.

The mechanical properties of the sample can be extracted accepting these values of Young's modulus and Poisson's ratio and applying the following expressions [30]:

$$\frac{c_{\text{rig}}(n) - c}{c - c_{\text{el}}} = \kappa \frac{W_{\text{el}}}{W_{\text{pl}}} \quad (18)$$

and

$$\frac{W_{\text{el}}}{W_{\text{pl}}} = \frac{1 + n}{2n} \left(\frac{n\sigma_y}{\varepsilon_{\text{eff}} E} \right)^{1-n} \quad (19)$$

where c is the ratio between the indentation depth from the contact level and the total indentation depth as measured by nanoindentation, $c_{\text{rig}}(n)$ is the value of c for rigid materials with a work-hardening exponent equal to n , $c_{\text{el}} = 0.636$ is the value of c for the elastic contact with conical indenters, $\kappa \sim 2$ for conical and Berkovich indenters and $\varepsilon_{\text{eff}} \sim 0.026$ for conical indenters ($\varepsilon_{\text{eff}} \sim 0.028$ for Berkovich [32]), σ_y is the yield stress, W_{el} is the released energy during unloading and $W_{\text{pl}} = W_{\text{tot}} - W_{\text{el}}$, where W_{tot} is the work done during the loading. The value of $c_{\text{rig}}(n)$ obtained from Eq. (18) can be compared with the values obtained from finite element analyses [30] in order to extract the work-hardening exponent. Note that the yield stress in Eq. (19) corresponds to the elastoplastic behaviour considered by Alkorta et al. [30]:

$$\varepsilon_0 = (1 - n) \cdot \varepsilon_y = (1 - n) \frac{Y}{E} \quad (20)$$

$$K = Y \left(n \frac{Y}{E} \right)^{-n}$$

However, if the same argument is followed for a Hollomon stress–strain relationship, then the elastic limit associated with Hollomon's law obeys the following expression:

$$\frac{W_{\text{el}}}{W_{\text{pl}}} = \frac{1 + n}{2} \left(\frac{\sigma_{yH}}{\varepsilon_{\text{eff}} E} \right)^{1-n} \quad (21)$$

The main advantage of considering the latter is that it avoids the singularity in $n = 0$. Moreover, it is closer to the experimental $\sigma_{0.2\%}$ (tensile yield stress at 0.2% of plastic deformation).

Once the pile-up/sink-in (c) was corrected by Eq. (17) and assuming c independent of depth, H^2 (H is hardness) vs. $1/h$ (the inverse of the tip displacement) plots of about 100 nanoindentation experiments carried out for the same sample (covering many different grains) were fitted to a β -cubic spline smoothing (β -CSS). The same procedure was followed for the five different samples (B0, B1, B2, B4 and B8). The extrapolation of hardness when $1/h \rightarrow 0$ provides an estimate of the mechanical properties of the sample in the absence of ISE. For instance, the current SSD density of each sample can be estimated assuming the modified dislocation strengthening model (Eq. (14)) once the tensile yield stress has been estimated from Eqs. (18) and (20).

The experimental nanoindentation hardness results have been compared with those obtained from adding the analytically calculated GND density (Eq. (8)) to the obtained SSD density, again making use of the corrected dislocation strengthening relationship (Eq. (14)). The ratio β between the GND density extracted from experimental results and that calculated through Eq. (8) has also been computed.

4. Results

4.1. AFM measurements

Fig. 6 shows the evolution of c with indentation depth for B0 and B8. As expected, B8 shows an important pile-up due to its low work-hardening ability compared with B0. Use of the OP method would lead to considerable error in this case, since B8 is markedly harder than B0 and it should show higher elastic deflection (so smaller indentation area) than B0. Filled symbols correspond to the average value of c for 100 nanoindentation measurements using Eq. (17) and assuming $E = 104.9$ GPa, $\nu = 0.39$, $E_i = 1141$ GPa, $\nu_i = 0.07$ and $\gamma = 1.11$.

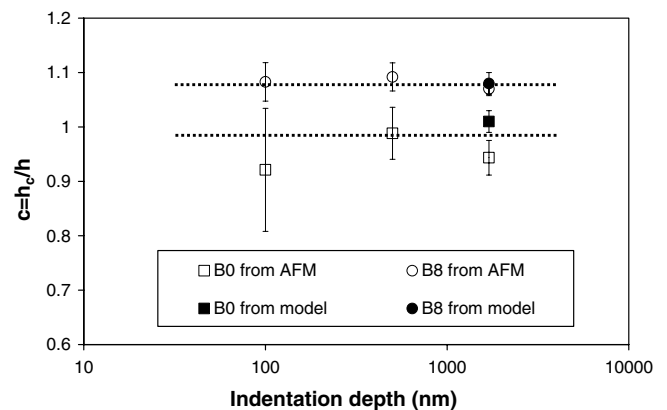


Fig. 6. Evolution of c with indentation depth obtained from AFM measurements (open symbols). Filled symbols correspond to the nanoindentation results using Eq. (17).

4.2. Mechanical properties

Fig. 7 shows the square of hardness vs. inverse of depth (once pile-up has been corrected and assuming c independent of depth) for 100 different indentations for B1. It can be seen that a linear NG relation does not hold; only a linear approximation is apparent for $h > 200$ nm ($1/h < 0.005$ nm⁻¹) but the average curve shows a constant slope decrease, as previously reported by Elm Mustafa [34].

The extrapolation of the β -CSS (black dots) to very large depths, i.e., small ISE, provides a full description of the mechanical properties by means of Eqs. (18) and (20). Moreover, Eq. (14) is suitable for estimating the value of the SSD density for each ECA level according to the modified dislocation strengthening model (with) and assuming the Schmid factor is 3.06 for bcc [35]. The results are shown in Table 1.

As expected, both the yield stress and the SSD density increase with the induced deformation (number of ECA pressings). In contrast, the Hollomon exponent decreases already after the first ECA pressing from 0.24 to less than 0.05.

4.3. Recalculated hardness

Starting from the recalculated dislocation density (SSD density in Table 1 + GND density in Eq. (8)), hardness

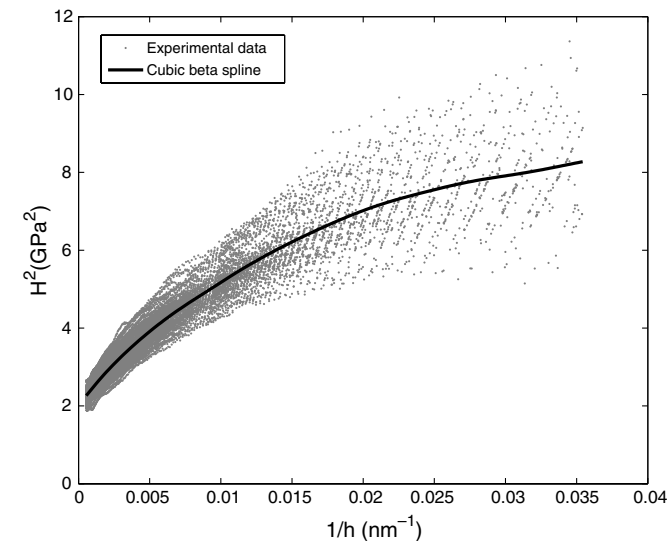


Fig. 7. Square of hardness vs. inverse of pile-up-corrected indentation depth for sample B1. The black line corresponds to the β -CSS.

can be recalculated by means of the corrected dislocation density strengthening relationship (Eq. (14) with a Schmid factor $M = 3.06$) assuming that both the Hollomon exponent and the pile-up value c are independent of depth as follows:

$$\frac{H_{\text{rec}}}{H_{\text{exp}}} = \frac{(W_{\text{el}}/W_{\text{tot}})_{\text{rec}}}{(W_{\text{el}}/W_{\text{tot}})_{\text{exp}}} \quad (22)$$

The results show, in all cases, that the recalculated hardness is well below the experimental hardness (as an example, see Fig. 8 for B1). This means that the GND density calculated by means of the modified NG relationship (including the tip roundness effect in Eq. (8) and the modified dislocation strengthening model), is well below the actual GND density which can be extracted from experimental data. In other words, the actual dislocation pattern under the indenter must be much more populated by dislocations than the idealized pattern of Fig. 1, which in fact provides the lowest bound for the GND density responsible for the ISE.

Fig. 9 shows the ratio between the GND density extracted from the experimental data and the GND density calculated by means of Eq. (8), β , vs. the inverse of the indentation depth. The factor β is about 2–5 for samples with a high initial dislocation density; i.e., the actual GND density related to rounded conical indentation is

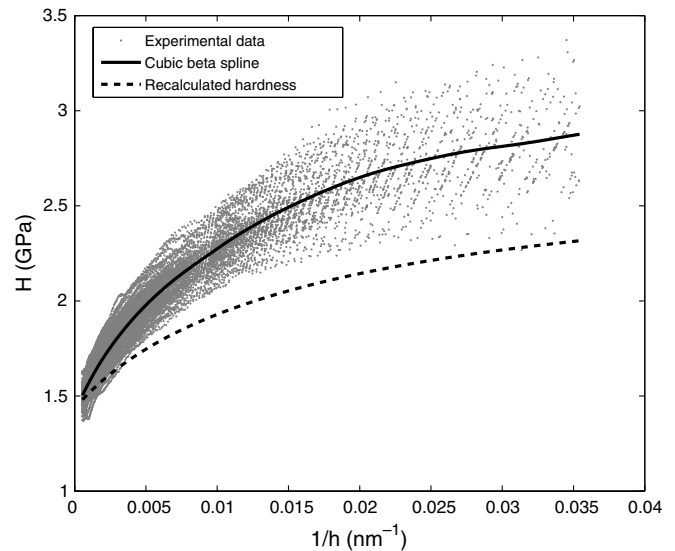


Fig. 8. Hardness vs. inverse of indentation depth for sample B1. Dark grey dots, straight line and dashed line correspond, respectively, to the experimental data, the β -CSS and the recalculated hardness.

Table 1
Mechanical properties calculated from nanoindentation measurements for the five samples

	B0	B1	B2	B4	B8
σ_{yH} (MPa)	120 ± 20	550 ± 30	620 ± 50	660 ± 40	640 ± 40
n	0.24 ± 0.02	0.03 ± 0.01	0.01 ± 0.01	0.02 ± 0.01	0.07 ± 0.01
c	1.01 ± 0.02	1.13 ± 0.01	1.14 ± 0.01	1.12 ± 0.01	1.08 ± 0.02
ρ_s (10 ¹⁴ m ⁻²)	0.8 ± 0.3	37 ± 6	50 ± 20	60 ± 10	60 ± 10

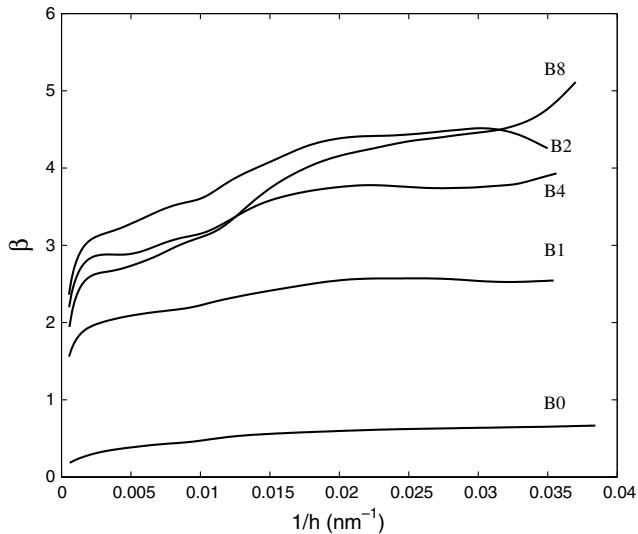


Fig. 9. Evolution of β (the ratio between the measured GND density and the density corresponding to the Nix pattern of prismatic dislocation loops) with the indentation depth for the different samples.

about 2–5 times higher than that expected from the modified NG relationship. The low values of β observed for B0 could be due to the fact that the Hollomon exponent has been assumed to be independent of the indentation depth; strictly, for very high values of dislocation density a reduction of the Hollomon exponent is expected which would lead to an increase in the value of β .

Also, an unexpected progressive evolution of β towards higher values is observed for increasing SSD density prior to the nanoindentation procedure.

5. Discussion

A modified version of the NG relationship has been proposed which accounts for both the correction due to the rounded tip as proposed in Eq. (8) and for the alternative expression for the dislocation strengthening model fitted to the experimental data obtained by Basinski and Basinski [21]. These modifications are able to reproduce the deviation from the classic NG relationship observed for very low indentation depths. Moreover, Eq. (8) has been found to be very accurate in comparison with finite element analyses carried out by Xue et al. [12].

However, the experimental results show that the actual GND density generated by a rounded conical indenter is about 2–5 times higher than that predicted by the modified NG relationship. Indeed, this modified NG model seems to be a lower bound of the actual GND density.

The correction parameter β shows an important dependence on the initial SSD density. An explanation could be the GNDs are obliged to interact with an increasing dislocation density already present in the material and the formation of effective low-energy GND patterns is progressively hindered as such initial dislocation density increases.

A practical consequence of our results is that the presence of GNDs (i.e., ISE) leads to inherent difficulties for accurately obtaining the bulk mechanical properties of materials with very low dislocation density from nanoindentation measurements. For instance, if we had a sample with a very low Peierls stress and with a SSD density of 10^{12} m^{-2} , then $\sim 92\%$ of the hardness measured at an indentation depth of about 1700 nm (about 20 μm imprint diameter) should be due to the contribution of GNDs generated during the indentation process according to Eqs. (8) and (14). Moreover, only at indentation depths of the order of 170 μm (about 3 mm diameter) would the contribution of GNDs correspond to less than a 50% of the measured hardness. Therefore, it would be practically impossible to extract the mechanical properties of very soft thin films using nanoindentation, since, with the available testing depth, the information would be totally hidden by the GNDs generated unless the relative error of the measurements was extremely small.

Another practical implication of the results presented is that GND density can reach much higher values than SSD density. The calculated SSD density of the most severely deformed Nb sample available in this study (B8, $\varepsilon \approx 9$) is well below the level of achievable GND densities calculated under the indentations ($6 \times 10^{15} \text{ m}^{-2}$ vs. $\sim 10^{17} - 2 \times 10^{17} \text{ m}^{-2}$). Such GND densities are of the same order of magnitude of and not far from the saturation density of GNDs calculated from the limit tensile strength observed for heavily drawn Nb [23]. Therefore, those severe plastic deformation (SPD) processes (such as high-pressure torsion, HPT) that introduce large amounts of GNDs because of their associated strain gradients are expected to be more effective for developing ultrafine-grained (UFG) structures than ECAP or other SPD processes lacking such macroscopic or mesoscopic strain gradients. Most experimental results point in this direction [36].

6. Conclusions

- A correction of the NG model for rounded tip conical indentations that considers the correct dislocation density strengthening relationship has been proposed which succeeds in reproducing the deviation from the NG relationship occurring at very low indentation depths.
- The value of the actual average GND density under an indentation appears to be about 2–5 times higher than that expected from the modified NG model, which implies that the generated GND pattern is much more complicated than the simple dislocation loops model proposed by Nix and Gao.
- The calculated SSD density of the most severely deformed Nb sample available in this study (B8, $\varepsilon \approx 9$) is well below the level of achievable GND densities calculated under the indentations ($6 \times 10^{15} \text{ m}^{-2}$ vs. $\sim 10^{17} - 2 \times 10^{17} \text{ m}^{-2}$). Such GND densities are of the same order of magnitude of and not far from the saturation density of GNDs observed for heavily drawn Nb [23].

Acknowledgements

This research (Project Nos. MAT2002-04343-C03-03 and MAT2003-04314) was funded by the Spanish Ministry of Science and Technology (MCYT, Plan Nacional de I+D+I, 2000–2003) and by the Department of Education, Universities and Research of the Basque Government (Project PI-2002-7). J.A. gratefully acknowledges a research grant from the Basque Government. The authors are grateful to Prof. Carmelo Luis Pérez and Pedro A. González, from the Public University of Navarre, for their support with the equal channel angular pressing facility.

References

- [1] Ma Q, Clarke DR. *J Mater Res* 1995;10:853.
- [2] Nix WD, Gao HJ. *J Mech Phys Solids* 1998;46:411.
- [3] Stelmashenko NA, Walls MG, Brown LM, Milman YV. *Acta Metall Mater* 1993;41:2855.
- [4] Atkinson M. *J Mater Res* 1995;10:2908.
- [5] McElhaney KW, Vlassak JJ, Nix WD. *J Mater Res* 1998;13: 1300.
- [6] Swadener JG, George EP, Pharr GM. *J Mech Phys Solids* 2002;50:681.
- [7] Lim YY, Chaudhri MM. *Philos Mag A* 1999;79:2979.
- [8] Feng G, Nix WD. *Scripta Mater* 2004;51:599.
- [9] Elmestafa AA, Stone DS. *J Mech Phys Solids* 2003;51:357.
- [10] Huang Y, Qu S, Hwang KC, Li M, Gao H. *Int J Plasticity* 2004;20:753.
- [11] Qu S, Huang Y, Nix WD, Jiang H, Zhang F, Hwang KC. *J Mater Res* 2004;19:3423.
- [12] Xue Z, Huang Y, Hwang KC, Li M. *J Eng Mater Trans ASME* 2002;124:371.
- [13] Tabor D. In: Jackson W, Fröhlich H, Mott NF, editors. *The hardness of metals. Monographs on the physics and chemistry of materials*. London: Oxford University Press; 1951.
- [14] Johnson KL. *J Mech Phys Solids* 1970;18:115.
- [15] Frost HJ, Ashby MF. *Deformation-mechanisms maps*. Oxford: Pergamon Press; 1982.
- [16] Gil Sevillano J. In: Mughrabi H, editor. *Flow stress and work hardening. Plastic deformation and fracture of materials*, vol. 6. Weinheim: VCH; 1993. p. 19.
- [17] Sneddon IN. *Int J Eng Sci* 1965;3:47.
- [18] Sneddon IN. *Proc Camb Philos Soc* 1948;44:492.
- [19] Foreman AJE. *Philos Mag* 1967;15:1011.
- [20] Brown LM, Ham RK. In: Kelly A, Nicholson RB, editors. *Strengthening methods in crystals*. London: Applied Science Publishers; 1971. p. 9.
- [21] Basinski ZS, Basinski SJ. In: Nabarro FRN, editor. *Dislocations in solids*, vol. 4. New York (NY): North-Holland; 1979. p. 261.
- [22] Madec R, Devincre B, Kubin LP. *Phys Rev Lett* 2002;89:255508.
- [23] Spitzig WA, Trybus CL, Laabs FC. *Mater Sci Eng A* 1991;145: 179.
- [24] Gil Sevillano J, Garcia-Rosales C, Fuster JF. *Philos Trans R Soc A* 1999;357:1603.
- [25] Valiev RZ, Islamgaliev RK, Alexandrov IV. *Prog Mater Sci* 2000;45:103.
- [26] Segal VM. *Mater Sci Eng A* 1995;197:157.
- [27] Alkorta J, Gil Sevillano J. *J Mater Res* 2004;19:282.
- [28] Lucas BN, Oliver WC. *Metall Mater Trans A* 1999;30:601.
- [29] Oliver WC, Pharr GM. *J Mater Res* 1992;7:1564.
- [30] Alkorta J, Martinez-Esnaola JM, Gil Sevillano J. *J Mater Res* 2005;20:432.
- [31] Hay JC, Bolshakov A, Pharr GM. *J Mater Res* 1999;14:2296.
- [32] Alkorta J. Ph.D. Thesis, TECNUN (University of Navarra); 2005.
- [33] Levy M, Bass HE, R. SR. *Handbook of elastic properties of solids, liquids, and gases*, vol. 2. London: Academic Press; 2001.
- [34] Elmestafa AA, Stone DS. *Acta Mater* 2002;50:3641.
- [35] Kocks UF. *Metall Trans* 1970;1:1121.
- [36] Gil Sevillano J. Strengthening by plastic work: from LPS to SPD. A 25 years perspective. In: *Proceedings of the 25th Risø international symposium on materials science*, Roskilde, Denmark; 2004.

Fracture characterization in patterned thin films by cross-sectional nanoindentation [☆]

I. Ocaña ^a, J.M. Molina-Aldareguia ^a, D. Gonzalez ^a, M.R. Elizalde ^{a,*}, J.M. Sánchez ^a,
J.M. Martínez-Esnaola ^a, J. Gil Sevillano ^a, T. Scherban, D. Pantuso ^b, B. Sun ^b,
G. Xu ^b, B. Miner ^b, J. He ^b, J. Maiz ^b

^a CEIT and TECNUN (University of Navarra), P. Manuel Lardizabal 15, 20018 San Sebastián, Spain

^b Logic Technology Development, Intel Corporation, Hillsboro, OR 97124, USA

Received 14 October 2005; received in revised form 14 February 2006; accepted 23 March 2006

Available online 9 June 2006

Abstract

A testing technique based on cross-sectional nanoindentation has been used to assess the mechanical reliability of interconnect structures. A Berkovich indenter was used to initiate fracture in a silicon substrate and cracks propagated through the structure. To better control crack growth and to convert the problem into two dimensions, a trench parallel to the indentation surface was previously machined using a focused ion beam. The crack lengths obtained for different material systems in the interconnect structure correlate well with the fracture energies measured for the same materials in blanket films. Finite element model simulations incorporating cohesive elements have been used to model the fracture processes and to explain the different cracking behaviour observed.

© 2006 Acta Materialia Inc. Published by Elsevier Ltd. All rights reserved.

Keywords: Thin films; Interfaces; Fracture; Nanoindentation; Cohesive model

1. Introduction

The complexity of the thermomechanical assessment of integrated circuits has increased dramatically during the last few decades. The miniaturization process and the use of processing routes, not always optimized from the mechanical point of view, result in an increase of the thermal stresses within the systems [1]. Moreover, introduction of new low dielectric constant (low- k) materials with deteriorated mechanical strength (i.e., Young's modulus decreases exponentially with k for the low- k materials used at present) to meet the RC delay goals increases the risk of

mechanical failure of devices during packaging or even in service [2,3].

The residual stresses that cause film decohesion arise from two main sources: the tendency of thin films to shrink or expand once they have been deposited on the substrate (intrinsic stresses) and the thermal expansion misfit between constituents [4]. The residual stresses can reach values as high as 1 GPa [5]. Over the last decade several studies have been carried out for the analysis of the interfacial decohesion by combining fracture mechanics models [6–16] with experimental calibration tests [15–18].

Among the experimental techniques, one of the most widely accepted for measuring the interfacial fracture energy in thin films for multilayer structures is four-point bending (4PB) [18–20]. Some efforts have been made to extend the use of this technique from blanket to patterned structures [21,22].

Cross-sectional nanoindentation (CSN) was designed to study the fracture energy of blanket thin films [23,24].

[☆] This manuscript was presented at the “Micromechanics and Microstructure Evolution: Modeling, Simulation and Experiments” held in Madrid/Spain September 11–16, 2005.

* Corresponding author. Tel.: +34 943 212800; fax: +34 943 213076.
E-mail addresses: relizalde@ceit.es (M.R. Elizalde), Tracey_Scherban@hotmail.com (T. Scherban).

Cracks are initiated in a brittle silicon substrate by indentation with a Berkovich diamond tip close to the interface of interest. The cracks propagate from the corners of the indentation to the weakest interface of the stack, producing delamination of the film. By measuring the delaminated area and using analytical or finite element models, the interfacial fracture energy of both ceramic [15,23] and metallic [16,24] thin films can be obtained. The delaminated areas are measured for each test combining data from a scanning electron microscopy (SEM) image of the cross-section and an optical micrograph of the wafer top view. This technique gives a quick and reproducible qualitative measurement of the interfacial adhesion. It is quantitative through the modelling and allows direct observation by SEM of the crack interaction with the thin-film stack. In addition, the technique has the potential of being applied directly to interconnect structures and allows one to study the interaction of the crack with the patterned film. This method of characterizing adhesion in test chips with full process conditions is preferable to using blanket films with simplified process flows. Earlier qualitative attempts at studying patterned structures using CSN were very promising [24].

In this paper a modification of the CSN technique, using a focused ion beam (FIB) system for sample preparation, is applied to the interconnect structure of a test chip. The samples tested are composed of a three-level metallization structure. Each metallization line is composed of Cu lines embedded in a dielectric material. Good qualitative agreement has been obtained between the results obtained by CSN in patterned films and those obtained by 4PB testing [18–22] for the interfacial adhesion and by channel cracking for the fracture energy of the interlayer dielectrics (ILDs) [25] in blanket films of the same materials. One of the advantages of the CSN technique is that it allows the observation of the crack path and the study of the interaction of the crack with the different features of the interconnect structure. In order to understand the cracking behaviour observed experimentally in terms of crack driving force and material properties, the general purpose finite element model (FEM) code ABAQUS combined with in-house developed cohesive elements has been used to model the experiment. Very good agreement has been obtained between experiments and simulations, proving the predictive capabilities of the model developed.

2. Experimental

The samples studied in the present work were test chips simulating a portion of the interconnect structure of 90 nm microprocessor technology [26]. The test chips consisted of three levels of Cu metallization embedded in an ILD with etch stop (ES) dielectric films separating the levels (see Fig. 1). The top metal layer was unpatterned, the middle level was patterned with metal lines and the lowest level was patterned with metal squares. Samples were prepared using three types of low-*k* ILD films (designated ILD-1, -2 and -3). For the particular case of the samples with ILD-2, four types of ES films (ES-1 to ES-4) were used at the lowest metal level (between M1 and M2), with all other components of the system remaining invariant.

Cross-sections were prepared by cleaving the samples following silicon single-crystal cleavage planes. After cleaving, the FIB system was used first to eliminate the cross-section roughness induced by the plastic deformation of the Cu and then to mill a trench parallel to the indentation surface (Fig. 2). The objective of this trench (which is not present in conventional CSN) was to facilitate the study of the crack path forcing the crack to grow only in the *x*-direction, and hence turning the problem into a two-dimensional one. Typically the FIB trench depth and distance from the cross-sectional surface were both 5 μm .

Once the sample was prepared, the indentation procedure described by Sánchez et al. [23] was followed using a Nano Indenter[®] XP (MTS). The distance from the indentation to the free surface was fixed between 5 and 7 μm in all cases. The process included a loading ramp at constant displacement rate until the cracks were initiated and delamination occurred. This event can be clearly seen in the load–displacement record as a sudden jump in displacement.

Fractography of the tested samples in an SEM instrument was performed to study the crack path and to measure the crack length along the different interfaces in the system. To confirm that the crack was forced to grow in the *x*-direction (see Fig. 2) some CSN test sections were milled by the FIB (Fig. 3(a)) and observed using SEM.

3. Results

A typical CSN test is shown in Fig. 3(a). As in conventional CSN, a wedge is formed that pushes the structure in

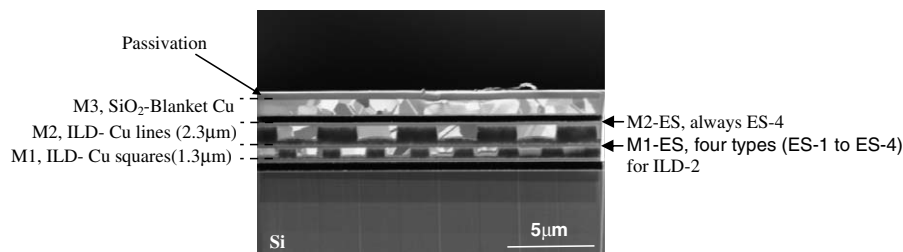


Fig. 1. Stack arrangement of the samples tested corresponding to 90 nm microprocessor technology [26] with three levels of metallization.

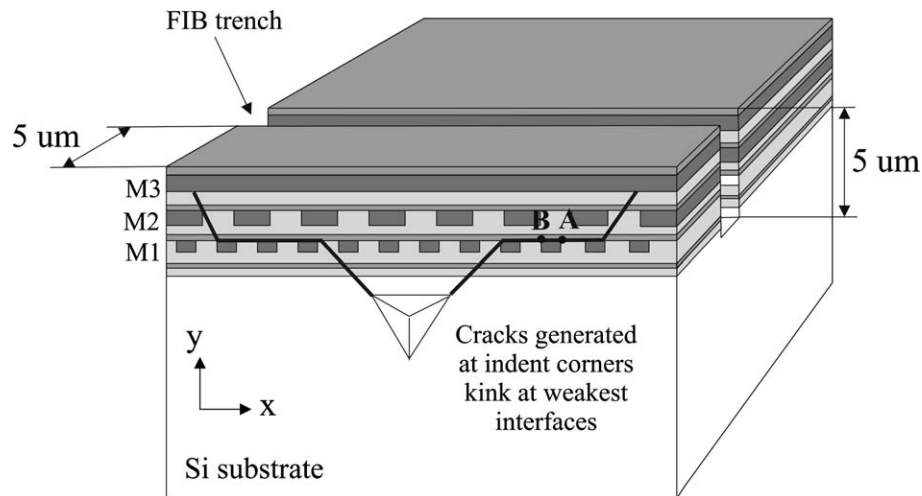


Fig. 2. Schematic of sample preparation and indentation procedure for CSN test.

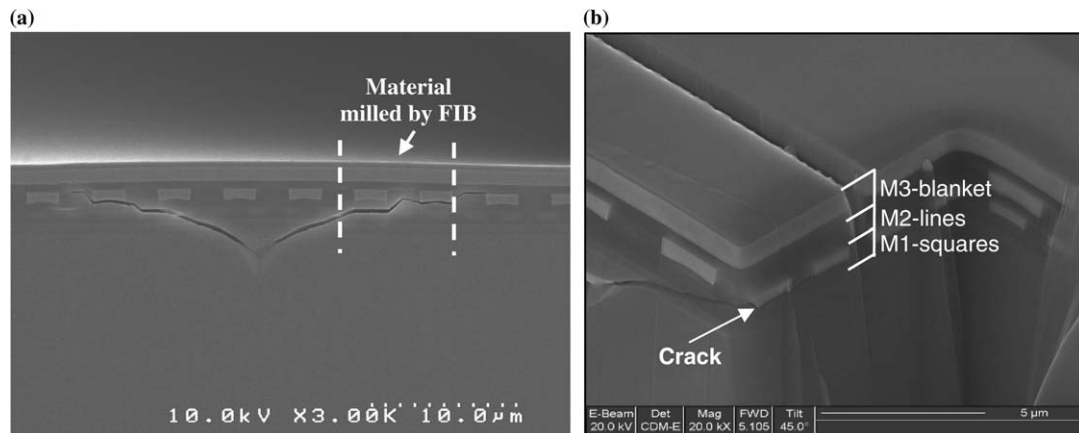


Fig. 3. SEM micrographs of (a) a MCSN test performed on an interconnect structure and (b) crack propagation observed on a milled section as described in (a) (sample tilted $45^\circ + 45^\circ$).

the y -direction (see Fig. 2) producing the bending of a beam of constant width as the crack propagates through the interconnect structure. Fig. 3(b) shows one of the beam sections, where the crack is observed to propagate at the same plane in the whole beam width between the indented plane and the trench milled with the FIB.

For each of the samples tested the load–displacement record was studied. The indentation load at which fracture occurred was found to be only dependent on the distance from the indentation to the free surface, and hence was insensitive to changes in the materials. As can be observed in Fig. 4, the load–displacement records reveal a distinct behaviour in terms of a jump in displacement during delamination for the different ILD films (Fig. 4(a)), and, in the case of ILD-2, for the different ES films (Fig. 4(b)).

These differences become more apparent in terms of the magnitude of the crack length along the interfaces in the system. Fig. 5 shows the differences in the cracking behaviour of the samples with different ES film types. These

samples were fabricated with identical materials, except for the ES film on top of M1. Note that for the interface between the ES film and the patterned Cu-ILD film in M2, for which the ES film is the same for all the samples studied, there are no significant differences in the mean values of the measured crack lengths; however, for the interface between the ES film and the patterned Cu metalization in M1, the crack length decreases from ES-1 to ES-4, suggesting that the interfacial fracture energies increase from ES-1 to ES-4.

The ability of the CSN method to provide quick qualitative monitoring of the mechanical reliability of the interconnect structure was assessed by comparing the crack lengths measured after the tests with the fracture energy values obtained by the methods currently used in the industry [18–20,25] for the mechanical characterization of blanket thin films of the same material systems. Figs. 6 and 7 summarize these measurements. The fracture energies of the ES/Cu interface obtained by 4PB are compared in

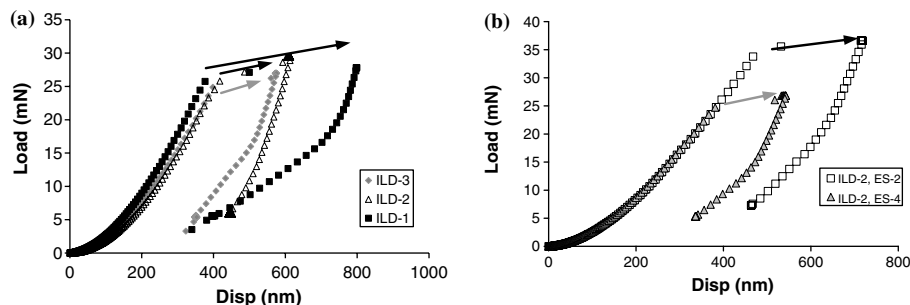


Fig. 4. Load–displacement records from MCSN tests for (a) a set of samples with ES-4 and different ILDs and (b) two samples with ILD-2 and two ES.

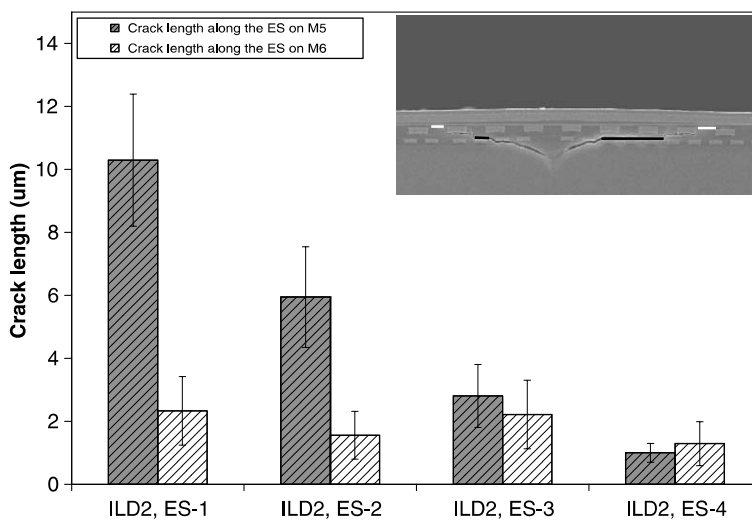


Fig. 5. Crack length along the ES to patterned Cu interfaces above M1 and M2 metallization levels (as marked) with ILD-2 film type. The ES film above M2 is the same for all samples (ES-4) while the ES film above M1 varies.

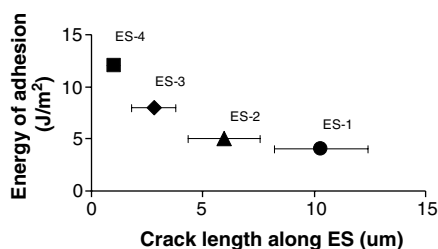


Fig. 6. Correlation between the fracture energy for the ES/Cu interface measured by 4 point bending in blanket samples (typical standard deviation 10%) and crack length along the same interface measured by MCSN for the case of ILD-2 (ES/ILD-2 adhesion energy is about 3 J/m² in all cases) in interconnect structures. Error bars represent the standard deviation for the mean value for 5–7 indentation experiments.

Fig. 6 with the crack length measured at the ES to patterned Cu interface at the lowest metallization level. Although two different interfaces are involved in crack growth (ES/Cu and ES/ILD), only the adhesion energy of the ES/Cu interface varies significantly (ES/ILD adhesion energy is about 3 J/m² in all cases). It is interesting to note that the crack lengths measured for ES-1 and

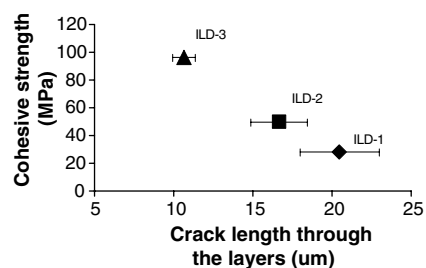


Fig. 7. Correlation between cohesive strength of the different ILDs measured by channel cracking in blanket samples (typical standard deviation 10%) and crack length through the stack measured by MCSN in interconnect structures. Error bars represent the standard deviation for the mean value for 5–7 indentation experiments.

ES-2 are different, even though the adhesion strengths are very similar. This behaviour will become clear when the simulation results are presented.

Fig. 7 compares data for the cohesive strength obtained by channel cracking [25] with the crack length through the whole stack induced by CSN. As can be observed, the total crack length increases as the cohesive strength of the ILD

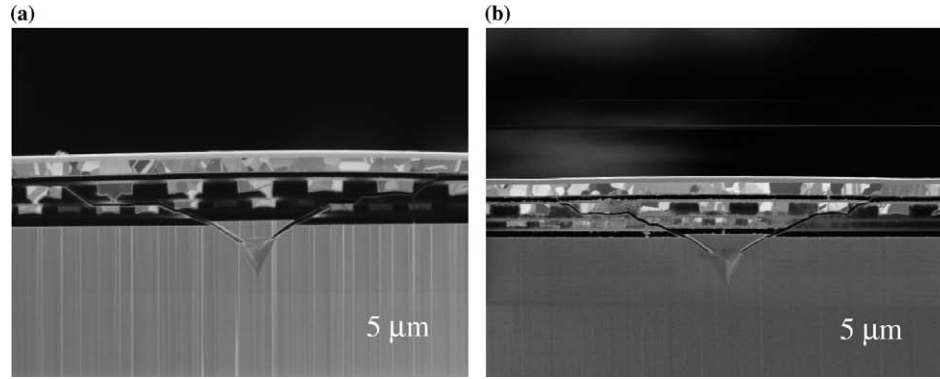


Fig. 8. SEM images of the crack path in two different samples: (a) ES-1 (poor adhesion; the crack kinks at the interface); (b) ES-4 (good adhesion; almost all the cracking occurs through the ILD).

decreases. In summary, CSN results correlate very well with those obtained in 4PB and channel cracking experiments. Moreover, the size of the jump in the load–displacement records follows the same tendency: the jump increases as the ILD cohesive strength decreases for a constant ES (Fig. 4(a)) and as the fracture energy of the ES/Cu interface decreases with all the other properties remaining invariant. These results prove that the CSN technique can be used as a qualitative quick monitor to study the fracture properties of an interconnect structure in situ, without the need to fabricate blanket films of the same materials, and allows one to study patterning and full processing effects.

In addition to providing a quick qualitative monitor of interface adhesion and ILD toughness in patterned structures, one of the main advantages of the CSN technique is that it allows the direct observation of the crack path. For instance, Fig. 8 shows the differences between the crack paths in the two extreme cases of ES-1 and ES-4. In the case of ES-1 (poorest adhesion), the crack kinks at the interface and runs along it for a considerable distance before kinking again towards the free surface. In the case of ES-4 (best adhesion), the crack travels through the interconnect structure towards the top surface, almost without any kinking at the ES interfaces.

4. Finite element modelling

4.1. Cohesive zone model (CZM)

The experimental test described above has been modelled using finite elements. The main objective of this part of the work was to assess whether the differences in the stress fields resulting from the different combinations of elastic–plastic properties of the materials in the patterned films in combination with their fracture properties could explain the various crack path tendencies observed in the experiments. The result has been a model that is able to predict the most important experimental observations.

The fracture process has been characterized using the CZM, which can be used to describe a broad range of fracture problems in a wide variety of material systems. For

each material and interface in the structure, the model is specified by a traction–separation law, σ – δ , which drops to zero when the opening δ reaches a critical value δ_c .

A convenient formulation of mixed-mode cohesive laws is based on the existence of a potential Φ that represents the energy consumption in the separation process along the process zone [27]. First, we introduce an effective opening displacement, δ , as

$$\delta = \sqrt{\delta_n^2 + q^2 \delta_t^2} \quad (1)$$

where δ_n and δ_t are the normal and tangential components, respectively, of the displacement jump across the cohesive surface. The weighting coefficient q defines the ratio between the normal and tangential critical openings (and thus it also roughly represents the ratio of K_{IIC} to K_{IC}). The model then assumes that the potential Φ depends on the separation only through the effective opening δ as

$$\Phi(\delta_n, \delta_t) = \int_0^\delta \sigma(x) dx \quad (2)$$

where the function $\sigma(\delta)$ represents the (mode I) normal traction in the absence of tangential separation. In the general case of mixed modes, the normal and tangential components of the tractions, σ_n and σ_t , acting on the fracture process zone are obtained as derivatives of the cohesive zone potential with respect to the displacement jumps

$$\begin{aligned} \sigma_n &= \frac{\partial \Phi}{\partial \delta_n} = \sigma(\delta) \frac{\delta_n}{\delta} \\ \sigma_t &= \frac{\partial \Phi}{\partial \delta_t} = \sigma(\delta) q^2 \frac{\delta_t}{\delta} \end{aligned} \quad (3)$$

A number of σ – δ laws have been used in fracture problems. In a recent review, Chandra et al. [28] examined the most popular CZMs in terms of their forms, physical significance and applications. For instance, a dependence of the shape of the σ – δ law on the nonlinear processes occurring at the micromechanical level should be expected. However, Tvergaard and Hutchinson [6,29] noted that the shape of the traction–separation law is relatively unimportant and

that the two most important parameters characterizing the fracture process are the area under the curve (work of separation, G_0) and the peak stress (fracture strength, σ_{\max}).

The cohesive model approach used in this work is regarded as a suitable phenomenological description of the fracture process zone. In particular, we have used a triangular traction–separation law, as shown in Fig. 9, for which the work of fracture is given by

$$G_0 = \int_0^{\delta_c} \sigma(\delta) d\delta = \frac{1}{2} \sigma_{\max} \delta_c \quad (4)$$

The initial slope of the σ – δ curve is a parameter that should be selected in the numerical implementation. Ideally, it has to be high enough so that the stress field in the process zone is not significantly affected in the absence of damage (prior to σ_{\max}) and, at the same time, low enough to avoid numerical instabilities. Damage of the material is assumed when $\delta > \delta_0$ (see Fig. 9). In order to define fully the behaviour of the process zone, the unloading response must also be specified. In this model, the cohesive law is assumed to remain reversible (with no permanent damage) if the maximum effective opening during the deformation history, δ_{\max} , is $\delta_{\max} < \delta_0$. When $\delta_{\max} > \delta_0$, material degradation occurs and an irreversible unloading path to the origin is used, as shown in Fig. 9.

A particularly appealing characteristic of cohesive models is that they fit in a natural manner within the conventional framework of finite element analysis. One possible approach is to implement the cohesive law as a mixed boundary condition, relating tractions to displacements at certain regions [6,27,29]. The approach we adopt here is

to embed the cohesive law into special finite elements, the so-called “cohesive elements”. The general-purpose commercial finite element package ABAQUS [30] has been used to carry out the analysis. The cohesive model is incorporated into the main program as a user-defined element subroutine UEL. In particular, plane strain cohesive elements with variable number of nodes and integration points have been employed in the simulations. A detailed account of the finite element implementation may be found elsewhere [31,32].

4.2. Model description

As the crack grows only in one direction during the CSN test and considering the geometry of the beam, a plane strain state has been assumed to simplify the simulations. Hence the CSN test has been modelled as a symmetric beam using continuum plane strain elements. The nodes at the bottom of the M1 metallization level (Fig. 1) and

Table 1
Material properties for the FEM simulations

	Young's modulus (GPa)	Residual stress (MPa)	G , cohesive (J/m ²)	$G_{\text{ES-Cu}}$ from CSN (J/m ²)	$G_{\text{ES-Cu}}$ from 4PB (J/m ²)
ES-1	85	–200	6	3	4
ES-2	53	–150	5	3	5
ES-3	170	–250	7	5	8
ES-4	118	–250	6	8	12
ILD-1	8.9	50	1.4	–	–
ILD-2	10	50	2.5	–	–
SiO ₂	85	–300	16.5	–	–
Cu	125	250	–	–	–

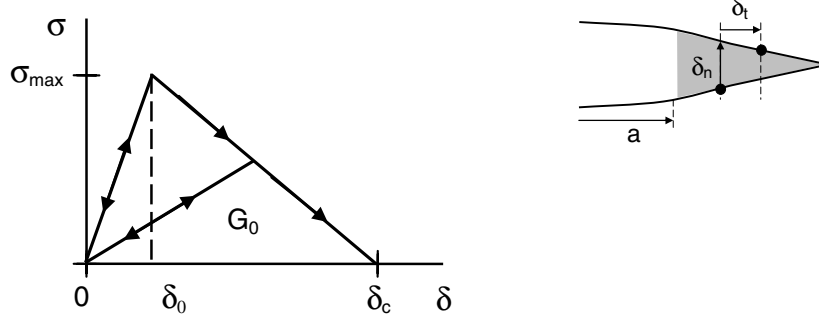


Fig. 9. Traction–separation law of the cohesive model for fracture process.

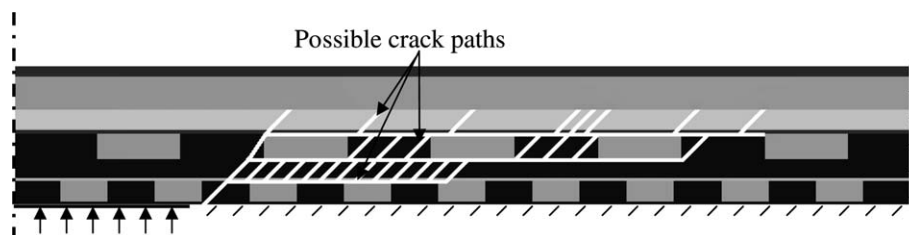


Fig. 10. Schematic of the MCSN FEM. Cohesive elements are placed in the possible crack paths determined from experimental results.

at the end of the beam are considered to be clamped and a uniform vertical displacement is imposed to the nodes in contact with the wedge (Fig. 10). Cu is considered as elastic, perfectly plastic ($\sigma_y = 525$ MPa) and all the other mate-

rials in the stack have been modelled as purely elastic (see Table 1). The cohesive elements described in the previous section have been introduced in the model, at the positions indicated by the white lines in Fig. 10, to cover all the

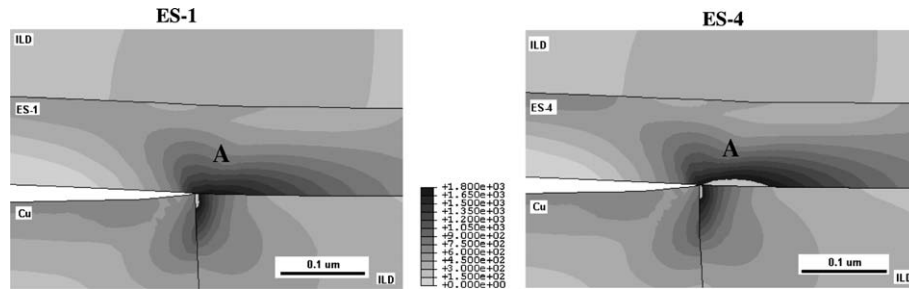


Fig. 11. Maximum principal stress plot in the vicinity of the crack tip (at point A in Fig. 2) for the most dissimilar ES in the lot: ES-1 and ES-4. The small differences observed are confined to the immediate vicinity of the crack.

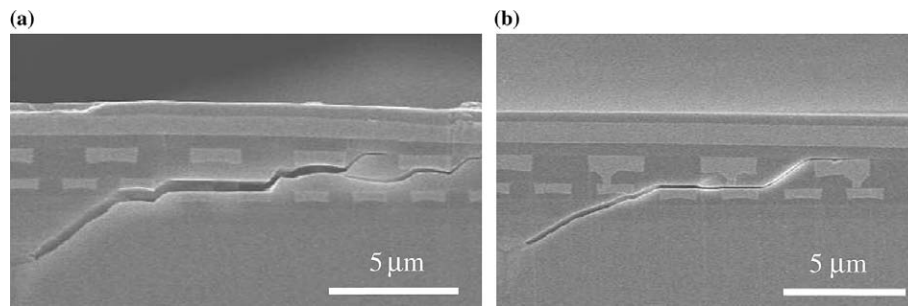


Fig. 12. (a) SEM image of the crack path in the sample with the weakest ILD (ILD-1). (b) SEM image of the crack path in a sample with a tougher ILD (ILD-2). A much more tortuous crack path can be observed in the first case.

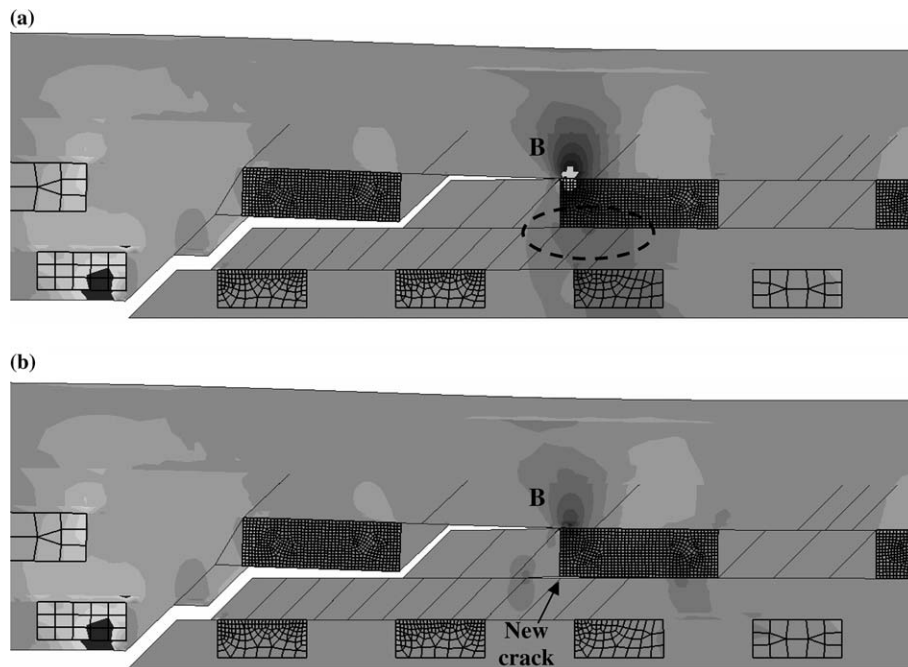


Fig. 13. Showing that the simulation is able to predict the crack initiation observed under the Cu lines of M2 layer for the weakest ILD material: (a) the crack tip is at ES/ILD interface in M2 and a stress concentration appears under the Cu line (indicated by the dashed ellipse); (b) a crack initiates under the Cu line in M2 and the stress concentration disappears.

possible crack paths obtained experimentally with all the combinations of materials used. This way, the crack can choose its path through the patterned stack as the wedge is displaced vertically, driven by the stress field and the fracture properties of the material. Note that cohesive elements have been only introduced at locations where cracks were observed experimentally. For instance, no crack has been permitted at any interface between the top surface of an ES layer and the ILD material, since no cracks were found experimentally at this interface. The fracture properties used for each material and interface in the system can be found in Table 1, and, as previously mentioned, the ES/

ILD adhesion energy was 3 J/m^2 in all cases. The parameter δ_c introduced in the previous section was chosen to be 10 nm in all cases.

4.3. Modelling results

Fig. 11 shows the maximum principal stress in the vicinity of the crack tip when this reaches the corner of a Cu square (point A in Fig. 2) for ES-1 and ES-4. The differences in the calculated values of the maximum principal stress (that in both cases would drive the crack out of the interface) are very similar. As a result, it appears that

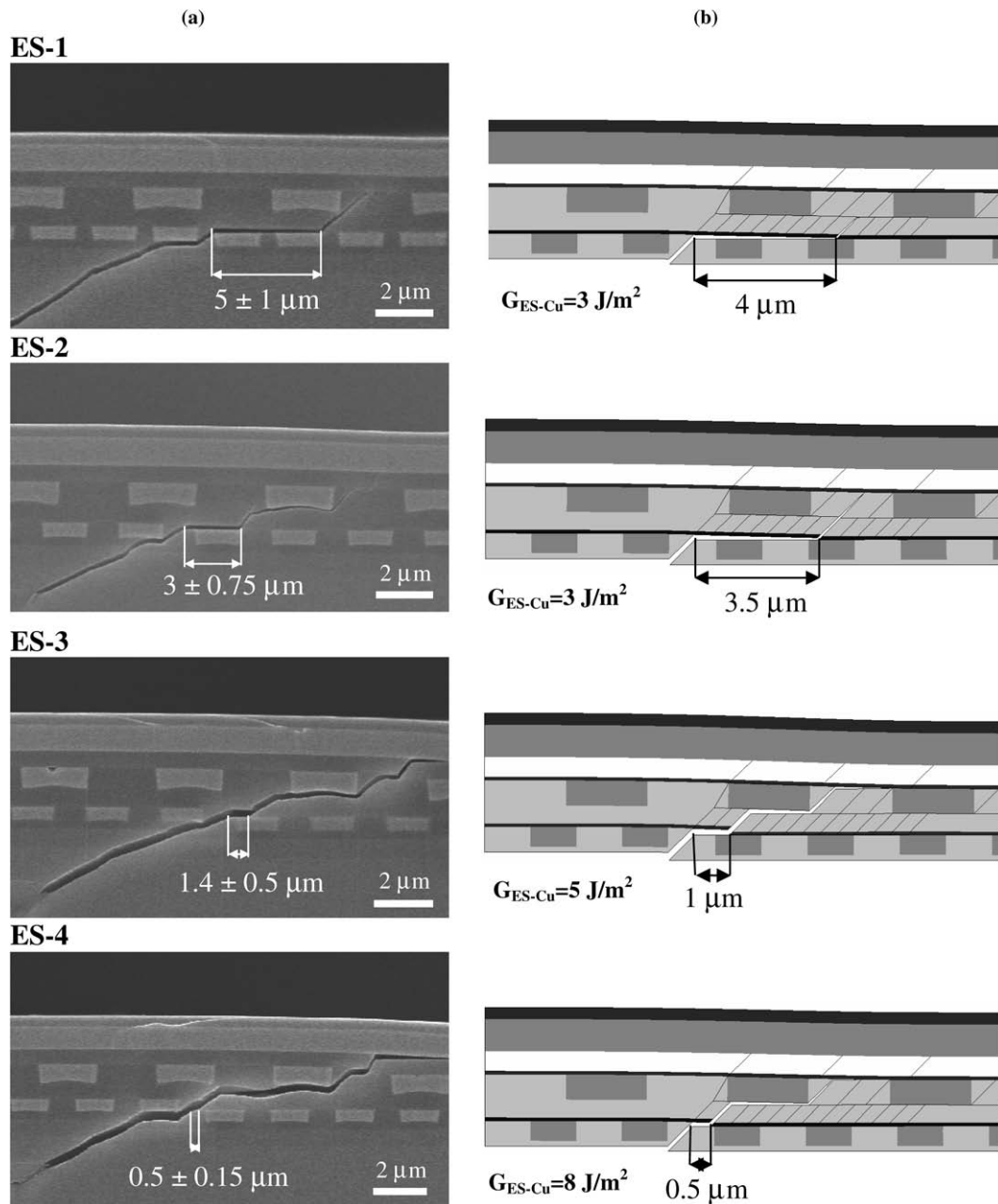


Fig. 14. (a) Experimental crack paths (mean M1–ES crack lengths measured and standard deviation) and (b) FEM simulations of the crack length below M1–ES for the set of samples with different ES materials at M1. The experiments and the simulations show the same trend, with the adhesion strength increasing from top to bottom.

the measured crack lengths are a direct consequence of the adhesion properties of each interface. However, in a general case, the elastic mismatch at the interface and/or the state of residual stress can vary depending on the material system, influencing the crack driving force. The crack length along a particular interface should be affected both by the stress field and the fracture properties of the interface, and therefore it is not a direct measurement of the true adhesion energy of the interface. The FEMs developed using cohesive elements are able to capture these effects and this is why they have turned out to be very useful for analysing the cracking behaviour of the patterned films.

An example of the predictive capabilities of the model is shown in Figs. 12 and 13. Fig. 12(a) shows the typical cracking observed in the interconnect structure made of the weakest ILD material (ILD-1). In this case, the crack follows a tortuous path, going up and down around the Cu lines. This behaviour is rarely observed for the tougher ILD-2 and ILD-3 materials, as shown in Fig. 12(b), and can be explained by the extremely poor cohesive strength of ILD-1 and by the stress concentration that appears around the crack tip due to the patterned structure. As shown in the finite element calculation of Fig. 13(a), when the growing crack arrives at the ES to ILD interface in M2, it kinks and travels along this interface. However, when the crack tip reaches the Cu line at point B, it is arrested due to the superior adhesion strength of the ES to Cu interface and the cohesive strength of the ES material. It should be noted that the ES/Cu adhesion energies used for these simulations are the ones derived from the CSN tests. Due to the patterned structure, a stress concentration develops just below the Cu line, indicated by the dashed ellipse. Although the level of stress is much lower than the stress at the crack tip, it is enough to initiate a second crack at this point, because of the low cohesive strength of ILD-1. The second crack relieves stresses (Fig. 13(b)) and eventually merges with the principal one. The explanation is consistent with the fact that this type of secondary crack initiation does not occur for materials ILD-2 and ILD-3, due to their superior fracture properties.

The model is also able to capture the effect of the different energies of adhesion ES/Cu for the tested materials. Fig. 14 shows selected experimental results for each ES and the corresponding outcome of the simulations. Mimicking the experiments, the only varying parameter in the four simulations is the adhesion energy between the ES and the Cu line, $G_{\text{ES-Cu}}$, while the rest of the parameters remain constant. As a first guess the $G_{\text{ES-Cu}}$ values obtained from 4PB tests in blanket films of the same materials were used (Table 1). The actual adhesion energy $G_{\text{ES-Cu}}$ was chosen so that the crack length at this interface matched the average crack length measured in the CSN experiments (Figs. 5 and 14) for the same interface. The experiments and the simulations show the same trend, displaying shorter crack lengths at this interface as the adhesion strength between the ES and the Cu line increases from top to bottom. The values of the adhesion energies

used to match the experimental results agree well with the adhesion strength measured by 4PB in blanket films of the same materials. Moreover, the relation obtained between the intrinsic energy of adhesion and the macroscopic fracture energy measured in 4PB experiments is similar to the results from previous work on the effect of plasticity on adhesion between Cu and ceramic thin layers [33]. The simulations also capture the fact that the crack lengths measured for ES-1 and ES-2 are different even though the adhesion strengths are very similar (see Fig. 5). In fact, the value of $G_{\text{ES-Cu}}$ used in the simulations in both cases is exactly the same but the crack length is longer for ES-1. This occurs because the crack length at a particular interface will be affected not only by the adhesion strength, but also by the residual stresses, the elastic mismatch at the interface and the cohesive strengths of the surrounding materials. In this case, the stress field drives the crack out of the interface earlier for ES-2 than for ES-1, even when the true adhesion is similar in both cases, resulting in a shorter crack length for ES-2.

5. Conclusions

A technique based on CSN has been used to evaluate the fracture behaviour of patterned interconnect structures made of different materials. The results correlate well with those obtained for the same materials in blanket form using widely accepted techniques and allow a quick and repeatable classification of both ILD films and ES films in terms of their resistance to crack propagation. CSN also provides a straightforward method to study crack propagation within the interconnect structure.

A FEM incorporating cohesive elements has been developed that allows the prediction of the crack path and the study of the interaction between the crack and the different features in the structure. Very good agreement has been obtained between the experimental results and the simulations, proving the predictive capabilities of the model. The CSN test, in combination with numerical simulations, constitutes a powerful tool to study the key features that determine the resistance to crack propagation in patterned structures.

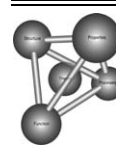
Acknowledgements

The authors gratefully acknowledge the financial support of Intel Corporation for the realization of this work. The Ministerio de Educación y Ciencia (Spanish Government) (MAT2003-04314) and the Basque Government (EX2002-6) are also acknowledged for the funds received. J.M.M.-A. acknowledges funding from the “Programa Torres Quevedo” of the Spanish Ministerio de Educación y Ciencia.

References

- [1] Nix WD. *Metall Mater Trans A* 1989;20A:2217.
- [2] Iwai H, Ohmi S. *Microelectron Reliab* 2002;42:465.

- [3] Hussein MA, He J. *IEEE Trans Semicond Manufact* 2005;18:69.
- [4] Evans AG, Hutchinson JW. *Acta Metall Mater* 1995;43:2507.
- [5] Liu XH, Suo Z, Ma Q, Fujimoto H. In: Bravman JC, Marieb TN, Lloyd TR, Korhonen MA, editors. *MRS proceedings 516. Materials reliability in microelectronics VIII*; 1998. p. 313.
- [6] Tvergaard V, Hutchinson JW. *J Mech Phys Solids* 1992;40:1377.
- [7] Suo Z, Shih CF, Varias AG. *Acta Metall Mater* 1993;41:1551.
- [8] Wei Y, Hutchinson JW. *J Mech Phys Solids* 1997;45:1137.
- [9] Wei Y, Hutchinson JW. *J Mech Phys Solids* 1997;45:1253.
- [10] Fleck NA, Hutchinson JW. *Adv Appl Mech* 1997;33:296.
- [11] Wei Y, Hutchinson JW. *Int J Fract* 1999;95:1.
- [12] Hutchinson JW, Evans AG. *Acta Mater* 2000;48:125.
- [13] Tvergaard V. *J Mech Phys Solids* 2001;49:2689.
- [14] Liu P, Cheng L, Zhang YW. *Acta Mater* 2001;49:817.
- [15] Martínez-Esnaola JM, Sánchez JM, Elizalde MR, Martín-Meizoso A. In: Fuentes M, Elices M, Martín-Meizoso A, Martínez-Esnaola JM, editors. *Fracture mechanics: applications and challenges*.ESIS publication 26. Oxford: Elsevier Science; 2000. p. 47.
- [16] Elizalde MR, Sánchez JM, Martínez-Esnaola JM, Pantuso D, Scherban T, Sun B, et al. *Acta Mater* 2003;51:4295.
- [17] Volinsky AA, Moody NR, Gerberich WW. *Acta Mater*. 2002;50:441.
- [18] Dauskardt RH, Lane M, Ma Q, Krishna N. *Eng Fract Mech* 1998;61:141.
- [19] Scherban T, Sun B, Blaine J, Block C, Andideh E. *IEEE IITC Proc* 2001:242.
- [20] Kloster G, Scherban T, Xu G, Blaine J, Sun B, Zhou Y. *IEEE IITC Proc* 2002:257.
- [21] Litteken CS, Dauskardt RH. *Int J Fract* 2003;119/120:475.
- [22] Litteken C, Dauskardt R, Scherban T, Xu G, Leu J, Gracias D, et al. *IEEE IITC Proc* 2003:168.
- [23] Sánchez JM, El-Mansy S, Sun B, Scherban T, Fang N, Pantuso D, et al. *Acta Mater* 1999;47:4405.
- [24] Scherban T, Pantuso D, Sun B, El-Mansy S, Xu G, Elizalde MR, et al. *Int J Fract* 2003;119/120:421.
- [25] Xu G, He J, Andideh E, Bielefeld J, Scherban T. *IEEE IITC Proc* 2002:57.
- [26] Jan CH, Bielefeld J, Buehler M, Chikamane V, Fischer K, Hepburn T, et al. *IEEE IITC Proc* 2003:15.
- [27] Needleman A. *J Mech Phys Solids* 1990;38:289.
- [28] Chandra N, Li H, Shet C, Ghonem H. *Int J Solids Struct* 2002;39:2827.
- [29] Tvergaard V, Hutchinson JW. *J Mech Phys Solids* 1993;41:1119.
- [30] ABAQUS. Reference manuals, version 6.5. Hibbit, Karlsson and Sorensen. Providence, RI, 2004.
- [31] Segurado J, Llorca J. *Int J Solids Struct* 2004;41:2977.
- [32] González D. Implementation of cohesive elements in ABAQUS. Report MAT 1261-01, 2005. CEIT, San Sebastián, Spain.
- [33] Lane M, Dauskardt RH, Vainchtein A, Gao H. *J Mater Res* 2000;15:2758.



Simulation of microstructure evolution in polycrystalline ferroelectrics–ferroelastics [☆]

A.Yu. Belov ^{*}, W.S. Kreher

Technische Universität Dresden, Institut für Werkstoffwissenschaft, Hallwachsstrasse 3, 01062 Dresden, Germany

Received 14 October 2005; received in revised form 20 February 2006; accepted 23 March 2006

Available online 15 June 2006

Abstract

A thermoactivation analysis of experimental data is used along with a constitutive model to determine the microscopic parameters of domain wall dynamics in polycrystalline ferroelectrics–ferroelastics. The proposed constitutive model takes into account thermally activated processes assisting domain walls to overcome the energy barriers of short-range obstacles. The microstructure in polycrystals is described effectively, employing the volume fractions of ferroelectric domains with different polarization orientations as structural (internal) variables, and its evolution is given in terms of rate equations for these variables. The average polycrystal properties are computed using a discrete orientations approximation (a set of representative orientations) for the distribution function of grain orientations. Assuming that the domain wall mobility depends on temperature according to the Arrhenius equation, the microscopic parameters of the model including the obstacle strength and activation energy are extracted from the temperature dependence of the coercive field. Using experimental data for doped lead zirconate titanate (PZT) ceramics, it is shown that within the framework of the constitutive model the “soft” and “hard” PZT compositions differ considerably, not only in defect strength but also in activation volume.

© 2006 Acta Materialia Inc. Published by Elsevier Ltd. All rights reserved.

Keywords: Ferroelectric ceramics; Domain switching; Microstructure; Modelling

1. Introduction

Apart from the traditional use as high-dielectric-constant capacitors, ferroelectric materials are being increasingly utilized in many key technologies such as information storage or energy conversion [1]. In most of the applications of ferroelectrics two underlying properties are commonly employed. First, ferroelectric crystals possess two (or more) orientation states, which differ from each other by the polarization direction but have the same energy unless an external electric field is applied. The net polarization of polydomain structures depends on the volume frac-

tions of regions (domains) occupied by different variants. Ferroelectric random access memories (FeRAM) use remanent polarization for non-volatile information storage, with the polarization switching current being utilized for read operations. Second, many ferroelectric ceramics, such as lead zirconate titanate ($\text{PbZr}_x\text{Ti}_{1-x}\text{O}_3$, PZT) solid solutions, have excellent piezoelectric properties and are referred to as piezoceramics. They are used in sensors and actuators because of their high electromechanical coupling factor. However, the response of piezoceramics differs from the intrinsic piezoeffect, as observed in single-domain crystals. In the unpoled state piezoceramics are macroscopically isotropic due to the random orientation of grains and show no directional behaviour, including the spontaneous polarization and piezoelectricity. These properties are acquired only upon poling in an electric field, which must be sufficiently strong to induce the domain reorientation.

The performance of piezoceramics depends on the complex interplay among structural defects at many levels.

[☆] This manuscript was presented at the “Micromechanics and Microstructure Evolution: Modeling, Simulation and Experiments” held in Madrid/Spain, September 11–16, 2005.

^{*} Corresponding author. Permanent address: Institute of Crystallography RAS, Moscow, Russia. Tel.: +49 0351 463 31409; fax: +49 351 463 31422.

E-mail address: belov@tmfs.mpgfk.tu-dresden.de (A.Yu. Belov).

Because these materials are polycrystalline, their microstructures (grain size and orientation distribution, phase distribution, phase and domain morphology) play crucial roles in determining their properties. Likewise, the defect structures (atomic structures of domain walls, native defects, impurities) can also strongly influence the properties. In many cases, some of these factors act simultaneously, making the polarization switching phenomena very intricate.

The cornerstone of simulations of microstructure evolution in ferroelectrics is the choice of a physical model correctly accounting for the time scale. In general, polycrystalline ferroelectrics–ferroelastics can respond to electromechanical loading in two ways: either by growth of the existing domains with energetically favourable lattice orientation or by nucleation of new ones, resulting in the formation of domain structures of complex morphologies within grains as well as in the grain accommodation processes to minimize the thermodynamic potential of the entire polycrystal. The relative contribution of these two mechanisms is determined by the activation energies for growth and nucleation and, therefore, strongly depends on the field magnitude. In principle, it can be assessed from the temperature and field dependencies of the polarization switching rate (switching current). The kinetics of polarization reversal in ferroelectrics has been extensively studied since the work of Merz [2] on BaTiO₃ single crystals. According to Ref. [2], the switching rate depends exponentially on the inverse applied field and is controlled by the nucleation rate of triangular nuclei with one atomic layer thickness. Taking into account the long-range interaction between bound charges (depolarization field) neglected in Ref. [2], Miller and Weinreich [3] proposed an alternative interpretation of the experimental results [2]. Having calculated the activation energy for nucleation of triangular single-layer steps (two-dimensional kinks) on an existing 180° domain wall, they showed that it has the same dependence on the electric field as found by Merz under other assumptions. Correspondingly, the lateral velocity of the domain wall in Refs. [2,3] follows the Arrhenius law

$$v = v_0 \exp \left\{ -\frac{\Delta G}{kT} \right\}, \quad (1)$$

with the Gibbs free energy¹ of activation (in the following, for brevity, referred to as the activation energy) decreasing with the electric field magnitude E as $\Delta G \propto 1/E$. Similar results were also reported for some polycrystalline ferroelectrics, including both bulk ceramics [4] and thin films [5]. In particular, the switching current measurements [4] in Nb-doped PZT ceramics appear to be consistent with Eq. (1). It can be shown that Eq. (1) leads to the following dependence of the coercive field E_c on the applied field frequency ν :

$$\frac{1}{E_c} \propto \ln \left(\frac{\nu}{\nu_0} \right). \quad (2)$$

This scaling law was reported [5] for La-modified PTZ thin films. The Merz Eq. (1) is, however, limited to sufficiently low fields, e.g. in BaTiO₃ as low as 0.2 MV/m, while at higher applied fields nucleation of multilayer steps on domain walls should be taken into account, giving rise to the power law $\nu \propto E^{1.4}$ for the sidewise domain wall velocity [6].

An especially strong effect of microstructure on the switching speed is observed in polycrystalline thin-film ferroelectrics, where the density of mobile domain walls can be very low. The experimental dependence

$$\frac{1}{E_c^2} \propto \ln \left(\frac{\nu}{\nu_0} \right) \quad (3)$$

of the coercive field on frequency in PZT thin films [7,8] indicates the change in the polarization switching mechanism. At present, there is no consistent theoretical model explaining the scaling law given in Eq. (3). It has been proposed by Du and Chen [7] that this frequency dependence occurs provided that domain wall mobility is controlled by the nucleation rate of semi-spherical bulges necessary to unlock the strongly bound with defects parts of a domain wall. The sidewise velocity in this case is described by Eq. (1) with the activation energy $\Delta G \propto 1/E^2$. In their calculations, however, Du and Chen [7] neglect the depolarization field energy. A proper account of depolarization fields invalidates this model. In addition, the coercive field was found to depend on the electrode size [8]. This circumstance makes it rather difficult, if possible at all, to formulate a reasonable constitutive model for polycrystalline thin-film ferroelectrics.

However, the available experimental data allow one to formulate a microstructure-based constitutive model for an important class of ferroelectric ceramics including doped ceramics of the PZT family. The experimental data [9] for the temperature dependence of ferroelectric hysteresis in both hard (PZT-4) and soft (PZT-5A, PZT-5H) commercial ceramics show that in a wide temperature range E_c decreases with temperature nearly linearly, implying that the governing mechanism of polarization reversal may be related to the thermally activated motion of domain walls in a random field of short-range obstacles. In a simple approximation, the activation energy $\Delta G = \Delta G_0 (1 - E/E_*)$ of this process decreases linearly with the electric field E and contains only two microscopic parameters: the defect strength E_* and the activation energy at zero field, ΔG_0 .

Starting from this observation, in this work we evaluate the temperature and frequency dependence of the ferroelectric hysteresis in doped PZT ceramics within the framework of a time-dependent constitutive model for ferroelectric–ferroelastic polycrystals. The main ingredients of the model are the following. At the atomic level, it incorporates the thermally activated processes assisting domain

¹ In ferroelectrics the Gibbs free energy G is related to the free energy F as $G = F - \sigma_{ij} \varepsilon_{ij} - D_i E_i$ and is the thermodynamic potential with respect to the temperature T , stress σ_{ij} , and electric field E_i .

walls to surmount the energy barriers of the obstacles. The microscopic parameters of the model (defect strength and activation energy) are determined from the experimental data of Hooker [9]. At the mesoscopic level, microstructure evolution is described in terms of rate equations for the volume fractions of domains with different polarization orientations.

2. The model of microstructure

The microstructure in ferroelectric ceramics arises spontaneously upon cooling from sintering temperatures to the Curie point, where the material undergoes a structural phase transition and the constituent crystallites (grains) acquire the spontaneous polarization and strain. Due to the grain misorientations, the polarization varies from grain to grain in accordance with the local lattice orientation, generating the electric and elastic fields. The minimization of their energy is the driving force for the spontaneous microstructure formation in ferroelectric ceramics. To reduce the intragranular fields, single-crystal grains split into a set of domains with different polarization directions, giving rise to complicated banded domain configurations with preferred head-to-tail domain morphologies. Obviously, the formation of domain structures in different grains is not independent. It proceeds self-consistently to eliminate the macroscopic depolarization fields. In general, for modelling of such microstructures both the grain orientation distribution function and the domain structure characteristics inside grains are required.

We consider a ferroelectric with M distinct domain orientations in a grain. For instance, in tetragonal and rhombohedral crystals M is equal to 6 and 8, respectively. Each variant I is characterized by its volume fraction ξ_I as well as its spontaneous strain $\boldsymbol{\varepsilon}^{s(I)}$ and polarization $\mathbf{P}^{s(I)}$. The average values of the spontaneous strain and polarization in a single crystal (or grain) with a polydomain structure have the form

$$\begin{bmatrix} \boldsymbol{\varepsilon}^s \\ \mathbf{P}^s \end{bmatrix} = \sum_{I=1}^M \begin{bmatrix} \boldsymbol{\varepsilon}^{s(I)} \\ \mathbf{P}^{s(I)} \end{bmatrix} \xi_I. \quad (4)$$

The corresponding constitutive relations for the crystal (grain) are derived under an assumption (known as the Reuss method) that the electric field \mathbf{E} and stress $\boldsymbol{\sigma}$ are identical in all variants:

$$\begin{bmatrix} \boldsymbol{\varepsilon} \\ \mathbf{D} \end{bmatrix} = \left(\sum_{I=1}^M \begin{bmatrix} \mathbf{S}^{(I)} & \mathbf{d}^{(I)T} \\ \mathbf{d}^{(I)} & \boldsymbol{\kappa}^{(I)} \end{bmatrix} \xi_I \right) \begin{bmatrix} \boldsymbol{\sigma} \\ \mathbf{E} \end{bmatrix} + \begin{bmatrix} \boldsymbol{\varepsilon}^s \\ \mathbf{P}^s \end{bmatrix}. \quad (5)$$

Here, $\mathbf{S}^{(I)}$, $\mathbf{d}^{(I)}$, and $\boldsymbol{\kappa}^{(I)}$ are the tensors of elastic, piezoelectric, and dielectric constants of the I variant. In ceramics the relations given in Eqs. (4) and (5) must be further averaged over grain orientations. Following Refs. [10,11], this can be done by means of the discrete orientations approximation using a set of representative grain orientations instead of a continuous distribution function. Each orientation in the set possesses a system of M variants, with

the total number of variants used for averaging being $N = MK$, where K is the number of the systems. Eqs. (4) and (5) remain valid provided that summation is expanded over all N variants. However, within this model switching is possible only between M variants, which belong to one system. The proper choice of the representative orientations should provide a nearly isotropic behaviour of an unpoled ceramic. The corresponding examples for ferroelectrics undergoing a cubic-to-tetragonal phase transition are given in Refs. [10,11]. Here we consider a simple approximation with $K = 1$, which turns out to give reasonable results provided that $M \geq 6$.

3. A constitutive model

3.1. Domain wall mobility

As noted above, the existence of the linear region in the E_c - T curves for the ceramics of the PZT family [9] indicates that the motion of domain walls in these ceramics at the field magnitude near E_c may have a thermally activated character. Similar linear behaviour of the coercive field was observed in relaxor ferroelectrics $\text{Pb}(\text{Mg}_{1/3}\text{Nb}_{2/3})\text{O}_3$ (PMN) at low temperatures, where they are normal ferroelectrics [12]. It was suggested in Ref. [12] that the temperature dependence of E_c in PMN can be related with the thermally activated processes of surmounting of local barriers by domain walls. However, no evidence was presented as to why this dependence is linear. To substantiate this hypothesis, we consider by analogy with the dislocation theory [13] the following dependence of the domain wall velocity on the driving force f :

$$v = \begin{cases} l_p v_0 \left(\exp \left\{ -\frac{\Delta G(f)}{kT} \right\} - \exp \left\{ -\frac{\Delta G_0}{kT} \right\} \right), & f \leq f_* \\ \frac{f}{B}, & f > f_* \end{cases} \quad (6)$$

describing the thermally activated motion in the field of short-range obstacles. Here v_0 is the attempt frequency related to the domain wall vibrations between pinning points, l_p is the distance between subsequent obstacles (the domain wall free-length), and f_* is the critical driving force (defect strength), above which the domain wall motion becomes purely dissipative and the wall velocity depends on temperature only through the drag coefficient B . The frequency v_0 depends on the defect concentration, decreasing with the distance between pinning points as $1/l_p$. Here, it was assumed that for uniform obstacle distributions the domain wall free-length and the distance between pinning points coincide. In fact, the magnitude of f_* is not known and has to be extracted from the experimental data. At sufficiently low values of the driving force the second exponential in Eq. (6) accounts for possible back jumps, providing the zero wall velocity as f vanishes. The simple expression for the frequency of back jumps used here is valid only in the limit of low f . Following Ref. [13], we adopt the following empirical expression for the activation energy:

$$\Delta G(f) = \Delta G_0 \left\{ 1 - \left(\frac{f}{f_*} \right)^p \right\}^q. \quad (7)$$

In ferroelectrics–ferroelastics, the most significant part of the driving force for the transformation $I \rightarrow J$ is linear in the applied fields

$$f_{IJ} = -E_i \Delta P_i^s - \sigma_{ij} \Delta e_{ij}^s \quad (8)$$

where $\Delta P_i^s = P_i^{s(I)} - P_i^{s(J)}$ and $\Delta e_{ij}^s = e_{ij}^{s(I)} - e_{ij}^{s(J)}$ are the jumps of the spontaneous polarization and strain across the domain wall. The kinematics of the domain wall motion can be illustrated for a system of parallel domain walls separating domains of types I and J . An increase in the volume fraction ξ_I of energetically favourable I domains due to the wall displacement can be represented in the form similar to the Orowan equation of the dislocation theory:

$$\dot{\xi}_I = \rho v \quad (9)$$

where ρ is the mobile domain wall density (per unit length normal to the wall).

3.2. Constitutive framework

To formulate a constitutive model we generalize Eqs. (6) and (9) in the following way. The mesoscale switching rate for each variant I is represented as

$$\dot{\xi}_I = \sum_{J=1, J \neq I}^M \{-w_{IJ} + w_{JI}\} \quad (10)$$

with the transition rates

$$w_{IJ} = w_0 \left(\exp \left\{ -\frac{\Delta G(f_{IJ})}{kT} \right\} - \exp \left\{ -\frac{\Delta G_0}{kT} \right\} \right) \xi_J^\alpha. \quad (11)$$

Here $w_0 = \rho l_p v_0$ is the transition rate at zero activation energy, and the switching fraction ξ_I^α , where the exponent α is a model parameter, is introduced following Ref. [14] to account for the processes of annihilation of domain walls as the volume occupied by the variant I vanishes. In general, the pre-exponential factor w_0 depends on microstructure parameters such as the defect concentration or the mobile domain wall density, which are difficult to estimate. Therefore, here it is considered as a model parameter. However, an order of magnitude estimate for w_0 can be obtained from the experimental data on low-frequency internal friction in PZT ceramics. As was shown in Ref. [15], the temperature dependence curve of internal friction had some relaxation peaks in the temperature range corresponding to ferroelectric phase. One peak was demonstrated to be due to interaction of domain walls and point defects, which are oxygen vacancies or their clusters. Recent studies [16–18] of internal friction in PZT ceramics give a value of about 10^{11} – 10^{14} Hz for the pre-exponential factor in the temperature dependence of inverse relaxation time. Therefore, as a first approximation we accept an estimate $w_0 = 10^{11}$ Hz. A further refinement of this parameter can

be achieved by comparison of results of micromechanical modelling with experiment. In what follows we show that in doped PZT ceramics the coercive field E_c depends on w_0 only logarithmically and therefore already the first approximation gives good agreement with experiment. The constitutive model introduced by Eqs. (10) and (11) is rather simple. It requires only integration in time (in general, numerically) of the differential equations for the mesoscale switching rates.

3.3. Assessment of the model parameters

To begin with, we present a method for a direct assessment of the defect strength f_* and activation energy ΔG_0 . Let us consider a ferroelectric with only two variants I and J corresponding to 180° domain switching with driving force $f = 2P^0 E$. In the case of a triangular electric field with the amplitude E_0 and frequency ν , the system of Eqs. (10) and (11) admits an analytical solution, which can be used as a basis for the experimental data analysis. The volume fraction ξ_J of the growing, energetically favourable variant J increases with a rate

$$\dot{\xi}_J = w(t)(1 - \xi_J)^\alpha. \quad (12)$$

The function $w(t)$ is defined in Eqs. (7) and (11), where it was assumed for simplicity that $q = 1$. Eq. (12) is elementary integrated with the initial condition $\xi_J(0) = 0$, yielding the volume fraction ξ_J as

$$\xi_J^{1-\alpha}(t) - 1 = -(1 - \alpha)\nu(t) \quad (13)$$

with $\nu(t)$ having the form

$$\nu(t) = \frac{w_0 e^{-b}}{4\nu k^{1/p}} \int_0^{4\nu t k^{1/p}} (e^{u^p} - 1) du \quad (14)$$

and

$$b = \frac{\Delta G_0}{kT}, \quad k^{1/p} = b^{1/p} \left(\frac{E_0}{E_*} \right). \quad (15)$$

The normalized defect strength E_* is defined as

$$f_* = 2P^0 E_*. \quad (16)$$

In the two-variant model under consideration, the relation between the average spontaneous polarization and the volume fractions of variants reduces to

$$P^s = P^0(\xi_J - \xi_I) \quad (17)$$

and the coercive field can be approximately found from the condition $\xi_J = \xi_I = 1/2$, that is, at $P^s = 0$. Taking into account the asymptotic behaviour of the integral on the right-hand side of Eq. (14)

$$\int_0^z \exp u^p du = \frac{z^{1-p} \exp z^p}{p} \left(1 + O\left(\frac{1}{z^p}\right) \right)$$

at $z \gg 1$, we finally obtain the following equation:

$$\left(\frac{E_c}{E_*}\right)^p = 1 + \frac{p-1}{b} \ln\left(\frac{E_c}{E_*}\right) - \frac{1}{b} \ln\left(\frac{w_0}{4v} \frac{1}{g(\alpha)pb} \left(\frac{E_*}{E_0}\right)\right). \quad (18)$$

It relates the coercive field with temperature and the model parameters α , p , ΔG_0 , and E_* . The function $g(\alpha)$ is expressed by

$$g(\alpha) = \frac{1}{(1-\alpha)} \left\{ 1 - (1/2)^{1-\alpha} \right\}.$$

Its value is about unity; e.g. $g(1) = \ln 2$. Because it is expected that the parameter b must be large, the second term on the right-hand side of Eq. (18) can be omitted and the temperature dependence of the coercive field takes the form

$$\frac{E_c}{E_*} = \left(1 - \frac{kT}{\Delta G_0} \left\{ \ln\left(\frac{w_0}{4v}\right) + \ln\left(\frac{E_*}{E_0} \frac{kT}{\Delta G_0} \frac{1}{pg(\alpha)}\right) \right\} \right)^{1/p}. \quad (19)$$

Eq. (19) yields some important conclusions on the domain dynamics. First, the coercive field depends on both the applied field magnitude and frequency only logarithmically. This frequency dependence is very weak in comparison with the corresponding single-crystal or thin-film results given in Eqs. (2) and (3). The choice of the model parameter α controlling the switching function in Eq. (11) also causes only a minor effect on E_c . Second, the observed experimentally linear dependencies of E_c on temperature in PZT ceramics favour the model of square obstacles corresponding to the case $p = 1$ and $q = 1$.

4. Comparison with experiment

Fig. 1 presents the results of the simulations performed within the framework of the two-variant model described above along with the experimental data of Hooker [9] for three ceramics of the PZT family. A common feature of the E_c - T plots for all ceramics is the region of a nearly linear behaviour consistent with Eq. (19) provided that one sets $p = 1$. Therefore, accepting the model of square obstacles, we obtain the following temperature dependence of E_c :

$$\frac{E_c}{E_*} = 1 - \frac{kT}{\Delta G_0} \left\{ \ln\left(\frac{w_0}{4v}\right) + \ln\left(\frac{E_*}{E_0} \frac{kT}{\Delta G_0} \frac{1}{\ln 2}\right) \right\}. \quad (20)$$

The parameter adjustment can be done in the linear region by means of two quantities: the obstacle strength E_* and characteristic temperature T_* :

$$\frac{E_c(T)}{E_*} = 1 - \frac{T}{T_*}, \quad (21)$$

where the weak logarithmic dependence of T_* on T is neglected. The parameters E_* and T_* are directly extracted from experimental plots presented in Fig. 1, after which the activation barrier ΔG_0 is calculated from Eq. (20). The results of the calculations are summarized in Table 1. The

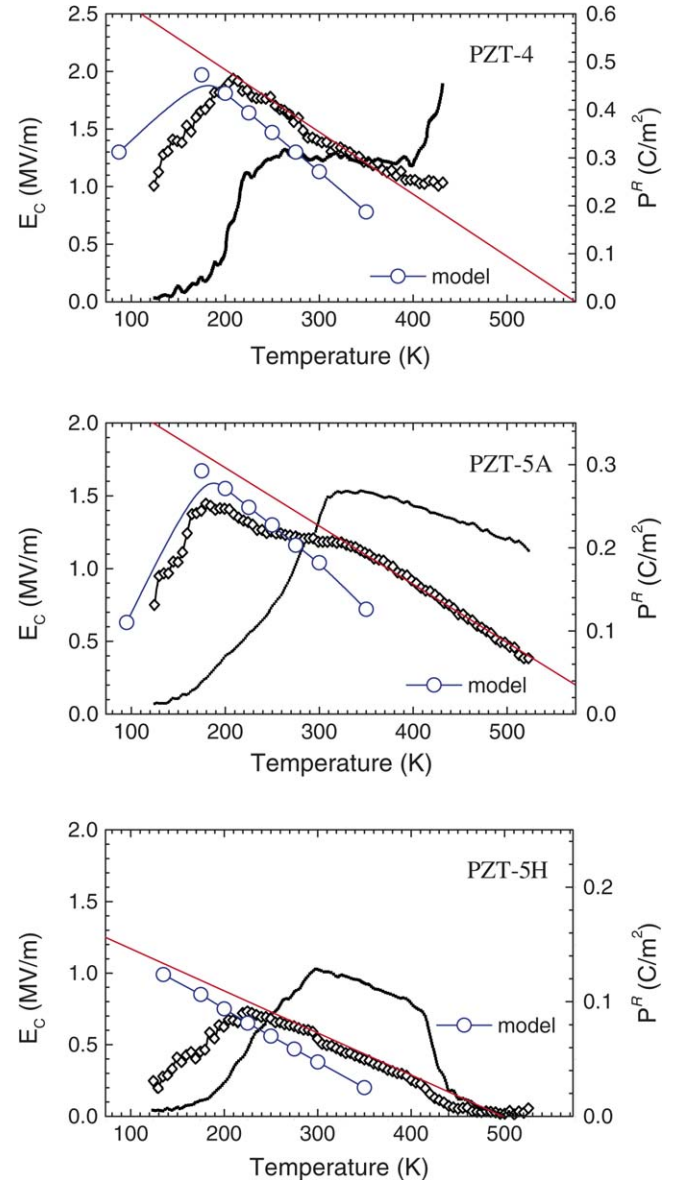


Fig. 1. Computed coercive field vs. temperature for three ceramics (PZT-4, PZT-5A, PZT-5H) within the framework of a two-variant model. The experimental plots of the coercive field and remanent polarization vs. temperature from Ref. [9] are used for the model calibration.

values used for the field amplitude (see Table 1) and frequency of 1 Hz correspond to the experimental conditions.

Table 1 shows the main trends in the parameter variations from hard to soft PZT. In all cases the defect strength E_* is about twice as large as the room temperature coercive field. However, the value of E_* in hard PZT-4 exceeds by almost 2.5 times the obstacle strength in soft PZT-5 H. The activation volume defined as

$$V_* = -\frac{\partial}{\partial f} \Delta G(f) \quad (22)$$

and characterizing variation of the activation energy with the driving force shows the inverse trend, increasing in the direction from hard to soft ceramics. For the model

Table 1
Parameters for obstacles in PZT ceramics extracted from Fig. 1 and conditions of the measurements [9]

	PZT-4	PZT-5A	PZT-5H
E_0 (MV/m)	2.5	2.0	1.25
$2P^0$ (C/m ²)	0.60	0.50	0.25
T_* (K)	575	625	500
E_* (MV/m)	3.1	2.5	1.45
V_* (nm ³)	4.2 ³ (4.0 ³)	4.9 ³ (4.7 ³)	6.9 ³ (6.6 ³)
ΔG_0 (eV)	0.85 (0.74)	0.92 (0.80)	0.73 (0.64)
T_0 (K)	9821 (8579)	10681 (9331)	8510 (7425)

Here $T_0 = \Delta G_0/k$ is the activation barrier height in kelvin and $V_* = \Delta G_0/2E_*P^0$ is the activation volume. The results of calculations are given for $\omega_0 = 10^{11}$ and 10^{10} Hz (in parentheses).

of square obstacles with $p = 1$ and $q = 1$, Eq. (22) yields merely $V_* = \Delta G_0/f_*$. Thus, in soft PZT the domain wall surmounts wide weak obstacles. As concerns the height of the activation barrier ΔG_0 , this achieves a maximum value in soft PZT-5A ceramic and a minimum one in soft PZT-5H. However, the difference between these values is not large.

To assess the accuracy of the simplified model with only two variants, the simulations were also carried out for a model with six variants [10,11], corresponding to a tetragonal ceramic. Within the framework of this model the polarization reversal proceeds by two consecutive switches of 90° domains instead of one 180° switch employed in the previous model. The results of the simulations for PZT-4 for the same values of the parameters E_* and ΔG_0 (see Table 1) for the velocity of 90° domain walls are illustrated in Fig. 2. In the case of the 90° polarization reversal the critical driving force f_* is related to the normalized defect strength E_* as $f_* = P^0 E_*$. Interestingly, after the parameter renormalization, the two models give practically identical results, substantiating the efficacy of the analytical estimates given above. In fact, in tetragonal ferroelectrics there exist both 180° and 90° domain walls, and therefore two sets of the parameters are required. In turn, rhombohedral crystals allow for 180°, 109°, and 71° polarization switching, and domain wall dynamics must be described by three

parameter sets. A special situation occurs in some ceramics, like PZT with compositions near the morphotropic phase boundary, which admit a coexistence of the tetragonal and rhombohedral phases and hence the transformation systems of both phases have to be incorporated into the model. The experimental plots appear to allow for the parameters of only one active transformation system with the lowest activation energy for the domain wall motion to be identified.

5. Conclusions

The proposed constitutive model for ferroelectric ceramics shows a high degree of transferability. Being calibrated using the data for only the linear branch of E_c – T plots, where E_c decreases with temperature, it predicts, in agreement with experiment, an overall non-monotonic behaviour of the coercive field, including its growth in the low-temperature region. The prediction of the peak is the most important result of this paper. The theoretical position of the maximum, however, is not fully consistent with experiment and is shifted to lower temperatures. An essential feature of the model is that it provides a simple criterion for the transition from the thermally activated regime of polarization switching to dissipative. According to Table 1, for typical values of the electric field magnitude of 2 MV/m, the polarization switching in PZT-4 and PZT-5A is thermally activated. Thus, it cannot be described by constitutive models with a linear dependence of the switching rate on the driving force. The most interesting situation occurs in PZT-5H. This ceramic shows a change in the physical mechanism of the domain wall motion at $E = 1.45$ MV/m, which may turn out to be lower than the operating field in some applications. This observation shows the limitations of micromechanical models [14,19,20] for polarization switching in ferroelectric ceramics.

Acknowledgement

Support by Deutsche Forschungsgemeinschaft is gratefully acknowledged.

References

- [1] Haertling GH. J Am Ceram Soc 1999;82:797.
- [2] Merz WJ. Phys Rev 1954;95:690.
- [3] Miller RC, Weinreich G. Phys Rev 1960;117:1460.
- [4] White PH, Withey BR. J Phys D 1969;2:1487.
- [5] Chen IW, Wang Y. Appl Phys Lett 1999;75:4186.
- [6] Stadler HL, Zachmanidis PJ. J Appl Phys 1963;34:3255.
- [7] Du X, Chen IW. Mater Res Soc Symp Proc 1998;493:311.
- [8] Nam SM, Kil YB, Wada S, Tsurumi T. Jpn J Appl Phys 2003;42:L1519.
- [9] Hooker MW, NASA Report CR-1998-20878 (1998).
- [10] Belov AYU, Kreher WS. J Eur Ceram Soc 2005;25:2567.
- [11] Belov AYU, Kreher WS. Mater Sci Eng B 2005;118:7.
- [12] Chen IW, Wang Y. Ferroelectrics 1998;206–207:245.
- [13] Kocks UF, Argon AS, Ashby MF. Prog Mater Sci 1975;19:1.
- [14] Huber JE, Fleck NA. J Mech Phys Solids 2001;49:785.

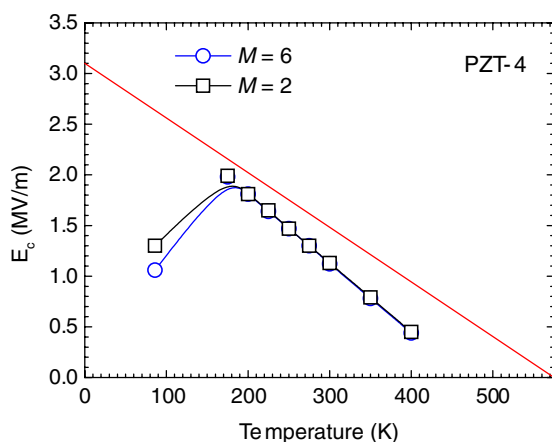
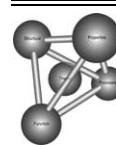


Fig. 2. Computed coercive field vs. temperature for PZT-4 ceramic within the framework of two models, one with six and the other with two variants.

- [15] Postnikov VS, Pavlov VS, Turkov SK. J Phys Chem Solids 1970;31:1785.
- [16] Bourim EM, Tanaka H, Gabbay M, Fantozzi G, Cheng BL. J Appl Phys 2002;91:6662.
- [17] Frayssignes H, Gabbay M, Fantozzi G, Porch NJ, Cheng BL, Button TW. J Eur Ceram Soc 2004;24:2989.
- [18] He LX, Li CE, Wang ZY, Yang HX, Liu W. Phys Stat Sol (a) 2000;179:275.
- [19] Hwang SC, Lynch CS, McMeeking RM. Acta Metall Mater 1995;43:2073.
- [20] Hwang SC, Huber JE, McMeeking RM, Fleck NA. J Appl Phys 1998;84:1530.



Determination of the critical size of a statistical representative volume element (SRVE) for carbon reinforced polymers [☆]

D. Trias ^{a,*}, J. Costa ^a, A. Turon ^a, J.E. Hurtado ^b

^a AMADE, Polytechnic School, University of Girona, Engineering Mechanics and Industrial Construction, Campus Montilivi s/n, 17071 Girona, Spain

^b Universidad Nacional de Colombia, Sede Manizales, Apartado 127, Manizales, Colombia

Received 14 October 2005; received in revised form 22 March 2006; accepted 23 March 2006

Available online 12 June 2006

Abstract

Representative volume elements (RVEs) have been extensively used to estimate the elastic properties of fibre-reinforced composites. Most of them rely on the assumption of a periodic distribution of fibres which is not realistic. In order to reproduce damage phenomena, such as matrix cracking, it is necessary for volume element to represent properly the random distribution of fibres (distance to first neighbors, occurrence of clusters of fibres, etc.). Therefore, a statistical RVE (SRVE) should satisfy both mechanical and point pattern criteria. The present work establishes the size of a SRVE for a typical carbon fibre reinforced polymer. It is concluded that the minimum size is $\delta = L/R = 50$ (L the side of the element and R the fibre radius).

© 2006 Acta Materialia Inc. Published by Elsevier Ltd. All rights reserved.

Keywords: Fibre reinforced composites; Finite element analysis; Fracture

1. Introduction

Fibre-reinforced polymeric composites are widely used in structural applications because of their good specific stiffness and strength. However, the use of these materials is limited by the lack of efficient tools to predict their degradation and lifetime under service loads and environment. The inhomogeneity and anisotropy of their microstructure leads to complex damage mechanisms (basically: fibre breakage, matrix cracking and yielding, fibre–matrix debonding and delamination).

The development of specific design tools for composites is being pursued since the early stages of their application in aircraft structures. Two approaches may be distinguished: a phenomenological approach and a mechanistic approach. Phenomenological approaches are based on the empirical

laws of mechanical behavior obtained from experimental tests. These models require a heavy experimental background and are not general in the sense that the behavior of a particular material and ply sequence cannot be inferred from the behavior of a simpler configuration, that is, each laminate requires a complete experimental characterization. The simplest, and more extensively used, design tools assume a complete elastic behavior of the material until a failure criterion is satisfied. Once this happens, it may be considered as either a complete breakage of the structural element or a stiffness reduction by an arbitrary factor. However, there is no agreement concerning the failure criteria to be used in the design of composite structures [1].

On the other hand, mechanistic approaches aim to simulate the occurrence of damage on the constituent scale and to reproduce the interaction of the different damage mechanisms. Moreover, the final objective of these models is to establish the degraded mechanical properties of the composite resulting from the damaged microstructure. Although this is a complex and computationally expensive task, the powerfulness of such a model as a design tool motivates the research activity in this field. Moreover, they

[☆] This manuscript was presented at the “Micromechanics and Microstructure Evolution: Modeling, Simulation and Experiments” held in Madrid/Spain, September 11–16, 2005.

* Corresponding author.

E-mail addresses: dani@emci.udg.es, dani.trias@gmail.com (D. Trias).

can certainly contribute to clarify the physics of the damage processes.

For a more realistic simulation of the microstructure of these materials, a representative volume element (RVE) may be used. Because of its ability in reproducing the real stress and strain evolution, the simulation through a RVE may provide the understanding of damage mechanisms and the identification of the possible sources and scenarios, which cause their initiation. This understanding is a need for the proposal of macroscopical failure criteria and failure laws. On the other hand, the simulation of a RVE can also be employed in a two-scale method and then, for the simulation of failure and fracture in real structural components.

In the analysis of the microstructure, the periodicity hypothesis of the fibre within the composite has been traditionally employed. This hypothesis reduces the analysis of the microstructure to the analysis of a single unit cell (the simpler RVE) and may lead to analytical solutions. Although these unit cells can be useful for some purposes and can be employed successfully in two-scale methods to reproduce macroscopical behavior [2,3], they do not reflect the reality of composite materials, in which the fibre is randomly distributed, and consequently, they are not usable to simulate some of the complex mechanisms which take place in long fibre reinforced polymers and which may cause microscopic failure [4].

One of the most revealing simulations which can be performed with a RVE is the mechanical analysis of the plane which is perpendicular to the fibres in long fibre reinforced polymers (FRPs), the transverse plane. In this plane, the mechanical behavior is dominated by the matrix properties, both in the elastic and in the failure regime.

Due to the complex geometries and the extended use of laminates with multiple ply orientations, usual laminates in structural components may have plies which work mainly in the direction perpendicular to the fibres. Also because of this design approach, transverse failure of composites is normally not critical but, of course, it has to be verified in the design process. Matrix cracking also contributes to other degradation phenomena like in stiffness degradation [5], damage [6,7] and fatigue [8] and are related to delamination [9] and even fibre breakage [10]. Furthermore, matrix cracking is crucial for some applications such as hydrogen tanks and aerospace vehicles in which this phenomena must be avoided.

The simulation through RVEs of the transverse plane can also provide useful information on other damage agents like residual thermal stresses, the role of voids and defects, or the influence of fibre–matrix interface and it be applied to quantify reliability of carbon fibre reinforced polymers (CFRPs).

The phenomena of matrix cracking has been in depth analyzed by Asp et al. [11–14]. The main conclusions of this analysis are that the large mismatch in the elastic properties between usual fibres (glass or carbon fibres) and matrix (epoxy), under these load circumstances, submits the matrix to a triaxial stress state [11,12] and that the cracking

phenomena is closely related to the dilatational energy density [12–14] in the matrix, given by:

$$U_v = \frac{1-2\nu}{6E} (\sigma_1 + \sigma_2 + \sigma_3)^2 \quad (1)$$

where E and ν are the Young's modulus and Poisson's ratio of the matrix and σ_i are the principal stresses.

More recently, Fiedler et al. [15] have performed finite element simulations using periodic unit cells which also confirm the importance of the triaxial stress state in matrix cracking of CFRPs loaded transversely and additionally consider a parabolic criterion for its prediction.

The present work is a part of a deeper research project whose main objective is to model the random microstructure in carbon fibre reinforced polymers and simulate the probability of failure associated to matrix cracking. For this purpose, the employed model must precisely reproduce the stress maps present in the microstructure of real materials. These real material stress maps are caused by the real distribution of the fibre within the composite and they differ from those stress maps obtained with the periodic models which have been classically employed [16].

This work establishes some criteria which a microstructure model (a statistical representative volume element) must satisfy for the probabilistic simulation of matrix cracking failure in long fibre reinforced polymers and according to them, determines the critical size for the SRVE. First, some definitions and some criteria (including both mechanically and statistically based) from the scientific literature are reviewed. The criteria which, determine the validity of the micro-model, are then selected and analyzed in a scale-dependent analysis. Each criterion is satisfied by a critical RVE size. The criteria which needs a larger size to be satisfied determines the minimal size for a valid RVE.

2. Mechanical definitions and criteria for a RVE

In the mechanics and thermodynamics of solids, the definition of a RVE is of paramount importance. According to the very first definition by Hill [17] a RVE is:

“a sample that (a) is structurally entirely typical of the whole mixture on average, and (b) contains a sufficient number of inclusions for the apparent overall moduli to be effectively independent of the surface values of traction and displacement, so long as these values are “macroscopically uniform”. That is, they fluctuate about a mean with a wavelength small compared with the dimensions of the sample, and the effects of such fluctuations become insignificant within a few wavelengths of the surface. The contributions of this surface layer to any average can be made negligible by taking the sample large enough”.

Although the RVE concept has been used widely in theoretical solid mechanics, for which an infinitesimal RVE is of practical usefulness in the developments of theories and formulae, in computational mechanics a finite size

RVE is required. Then, according to the RVE concept, it is necessary to define some quantitative criteria that a sample of the material must satisfy to be considered as *representative*. The interest is to determine the minimal element size that satisfies the criteria in order to reduce the computation time. Usually these criteria are closely related to the purpose of the simulation in which the RVE is intended to be used. In consequence, there is a large diversity of criteria used by the different authors that have worked in this field. Additionally, the size of the RVE used by one author may not satisfy the criteria considered by another author. This may lead to some confusion when the decision about the RVE size is taken.

Some analysis only require the RVE to have the same effective mechanical properties than the bulk material. The methodologies used were variational principles [18], periodic boundary conditions for the RVE [19], homogenization theory [20] and some improved the accuracy of a RVE of smaller size using Monte Carlo simulation [21].

Another criteria which appears in the scientific literature is the Hill condition [22]. According to this, a valid RVE must satisfy the following equation:

$$\langle \sigma : \varepsilon \rangle = \langle \sigma \rangle : \langle \varepsilon \rangle \quad (2)$$

where $\langle \cdot \rangle$ is the mean operator, σ the stress tensor and ε the strain tensor. This condition has been formerly analyzed [23] and employed for the determination of the critical size of the RVE analyzing both types of boundary conditions: imposed forces and imposed displacements [24,25].

Some other works consider statistical evaluation of mechanical properties for the determination of the critical size of the RVE, like computing confidence intervals for the effective properties [26].

3. Random geometry criteria for the RVE size

A quite different statistical approach is to analyze the point pattern formed by the distribution of fibres or inclusions centers in the matrix, that is to focus on the representativeness of the random geometry. The statistical functions which, describe these point patterns, are well established. For the long-range interaction, Ripley's K -function ($K(r)$, or second-order intensity function) and the pair distribution function ($g(r)$) are useful [27]. Ripley's K -function can be defined as the number of further points expected to lie within a radial distance r of an arbitrary point and divided by the number of points per unit area. Ripley's estimator [28] seems to be the most appropriate [29]:

$$K(r) = \frac{A}{N^2} \sum_{k=1}^N w_k^{-1} I_K(r) \quad (3)$$

where N is the number of points in the observation area A , $I_K(r)$ is the number of points in the circle with center at one of the points and radius r and w_k is the proportion of the circumference contained within the sampling area A to the whole circumference with radius r . The second-order intensity function of a complete random pattern (CSR or

Poisson set), $K_P(r)$, in a two-dimensional dominium is given by [30,31]:

$$K_P(r) = \pi r^2 \quad r > 0 \quad (4)$$

The pair distribution function $g(r)$ describes the probability of finding an inclusion whose center lies in an infinitesimal circular region of radius dr about the point r , provided that the coordinate system is located at the center of a second inclusion. The following relation between $g(r)$ and $K(r)$ can be found [32]:

$$g(r) = \frac{1}{2\pi r} \frac{dK(r)}{dr} \quad (5)$$

Although $g(r)$ and $K(r)$ are related, they provide quite different physical information. $K(r)$ can distinguish between different patterns and detect regularities, whereas the pair distribution function $g(r)$ describes the occurrence intensity of inter-inclusion distances. In this later function a local maxima indicates the most frequent distances between points and a local minima the least frequent ones in the pattern. The pair distribution function can be used for the statistical description of a composite sample, instead of the two-point probability function when the material can be considered ergodic and statistically isotropic.

Some authors have defined the RVE size from the analysis of the point patterns described by the geometrical distribution of the fibres in the matrix. Povirk [33] proposed a method to consider the inherent randomness in heterogeneous material within a usual homogenization technique, which deals with periodic materials. The main idea of this method is to find a periodic RVE with random position of the reinforcement but which is *optimally* representative of the material. The comparison between the real material and the objective RVE is done by computing the power spectral density (which can be interpreted as the probability density function in the frequency domain). Given the length of the RVE and the number of reinforcements contained therein, an *optimal* RVE is found by solving a minimization problem with an objective function which compares the power spectral density of the material and the one corresponding to the RVE. An *optimal* for the RVE was found by minimizing the second-order intensity function $K(r)$ [34].

The second-order intensity function, $K(r)$, and the pair distribution function, $g(r)$, are useful in describing long-range interactions between points. Another interesting measure of how inclusions or fibres are distributed within the material is given by the *nearest-neighbor distribution* which can be obtained easily as the probability distribution function of the smallest distance to a fibre for each fibre. Analogously, second or third-nearest-neighbor distributions may be computed. This nearest neighbor functions focus on short-range interactions between points.

Some researchers have used the elastic properties together with the nearest-neighbor distance distribution to define the critical size of a RVE [35].

The works reviewed follow either mechanical or statistical criteria but, so far, to the authors' knowledge, it has not been published any work which takes into account both groups of criteria in depth: some were only based on the Hill condition, some others analyzed only the fibre position and none considered the statistics and the distribution functions of the stress and strain fields. Moreover, the works concerned with the size of the RVE consider criterium assuming only the application of the RVE for the simulation of the elastic properties, although some of them use the RVE for damage and fracture [36] simulation.

Another important conclusion when reviewing the works which try to determine the finite size of the RVE is that different criterium lead to different sizes and, since no comparative study for determining which criteria is the most critical has been performed, no clear conclusion about which criteria have to be used is available.

For these reasons, a scale-dependent comparative study of the different criteria which characterize somehow the finite RVE size is performed in the present work. Moreover, these criteria are analyzed with the aim of defining a statistical representative volume element (SRVE). This SRVE has to reproduce the same statistics related to the stress and strain fields than the whole material and also those statistics related to the fibre distribution. This way, this SRVE will be able to reproduce the random failure behavior of the composite.

4. Methodology

For the determination of the finite size of the statistical representative volume element, models of increasing size are constructed and the evolution of some variables or functions versus the size of the SRVE are analyzed.

First, let us define the dimensionless variable δ , which relates the side length of the SRVE L and the fibre radius R :

$$\delta = \frac{L}{R} \quad (6)$$

From the literature review values of δ between 4 and 100 are chosen. The upper limit for the analysis is chosen from both preexisting literature and trial-error process. The models are transformed into finite element models to which boundary conditions are applied using the embedded cell approach (ECA) [37] and then, they are solved for two different loadcases: imposed displacement and imposed force. In the analysis, the following hypotheses are considered:

- A criteria is only satisfied by a SRVE candidate when all the bigger SRVE candidates satisfy this criteria.
- The biggest SRVE candidate is considered to be an SRVE, and so to have the same behavior of that of the material.

The variables and functions which are considered as criteria for the determination of the size of the SRVE are the following: fibre content, effective properties, Hill condition, main statistics of stress and strain fields, probability density functions of stress and strain in the matrix, distance statistical distributions (Ripley's K -function and pair distribution function). The dependency of these variables and functions on the SRVE size (δ) will be analyzed to determine for which size each of them is satisfied. Consequently, the criterion which is satisfied for a larger δ , will determine the required minimal size for a valid SRVE.

4.1. Material

The present analysis is performed for a typical carbon fibre reinforced polymer (CFRP), whose main properties are set to be: $E_f = 23,000$ MPa, $E_m = 4000$ MPa, $\nu_f = 0.22$, $\nu_m = 0.34$, $\nu_f = 0.5$. Where E is the Young Modulus, ν the Poisson's ratio, ν_f the fibre content and the subscripts 'f' and 'm' stand for the fibre and the matrix, respectively.

4.2. Relation between number of fibres and fibre content

The material is considered to be ergodic and statistically isotropic when considering the stress and strain fields and the fibre position as random fields. The position of the fibres is assumed to satisfy the conditions of a hard-core point field or Mathern's model [30]. That means that every point in the domain has the same probability to contain a fibre and fibres cannot overlap. The number of fibres is drawn from a Poisson distribution and, since complete spatial randomness (CSR) is assumed, the fibre position is drawn from an homogeneous distribution. The Poisson parameter λ is obtained from a fixed fibre volume ν_f , through the following expression:

$$\lambda = \frac{\langle n \rangle}{A} \quad (7)$$

where $\langle n \rangle$ is the expected number of fibres which lay in the considered dominium and A the area of that dominium. On the other hand, the fibre volume ν_f is the ratio between the total area which is occupied by fibres and the total area of the dominium under consideration [16]:

$$\lambda = \frac{\langle n \rangle}{A} = \frac{\nu_f}{a_f \cdot A \cdot a_t} [a_1^2 + a_2^2 + a_3^2] \quad (8)$$

where:

$$a_1 = (L - d)^2 \quad (9)$$

$$a_2 = 4 \cdot (d - \xi) \cdot (L - d) \quad (10)$$

$$a_3 = 4 \cdot (d - \xi)^2 \quad (11)$$

$$a_t = a_1 + a_2 + a_3 = (L + d - 2\xi)^2 \quad (12)$$

and L is the side length of the SRVE, d is the fibre diameter, and ξ is a small value set to avoid troubles in the finite element meshing process.

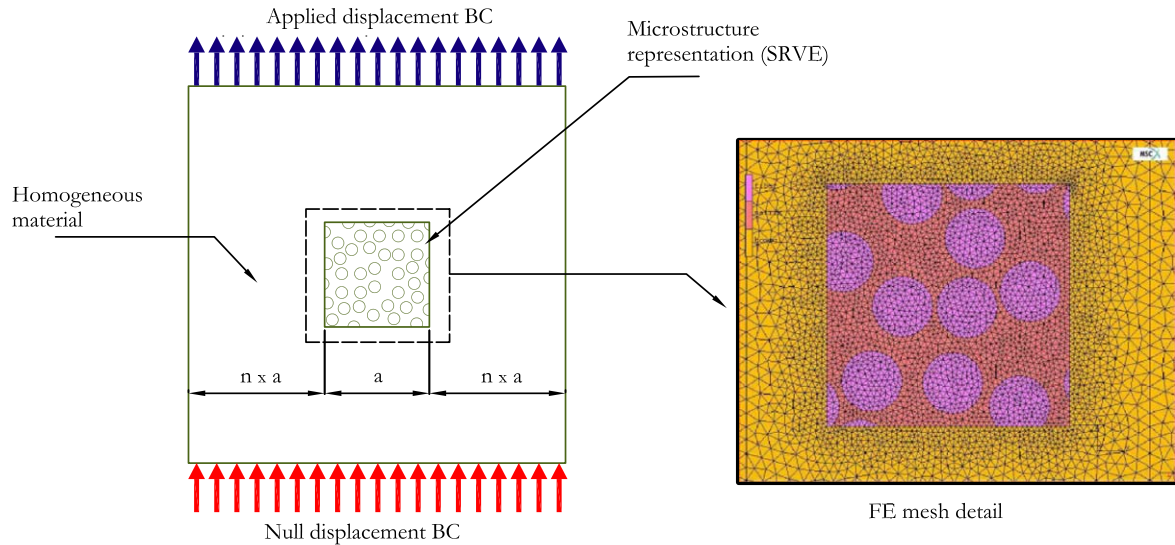


Fig. 1. Illustration of the embedded cell approach and FE mesh in one of the RVE candidate models.

4.3. Random generation of fibre positions

For the generation of the position of the fibres in each model the usual Random Sequential Absorption Algorithm [30] is used: the position of fibres is randomly drawn from a uniform distribution; then this location is accepted if it produces no overlaps, if not it is rejected.

4.4. Finite element modeling

The embedded cell approach [37] is applied by surrounding the RVE cell by an homogeneous material whose elastic constants are computed through the Halpin–Tsai equations [38], as schematized in Fig. 1. Each model is meshed with triangular elements, using MSC MARC's three-node plain strain element #6, as shown in Fig. 1. Although the

stress gradient in the fibres is much smaller than in the matrix, the core region is required to have a regular mesh to allow the estimation of the stress and strain statistics without element-size correction.

The boundary conditions are then applied to the boundary of this homogeneous material. Since an important requirement for the RVE is the equivalency of boundary conditions (displacement and force) two load cases – one with constant forces and one with constants displacements – are applied, as shown in Fig. 1.

The main data relative to the finite element models is shown in Fig. 2. The number of nodes (and the number of elements) is a power function of δ with exponent about 1.84 (about 1.85 for the number of elements). This fact shows the importance of defining the minimal usable size of the SRVE.

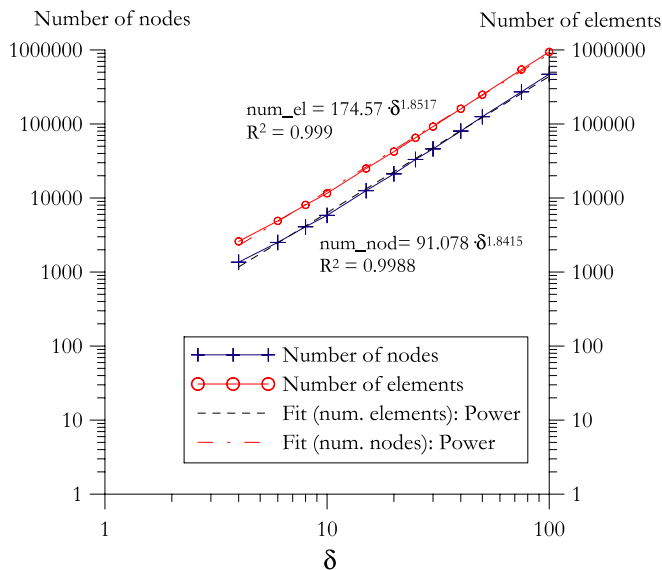


Fig. 2. Number of nodes and number of elements of the SRVE candidates.

5. Effective properties

Following Hill's very first definition of the RVE, a valid RVE has to be typical of the whole material in average. That means that the effective properties of the RVE are the same of those of the material. Although the elastic properties of a unidirectional lamina can be modelled as a linear function of the fibre content [38], in a microscopic scale they can show some deviation from this relation. Consequently, an analysis of scale-dependency of the elastic properties is performed in this section.

The elastic constants are computed for each SRVE candidate, using both type of boundary conditions: displacements and forces. Results, which are nearly proportional to those of volume fraction, are shown in Fig. 3. Small variations of the elastic constant are obtained for $\delta > 30$. If the variation with respect to the immediately smaller SRVE candidate is computed the same conclusion is obtained: from $\delta = 30$ variations lower than 10% are obtained when applying displacements and forces.

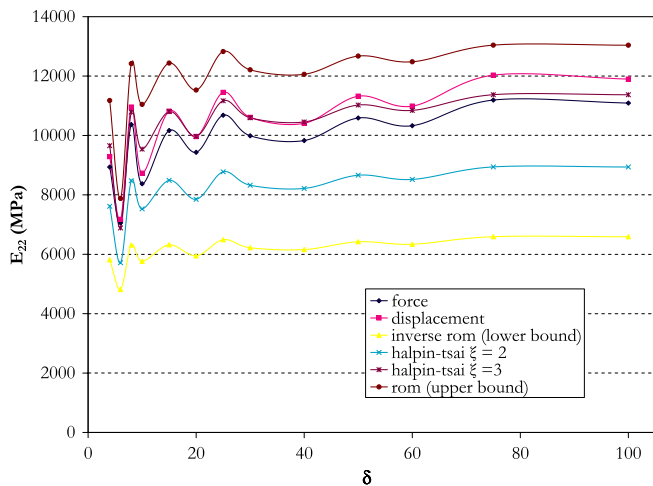
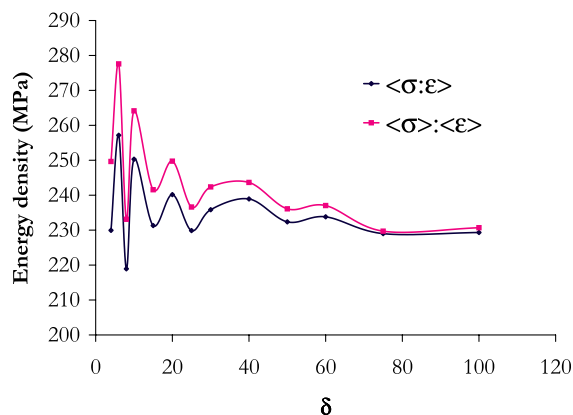


Fig. 3. Comparison of computed E_{22} with theoretical formulae.

The values obtained for E_{22} can also be compared with the estimations of different formulae, like the rule of mixtures and the Halpin–Tsai expressions [38]. The results of this comparison are shown in Fig. 3. As a verification of the FE modeling and computational tasks, it can be observed that the computed effective modulus lies between the rule of mixtures (upper limit) and the inverse rule of mixtures (lower limit) and it is close to the Halpin–Tsai equations.

6. Hill condition

The so-called Hill condition of Eq. (2) should be satisfied by any RVE. To verify the satisfaction of this criteria, both sides of equality (2) have been computed for each SRVE candidate. Results (plotted in Fig. 4) show as the bigger the SRVE size is, the closer are the measures of the energy. Fig. 4 also shows the relative difference between energy bounds is plotted. In the same figure, a tendency line with a exponential fit is shown. It can be verified that for $\delta > 15$ the relative difference is lower than 5%, which can be considered a small enough difference.



7. Convergence of stress and strain fields

In a probabilistic mechanical analysis, mechanical properties as seen as random variables, which can be fitted with a probability density function, characterized by some statistics (for instance, the mean and the variance fully characterize a normal distribution). According to the criterion established by Asp and co-workers for matrix cracking [14], each polymer has a constant critical value of the dilatational energy density U_v of Eq. (1), U_v^{crit} . When the value of U_v at a point in the matrix (which can be computed as a function of its elastic constants and the principal stresses) reaches U_v^{crit} , then a crack nucleates. The stress and strain tensor at any point in a geometrically random composite is a random tensor and consequently, a SRVE must reproduce this randomness. In this section the convergence of the mean, the variance and the coefficient of variation of the stress and strain fields is analyzed.

In some of the works reviewed [24,25], the requirement of obtaining the same effective results using the different types of boundary conditions is pointed out. For these reason, additionally the analysis of the statistics is performed for both cases of boundary conditions, displacements and forces.

7.1. Mean of stress and strain fields

Fig. 5 shows the evolution of the mean strain and the mean stress in each constituent and in the composite when the size of the SRVE increases. Since the fibre content in each candidate is a random variable, these plots have to be seen as variations around a tendency. Moreover, since the volume fraction is not constant within the SRVE candidates, the mean strain may tend to converge slowly. Nevertheless, this is a normal situation, since the SRVE has to take into account the fibre content variation, which causes variation in the elastic constants. Since the SRVE model with $\delta = 100$ is considered to have the same statistics than the bulk material, the following hypotheses can be tested [39]:

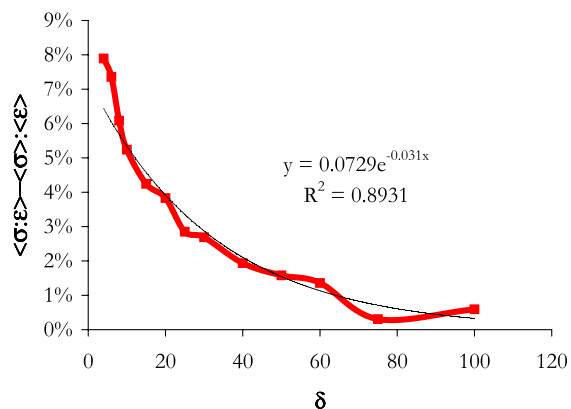


Fig. 4. Energy bounds for the RVE candidates: value of each bound (left) and difference (right).

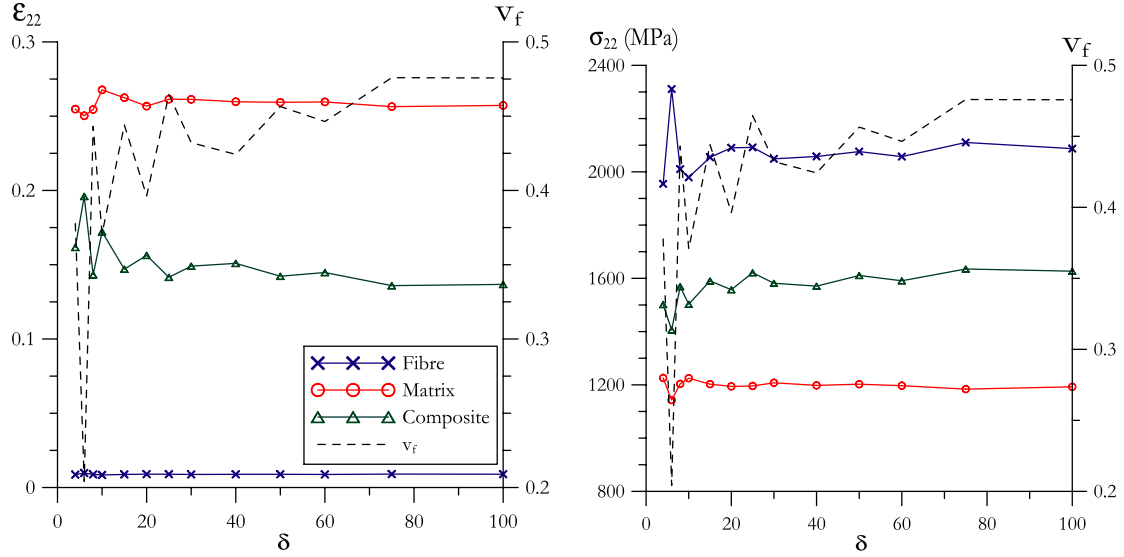


Fig. 5. Mean strain (left) and mean stress (right) for displacement boundary condition. Analogous results are obtained for force boundary condition.

$$\begin{aligned} H_0 : \mu(\varepsilon_{22}^{(\delta)}) &= \mu(\varepsilon_{22}^{(100)}) \\ H_1 : \mu(\varepsilon_{22}^{(\delta)}) &\neq \mu(\varepsilon_{22}^{(100)}) \end{aligned} \quad (13)$$

where the superscripts 100 and δ stand for the mean in the model $\delta = 100$ and any other model with size δ , respectively. The hypothesis test is used here for detecting when the mean obtained from a SRVE candidate model can be considered to be equal to the mean of the whole composite (computed through the model with $\delta = 100$).

A hypothesis test with $\alpha = 1\%$ (when performing a hypotheses test α is the error of rejecting the null hypothesis when it is true) has been performed for $\mu(\varepsilon_{22})$ in the composite, in the fibre and in the matrix. Fig. 6 shows the results of this test for each δ . These results show how the

null hypothesis can be accepted for $\delta \geq 15$, since from this value and for all the considered cases $|z_0| - z > 0$ and, consequently, H_0 is accepted for $\delta \geq 15$.

Analogously, the following hypothesis related to the mean of σ_{22} can be tested:

$$\begin{aligned} H_0 : \mu(\sigma_{22}^{(\delta)}) &= \mu(\sigma_{22}^{(100)}) \\ H_1 : \mu(\sigma_{22}^{(\delta)}) &\neq \mu(\sigma_{22}^{(100)}) \end{aligned} \quad (14)$$

with the superscripts having the same meaning than in the former test. Again, the hypothesis test for $\mu(\sigma_{22})$ in the composite, in the matrix and in the fibre has been performed and results plotted in Fig. 6. Following the same criteria that was used for $\mu(\varepsilon_{22})$, in this case H_0 can be accepted for $\delta \geq 10$.

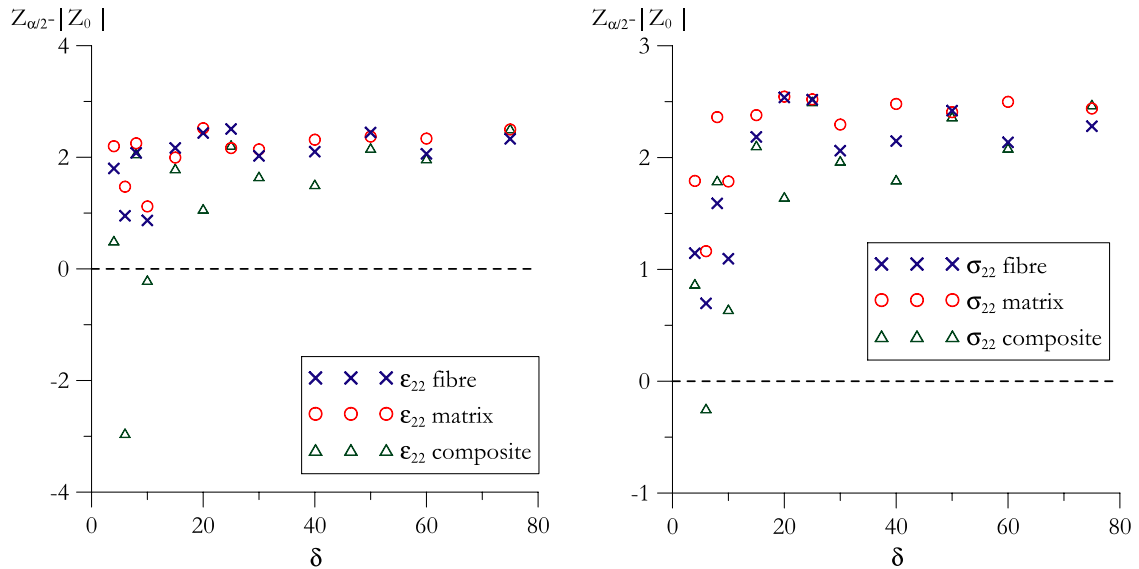


Fig. 6. Hypothesis test for: the mean of ε_{22} (left) and the mean of σ_{22} (right) for displacement boundary condition. Same results are obtained for force boundary condition.

7.2. Variance of stress and strain fields

Fig. 7 shows the evolution of the variances of ε_{22} and σ_{22} .

The variance is a useful statistic to determine if two samples come from the same population [40]. That means, the variance of each SRVE candidate and the variance of the model with $\delta = 100$ can be compared using an appropriate hypotheses test [39]:

$$\begin{aligned} H_0 : \sigma^2(\varepsilon_{22}^{(\delta)}) &= \sigma^2(\varepsilon_{22}^{(100)}) \\ H_1 : \sigma^2(\varepsilon_{22}^{(\delta)}) &\neq \sigma^2(\varepsilon_{22}^{(100)}) \end{aligned} \quad (15)$$

The analogous hypothesis regarding the variance of σ_{22} can also be written:

$$\begin{aligned} H_0 : \sigma^2(\sigma_{22}^{(\delta)}) &= \sigma^2(\sigma_{22}^{(100)}) \\ H_1 : \sigma^2(\sigma_{22}^{(\delta)}) &\neq \sigma^2(\sigma_{22}^{(100)}) \end{aligned} \quad (16)$$

In Fig. 8 the results of the test for the variance of ε_{22} and σ_{22} have been plotted, for a significance of 99%. These figures show that H_0 can be accepted for $\delta \geq 25$, since from this SRVE size a positive value of $F_0 - F$ is obtained.

7.3. Coefficient of variation of stress and strain fields

Another useful statistic to analyze the variation within a sample is the coefficient of variation ρ , defined as:

$$\rho = \frac{\sigma}{\mu} \quad (17)$$

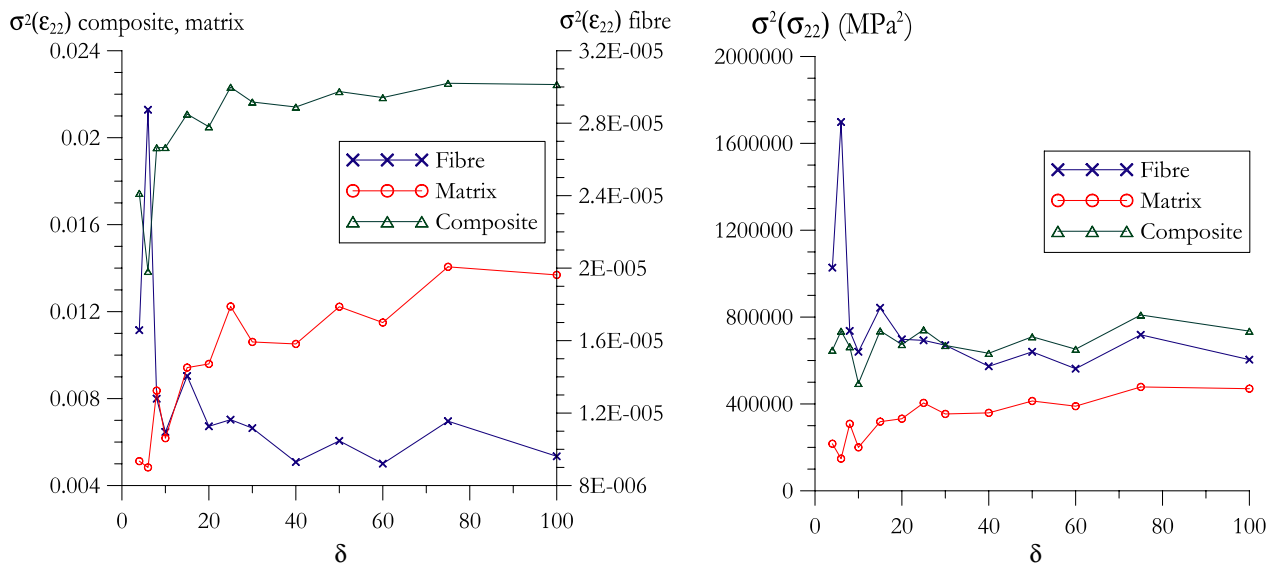


Fig. 7. Variance of: the strain (left) and the stress (right) in the composite and in each constituent for displacement boundary condition. Analogous results are obtained for force boundary condition.

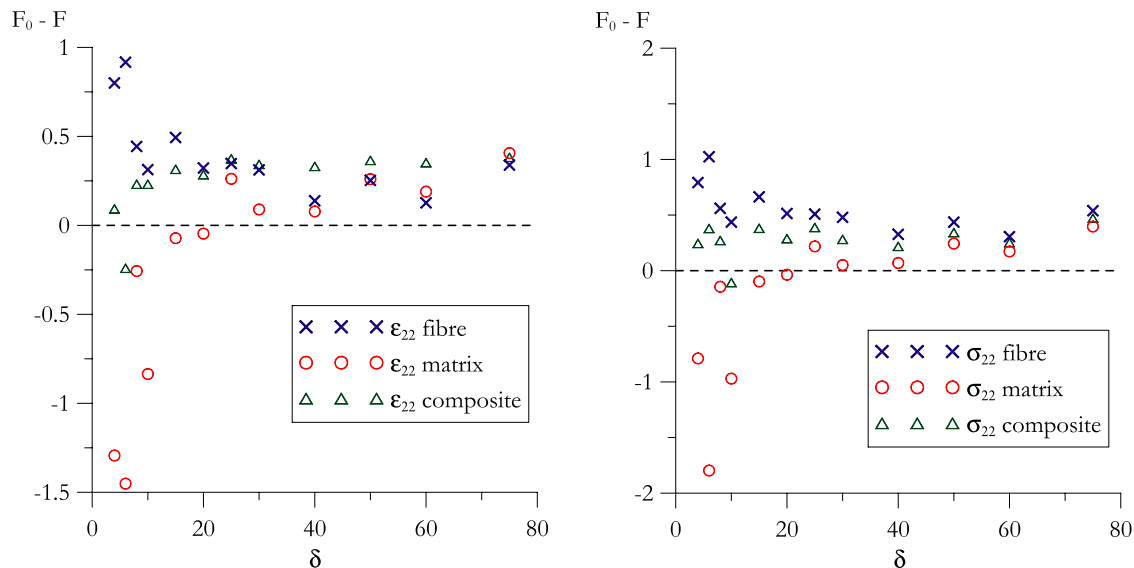


Fig. 8. Hypothesis test for: $\sigma^2(\varepsilon_{22})$ (left) and $\sigma^2(\sigma_{22})$ (right) for displacement boundary condition. Same results are obtained for force boundary condition.

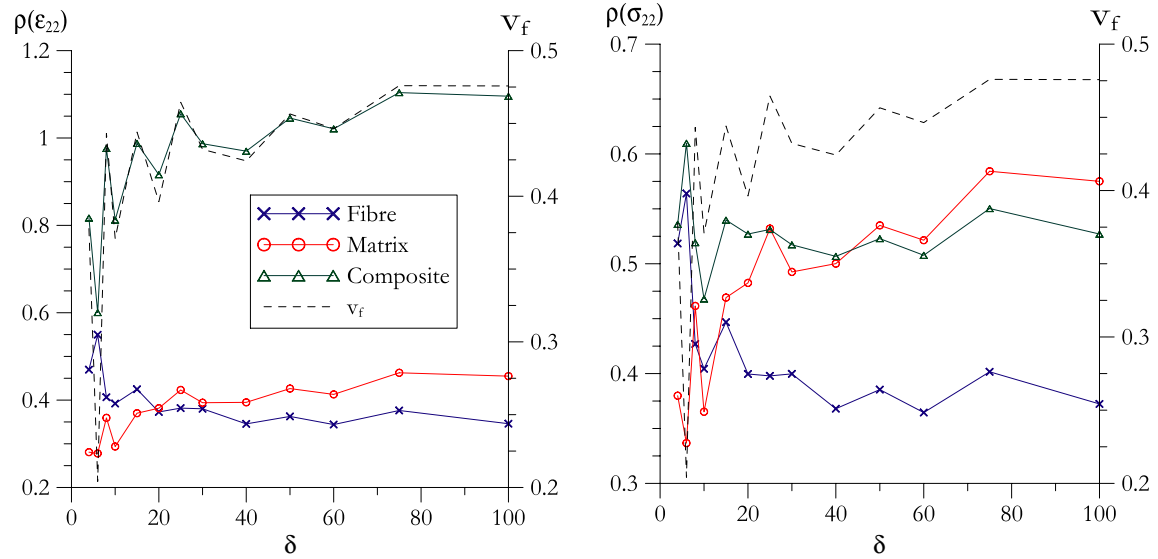


Fig. 9. Coefficient of variation of: the strain (left) and the stress (right) in the composite and in each constituent for displacement boundary condition. Same results are obtained for force boundary condition.

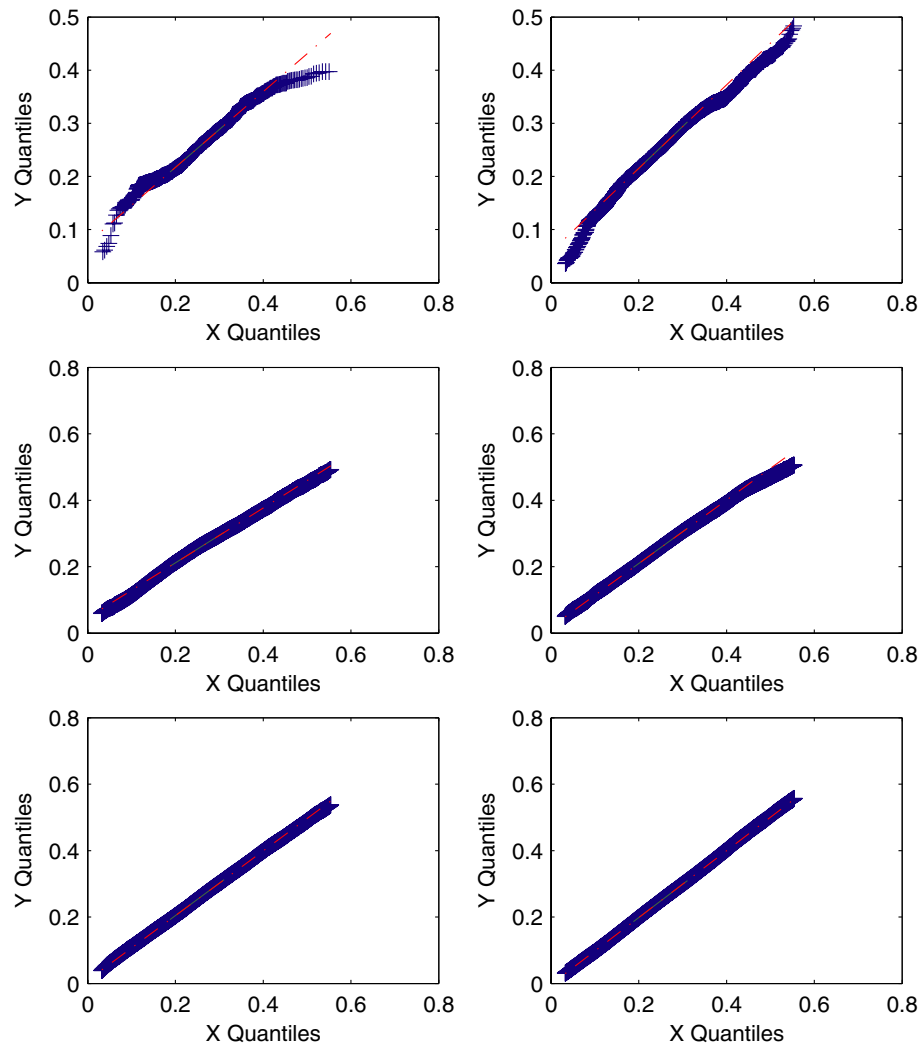


Fig. 10. QQ-plots of ϵ_{22} in the matrix for $\delta = 4, 8, 20, 30, 50$ and 75 (left to right, top to bottom).

Since the mean value of the stress and strain is allowed to have some variation, the coefficient of variation can be used to analyze the standard deviation independently of the mean. The plots of the coefficient of variation of σ_{22} and ε_{22} for the fibre, the matrix and the composite for each SRVE candidate are shown in Fig. 9.

If the biggest SRVE candidate ($\delta = 100$) is considered to have the same statistics of the whole population, the error can be computed with respect to the value obtained for this SRVE. Results show that the relative error is lower than 10% for $\delta \geq 50$.

8. Probability density functions of stress and strain fields in the matrix

Most of the failure criteria for the composite transverse direction consider that the failure is caused by cracks in the matrix [13,41]. One of the objectives of this work is to find

probability distribution functions for the failure in the transverse direction. For this reason, when trying to develop a statistical representative volume element, the stress and strain probability distribution functions in the matrix have to be analyzed.

The probability distribution function for ε_{22} in the matrix is obtained for all the SRVE candidates. For small SRVE sizes the distributions seem to be nearly symmetric, but from $\delta = 25$ this tendency disappears and distributions have a right tail longer than the left tail. One should note the importance of well reproducing the distributions tails, since the failure of the composite will be related to the values which are in these tails. It is important to notice, that a random model of the composite will reproduce in a more realistic way these tails than classical periodic models do [16]. This fact provides random models of the capacity of determining the failure of the composite more accurately.

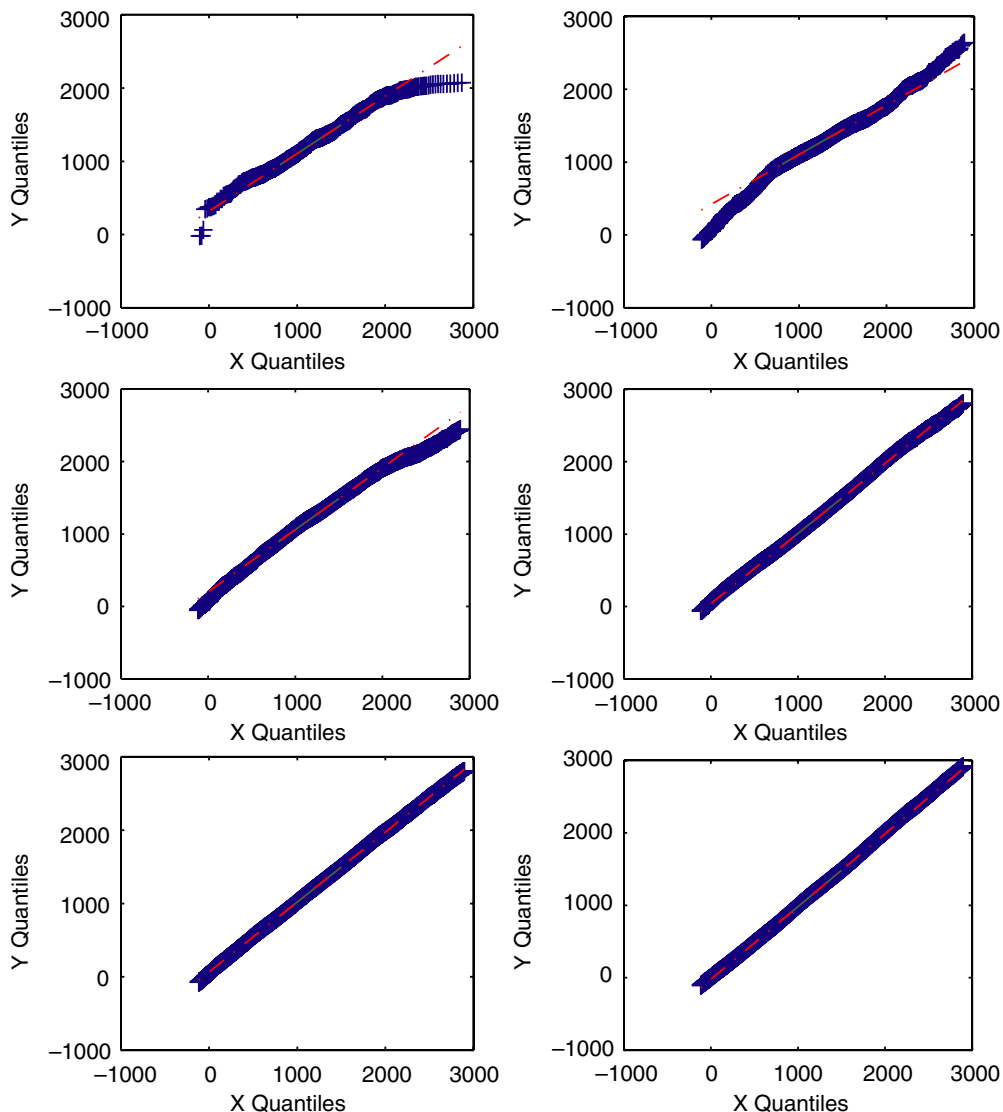


Fig. 11. QQ-plots of σ_{22} in the matrix for $\delta = 4, 8, 15, 25, 50$ and 5 (left to right, top to bottom).

The same results are obtained for the probability density function of σ_{22} in the matrix.

The similitude between two probability distributions can be observed with a QQ-plot. In this plot, if the distributions are equivalent the plot shows a line with slope 1. Fig. 10 shows QQ-plots for ε_{22} in the matrix and Fig. 11 shows QQ-plots for σ_{22} in the matrix. From these figures, the distribution function obtained in each SRVE candidate is compared with the distribution function of the model with $\delta = 100$.

From all these plots it can be considered that the probability distribution of ε_{22} in the matrix for the model $\delta = 20$ is equivalent to that corresponding to the model $\delta = 100$. Regarding σ_{22} the analogous conclusion can be derived for $\delta = 25$.

9. Distance distributions

The clustering or homogeneity of fibre (particle) distribution may affect strongly the damage behavior of a composite [42]. Moreover, the random distribution of fibres within the composite gives place to different statistical stress and strain distributions than an ideal periodical distribution of fibres [16]. For this reason, the SRVE has to represent the real statistical distance distribution of the fibres in the bulk material. As described in Section 2, a useful way to analyze inclusions or fibres within a matrix is to use the second-order intensity function and the pair distribution function. In the following, these functions, together with the nearest neighbor distance functions, for the different SRVE candidates are analyzed.

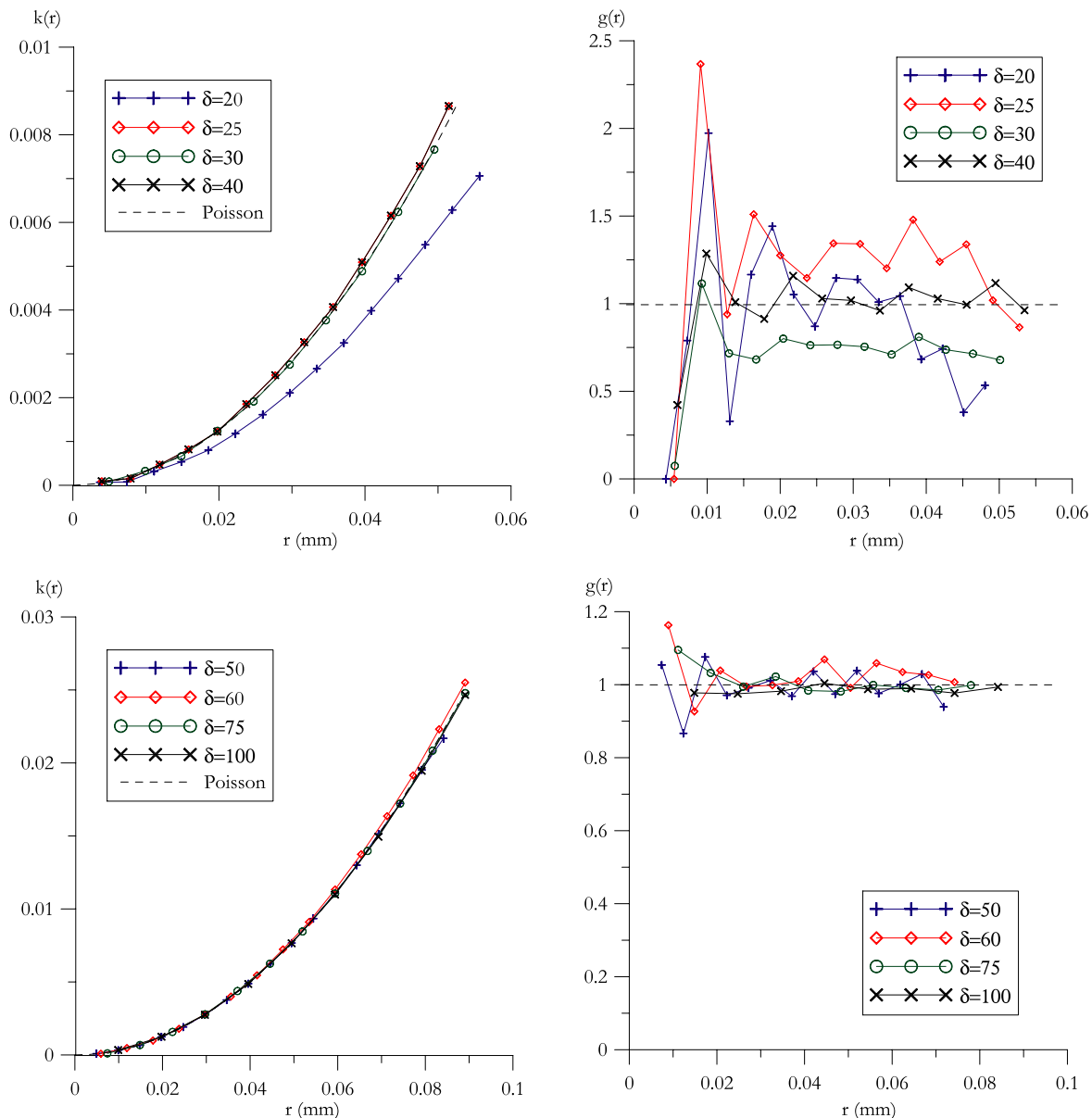


Fig. 12. Second-order intensity function and pair distribution function for the SRVE candidates.

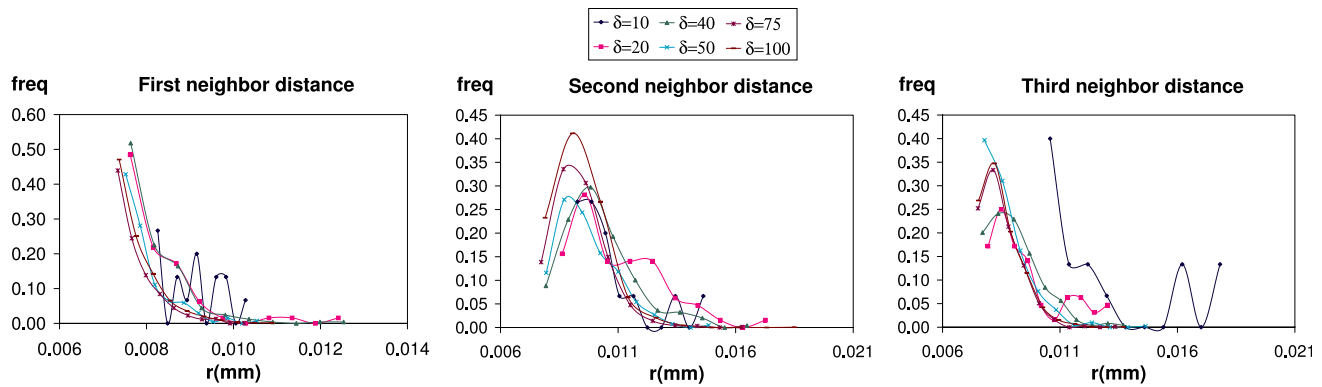


Fig. 13. Neighbor distance functions for $\delta = 10, 20, 40, 50, 75, 100$.

9.1. Second-order intensity function

The second-order intensity function $K(r)$ (Eq. (3)) can be seen as the expected number of fibres to be found inside a circle of radius r , divided by the Poisson parameter, λ . For the SRVE candidates corresponding to $\delta = 4$ to $\delta = 8$, $K(r)$ is not computable with the estimator of Eq. (3). Fig. 12 shows the second-order intensity function for $\delta = 15$ –25, $\delta = 30$ –50, and $\delta = 60$ –100. Besides that, this figure includes a plot of $K(r)$ corresponding to a random pattern (that is, a Poisson process). Results show that when δ grows $K(r)$ tends to that of the random process.

It is also important to notice that $K(r)$ tends to be linear. That means, from a certain value of r the expected number of fibres to be found is proportional to the sampling area.

9.2. Pair distribution function

Recalling Eq. (5), the pair distribution function is a function of the derivative of $K(r)$, and consequently, can be easily computed by numerical differentiation. Fig. 12 shows the estimated pair distribution function for each SRVE candidate. The plots in Fig. 12 also show this function for a Poisson process (for which $g(r) = 1$).

The employed estimator of $K(r)$ counts the number of fibres which are within a circle of radius r with center in a fibre. Since all the sampling points are fibre centers the derivative of $K(r)$ is overestimated for the lower values of r . For this reason most of the plots show peaks for the lower values of r .

For $\delta = 8$, $\delta = 10$ and $\delta = 15$, $g(r)$ does not converge to any constant value since the number of fibres in these models is not large enough. For $\delta = 20$ the pair distribution function shows large fluctuations around a constant value. For $\delta = 25$ and $\delta = 30$ $g(r)$, seem to converge but for a higher (in the case of $\delta = 25$) and for a lower value (for $\delta = 30$) to that of a CSR pattern. For the SRVE candidates with $\delta \geq 40$ it can be considered that $g(r)$ is equivalent to a Poisson process.

9.3. Neighbor distances

As described before, nearest neighbor distances provide information about the short-range interaction between particles. It is important for the SRVE to reproduce the short-range interaction between fibres of the bulk composite because this may have strong influence in the failure properties of the material. In Fig. 13, plots for the first, second and third nearest neighbor probability distribution function are given. Those plots corresponding to small values of δ ($\delta = 4, 6, 8$) show some peaks which may lead to the wrong conclusion of presence of some regularity. However, these peaks are due to the small number of fibres present in those models, more than to regularity. Those plots corresponding to $\delta = 10, 15, 20, 25$ and 30 show nearest neighbor distributions which are still not smooth enough. For $\delta \geq 40$ the nearest neighbor functions show typical shapes of random point patterns.

10. Concluding remarks

This paper has reviewed the criteria which can be used to define the minimal required size for a SRVE. The SRVE defined this way reproduces the mechanical and the statistical behavior of the material. The criteria which have been analyzed are: the effective properties, the Hill condition, the mean and the variance of the stress and strain components in the fibre, the matrix and the composite, the probability density function of the stress and strain components in the matrix and the typical inter-fibre distance distributions (second-order intensity function or Riley's K -function, pair distribution function and nearest neighbor distances).

Each of these criteria has a minimum model size (δ) which satisfies it and, consequently, the largest of these δ values defines the minimal size for a valid statistical representative volume element. Table 1 summarizes the results obtained for each criteria.

According to the obtained results, the most demanding criteria are the coefficient of variation (for which $\delta \geq 50$) and the statistical functions of the distances between fibres (for which $\delta \geq 40$). Then, for the analyzed material, a

Table 1
Summary of analyzed criteria and results

Criteria	Description	Result
Effective properties	Percentual difference lower than 10%	$\delta \geq 30$
Hill condition	Difference between energy bounds lower than 5%	$\delta \geq 15$
Strain field	Hypothesis test for the mean	$\delta \geq 15$
	Hypothesis test for the variance	$\delta \geq 25$
	Coefficient of correlation	$\delta \geq 50$
	Percentual difference	
Stress field	Hypothesis test for the mean	$\delta \geq 10$
	Hypothesis test for the variance	$\delta \geq 25$
	Coefficient of correlation	$\delta \geq 50$
	Percentual difference	
Strain in matrix pdf	Similarity of probability density functions	$\delta \geq 30$
Stress in matrix pdf	Similarity of probability density functions	$\delta \geq 25$
Distance distributions	Comparison with Poisson process	$\delta \geq 40$

carbon fibre reinforced epoxy, the minimal size of a SRVE is $\delta = 50$. This result is valid for other composite materials having similar mismatch. The most demanding criteria should be computed again for materials with sensibly different values of the contrast.

However, it is important to notice that the criteria that the RVE or SRVE must satisfy are defined in terms of the application. The simulation of the mean value of the effective properties may require only the analysis of the effective properties themselves and the Hill condition; the probabilistic simulation of these effective properties may require, additionally, the analysis of the main statistics of stress and strain; the probabilistic simulation of the elastic failure requires additionally the analysis of the probability density function of stress and strain; and the simulation of non-linear phenomena, probabilistic damage and effects of clustering, all of the above criteria and the analysis of the statistical functions which describe the inter-fibre distance ($K(r)$, $g(r)$ and the nearest neighbor distances).

Acknowledgements

This work has been enriched by some discussions at the Congress “Micromechanics and Microstructure Evolution: Modeling, Simulation and Experiments” held in Madrid, specially those by professor Helmut Böhm.

The present work has been partially funded by the Spanish Government under research project MAT2003-09768-C03-001. The first author express gratitude to the University of Girona for research Grant BRAE00/02.

References

- [1] Soden P, Hinton MJ, Kaddour AS. A comparison of the predictive capabilities of current failure theories for composite laminates. *Compos Sci Technol* 1998;58(7):1225–54.
- [2] Car E, Zalamea F, Oller S, Miquel J, Oñate E. Numerical simulation of composite materials: two procedures. *Inter J Solid Struct* 2002;39(7):1967–86.
- [3] Feyel F. A multilevel finite element method (FE²) to describe the response of highly non-linear structures using generalized continua. *Comput Meth Appl Mech Eng* 2003;192(28–30):3233–44.
- [4] Matsuda T, Ohno N, Tanaka H, Shimizu T. Effects of fibre distribution on elastic–viscoplastic behavior of long fibre-reinforced laminates. *Int J Mech Sci* 2003;45:1583–98.
- [5] Adolfsson E, Gudmundson P. Matrix crack initiation and progression in composite laminates subjected to bending and extension. *Inter J Solid Struct* 1999;36:3131–69.
- [6] Li S. Modeling of the characteristics of fiber-reinforced composite materials damaged by matrix-cracking. *Compos Sci Technol* 1992;43(2):185–95.
- [7] Henaff-Gardin C, Lafarie-Frenot M, Gamby D. Doubly periodic cracking in composite laminates: Part I. General in-plane loading. *Compos Struct* 1996;36:113–30.
- [8] Caron JF, Ehrlacher A. Modelling of fatigue microcracking kinetics in crossply composites and experimental validation. *Compos Sci Technol* 1999;59:1349–59.
- [9] Ogihara S, Takeda N. Interaction between transverse cracks and delamination during damage in cfrp cross-ply laminates. *Compos Sci Technol* 1995;54:395–404.
- [10] Gamstedt EK, Sjögren BA. Micromechanics in tension–compression fatigue of composite laminates containing transverse plies. *Compos Sci Technol* 1999;59:167–78.
- [11] Asp LE, Berglund LA, Gudmundson P. Effects of a composite-like stress state on the fracture epoxies. *Compos Sci Technol* 1995;53(1):27–37.
- [12] Asp LE, Berglund LA, Talreja R. Effects of fibre and interphase on matrix-initiated transverse failure in polymer composites. *Compos Sci Technol* 1996;56(6):657–65.
- [13] Asp LE, Berglund LA, Talreja R. Prediction of matrix-initiated transverse failure in polymer composites. *Compos Sci Technol* 1996;56(9):1089–97.
- [14] Asp LE, Berglund LA, Talreja R. A criterion for crack initiation in glassy polymers subjected to a composite-like stress state. *Compos Sci Technol* 1996;56(11):1291–301.
- [15] Fiedler B, Hojo M, Ochiai S, Schulte K, Ochi M. Finite-element modeling of initial matrix failure in cfrp under static transverse tensile load. *Compos Sci Technol* 2001;61(1):95–105.
- [16] Trias D. Analysis and simulation of transverse random fracture of long fibre reinforced composites. Ph.D. Thesis, Departament d’Enginyeria Mecànica i de la Construcció Industrial, Universitat de Girona; 2005.
- [17] Hill R. Elastic properties of reinforced solids: some theoretical principles. *J Mech Phys Solid* 1963;11:357–72.
- [18] Drugan WJ, Willis JR. A micromechanics-based nonlocal constitutive equation and estimates of representative volume element size for elastic composites. *J Mech Phys Solid* 1996;44(4):497–524.
- [19] Gusev AA. Representative volume element size for elastic composites: a numerical study. *J Mech Phys Solid* 1997;45(9):1449–59.
- [20] Terada K, Hori M, Kyoya T, Kikuchi N. Simulation of the multi-scale convergence in computational homogenization approaches. *Inter J Solid Struct* 2000;37(16):2285–311.
- [21] Kanit T, Forest S, Galliet I, Mounory V, Jeulin D. Determination of the size of the representative volume element for random composites: statistical and numerical approach. *Inter J Solid Struct* 2003;40:3647–79.
- [22] Kröner E. Statistical continuum mechanics. Berlin: Springer; 1972.
- [23] Hazanov S. Hill condition and overall properties of composites. *Arch Appl Mech* 1998;68:385–94.
- [24] Ostoja-Starzewski M. Random field models of heterogeneous materials. *Inter J Solid Struct* 1998;35(19):2429–55.
- [25] Ostoja-Starzewski M, Wang X. Stochastic finite element as a bridge between random material microstructure and global response. *Comput Meth Appl Mech Eng* 1999;168:35–49.

- [26] Byström J. Influence of inclusions distribution on the effective properties of heterogeneous media. *Composites B* 2003;34(7):587–92.
- [27] Pyrz R. Correlation of microstructure variability and local stress field in two-phase materials. *Mater Sci Eng A* 1994;177:253–9.
- [28] Ripley B. The second-order analysis of stationary point processes. *J Appl Probab* 1976;13:255–66.
- [29] Mucharreira de Azeredo Lopes, S. Statistical analysis of particle distributions in composite materials. Ph.D. Thesis, University of Sheffield. Department of Probability and Statistics; 2000.
- [30] Ohser J, Mücklich F. Statistical analysis of microstructures in materials science. *Statistics in practice*. New York: Wiley; 2000.
- [31] Sobczyk K, Kirkner DJ. Stochastic modeling of microstructures. Modeling and simulation in science, engineering and technology. Basel: Birkhäuser; 2001.
- [32] Pyrz R. Quantitative description of the microstructure of composites. Part 1: morphology of unidirectional composite systems. *Compos Sci Technol* 1994;50(2):197–208.
- [33] Povirk GL. Incorporation of microstructural information into models of two-phase materials. *Acta Metall Mater* 1995;43(8):3199–206.
- [34] Zeman J, Sejnoha M. Numerical evaluation of effective elastic properties of graphite fibre tow impregnated by polymer matrix. *J Mech Phys Solid* 2001;49(1):69–90.
- [35] Shan Z, Gokhale AM. Representative volume element for non-uniform micro-structure. *Comput Mater Sci* 2002;24:361–79.
- [36] Alzebdeh K, Al-Ostaz A, Jasiuk I, Ostoj-Starzewski M. Fracture of random matrix-inclusion composites: scale effects and statistics. *Inter J Solid Struct* 1998;35(19):2537–66.
- [37] Brockenborough J, Suresh S, Wienecke H. Deformation of metal–matrix composites with continuous fibres: geometrical effects of fibre distribution and shape. *Acta Metall Mater* 1991;39(5):735–52.
- [38] Halpin JC, Tsai SW. Environmental factors in composite materials design, Technical Report AFML TR 67-423. US Air Force; 1967.
- [39] Box GEP, Hunter W, Hunter JS. Statistics for experimenters: an introduction to design data analysis and model building. New York: Wiley; 1978.
- [40] Montgomery D. Design and analysis of experiments. New York: - Wiley; 2001.
- [41] Puck A, Schürman H. Failure analysis of FRP laminates by means of physically based phenomenological models. *Compos Sci Technol* 1998;58:1045–67.
- [42] Segurado J, González C, Llorca J. A numerical investigation of the effect of particle clustering on the mechanical properties of composites. *Acta Mater* 2003;51(8):2355–69.

Multiscale modeling of materials by a multifield approach: Microscopic stress and strain distribution in fiber–matrix composites ☆

Vittorio Sansalone ^{a,*}, Patrizia Trovalusci ^b, Fabrizio Cleri ^a

^a *Ente Nuove Tecnologie, Energia e Ambiente, Unità Materiali e Nuove Tecnologie, Centro Ricerche Casaccia, CP 2400, 00100 Roma AD, Italy*

^b *Dipartimento di Ingegneria Strutturale e Geotecnica, Università La Sapienza, via Gramsci 53, 00197 Roma, Italy*

Received 28 October 2005; accepted 23 March 2006

Available online 14 June 2006

Abstract

A recently developed multiscale, multifield model is used to study the elastic response of a fiber-reinforced polymer composite material under different loading conditions. The multifield model is based on the theory of microstructured continua, and allows the introduction of microstructural variables (in this case the local microfiber orientation) within a standard continuum model. The numerical solution is implemented in a finite element approach. By simulated loading tests on a model system, we show that the multifield model goes well beyond the conventional anisotropic Cauchy solution, and can effectively incorporate the dependence of the elastic response on (i) an internal length scale, representing the actual fiber length, and (ii) the local fiber orientation.

© 2006 Acta Materialia Inc. Published by Elsevier Ltd. All rights reserved.

Keywords: Fiber-reinforced composites; Micromechanical modeling; Stress distribution; Elastic behavior

1. Introduction

Recent years have witnessed an increasing interest in the derivation of macroscopic mechanical properties of heterogeneous materials by multiscale and multilevel computational methods. Indeed, the demand for high-performance structural materials in several fields of engineering and technology has spurred research in the field of complex, composite materials, such as polyphase metallic alloy systems, polymer blends, polycrystalline, porous or textured media, fiber–matrix composites, and biocomposite materials [1,2]. In all such cases the improved materials properties are dictated by a complex internal microstructure, going beyond the elastic and mechanical properties of the bare components. The ability to design such materials and to derive their macroscopic properties relies, in

turn, on the ability to take into account the (possibly evolving) internal structure, size, shape, and spatial distribution of the microstructural constituents which can span several orders of magnitude in length, starting from the submicrometer scale. For example, the combined effect of thermal residual stresses and fiber packing on deformation of metal–matrix composites was studied in direct numerical simulations encompassing a huge number of degrees of freedom [3]. The role of local stresses can be so important, for example in active-fiber composites [4], to require a very fine meshing of the whole microstructure, in order to describe explicitly the fully three-dimensional structure of the fibers embedded in the matrix, thereby leading to nearly intractable computational problems.

In order to avoid a direct, “brute force” discretization of the microstructure, several homogenization methods have been introduced to deal with such a multiscale phenomenology (for a review, see Ref. [2]), starting from the early effective-medium approximation of Eshelby [5], to the variational bounding methods [6], to asymptotic homogenization [7]. While such methods, based on the standard Cauchy continua, have been quite successful in describing the

☆ This manuscript was presented at the “Micromechanics and Microstructure Evolution: Modeling, Simulation and Experiments” held in Madrid/Spain, September 11–16, 2005.

* Corresponding author.

E-mail address: vittorio.sansalone@devinci.fr (V. Sansalone).

global response of nonlinear composite materials with nearly periodic microstructures, as well as random polycrystalline materials [8], two major disadvantages of such “conventional” homogenization methods must be highlighted [9]. First, they cannot predict the effect of the size, shape, and orientation of the heterogeneities, since they deal with only the volume fraction and, in some cases, the morphology of the heterophase distribution. Second, they constrain any microscopic feature to be homothetic to the macroscopic deformation, which is likely to be inappropriate in critical regions of high gradients, e.g., in the vicinity of a macroscopic discontinuity such as a joint or a hole, or close to the point of application of a localized load.

Several models have tried to overcome such difficulties by introducing generalized continuum descriptions, e.g., Cosserat, couple stress, strain gradient, or nonlocal models [9–14]. In the present work we use a recently developed multiscale simulation approach [13,16] based on the theory of microstructured continua [17] to describe the distribution of microscopic stresses in a fiber-composite material, thereby providing a comparatively more accurate description of the microstructure with respect to conventional homogenization, and moreover at a reduced computational cost. For this purpose, we make use of a version of our multifield model focusing on the essential ingredient of local rotations, representing the change in orientation of the fibers in each volume element by means of a properly defined microstructural field [13]. The function of such an additional field is effectively to smear the microscopic heterogeneities (fibers) in the macroscopic continuum, allowing at the same time the introduction of a material length scale (the size of the fibers with respect to the leading dimension of the macroscopic system, as well as their orientation), besides the fiber density and aspect ratio already present in the conventional Cauchy continuum.

The paper is organized as follows. In Section 2 we give a brief summary of our multifield methodology (which is deployed in practice by a highly modular, custom-developed, finite element (FE) code, MUSCAFE, written in object-oriented C++ [16]). In Section 3 we present some results of microstructural modeling for a macroscopic truss, under simple traction loading, shear loading, and four-point bending. Without loss of generality, we make reference to a specific class of polymer-matrix fiber composites, such as epoxy/glass, to show that the model is able to capture the features of the elastic energy and microscopic stress distribution, as a function of fiber size and orientation. Finally, in Section 4 we draw some conclusions from our work.

2. Computational model

In the following we give a brief account of our multifield computational approach, already presented in great details in Refs. [15,16]. With respect to the formulation presented in those papers, in which the coupling between two scalar

microstructural fields was studied as an example, here we will focus on a single microstructural field, representing the local orientation of the fibers dispersed in the matrix.

The continuum model of a generalized homogeneous material (macromodel) is built up based on the kinematics of a discrete lattice model (micromodel) of the kind proposed in Refs. [13,15]. At the microscopic level a composite material is characterized by a given density and distribution of fibers much stiffer than the matrix in which they are embedded. If the material microstructure is periodic, or at least statistically homogeneous, a representative volume element (from here on referred as a module) can be defined. In the present work, the module describes the fibers arranged in a regular lattice, connected in pairs by linear elastic bonds (Fig. 1). For simplicity, we assumed a rhombic texture with bonds lying parallel to the Cartesian directions. Note that, since the fibers must overlap to be connected, such an arrangement will limit the geometrical density of the fibers to relatively small volume fractions for a given aspect ratio. However, this is not a limitation of our approach, since, with an appropriate geometry of the module, any value of density and texture can be simulated.

The procedure governing the scale transition between the micromodel and the macromodel is based on two key assumptions:

- (i) macroscopic homogeneous deformations are imposed to the module;
- (ii) the volume average of the strain energy of the module is posed equal to the strain energy density on the neighborhood of the macromodel.

Such assumptions are standard in the classic molecular theory of elasticity (e.g., Ref. [18]). In particular, the latter corresponds to the energy-averaging theorem known in the literature as the Hill–Mandel condition [19]. In such a

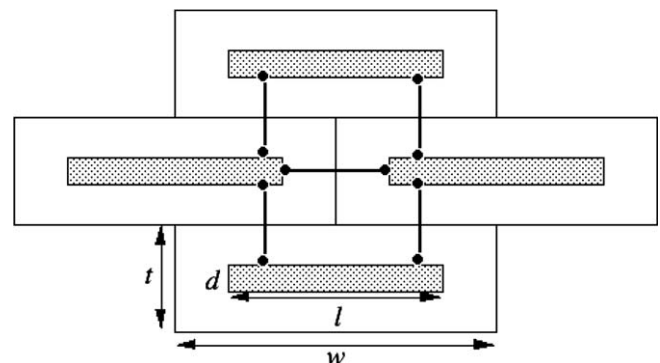


Fig. 1. Schematic of the module. The fiber is represented by the shaded area of size dl . The embedding volume, or block, of size wt , is the smallest unit explicitly represented by its center of mass. Each module contains four blocks and five bonds, and fills the entire space by periodic translation. The chosen arrangement for the five linear-elastic bonds corresponds to an orthotropic material.

manner a formula for the stored energy function (or elastic potential energy) of the macromodel can be written in terms of the continuum kinematical fields, and the macroscopic stress measures can be derived [15].

Briefly, the linearized strain measures of the module are: (1) the relative displacement between two fibers A and B placed at the positions \mathbf{a} and \mathbf{b} , represented by the vector $\mathbf{u}_i = \mathbf{u}^a - \mathbf{u}^b + \mathbf{W}^a(\mathbf{p}^a - \mathbf{a}) - \mathbf{W}^b(\mathbf{p}^b - \mathbf{b})$, where \mathbf{W}^a (\mathbf{W}^b) is the rotation of fiber A (B) and \mathbf{p}^a (\mathbf{p}^b) is a point on A (B) of the bond connecting the two fibers; (2) the relative rotation between A and B, represented by the skew-symmetric tensor $\mathbf{W}^a - \mathbf{W}^b$. In this framework, the module undergoes a homogeneous deformation if:

$$\begin{aligned} \mathbf{u}^a &= \mathbf{u}(\mathbf{x}) + \nabla \mathbf{u}(\mathbf{x}) [\mathbf{a} - \mathbf{x}] \\ \mathbf{W}^a &= \mathbf{W}(\mathbf{x}) + \nabla \mathbf{W}(\mathbf{x}) [\mathbf{a} - \mathbf{x}] \end{aligned} \quad (1)$$

where \mathbf{u} and \mathbf{W} are regular fields defined on the current configuration of the continuum, and \mathbf{x} is the center of the continuum neighborhood; \mathbf{u} is the standard displacement vector and \mathbf{W} is a skew-symmetric tensor describing the local rotation of the fibers.

The generalized forces associated with the above kinematical quantities are the force and the couple between A and B, represented by the vector \mathbf{t}^{ab} and the skew-symmetric tensor \mathbf{C}^{ab} , respectively [13]. The strain energy of a module of volume V is

$$\varepsilon = \frac{1}{V} \frac{1}{2} \sum_{ab} \left\{ \mathbf{t}^{ab} \cdot [\mathbf{u}_i - \mathbf{W}^b(\mathbf{p}^a - \mathbf{p}^b)] + \frac{1}{2} \mathbf{C}^{ab} \cdot (\mathbf{W}^a - \mathbf{W}^b) \right\} \quad (2)$$

Then, we substitute Eq. (1) for the unknown fields, and the linear-elastic laws of Ref. [15] for \mathbf{t}^{ab} and \mathbf{C}^{ab} . Finally, by using the energy equivalence principle (ii) above, obtain the energy density of the continuum as

$$E = \frac{1}{2} \left\{ \mathbf{S} \cdot (\nabla \mathbf{u} - \mathbf{W}) + \frac{1}{2} \mathbf{S} \cdot \nabla \mathbf{W} \right\} \quad (3)$$

where

$$\begin{aligned} \mathbf{S} &= \mathbf{A}(\nabla \mathbf{u} - \mathbf{W}) + \mathbf{B} \nabla \mathbf{W} \\ \mathbf{S} &= \mathbf{C}(\nabla \mathbf{u} - \mathbf{W}) + \mathbf{D} \nabla \mathbf{W} \end{aligned} \quad (4)$$

\mathbf{A} , \mathbf{B} , \mathbf{C} , and \mathbf{D} are constitutive tensors of order four, five, five, and six, respectively. The quantities \mathbf{S} and \mathbf{S} are generalized stress fields, the former being a generalization of the ordinary Cauchy stress tensor, and the latter the couple-stress tensor.

Eq. (4) is the constitutive equation for the multifield continuum model. The components of \mathbf{A} to \mathbf{D} depend on the elastic constants of the matrix/fibers and, moreover, on the shape and arrangement of the fibers and bonds in the module, as depicted in Fig. 1. Moreover, the components of \mathbf{B} to \mathbf{D} depend also on the fiber size. It can be shown [13] that $\mathbf{C} = \mathbf{B}^T$ and that, moreover, the tensor \mathbf{B} is null by the requirement of centrosymmetry. In practice, with regard to an isotropic matrix and the module arrange-

ment of Fig. 1, it is found that the only nonzero matrix elements of \mathbf{A} and \mathbf{D} are:

$$\begin{aligned} A_{1111} &= E\mu\rho & A_{2222} &= 2E \\ A_{1212} &= 2E\mu & A_{2121} &= E\mu \frac{\rho}{2} \\ D_{1212121} &= E \left(\frac{\mu}{2} + \frac{\rho^2}{16} \right) w^2 & D_{122122} &= E \left(\frac{1}{4} + \frac{2\mu}{\rho^3} \right) w^2 \end{aligned} \quad (5)$$

where $\mu = G/E$ and $\rho = w/t$ is the aspect ratio, with w the length and t the thickness of the block embedding the fiber (see Fig. 1). The local fiber orientation within each module is specified by a rotation of the \mathbf{A} and \mathbf{D} tensors by an angle φ . Note that in the elements of the \mathbf{D} tensor the square of the length parameter w appears explicitly, thereby endowing the multifield model with an intrinsic length-scale dependence, while the elements of \mathbf{A} , as pointed out above, have no such dependence.

By setting $\mathbf{D} = 0$ and $\mathbf{W} = \text{skw}(\nabla \mathbf{u})$ in Eqs. (3) and (4), the so-called “anisotropic Cauchy” (a-C) model is obtained [13]. Such a model can, indeed, describe the fiber orientation but the local deformation would be always homothetic to the global deformation, i.e., no local rotation of the fibers can be elucidated in the a-C model.

E and G are the effective elastic moduli of the bonds connecting the fibers. In general, they should represent a proper average of the matrix and fiber elastic moduli, eventually modified by the interfacial adhesion between matrix and fiber. A generally accepted formula for the lower bound to such an average is $E = E_f E_m / (E_f v_m + E_m v_f)$ (see, e.g., Ref. [20]). However, since we are considering materials with $E_f \gg E_m$ and, moreover, our choice for the module geometry is limited to relatively small fiber density, $v_f \leq 0.05$, we can safely retain $E \equiv E_m$ and $G \equiv G_m$.

3. Results

We will now employ the MUSCAFE code [16], which translates the model of Section 2 into a highly efficient, two-dimensional FE computational approach, to obtain some results on the elastic properties of model fiber-reinforced composites. We assume infinitely rigid, brittle fibers embedded in a ductile, tough, elastic matrix. Therefore, as already mentioned, the only numerical parameters appearing in the model will be the elastic moduli of the matrix, E and G , which will be, however, effectively coupled by the presence of the fibers, under the different loading conditions. A typical composite material to which such modeling applies could be a thermoset polymer matrix, such as epoxy resin, reinforced with short fibers, e.g., glass [21]. Such a kind of composites is widely adopted in a variety of technological applications, e.g., appliance frames and covers, packaging, impact shielding, and so on, with fiber volume proportions usually ranging from 1% to 50%. However, in the purely elastic regime, and up to the limit of an ideal adhesion between matrix and fibers, the same microstructural modeling may also apply to a brittle matrix, e.g., ceramic matrix composites.

In particular, thermoset polymers have covalent bonds linking the polymer chains in three dimensions. These links prevent the chains from sliding past one another resulting in a higher modulus and improved creep resistance. The polymer chains in thermosets are below their glass transition point at room temperature, making the material glassy. Therefore, the matrix can be assumed as elastically isotropic, i.e., characterized by the two single moduli E and G . As a reference material we will adopt the experimental values of $E = 3.5$ GPa and $G/E = 0.4$, common to epoxy and polyester. Both such thermosets have an experimental value of Poisson's ratio of $\nu = 0.25$, i.e., identical to the value $\nu_{\text{iso}} = E/2G - 1 = 0.25$ corresponding to an ideally isotropic material. Due to the scaling of Eq. (5) with respect to E , the same results illustrated below should also hold qualitatively similar for a range of commercial polymers, going from $E = 2.7$ GPa (corresponding to polycarbonate) to $E \sim 1.5\text{--}0.7$ GPa (rigid PVC, polypropylene, high-density polyethylene), the experimental G/E ratio for such plastics being in all cases around 0.4–0.45, with the only exception being polycarbonate for which $G/E = 0.36$. However, it should be noted that the Poisson ratio for such materials may be away from the isotropic value, the closest one being polycarbonate with a difference of -6% between the experimental ν and the theoretical isotropic value. Concerning the fibers, we have $E = 71$ GPa for the E-type glass usually employed in fiber reinforcement, giving a lower bound of 3.65 GPa for the average Young's modulus at $v_f = 0.05$ volume fraction. This is only 4% different from the bare matrix value, thus confirming the validity of our approximation.

Our two-dimensional reference system, shown in Fig. 2, is a truss of length L (parallel to the x Cartesian axis) and height $H = L/10$ (parallel to the y Cartesian axis), in plane-strain, constant-force loading condition. The system is discretized with a FE triangular mesh. Each mesh element may include several modules of the type described in Fig. 1, thereby implicitly describing a group of individual

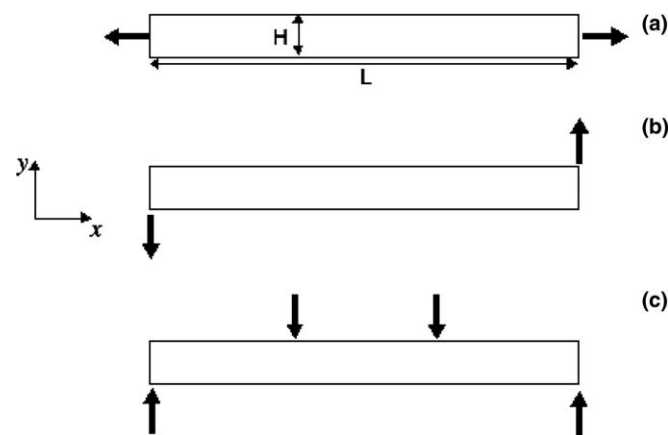


Fig. 2. Schematic of the simulated system, a truss of length L and height $H = L/10$. The system is discretized into a FE mesh. Each FE includes several modules (see Fig. 1). Loading modes: (a) traction test, (b) shear test, (c) four-point bending test.

fibers with the same local orientation. Three types of simulated loading tests will be considered: (1) traction, represented by a symmetric tensile loading at both ends of the truss (Fig. 2(a)); (2) shear, represented by two equal and opposite loadings at the two ends of the truss (Fig. 2(b)); (3) four-point bending, represented by two point loads applied on the top side, at a distance $L/3$ and $2L/3$ along the truss, while the two ends are held fixed at the bottom side (Fig. 2(c)). In all cases, the applied force is such that the maximum displacement is within 2–3%. All the results are presented as a function of the scale parameter $\lambda = w/L$, and of the fiber orientation φ , with $\varphi = 0$ indicating fibers parallel to the x -axis of the system, and $\varphi = \pi/2$ indicating fibers parallel to the y -axis.

In Fig. 3 we show the behavior of the energy density \mathcal{E} integrated over the whole system, as a function of the initial fiber orientation φ , at a fixed value of $\lambda = 4 \times 10^{-3}$. For each loading test the curves compare the multifield solution to the a-C solution. The \mathcal{E} values are scaled by the corresponding isotropic elasticity, φ -independent value. It can be seen that in each loading test the behavior of the multifield solution is close, or even equal, to the a-C, at $\varphi = 0$ and $\pi/2$. In contrast, very large differences are seen at any intermediate value, the maximum discrepancy always occurring around $\varphi = \pi/4$. In all cases, the multifield model appears to describe a less rigid composite than a corresponding a-C model, since the stored elastic energy is always higher under fixed forces.

The appearance of an intrinsic scale length in the multifield model is clearly demonstrated in Fig. 4, in which the integrated energy density \mathcal{E} is reported as a function of λ at constant aspect ratio, for $\varphi = 0, \pi/4, \pi/2$. The case

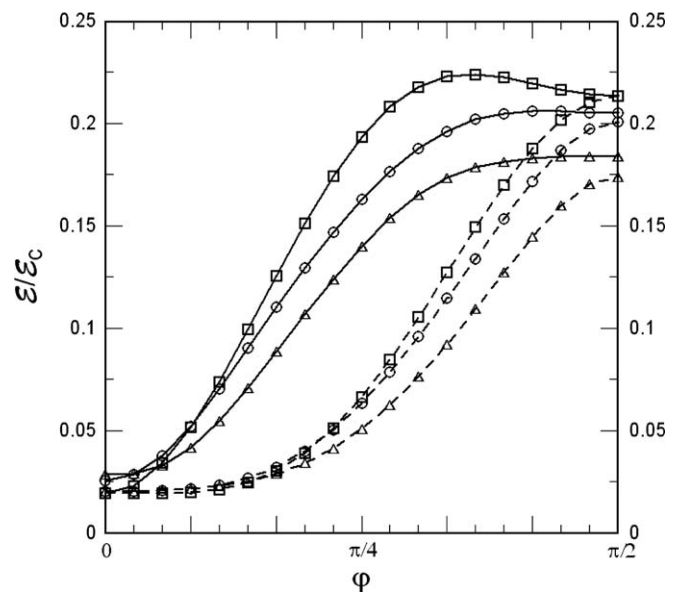


Fig. 3. Plot of the integrated energy density as a function of the initial fiber orientation φ , for $\lambda = 4 \times 10^{-3}$. Continuous curves: multifield model; dashed curves: anisotropic Cauchy model. Symbols: \square , traction test; \circ , four-point bending test; \triangle , shear test. Each curve is scaled by the value of the corresponding isotropic Cauchy model without fibers.

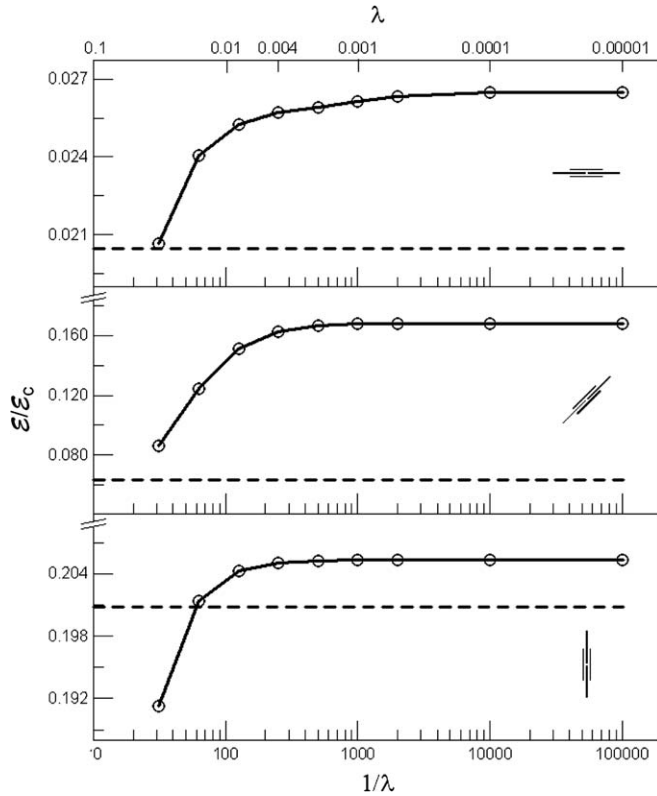


Fig. 4. Plot of the integrated energy density in the four-point bending test as a function of the scale length factor $\lambda = w/L$, for $\varphi = 0, \pi/4, \pi/2$. Continuous curves: multifield model; dashed curves: anisotropic Cauchy model.

shown is the four-point bending test, the shear test giving qualitatively similar curves. The traction test, conversely, would give no dependence of the results on λ since in that case $\nabla \mathbf{W} = \mathbf{0}$. In the figure, the a-C results are merely straight lines, since the a-C model is insensitive to the actual fiber length. Upon increasing λ , the effect of the fiber length dependence of the multifield model becomes more and more evident. By analogy with similar studies [13], we can speculate that the energy density curves would tend to drop below the a-C value, and should approach a different asymptotic value for $\lambda \rightarrow 1$. It should be noted, however, that our results at the largest values of λ may be affected by the size of the module approaching the mesh size.

The detailed analysis of the localization of the elastic response is a prominent feature of the multifield method allowing the extraction from the simulated loading experiments discussed above. By taking the four-point bending test at $\lambda = 4 \times 10^{-3}$ and $\varphi = 0, \pi/4$ and $\pi/2$ as an example, Fig. 5 shows the xy map of the energy density in a region around the point of application of the load. Once again, we compare the multifield and the a-C solutions with the aim of showing that, as anticipated in Section 1, the standard homogenized continuum treatment may fail badly in describing the rapid variation of stress and strain around a singularity. In fact, at $\varphi = \pi/4$ and $\pi/2$ the multifield solu-

tion displays much more pronounced energy maxima than the a-C case, moreover also decaying radially much faster, while the opposite is true at $\varphi = 0$.

The results of Figs. 3–5 demonstrate that the multifield model provides a qualitatively different response with respect to the a-C model. In view of the more approximate character of the latter, the multifield description should be regarded as preferable, even in the absence of a detailed comparison with a fully discretized FE solution which, for the above examples, would be computationally prohibitive.

An equal wealth of local information is available in the multifield model for all the various vector/tensor components of the displacement \mathbf{u} , rotation \mathbf{W} , and the \mathbf{S} and \mathbf{S} generalized stress fields. Using again the four-point bending test as an example, in Fig. 6 we plot the relative rotation $\mathbf{R} = \mathbf{W} - \text{skw}(\nabla \mathbf{u})$ (which in a two-dimensional frame has only one independent component, R) in the form of angular variation of the orientation of a stick, each stick representing the interpolated average of 2×2 mesh elements. The quantity R describes the actual physical rotation of the fibers, since it is obtained by subtracting from the field \mathbf{W} the macroscopic deformation corresponding to the applied load. It is instructive to compare the stick map superimposed to the energy density map, for the two cases of $\varphi = 0$ and $\pi/2$. As observed in Fig. 5, the elastic energy is localized around the points of loading, much more in the case $\varphi = 0$ than $\pi/2$. Such an increased localization can be easily understood by looking at the stick map, since the $\varphi = 0$ initial orientation of the fibers induces tangential stresses when paired with the couple stress (apparent from the “wiggles” in the stick orientation right below the loading point), whilst in the $\varphi = \pi/2$ orientation the fibers can more easily “glide” sideways in response to the torque. (One may think of the analogy with a deck of playing cards being pushed either on the flat side, $\varphi = 0$, or on the border, $\varphi = \pi/2$.) Moreover, it is very interesting to note that the two fiber orientations correspond to very different mechanisms of stress transfer between the four loading points: indeed, the “arching” effect from the center to the corners, extremely evident at $\varphi = 0$, appears to be completely hindered when the fibers are oriented at $\varphi = \pi/2$, a nontrivial result that warrants further, more detailed investigation. We stress once more that such local, independent rotations of the fibers would be impossible to describe in a conventional homogenized continuum model.

Another piece of relevant information that can also be extracted from our multifield model of a fiber-reinforced composite is the variation of the effective elastic moduli E^* and G^* as a function of, for example, fiber orientation. We use the traction and shear tests, respectively, to determine such effective values from the slope of the stress vs. displacement curve. In Figs. 7 and 8 we plot E^* , G^* as a function of φ and λ , respectively. It can be seen that both moduli are larger than the E , G values of the bare matrix, due to the presence of the fibers. As $\varphi \rightarrow 0$ and $\lambda \rightarrow 1$, the upper bound for E^* , G^* should be infinite since the fibers

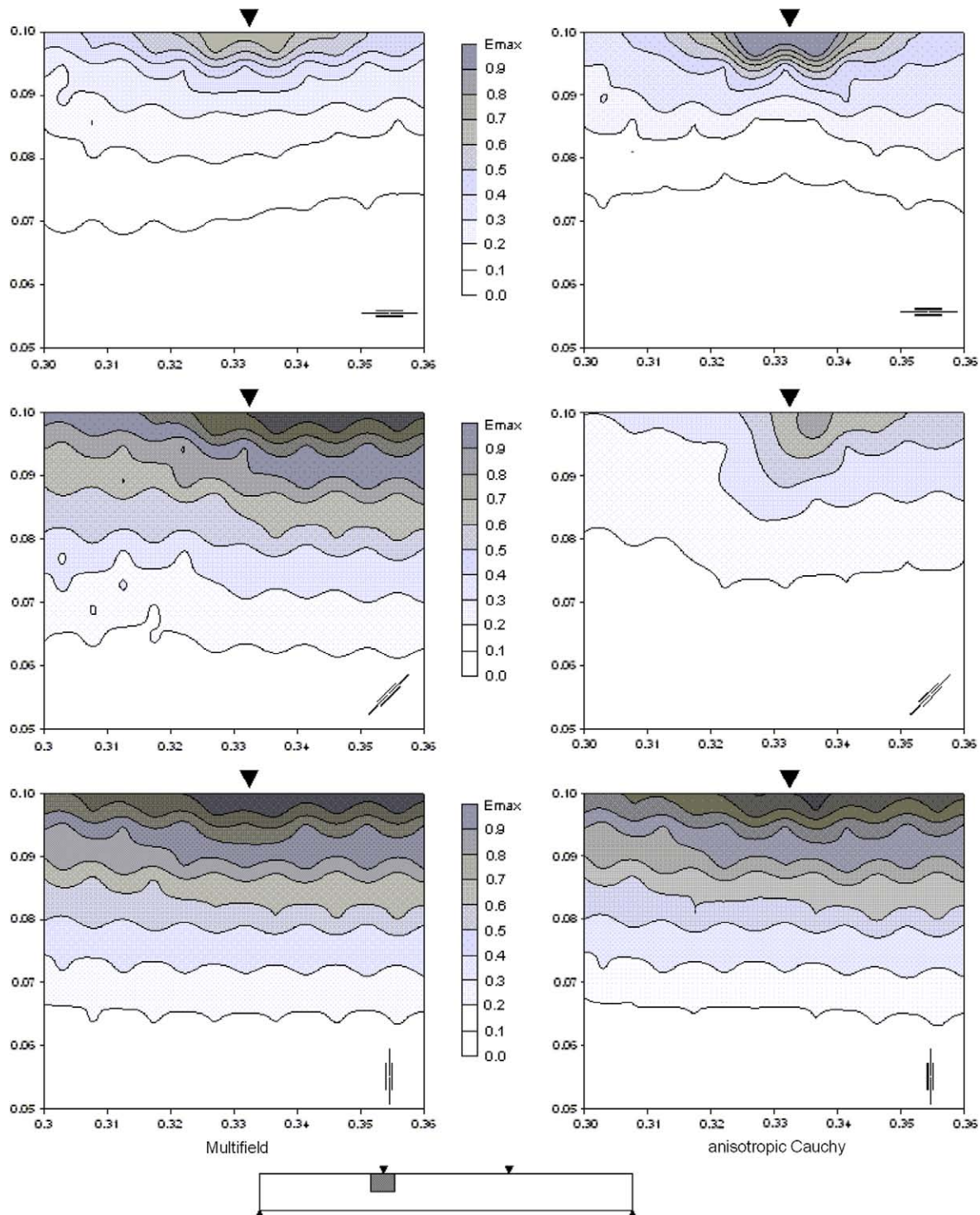


Fig. 5. Map of the energy density around one of the points of loading (top left, see schematic at the bottom of the figure) in the four-point bending test. Left panels: multifield model; right panels: anisotropic Cauchy model. Top row: $\varphi = 0$; center row: $\varphi = \pi/4$; bottom row: $\varphi = \pi/2$. The color scale of each map goes from 0 to E_{\max} .

have infinite rigidity. The actual numerical value of E^* , G^* at $\varphi = 0$ is determined by the value of λ and, to a lesser extent, by the fiber density.

Notably, the fiber orientation also has a sizeable effect on the effective moduli, the E^* , G^* values in Figs. 7 and 8 dropping by one order of magnitude when going from

$\varphi = 0$ to $\pi/2$. In analogy with these findings one may recall that, in a careful series of experiments on short-fiber-reinforced thermoplastic polymers, Blumentritt et al. [22,23] reported quite puzzling results for the effective E^* as a function of fiber aspect ratio and volume fraction. After about 30 years, it still appears that such results cannot yet be

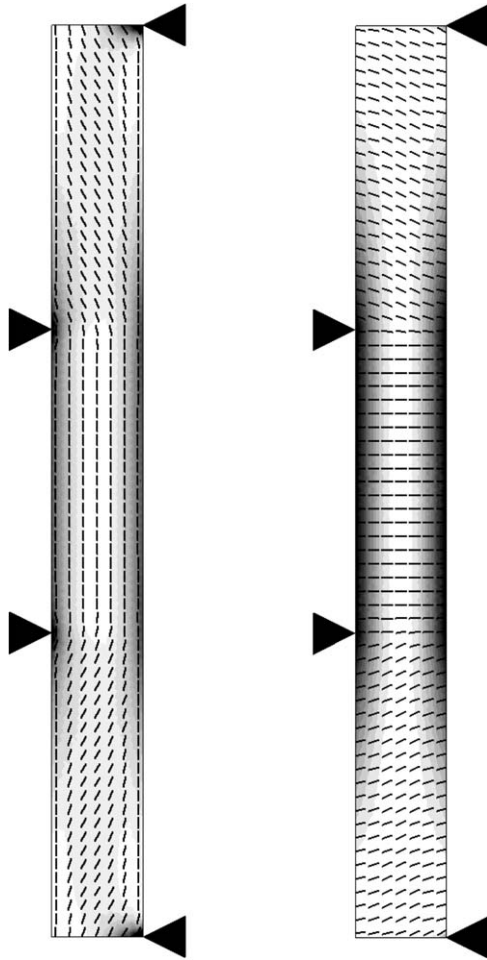


Fig. 6. Stick map describing the local fiber orientation, superimposed to the energy density map, for the four-point bending test. Top panel: initial fiber orientation $\varphi = 0$; bottom panel: initial fiber orientation $\varphi = \pi/2$. Each stick represents the average of 2×2 finite elements. Stick inclination is amplified by a factor of 50 for better visibility, after subtracting the global rotation of the applied deformation. The inclination is a measure of the actual physical rotation of the fibers. The color scale of the energy goes from 0 to E_{\max} .

understood in terms of conventional homogenization models [21]. In practice, lumped parameters such as the “effective aspect ratio” were introduced [24], trying to correlate the observed macroscopic properties with the average composite microstructure. While a detailed comparison with experimental data [22,23] is beyond the scope of the present work, we suggest that the strong coupling and the presence of local fiber rotations (described by the tensor \mathbf{W}) should make the multifield model a good candidate for understanding microstructure–property correlations in complex, composite materials.

4. Discussion and conclusions

In this work we presented the first application of a recently developed multiscale, multifield simulation method [15,16] to study the elastic response of a fiber-rein-

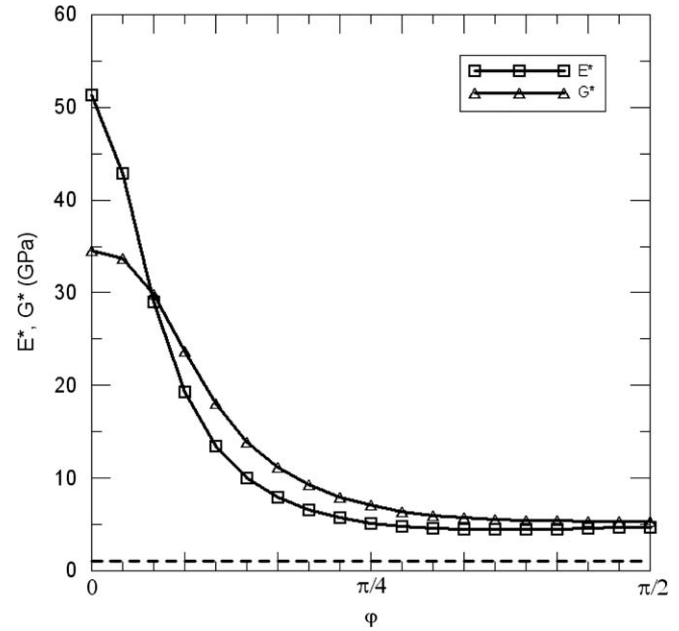


Fig. 7. Plot of the effective moduli E^* , G^* at $\lambda = 4 \times 10^{-3}$ as a function of the fiber orientation φ .

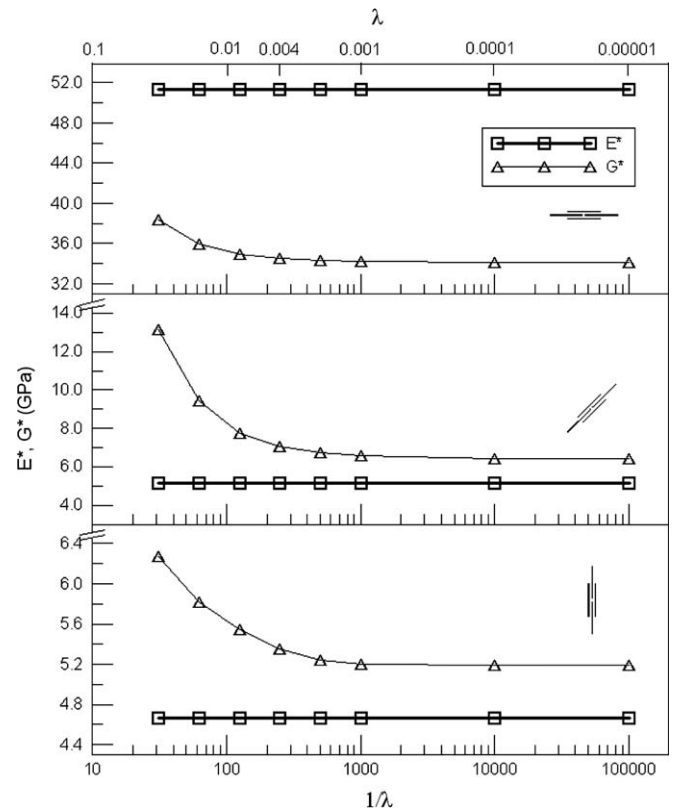


Fig. 8. Plot of the effective moduli E^* , G^* at $\varphi = 0, \pi/4, \pi/2$, as a function of the scale factor $\lambda = w/L$.

forced polymer matrix composite material. By taking epoxy/glass as an example of matrix/fiber combination, we studied different simulated loading conditions, corresponding to traction, shear and four-point bending.

The results clearly demonstrated the ability of the generalized continuum, multifield model to capture the detailed microstructural features of the elastic response, going beyond both the standard and the anisotropic Cauchy continuum analysis routinely used in conventional homogenization methods.

In particular, the additional microstructural field appearing in the generalized continuum has the function of effectively smearing the microscopic heterogeneities (fibers) in the macroscopic continuum. In this way, while simulating a coarse-grained continuum with a minimum mesh size equal to a few fiber lengths w , one can introduce the dependence on a material length scale, i.e., w divided by the leading dimension L of the macroscopic system. Moreover, the additional field explicitly describes the local fiber rotation, besides the fiber density and aspect ratio already present in the conventional Cauchy continuum, allowing one to map the local stresses and couple stresses at the microscopic level, as well as the local rotation of the fibers. Such features can be very important in designing the optimum arrangement of the fibers in a composite, so as to maximize the resistance to the various types of mechanical stresses the material can undergo.

Notably, the multifield results are obtained at a negligible computational cost with respect to a fully discrete analysis. As was shown in Refs. [13,15], by comparing the results of a similar multifield model to a fully discretized, numerical solution (albeit for a very different composite material, brick masonry), a comparable quality of the results could be reached only at the price of explicitly discretizing the whole continuum, by meshing the matrix and fibers down to an extremely fine scale, assigning different constitutive equations to each separate material, and, moreover, with a special treatment for the interfacial boundary layer.

The present multifield approach appears very promising for dealing with several, interacting microstructural fields, as was already demonstrated with a simple example in our previous work [16], dealing with an ideal material containing hard inclusions and microcracks. While the present version of the multifield FE code can solve only a static equilibrium problem, we are presently developing an extension of the MUSCAFE code which will allow one to follow the time evolution of the local constitutive equations, in

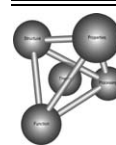
order to describe localized yielding and damage under static and dynamic loading conditions.

Acknowledgements

V.S. and F.C. collaborated with this work under the ENEA-MIUR Research Grant PROMOMAT.

References

- [1] Matthews FL, Davies GAO, Hitchings D. Finite element modelling of composite materials and structures. New York (NY): CRC Press; 2000.
- [2] Nemat-Nasser S, Hori M. Micromechanics: overall properties of heterogeneous materials. Amsterdam: Elsevier; 1993.
- [3] Nakamura T, Suresh S. *Acta Metall Mater* 1993;41:1665.
- [4] Kim SJ, Hwang JS, Paik SH. *Proc SPIE* 2003;5053:568.
- [5] Eshelby JD. *Proc R Soc Lond* 1957;A241:376.
- [6] Ponte Castaneda P, Suquet P. *Adv Appl Mech* 1998;34:171.
- [7] Sanchez-Palencia E. Non-homogeneous media and vibration theory. Lecture notes in physics, vol. 127. Berlin: Springer-Verlag; 1980. p. 45.
- [8] Sanchez-Palencia E, Zaoui E. Homogenization techniques for composite materials. Lecture notes in physics, vol. 272. Berlin: Springer-Verlag; 1985.
- [9] Kouznetsova V, Geers MGD, Brekelmans WAM. *Int J Numer Meth Eng* 2002;54:1235.
- [10] Zhu HT, Zbib HM, Aifantis EC. *Acta Mech* 1997;121:165.
- [11] Forest S, Sab K. *Mech Res Commun* 1998;25:449.
- [12] Ostoja-Starzewski M, Boccara SD, Jasiuk I. *Mech Res Commun* 1999;26:387.
- [13] Trovalusci P, Masiani R. *Int J Solids Struct* 2003;40:1281.
- [14] Trovalusci P. *Mater Sci Forum* 2003;426–432:2133.
- [15] Trovalusci P, Masiani R. *Int J Solids Struct* 2005;42:5578.
- [16] Sansalone V, Trovalusci P, Cleri F. *Int J Multiscale Comp Eng* 2005;3:463.
- [17] Capriz G. *Continua with microstructure*. Berlin: Springer-Verlag; 1989.
- [18] Ericksen JL. In: Yih CS, editor. *Advances in applied mechanics*, vol. 17. London: Academic Press; 1977. p. 189.
- [19] Hill R. *J Mech Phys Solids* 1963;11:357.
- [20] Jones RM. *Mechanics of composite materials*. London: Taylor & Francis; 1999.
- [21] Eduljee RF, McCulloch RL. In: Chou Tsu-Wei, editor. *Materials science and technology*, vol. 13. New York (NY): VCH Publishers; 1993. p. 381.
- [22] Blumentritt BF, Vu BT, Cooper SL. *Polym Eng Sci* 1974;14:633.
- [23] Blumentritt BF, Vu BT, Cooper SL. *Polym Eng Sci* 1975;15:482.
- [24] Kacir L, Narkis M, Ishai M. *Polym Eng Sci* 1978;18:45.



A two-dimensional mesoscale model for intergranular stress corrosion crack propagation [☆]

A.P. Jivkov ^{*}, N.P.C. Stevens, T.J. Marrow

School of Materials, University of Manchester, Grosvenor Street, Manchester M1 7HS, UK

Received 30 September 2005; received in revised form 10 January 2006; accepted 23 March 2006

Available online 5 June 2006

Abstract

A mechanical model for simulating intergranular stress corrosion cracking is presented. The model has been developed to address the limitations of percolation-like models, which do not account for the mechanical crack driving force and cannot capture experimentally observed phenomena such as the formation of ductile bridging ligaments by resistant boundaries. The model is based on a regular representation of material microstructure and a categorisation of grain boundaries as susceptible and resistant to corrosion. Crack propagation in two-dimensional microstructures with several fractions of experimentally observed susceptible boundaries is studied. Monte Carlo-type simulations with random distributions of boundaries and a range of susceptible and resistant boundary failure strengths are performed. The effects of crack bridging and crack branching are quantified. It is concluded that together with the fraction of susceptible boundaries, the resistant boundary failure strength is the significant parameter controlling the shielding effect of bridges on crack propagation.

© 2006 Acta Materialia Inc. Published by Elsevier Ltd. All rights reserved.

Keywords: Grain boundaries; Fracture; Finite element analysis; Stainless steels; Stress corrosion cracking

1. Introduction

It has increasingly been realised during the last two decades that the grain size is not the only mesoscale factor influencing the strength of polycrystalline materials. Two other factors have been brought to wider attention. The first is the grain boundary character distribution (GBCD) which describes the fractions of boundaries with different energies, with “special” or low-energy boundaries having higher resistance to intergranular degradation mechanisms and “random” or high-energy boundaries having lower resistance. The second factor is the topological connectivity of “random” boundaries. In connection with these findings, the concept of grain boundary engineering has been

introduced by Watanabe [1]. The primary purpose of grain boundary engineering has been to improve the bulk mechanical properties of polycrystalline materials by increasing the number of “special” or low-energy boundaries. Together with applications to enhance general fracture toughness [2,3], it has been shown that the “special” grain boundaries can be much less susceptible to intergranular corrosion and stress corrosion cracking (SCC) [4,5].

Predictive SCC models aim to determine the probability of crack arrest and distribution of arrested crack lengths for given grain boundary network characteristics. Previously proposed models [6–8] used a percolation-type process to determine the probable extent of crack growth. These are binary models, i.e. a grain boundary is assumed to be either entirely resistant or entirely susceptible to SCC. In the early models [6], the probability of crack advance at a junction is based on the GBCD and orientation of the grain boundary with respect to the applied stress. Later models [7,8] additionally account for the network connectivity via the distribution of triple junctions. All these

[☆] This manuscript was presented at the “Micromechanics and Microstructure Evolution: Modeling, Simulation and Experiments” held in Madrid/Spain September 11–16, 2005.

^{*} Corresponding author. Tel.: +44 161 3063556; fax: +44 161 3063586.
E-mail address: andrey.jivkov@manchester.ac.uk (A.P. Jivkov).

models, however, lack a way to describe the effects of the applied stress magnitude or stress redistribution during crack evolution. Hence, they stand close to a pure geometrical percolation model, giving the critical share of “random” boundaries above which a continuous crack path across a given microstructure is always possible. Previous models also cannot account for the experimentally observed crack bridging behaviour (see Fig. 1). Bridging is created by the yielding of ductile ligaments, formed by resistant boundaries left behind the advancing crack front in real three-dimensional (3D) geometry. A recently proposed analytical model [9] has attempted to take into account the effects of crack bridging on the local crack tip stress intensity factor, thus mimicking 3D crack behaviour.

All the percolation-type works mentioned above use a regular representation of the material microstructure. Regular two-dimensional (2D) models must choose either a square or hexagonal cell structure. The higher coordination number in hexagonal meshes is more representative of material microstructure, so this has been the standard unit cell used in previous percolation-like models. For the hexagonal cell structure, the critical share of susceptible boundaries, i.e. the percolation threshold, is found mathematically to be around 0.65 [7]. Below this value, a crack

will not necessarily percolate through the structure. The fraction of susceptible boundaries can be reduced by grain boundary engineering, through thermomechanical processing. Adopting the most widely used regular representations of 2D microstructures, the principle aim of this work was to develop 2D mechanical models for intergranular crack propagation in thermomechanically processed microstructures under the influence of applied stresses. The idea was to establish a finite element model of the microstructure chosen, and use it for calculations of the stress after each change in geometry due to crack advance. This approach allows for a more accurate simulation of crack evolution, as the probability of crack advance depends upon the actual mechanical conditions at the crack tip. These conditions are affected by the crack propagation history, i.e. the effects of crack branching, crack bridging, and redistribution of the initial stress state could be accounted for in a natural manner. This is viewed to be a necessary precursor to the development of 3D modelling, which is the ultimate goal of this work [10]. At present the model is relevant only to fully sensitised materials and the kinetics of crack propagation are not taken into account. Therefore, the proposed model should be viewed as an advance to the percolation-like models by including mechanical effects. In this sense, in the same manner as the percolation-like models, it is a tool for assessing the relative microstructure resistance to intergranular fracture that is applicable to intergranular SCC, rather than a model for SCC. It should be appreciated, however, that the proposed model allows for the incorporation of the dependence of propagation kinetics on the local mechanical fields, and this is a topic of ongoing work.

2. Model description

The model of intergranular crack propagation in a material microstructure used in this work has two levels of abstraction: physical and computational. These are described briefly in Sections 2.1 and 2.2. Section 2.3 is devoted to the computational strategy of crack advance adopted.

2.1. Physical level

At the physical level, the microstructure geometry is represented as a regular tessellation of space into identical cells, where each cell corresponds to one material grain. The assumptions concerning grain geometry, grain boundary character and properties and material failure are as follows:

- **Grain geometry.** Grains are assumed to be identical in shape and represented by regular hexagons. With the grain geometry assumption, a region of a polycrystalline solid is approximated by an assembly of identical cells. A major geometrical parameter is the unit cell diameter, D .

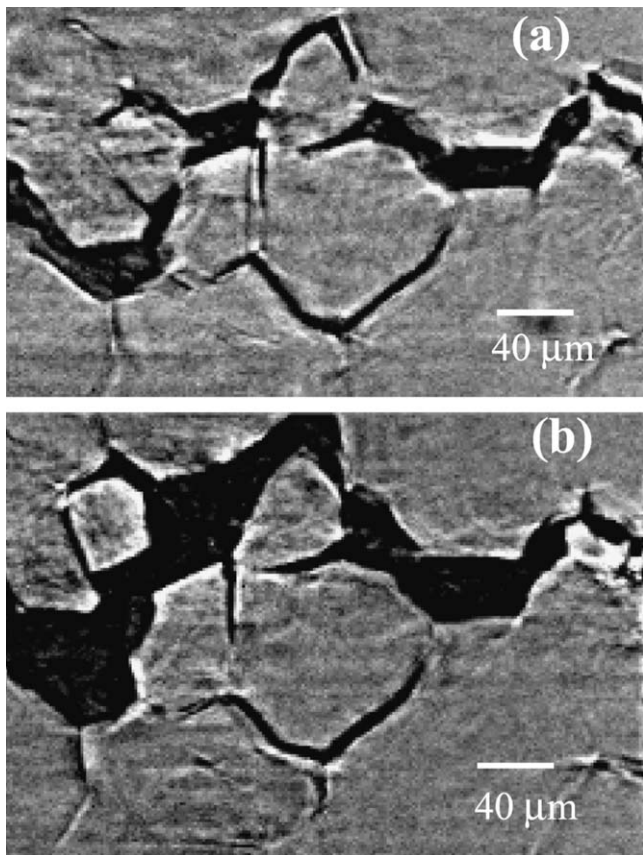


Fig. 1. In situ observation of the failure of a crack bridging ligament. (a) and (b) are successive images obtained by high resolution X-ray tomography of a propagating stress corrosion crack [9].

- *Grain boundary character.* Grain boundaries (the common faces in the assembly of cells) are assumed to belong to either of two classes. The first class is formed of the special (i.e. low-angle, low-energy) grain boundaries, which are generally accepted as resistant to corrosion. The second class includes the random (i.e. randomly oriented high-angle, high-energy) grain boundaries, which are accepted as susceptible to corrosion. The fraction of susceptible boundaries (the number of susceptible over the total number of boundaries), f , is a major parameter in the current studies. The distribution of susceptible boundaries is randomly assigned for given f .
- *Material failure and grain boundary properties.* Material is assumed to fail via the crack propagating along grain boundaries only. In the present model, the kinetics of the stress corrosion mechanism are not accounted for, so the real time dimension of crack propagation is not determined and crack velocities are not calculated. In principle, the model could be developed to include kinetic factors, however. Experimental observations of intergranular stress corrosion show that susceptible boundaries fail at crack opening displacements of the order of several nanometers with insignificant inelastic deformations [11]. This suggests that the failure strain of the susceptible boundaries, denoted by ε_{sf} , is around or below the apparent material yield strain, ε_y . The failure strain ε_{sf} is a second model parameter. Resistant boundaries, in contrast to the susceptible boundaries, can yield and rupture well into the inelastic region, as demonstrated by in situ high-resolution tomographic and fractographic observations of intergranular SCC [12]. Therefore, resistant boundaries in the model are allowed to fail after a significant amount of accumulated inelastic strain, denoted by ε_{rf} and defining a third model parameter. This failure strain is assumed to be a fraction of the material ultimate tensile strain, ε_u .

2.2. Computational level

A direct approach to model an assembly of cells in a finite element environment would be based on continuum mechanics. Each cell would have to be tessellated into available shapes of continuum elements and connected to the neighbouring cells with some interface elements, representing the grain boundaries. Such a direct modelling strategy has so far only been used for an assembly with limited number of grains (e.g. up to 50 grains in Ref. [13]) as it requires an enormous amount of computer resources, especially for 3D models. Therefore, at the computational level of modelling a discrete representation of the assembly was suggested. This is viewed as a good first approximation, while the continuum approach is left for the future as more computational power becomes available.

In the discrete model, each cell is represented as a geometrical point and its connections to the neighbouring cells, which are the grain boundaries in reality, are represented by structural members of linear extension. The idea

is illustrated in Fig. 2, where a portion of a plane hexagonal mesh and its corresponding structure are shown. The finite element model consists of nodes, placed in the centres of the grains, and beam-type finite elements for structural members. Thus, the grain deformability is transferred to the deformability of the adjacent beam elements. The discrete representation leads to a significant reduction of the nodes and elements in a model and hence of the computational effort. Essential to the discrete model is the question of how well it represents the solid behaviour. This question is connected to the selection of element cross-sections and elastic properties. Since the regular geometry introduces preferential directions in the assembly, it is generally impossible to make a selection so that the discrete assembly behaves as a continuum solid for all modes of deformation simultaneously. It is possible, however, to make such a selection for every particular deformation mode. In the present work, selections of beam cross-sections are made so that the assembly in question, when subject to tensile deformation in the elastic range, behaves like a solid under the same deformation. All elements have identical modulus of elasticity and Poisson's ratio.

The assumptions for the mechanical properties of the modelled polycrystalline solid and the beam elements of its discrete representation are as follows:

- *Solid mechanical properties.* The macroscopic mechanical properties are those of grade 304 austenitic stainless steel. The constitutive relationship chosen is elastic–plastic with linear isotropic hardening, which for the purposes of this work describes sufficiently well the stainless steel behaviour. The parameters involved in the constitutive description are Young's modulus $E = 206$ GPa, Poisson's ratio $\nu = 0.3$, yield (proof)

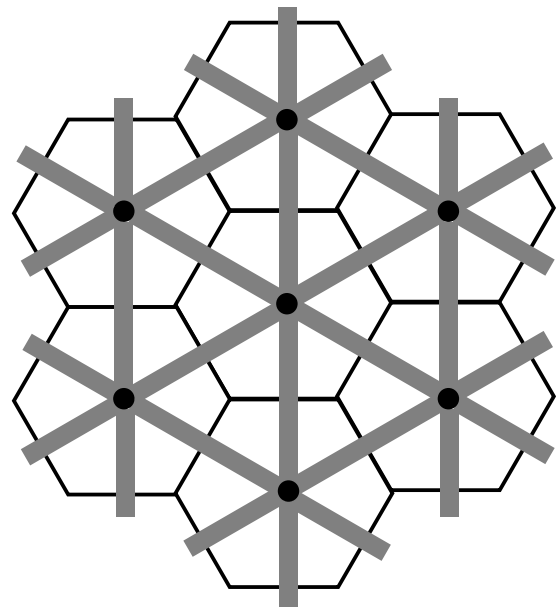


Fig. 2. The discrete model for the 2D hexagonal structure.

strength $\sigma_y = 205$ MPa, yield strain $\varepsilon_y = 0.002$, ultimate tensile strength $\sigma_u = 515$ MPa and ultimate tensile strain (elongation) $\varepsilon_u = 0.4$.

- *Beam elements mechanical properties.* Beam elements are ascribed the same mechanical properties as for the solid for the finite element solution. However, in the course of crack propagation, the beams representing susceptible boundaries would fail upon reaching their prescribed failure strain ε_{sf} , which is a fraction of the material yield strain ε_y , while the beams representing resistant boundaries would fail upon reaching their prescribed failure strain ε_{rf} , which is a fraction of the material ultimate tensile strain ε_u . This behaviour of the beam elements is shown schematically in Fig. 3. The average strain, i.e. the strain in the centre of the cross-section in beam elements, is used in the calculations.

2.3. Crack advance strategy

The strategy for crack advance in the computational model relies on a series of finite element solutions for equilibrium of the (evolving) assembly with the applied loads. Each solution provides the stresses and strains at the grain boundaries (midpoints of the beam elements) necessary to decide upon further crack propagation. If the failure strain of a grain boundary, being either resistant or susceptible, is reached, that boundary is a candidate for failure. In general only one boundary, the most critical, is allowed to fail at a time, i.e. one beam element is deleted from the discrete structure. As every failure event leads to redistribution of stresses and strains that cannot be judged in advance, the single-failure strategy ensures that the recalculated equilibrium will deliver the correct stresses and strains for the subsequent event. Strictly speaking, while the crack is advancing the mechanical equilibrium found by finite elements is physically unstable, and turns into physical equilibrium only at crack arrest.

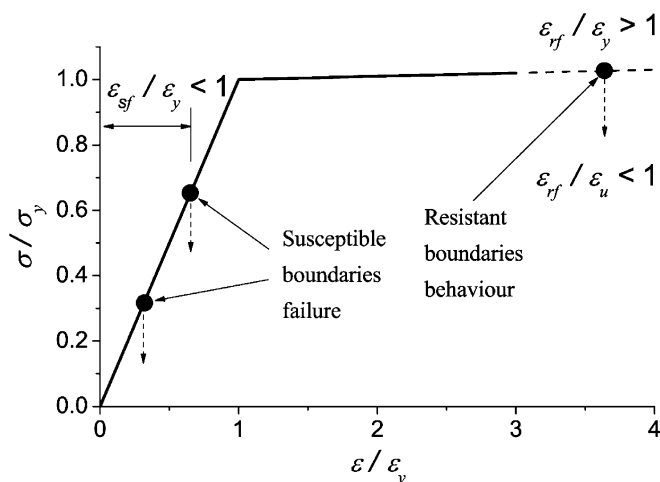


Fig. 3. Schematic illustration of the deformation and failure characteristics for susceptible and resistant boundaries.

The search for boundaries that are candidates for failure incorporates the possibility for bridge formation in the 2D settings. This is explained below, assuming a crack has grown to a certain stage and an equilibrium solution has been found for the corresponding discrete model. The approach to determine crack advance is illustrated in Fig. 4, where the current crack is shown with thick light grey lines, denoted by c , and all the boundaries that are in contact with the crack surface are shown in grey and are denoted by s . These surface boundaries are in direct contact with the corrosive environment, and are thus candidates for failure. In addition the subsurface boundaries, i.e. those in contact with surface boundaries, are shown in dark grey and are denoted by s' . The search for candidates for failure is performed first amongst the surface boundaries. For each of these boundaries, the difference between its calculated strain, ε , and its failure strain is obtained. Thus for susceptible boundaries this difference is $\delta = (\varepsilon - \varepsilon_{sf})$, while for resistant boundaries the difference is $\delta = (\varepsilon - \varepsilon_{rf})$. All boundaries with $\delta > 0$ are candidates for failure at the current solution step. If there are any such boundaries, the boundary with largest δ is accepted as being critical and the corresponding beam element is removed from the structure. The simulation then continues. If there are no surface boundaries with $\delta > 0$, the subsurface boundaries are considered. The reason for considering subsurface boundaries is to mimic the real 3D behaviour. For example, consider the boundary between point A and B in Fig. 3. If this was resistant, this would prevent it from failing at the current simulation step. In the real 3D situation the crack could pass from point A to point B via an out-of-plane path along susceptible boundaries. This places the subsurface boundaries adjacent to point B in contact with the environment, i.e. they become surface boundaries. The same possibility for bypassing the current surface boundaries exists for all of the subsurface boundaries. Depending on the total crack geometry (not only the portion shown in the figure) the critical subsurface boundary could be either adjacent to point B, or adjacent to point C, or somewhere else. Therefore if the surface boundaries cannot fail at a given

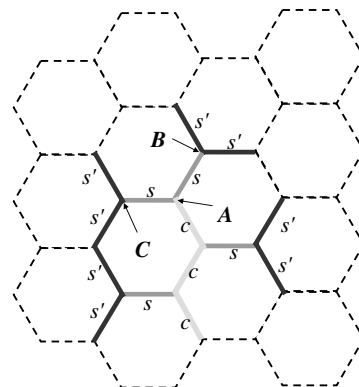


Fig. 4. Illustration of the search for failing boundaries in the model of crack advance for a crack tip located at point A.

simulation step, all subsurface boundaries are reconsidered as surface boundaries and the same strategy for failing holds. If there are no candidates for failure among subsurface boundaries, the crack is assumed arrested and simulations are terminated.

The crack advance strategy, described above, is implemented using an in-house computer program written in Java. The program is responsible for creating the initial model and consecutively calling external equilibrium solver, ABAQUS [14], deciding upon crack advance from the equilibrium solution and changing the model if required.

3. Problem description

With respect to a fixed coordinate system (X_1 , X_2), the assembly of grains studied fills the solid rectangular region $\{-50D \leq X_1 \leq 50D, 0 \leq X_2 \leq 50D\}$. This region contains 7740 grains, which form 22,850 internal grain boundaries, modelled by 7740 nodes and 22,850 beam elements in the finite element model. An initial crack, extending along three grain boundaries, is introduced from the surface point at the origin of the coordinate system and running in towards the centre of the element assembly.

The load is symmetric and applied via prescribed displacements: $u_1 = -0.025D$ along the boundary $\{X_1 = -50D, 0 \leq X_2 \leq 50D\}$ and $u_1 = 0.025D$ along the boundary $\{X_1 = 50D, 0 \leq X_2 \leq 50D\}$. Displacements $u_2 = 0$ are prescribed along the boundary $\{-50D \leq X_1 \leq 50D, X_2 = 50D\}$, while zero stresses are prescribed for all other boundary conditions. These boundary conditions introduce a homogeneous strain in the assembly $\varepsilon_\infty = 5 \times 10^{-4}$, equivalent to a homogeneous stress $\sigma_\infty \approx 0.5\sigma_y$.

For comparative purposes the analytical stress intensity factor for a straight edge crack in a finite geometry has been used [15]:

$$K_I = F(\alpha)\sigma_\infty\sqrt{\pi a} \quad (1)$$

where a is the crack length, σ_∞ is the remote tensile stress and $F(\alpha)$ is given by

$$F(\alpha) = 1.12 - 0.231\alpha + 10.55\alpha^2 - 21.72\alpha^3 + 30.39\alpha^4 \quad (2)$$

for parameter $\alpha = a/W$ with $W = 50D$. Eq. (2) gives an error of $\pm 0.5\%$ for $\alpha \leq 0.6$.

Computationally, the stress intensity factor is calculated in the way illustrated in Fig. 5, where a portion of the solid is shown. The actual crack is shown by a thick white line and a bridge along the crack path is depicted with grey. The corresponding straight, unbridged crack is also shown for comparison. The rectangle ahead of the crack tip shows the region that is accounted for in determining the stress intensity factor of the bridged crack. The possible crack tip plastic zone is dashed, while the rest of the rectangular region is taken to span over 10 grains. For any given distance from the crack tip, r , with a step one grain diameter, a stress σ_{11} has been calculated by averaging the stresses in all grains along the line shown in the figure. The approxi-

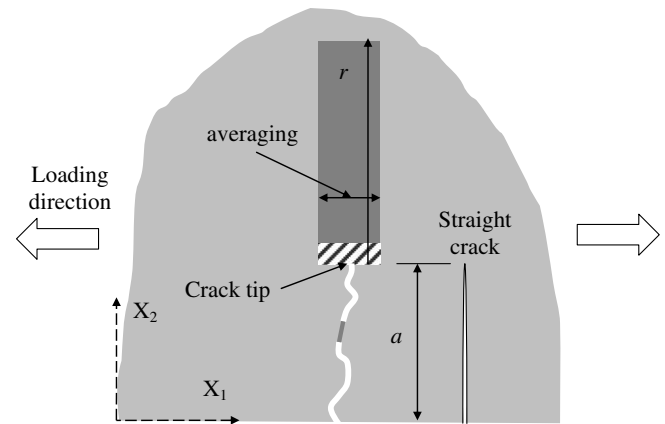


Fig. 5. Stress intensity factor calculation for the bridged crack in the finite element model, compared to a straight edge crack.

mate relationship $\sigma_{11}(r)$ established by this method is then used to calculate the stress intensity factor via

$$\sigma_{11}(r)\sqrt{2\pi r} \xrightarrow{r \rightarrow 0} K_I^{\text{FEM}} \quad (3)$$

A post-processing computer program has been developed to implement the computational procedure for determining the stress intensity factors. It delivers the stress intensity factor and the current crack geometry, including the number of bridges along the crack surface, after each step of the simulations. The bridges can be in the elastic regime or yielding plastically. In addition, the program calculates the shielding effect of the bridges via the stress intensity factor that the bridges create with respect to the corresponding crack fronts. The contribution from all bridges, and the fraction of this that is due to yielding bridges are obtained. The stress intensity due to all bridges is an algebraic sum of the contributions from every bridge, given by

$$K_{\text{br}} = F(\alpha)P\sqrt{\frac{\pi}{2r}} \quad (4)$$

where P is the force in the bridge parallel to the loading (crack opening) direction, r is the distance to the corresponding crack front and $F(\alpha)$ is given by Eq. (2). Eq. (4) is the solution for a crack loaded in mode I by a couple of symmetric concentrated forces of magnitude P placed on the crack surfaces at distance r from the tip [15]. The program has been checked with straight cracks without bridges or branches (i.e. zigzag cracks in the hexagonal microstructure) for the entire range of crack extensions between one grain and 25 grains. Comparison with theoretical values given by Eqs. (1) and (2) showed identical results for the stress intensity factors to within 0.1%.

4. Results and discussion

One approach to understand the sensitivity of SCC propagation to microstructure influences would be to develop a series of simulations with variable strengths of the susceptible and the resistant boundaries, together with

a variable fraction of the susceptible boundaries in the assembly, random distributions of the boundaries within the assembly. The aim with such a series would be to answer the following questions:

- Do the observed resistant boundaries control crack growth by dissipating energy in plastic deformation, or are they just energetically unimportant remnants left by crack propagation?
- How does this answer change with the strength and fraction of susceptible and resistant boundaries?

The microstructures of interest are those that have been experimentally studied. These had susceptible boundary fractions in the range $0.65 \leq f \leq 0.75$ [9,10].

Before commencing full-scale 2D parametric studies, it was advisable to check if the proposed mechanical model could reproduce the existing results from percolation models. This has been reported in Ref. [16], where simulations with 2D geometry have been run for the full series of susceptible boundary fraction, $0.1 \leq f \leq 0.9$ and for a number of susceptible boundary failure strains, $\varepsilon_{sf} = 0, 0.1\varepsilon_y, 0.2\varepsilon_y$. The resistant boundary failure strain has been fixed at $\varepsilon_{rf} = 10\varepsilon_y$. For each fraction f , 30 different random distributions of the boundaries have been considered and results have been averaged over these random distributions to give a single value for the given fraction. The parameters that have been monitored are the projected crack length, denoted by a , and the total crack surface, i.e. main crack including branches and kinks, denoted by A . From the results presented in Ref. [16] it is evident that the role of mechanical strain is to direct the crack growth by decreasing crack branching and kinking compared to the percolation models. For a given fraction of susceptible boundaries, the crack arrest length determined by the 2D model with bridges is always smaller than the 3D percolation prediction and larger than the 2D percolation prediction. Any decrease of the susceptible boundary failure strain, ε_{sf} ,

leads to an increase of the arrest length, i.e. shift towards the 3D percolation prediction, as expected. Conversely, an increase of ε_{sf} shifts the arrest length towards the lower limit that is given by the 2D percolation prediction. This influence of ε_{sf} , however, is pronounced only for microstructures that are dominated by resistant boundaries, $f < 0.5$, and becomes insignificant for the microstructures of interest, those with $0.65 \leq f \leq 0.75$. In addition, ε_{sf} is a parameter that controls crack branching. This is also most pronounced for $f < 0.5$, and is not significant for microstructures with $0.65 \leq f \leq 0.75$.

Returning therefore to the microstructures of interest, Fig. 6 gives an illustration of a crack grown in a 2D hexagonal microstructure with fraction of susceptible boundaries $f = 0.7$. The cracked boundaries are shown with thick white lines. The thin and thick black lines show susceptible and resistant boundaries, respectively. The bridges formed in the crack wake by resistant boundaries are clearly identifiable. In the model for crack advance used here, a bridge can always form when a subsurface boundary is in a critical state, i.e. it is assumed that the real 3D microstructure will always allow bypassing of a resistant boundary. Strictly this cannot be always the case, as it depends on the fraction and distribution of susceptible boundaries in 3D. This means that a direct correspondence of the results from the present model and the 3D microstructure for a given f cannot be claimed. It is anticipated that results for a given f obtained with the present model will correspond to a 3D microstructure with larger fraction of susceptible boundaries. Therefore a wider region of change has been adopted, namely $0.5 \leq f \leq 0.8$.

For the series of fractions $0.5 \leq f \leq 0.8$, with intervals of 0.05, simulations with different values of the variable $\varepsilon_{sf} = 0.1\varepsilon_y, 0.2\varepsilon_y, 0.3\varepsilon_y, 0.4\varepsilon_y$ and fixed $\varepsilon_{rf} = 10\varepsilon_y$, as well as simulations for three values of resistant boundaries failure strain, $\varepsilon_{rf} = 5\varepsilon_y, 10\varepsilon_y, 50\varepsilon_y$, and fixed $\varepsilon_{sf} = 0.1\varepsilon_y$ have been performed. For illustration, Fig. 7 gives the total number of bridges (Fig. 7(a)) and the number of yielding

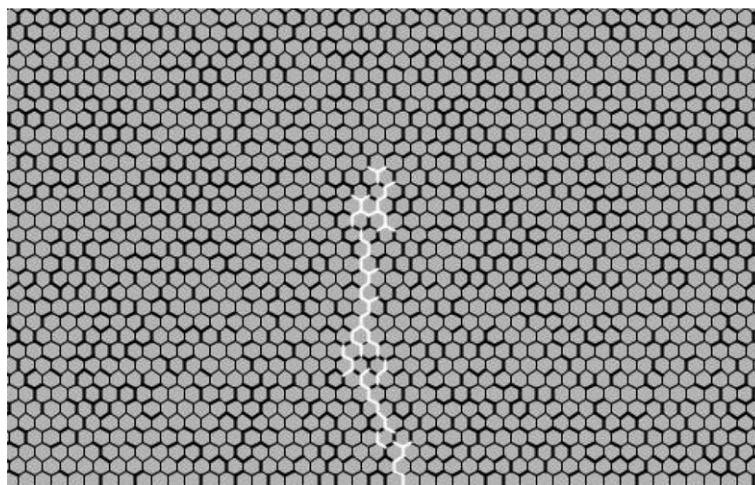


Fig. 6. Example of a crack propagated in a microstructure with $f = 0.7$.

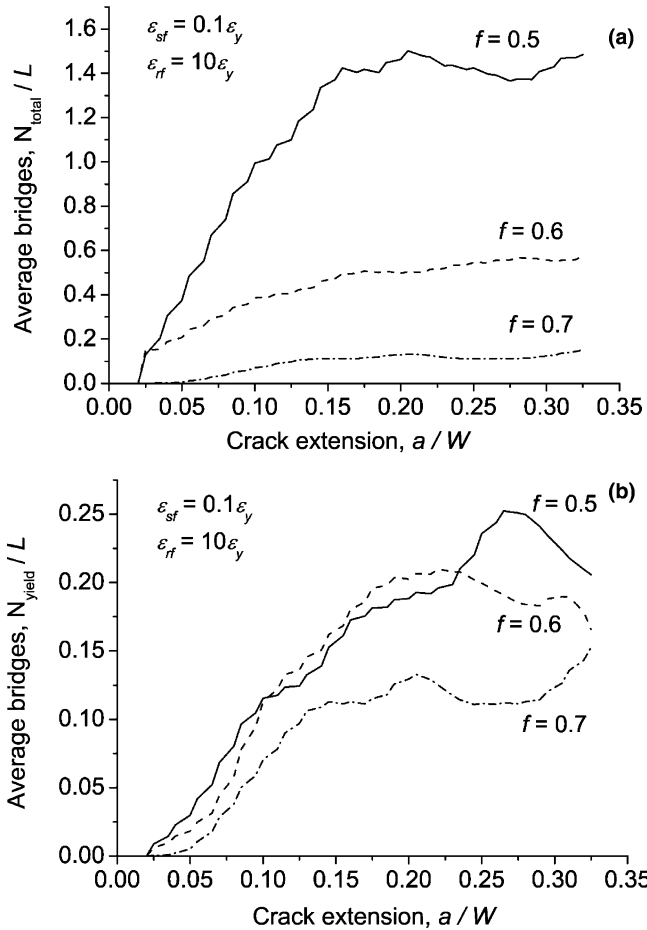


Fig. 7. Average number of bridges with crack extension: (a) all bridges (elastic and yielding); (b) yielding bridges only.

bridges (Fig. 7(b)) formed as the crack extends for the base case where $\varepsilon_{sf} = 0.1\varepsilon_y$ and $\varepsilon_{rf} = 10$ and three selected fractions of susceptible boundaries. The number of bridges is normalised with the projected crack length in terms of number of grains, $L = a/D$, while the crack extension, a , is normalised with the total assembly thickness, W . Values for the total number of bridges (N_{total}/L) in Fig. 7(a) that are larger than 1.0 indicate that there are a significant number of bridges formed not only along the main crack, but also along various crack branches. With increasing f , the number of branches decreases and N_{total}/L should become comparable to f . In theory, in the absence of branches, these two values must coincide, but this could be the case only if the crack has straight (zigzag) geometry. In reality, with increasing f the crack has more opportunities to grow by kinking from the straight geometry and bridges form only when other possibilities are exhausted. This makes the value N_{total}/L smaller than expected on theoretical grounds, and this is visible in the curves for $f = 0.6$ and $f = 0.7$ in Fig. 7(a). Fig. 7(b) shows that the number of yielding bridges is much less dependent on the fraction of susceptible boundaries in the region of interest and is more controlled by the current crack extension. It should be noted that decreases in the number of yielding bridges in

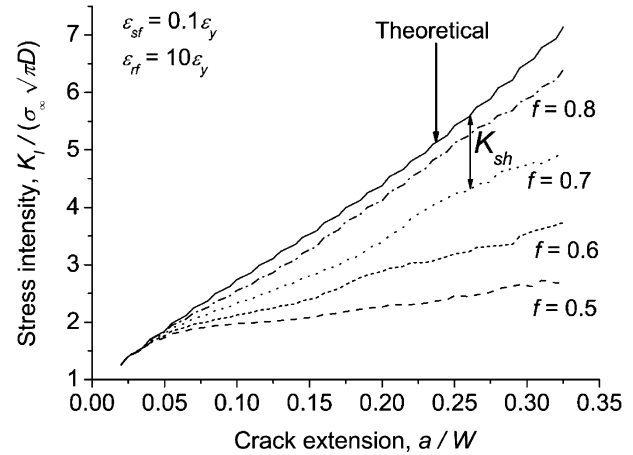


Fig. 8. Stress intensity factor evolution with crack extension with variation in f .

Fig. 7(b), reflecting decreases in the total number of bridges in Fig. 7(a), indicate failures of yielding ligaments. These failures occur earlier, i.e. at shorter crack extensions, for larger fractions of susceptible boundaries, since the total number of bridges that are shielding the crack decreases.

Fig. 8 shows the evolution of the stress intensity factors with crack extension for the base case $\varepsilon_{sf} = 0.1\varepsilon_y$ and $\varepsilon_{rf} = 10$ and four selected fractions of susceptible boundaries. Crack extension, a , is normalised with the total assembly thickness, W . Stress intensity factors are normalised as depicted in the figure, where σ_∞ represents the actual remote stress in the structure. As the load is applied via prescribed displacements, the actual stress depends on the current stiffness of the cracked assembly and is found from the finite element solution. With crack advance the remote stress decreases, by a factor of 8% for the stiffest structure with $f = 0.5$ and by 18% for the most compliant structure with $f = 0.8$, in the interval of crack extensions shown in the figure. The stress intensity development is obtained through the stress results from finite element solutions using Eq. (3), while the theoretical value is calculated using Eq. (1). In the figure, K_{sh} denotes the shielding effect of the microstructure, which includes not only the effect of bridges but also the effect of branches on the crack driving force reduction, as will become clear shortly.

The shielding effect is almost independent of the susceptible boundary failure strain, ε_{sf} , but depends on the resistant boundary failure strain, ε_{rf} , in the region of interest. This is demonstrated in Fig. 9, where the shielding stress intensity factor, K_{sh} , is plotted versus the susceptible boundaries fraction, f , for a selected crack extension, $a = 0.3W$, and for the series of failure strains of susceptible boundaries (Fig. 9(a)) and the series of failure strains of resistant boundaries (Fig. 9(b)). The stress intensity is normalised as in Fig. 8. The dependence on ε_{rf} comes from the larger contribution of bridges to the total shielding effect, which increases with the resistant boundary failure strain.

To quantify the relative effects of branching and bridging on the total shielding effect, the crack driving force

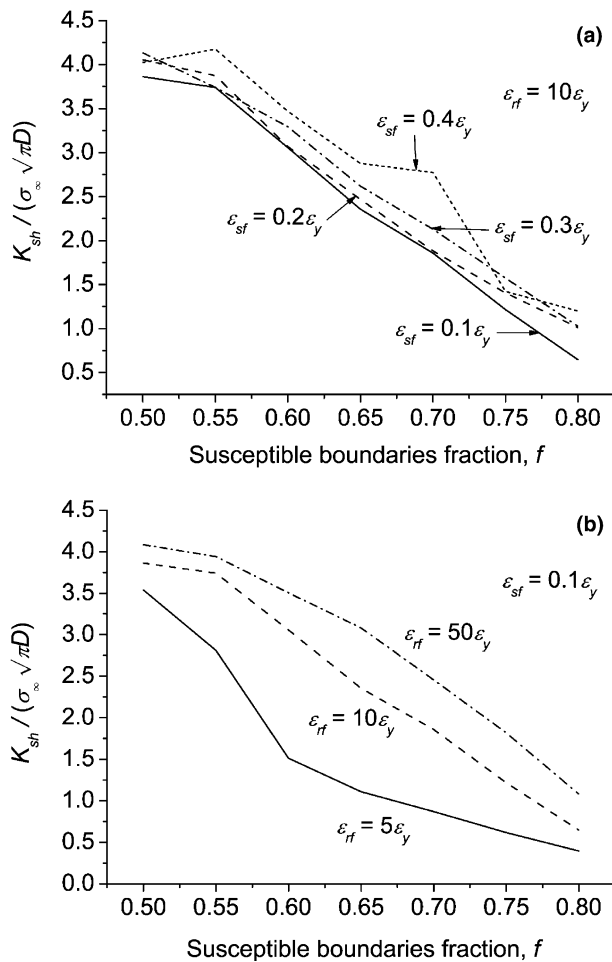


Fig. 9. Variation of shielding with boundary failure strain with fraction f : (a) the effect of susceptible boundaries failure strain; (b) the effect of resistant boundaries failure strain.

reduction solely due to bridges has been estimated. This was done by calculating the stress intensity factors using Eq. (4) and the stress results from finite element solutions. As an illustration, Fig. 10 presents the stress intensity fac-

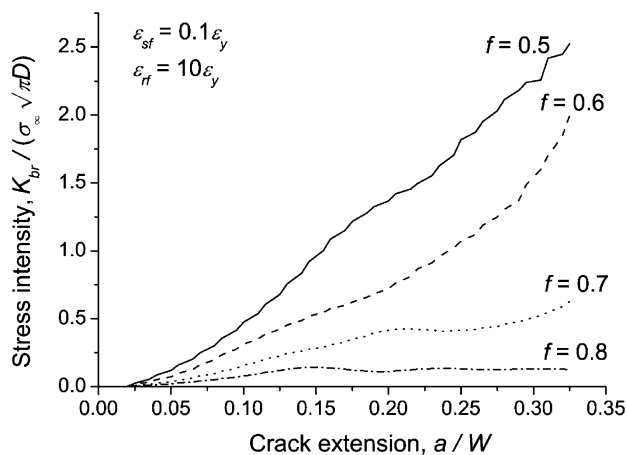


Fig. 10. Bridging stress intensity factor evolution with crack extension with variation in f .

tors due to bridges alone for the same grain boundary properties and fractions as in Fig. 8. The normalising factors for the two axes of the plot are also the same.

Fig. 11 demonstrates the effects of all bridges (Fig. 11(a)), only the elastic bridges (Fig. 11(b)) and only the yielding bridges (Fig. 11(c)) for the particular values of grain boundary properties depicted. Bridging effects are shown as fractions of the total shielding effect. The

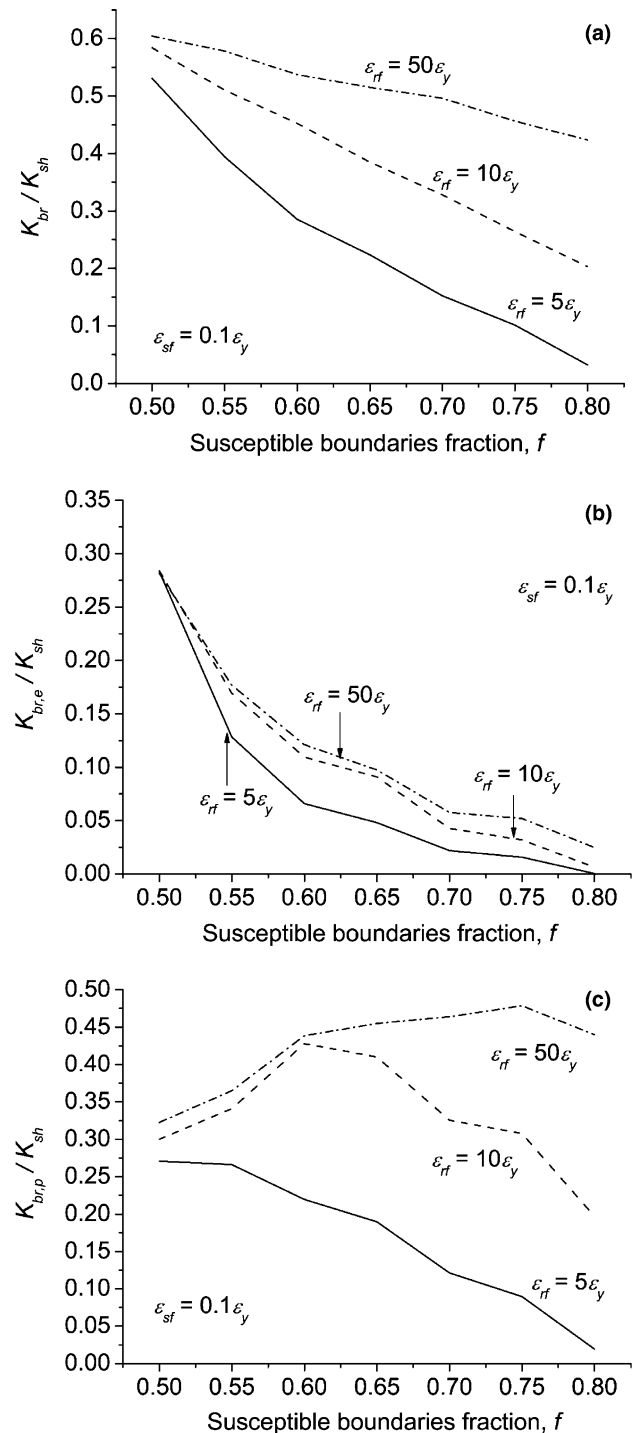


Fig. 11. The contribution of bridges to the shielding effect: (a) all bridges; (b) elastic bridges only; (c) yielding bridges only.

effect of elastic bridges is a nonlinear decreasing function of f , almost independent of ε_{rf} , while the effect of yielding bridges depends on ε_{rf} , and may turn into an increasing function of f , for sufficiently large ε_{rf} . Thus, in the region of interest for f , the yielding bridges provide the larger contribution to the crack shielding and this relative contribution increases with increasing f .

As a general observation from all the 2D simulations, the parameter controlling the effect of bridges is the resistant boundary failure strain and the parameter controlling branching is the susceptible boundary fraction. The effect of the susceptible boundary failure strain is negligible in the region of interest for fractions of susceptible boundaries in the constraints of the model. The initial crack extension (pre-crack) and the applied load set a threshold for the susceptible boundary failure strain above which the pre-crack cannot start propagating. For any value of the susceptible boundary failure strain smaller than this threshold the cracks will propagate and will have the behaviour presented by the above results. Conversely, a fixed value of the susceptible boundary failure strain will set a threshold on the applied load, below which the cracks cannot start propagating. It may therefore be considered to be a material/environment parameter.

5. Conclusions

The proposed discrete structural model has the potential to simulate intergranular crack propagation and crack coalescence in a realistic manner by including the phenomenon of crack bridging by ductile ligaments. It accounts for the effects of external load magnitude and the failure properties of susceptible and resistant boundaries. Crack arrest was not observed in the region of interest for susceptible boundary fraction, but a significant degree of crack tip shielding was developed, which would be expected to reduce the crack propagation rate. Increasing the fraction of resistant grain boundaries is therefore predicted to increase the resistance of short cracks to intergranular SCC.

Any further refinement of the model requires that it be related to experimental observations of intergranular SCC extensions and distributions to tune the model parameters. This is necessary in order to turn the model into a predictive tool. The first step is the identification of the sus-

ceptible boundary failure strain, ε_{sf} , which is essentially a local criterion for SCC advance. This could be estimated from experimental results without noticeable bridging. The influence of the bridging ligaments could then be determined, comparing the local crack driving force in the model with the stress intensity predicted theoretically for a non-bridged crack of the same geometry and applied load. Another tuning parameter is the failure strain of the resistant boundaries, ε_{rf} , which may be connected to twin thickness. This parameter could be estimated comparing experimental results showing failed bridging ligaments with model simulations.

Acknowledgements

The authors are grateful to Rolls-Royce Plc for the support of A.J., and BNFL Ltd., for the support of N.S. and T.J.M. The opinions expressed in this paper are those of the authors, and not necessarily those of their sponsors.

References

- [1] Watanabe T. *Res Mech* 1984;11:47.
- [2] Lim LC, Watanabe T. *Acta Metall Mater* 1990;38:2507.
- [3] Watanabe T, Tsurekawa S. *Acta Mater* 1999;47:4171.
- [4] Lehockey EM, Palumbo G, Lin P, Brennenstuhl AM. *Scripta Mater* 1997;36:1211.
- [5] Gertsman VY, Bruemmer SM. *Acta Mater* 2001;49:1589.
- [6] Palumbo G, King PJ, Aust KT, Erb U, Lichtenberger PC. *Scripta Metall Mater* 1991;25:1775.
- [7] Gertsman VY, Janeczek M, Tangri K. *Acta Mater* 1996;44:2869.
- [8] Lehockey EM, Brennenstuhl AM, Thompson I. *Corros Sci* 2004;46:2383.
- [9] Engelberg DL, Marrow TJ, Newman RC, Babout L. In: Shipilov S, editor. *Environmentally Induced Cracking of Materials*. Elsevier; 2005.
- [10] Marrow TJ, Babout L, Jivkov AP, Wood P, Engelberg D, Stevens N, et al., *J Nucl Mater* [in press].
- [11] Thomas LE, Bruemmer SM. *Corrosion* 2000;56:572.
- [12] Marrow TJ, Babout L, Connolly BJ, Engelberg D, Johnson G, Buffiere J-Y, et al. In: Shipilov S, editor. *Environmentally Induced Cracking of Materials*. Elsevier; 2005.
- [13] Wei YJ, Anand L. *J Mech Phys Solids* 2004;52:2587.
- [14] ABAQUS User's manual, version 6.4, Abaqus Inc.; 2004.
- [15] Tada H, Paris PC, Irwin GR. *The stress analysis of cracks handbook*. New York (NY): ASME; 2000.
- [16] Jivkov AP, Stevens NPC, Marrow TJ. In: Brebbia CA, DeGiorgi VG, Adey RA, editors. *Simulation of electrochemical processes*. WIT Press; 2005. p. 217.